Effects of Nucleon and Nuclear Structure in Neutrino Interactions

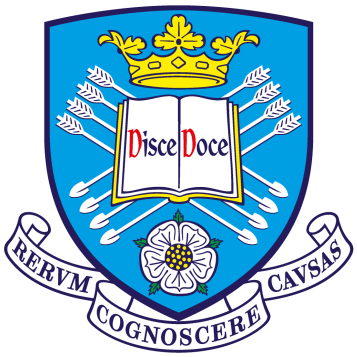

Patrick Stowell

Supervisor: Dr. Susan Cartwright

Department of Physics and Astronomy
University of Sheffield

A thesis submitted in fulfilment of the requirements for the degree of
Doctor of Philosophy in Physics

January 2019

Acknowledgements

First and foremost, I would like to thank Susan Cartwright for acting as my supervisor throughout my undergraduate and PhD studies. She has always pushed me to take every oppurtunity that peaked my interest, and her detailed comments have been invaluable when preparing this thesis. I must also thank Lee Thompson, without whom I would likely have never even started a PhD in the first place, and who has always been available to offer advice when needed.

I would also like to thank all the people I have had the pleasure of sharing on office with over the past few years. In particular, I'd like to thank Jon Perkins, for putting up with my neverending coding questions, Leon Pickard, for many hilarious nights out in Tokai, and Callum Wilkinson, for sparking my interest in neutrino interaction generators in the first place.

Working as part of the NUISANCE team has been the most satisfying part of my PhD only because I had the pleasure to work alongside Luke Pickering, Callum Wilkinson, and Clarence Wret. I owe each of them a great deal. All of the analyses in this thesis have benefited in some way from their insights.

I have enjoyed working as part of the T2K collaboration during my studies, and I must thank all those that made my visits to Japan an unforgettable experience. I am grateful to the members of the neutrino interactions working group for their feedback on the work presented in this thesis. In particular I would like to thank Sara Bolognesi, Yoshinari Hayato, Ryan Terri, and Kevin McFarland, for their valuable inputs as NIWG convenors over the years. I would also like to thank Kendall Mahn, for always being available for a friendly chat when faced with a problem. Her immense drive and enthusiasm has been an inspiration to me.

I would also like to thank the MINERvA collaboration for their hospitality during my stay at Fermilab. In particular, I would like to thank Minerba Betancourt for all her help, and Steve Dytman and Gabe Perdue for their guidance on the inner workings of GENIE.

I must also thank my family and friends for their support the last few years. Finally, I would like to thank Thalia, for being a constant source of love and support when it was needed most.

The work in this thesis was funded by the UK Science and Technolgies Facilities Council. The work presented in Chapter 8 was also partly supported by the Fermilab Neutrino Physics Center Scholar program.

Abstract

As the precision of neutrino experiments is steadily improving, new data is beginning to highlight problems with current models of neutrino interactions. There exist several unresolved tensions within the global neutrino scattering dataset, and faced with these problems, experiments are forced to turn to data-driven models with errors that can span the spread in experimental observations. The NUISANCE software package was developed to provide a flexible framework for the community to use in the building of these models. This thesis focuses on the extraction of empirical model corrections, to account for several observed tensions in the global scattering dataset, that could have an impact on the T2K oscillation analysis.

Charged current neutrino interaction measurements from MiniBooNE are used to study systematic shifts when tuning the NEUT event generator under different sterile neutrino mixing hypotheses. The results are used to derive an error rescaling method for use in future T2K short baseline oscillation fits.

Alternative models for the quasi-elastic axial form factor are developed, and implemented into NEUT. Data from neutrino-deuterium scattering is used to test each model's implementation, and extract systematic uncertainties for input to the T2K long baseline oscillation analysis. In addition, NEUT predictions are compared to CC-inclusive data from the MINERvA experiment, highlighting a clear deficiency in its CC0π model. An empirical correction to both the quasi-elastic and multi-nucleon contributions is developed to account for this.

Exclusive data from MINERvA is also used to test the GENIE event generator's pion production model. The standard GENIE dials are found to provide insufficient coverage of the chosen datasets, and clear tensions are found between these results and earlier tunings to deuterium scattering data. An ad-hoc model correction is developed to account for disagreements in the muon scattering angle distributions, reducing the tensions in the joint fits.

Table of contents

List of figures

List of tables

Chapter 1

Introduction

The first experimental hints of the existence of the neutrino came with the discovery of radioactive decay. It was suggested by Pauli in 1930 that an apparent lack of energy conservation in beta decay could be explained by the existence of an additional, electrically neutral, spin $1/2$ particle [1]. The presence of this particle , which came to be known as the 'neutrino', in the final state of beta decays, provided a path for the missing energy to be taken away. A formal theory for this was developed by Fermi in 1934 [2] that suggested neutrinos may be experimentally observed through a similar process, invese beta decay ($\nu_e + p \rightarrow e^- + n$). Unfortunately, in the same year, Bethe and Peierls used Fermi's theory to calculate the cross-section for this interaction, finding it to be too small to detect using the radioactive neutrino sources available at the time [3].

It took a further 20 years from being postulated for the neutrino's existence to be experimentally proven. With the harnessing of nuclear power came a terrestrial source of neutrinos that could provide sufficient statistics to overcome the limitations of the small neutrino cross-section. In 1953 Reines and Cowan attempted to detect neutrinos from the Hanford nuclear reactor using cadmium-loaded liquid scintillator to observe the reaction $\bar{\nu}_e + p \rightarrow e^+ + n$ [4]. The positron annihilation, followed by a delayed neutron capture on cadmium, would provide two clear gamma ray signatures that could be used to identify the reaction. Unfortunately the experiment was severely limited by backgrounds and did not provide conclusive evidence of the detection of a free neutrino. In 1955 Ray Davis also attempted to detect neutrinos from the Brookhaven reactor using a chlorine based detector to search for the process $\nu_e + {}^{37}\mathrm{Cl} \rightarrow {}^{37}\mathrm{Ar} + e^-$ [5], but observed no enhancement over the cosmic-ray background. Then in 1956 Reines and Cowan set a lower limit on the half-life of neutrino-less double beta decay in ${}^{180}\mathrm{Nd}$, coming to the conclusion that the neutrino may be a Dirac particle. This result suggested that neutrinos generated from beta decay are different from the antineutrinos produced in nuclear reactors, explaining the null result in Ray Davis' experiment. In the very same year, Reines and Cowan worked to scale up their original experiment and move it to the Savannah River nuclear reactor, and with a large reduction in cosmic ray backgrounds they were able to finally prove they had detected neutrinos [6].

In 1948 it was found that muons, μ, (discovered much earlier in 1937 [7]) decayed with a continuous energy spectrum characteristic of 3 body decay. The lack of observations of $\mu^- \to e^- + \gamma$ channels when studying these decays [8] led to the introduction of lepton flavour number, predicting that there must be at least 2 distinct flavours of neutrinos, ν_e and ν_μ, to mirror their charged lepton counterparts. If lepton number is conserved in the standard model then the dominant muon decay channel is $\mu^- \to e^- + \bar{\nu}_e + \nu_\mu$. In 1962 the AGS experiment at BNL produced the first accelerator neutrino beam, using the pion decay-in-flight method still used by modern experiments [9]. Over 99% of charged pions will decay through the $\pi^{+(-)} \to \mu^{+(-)} + \nu_\mu(\bar{\nu}_\mu)$ channel, producing an intense source of muons and neutrinos. A spark chamber placed in the path of this neutrino beam at BNL observed charged-current interactions which produced charged leptons in the final state. Analysis of the data showed a much larger ratio of muon to electron type final state leptons being produced than predictions for if there was only a single neutrino flavour. This result suggested that neutrino flavour must be intrinsically tied to the lepton flavour present at its production point, and in doing so, proved the existence of the muon neutrino.

The tau, τ, was discovered in 1976 at SLAC [10], and its existence suggested an additional neutrino flavour must be added to ensure lepton number was still conserved. In 1989 analyses of Z^0 decay widths at the LEP experiments provided indirect constraints on the possible particles that couple to the Z^0 boson, and supported claims that there must be a third type of neutrino. When all observed channels are subtracted from the Z^0 decay widths, the remaining invisible width shown in Figure 1.1 is assumed to be from decays into neutrinos with $2m_\nu < m_Z$. A combination of all the LEP analyses under this assumption provides a constraint on the number of active neutrinos to be $N_\nu = 2.984 \pm 0.0082$ [11]. In 2000 the DONUT experiment finally observed tau neutrinos [12], completing the set of active light neutrinos currently included in the standard model.

1.1 Neutrino Anomalies

By the 1950s a number of neutrino experiments had already been successfully performed. Around this time it was suggested that neutrinos might prove useful in resolving ongoing debates concerning the fusion processes that powered the sun. John Bahcall used the Standard Solar Model (SSM), which was being developed at the time [13], to calculate the expected flux of neutrinos from each of the different solar fusion chains (see Figure 1.2). His hope was that a direct measurement of these neutrinos would provide an independent way to test the SSM. In 1955 he worked with Ray Davis to produce a redesigned version of the earlier Ray Davis reactor experiment, moving it to the Homestake mine where backgrounds would be severely reduced in preperation for a solar neutrino measurement. The threshold reaction for the Homestake experiment was 814 keV, making it sensitive to only a small sample of the contributing solar neutrino flux predicted by the SSM in Figure 1.2. Analysis of the data showed around one third of the rate predicted by the SSM in this region, and doubt was cast on both the precision of the experiment and the expected neutrino flux

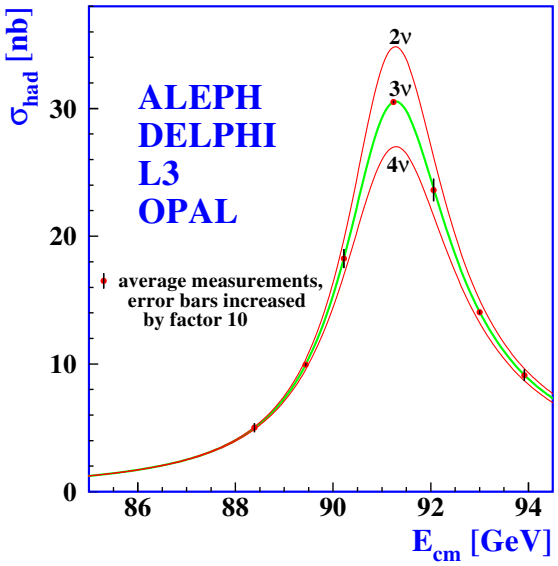

Fig. 1.1 Experimental data from the ALEPH, OPAL, L3, and DELPHI, experiments on the hadron production cross-section near the Z^0 resonance. The presence of additional neutrinos modify the invisible decay width of the Z boson, allowing constraints on the total neutrino count to be obtained. The predicted curves for the 2, 3, and 4 possible neutrinos coupling to the Z boson are shown overlaid. Figure taken from [11].

calculation [14]. Since the Homestake experiment only measured the higher energy region of the solar neutrinos, critics at the time suggested that changes in the assumptions on the inner structure of the sun could give rise to such large variations in this region of the model.

Nevertheless the Kamiokande experiment later confirmed Homestake's results [15]. Using 3 kilotons of pure water monitored by photomulitplier tubes, the Kamiokande experiment observed neutrino interactions by looking for Cerenkov radiation produced by the charged leptons in the final state of neutrino scattering events. The size, cleanliness, and direction of the observed cones of Cerenkov radiation observed in the Kamiokande experiment allowed the experiment to discriminate between electron and muon type neutrinos, estimate the incoming neutrino energy, and track the direction of the incoming neutrino on an event-by-event basis. Using a drastically different analysis technique to the Homestake experiment, the Kamiokande experiment still observed a reduction in the ν_e rate compared to that predicted by the SSM. In addition, the measurement of $\nu_x + e^- \rightarrow \nu_x + e^-$ allowed the Kamiokande detector to confirm that the neutrinos were indeed coming from the sun. The gallium based experiments, SAGE[16] and GALLEX [17], also observed a flux deficit, and their lower threshold of 233 keV meant the problem could be shown to exist down to even lower energies in the total SSM neutrino flux, further disputing some of the early criticisms of the homestake result. The gallium experiments both found a deficit of $\sim 50-60\%$ in the solar neutrino flux and the mounting evidence came to be known as the 'solar neutrino problem'.

In the late 1980s both the Kamiokande and IMB experiments also measured a deficit in the flux of muon neutrinos originating from cosmic rays. When high energy charged particles strike the

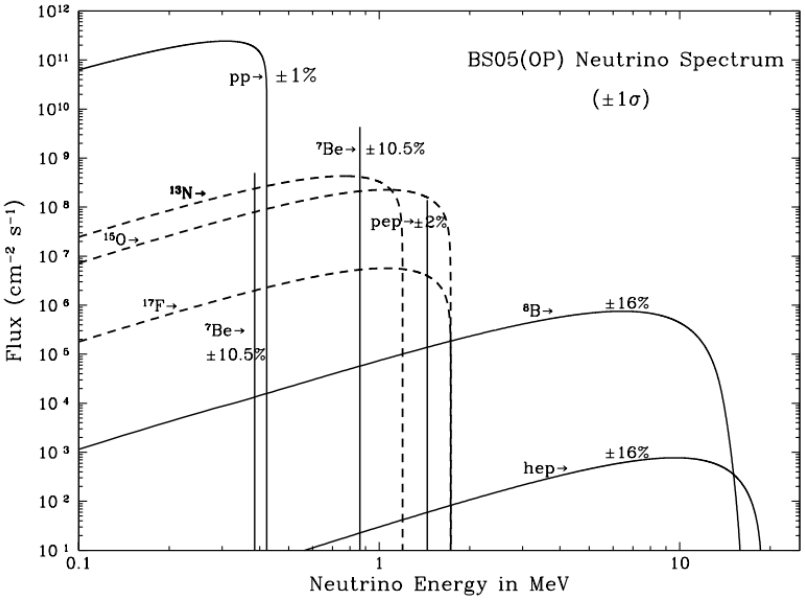

Fig. 1.2 SSM neutrino flux distributions as a function of energy for different components of the solar fusion chains. The solid lines indicate contributions from the dominant pp fusion chain, whilst the dashed lines show the contributions from the CNO cycle. Figure taken from [13].

upper atmosphere hadronic showers are produced. Many of the particles produced in these showers re-interact, or decay as they propogate down towards the earth's surface. Pions produced in these interactions decay via the $\pi^+ \rightarrow \mu^+ + \nu_\mu$ channel, and muons decay via the $\mu^+ \rightarrow e^+ + \nu_e + \bar{\nu}_e$ channel. Therefore one would expect a ratio of the number of electron and muon type neutrino events to be on the order of $N_e/N_\mu \sim 2/1$. When probing this ratio however, the Kamiokande experment observed an unexplained reduction in the muon neutrino rate, whilst the electron neutrino flux was still consistent with theory [18, 19]. This result came to be known as the atmospheric neutrino anomoly.

In fact, a solution for both the 'solar neutrino problem' and the 'atmospheric neutrino anomaly' had been suggested in 1967 by Bruno Pontecorvo [20], that the neutrino has a finite probability of changing its flavour as it propagates, and that in all the anomalous experiments these neutrino oscillations were causing the observed flux deficit.

1.2 Neutrino Oscillations

Whilst the flavour of charged leptons can be identified by both their mass and possible decay channels, the flavour of neutrinos are only identified by the properties of the observed charged lepton at an interaction vertex. Since their mass is not observed directly, their flavour state, $|\nu_\alpha\rangle$, can

be described as a superposition of possible mass states, $|\nu_i\rangle$, with the Pontecorvo-Maki-Nakagawa-Sakata (PMNS) rotation matrix defining the relative contributions from each state. Following the derivation in [21], the mass states can be described as

$$\begin{pmatrix} |\nu_1\rangle \\ |\nu_2\rangle \\ |\nu_3\rangle \\ \vdots \\ |\nu_N\rangle \end{pmatrix} = U \begin{pmatrix} |\nu_e\rangle \\ |\nu_\mu\rangle \\ |\nu_\tau\rangle \\ \vdots \\ |\nu_s\rangle \end{pmatrix}, \tag{1.1}$$

where U is the $N \times N$ PMNS matrix defining the relative contributions of each of the N flavour states to a single mass state. This is formed from the product of all the individual possible rotation matrices between each mass and flavour state.

In the case of simple two-neutrino mixing between ν_e and ν_μ states, the matrix is given by a simple (2×2) rotation matrix,

$$U_{2\nu} = \begin{pmatrix} U_{e1} & U_{e2} \\ U_{\mu 1} & U_{\mu 2} \end{pmatrix} = \begin{pmatrix} \cos\theta & \sin\theta \\ -\sin\theta & \cos\theta \end{pmatrix}. \tag{1.2}$$

If neutrinos are assumed to be plane waves travelling through a vacuum then the evolution of a single neutrino's flavour is given in terms of the propagation of each mass state as

$$|\nu_\alpha(t)\rangle = \sum_i^N U^*_{\alpha i} e^{-i(E_i t - \vec{p}_i \vec{x}_i)} |\nu_i\rangle . \tag{1.3}$$

A neutrino produced at the origin with flavour state α therefore has a probability of being detected in flavour state β given by

$$P(\nu_\alpha \to \nu_\beta) = |\langle \nu_\alpha | \nu_\beta(t) \rangle|^2 = \left| \sum_i^N U^*_{\alpha i} U_{\beta i} e^{-i(E_i t - \vec{p}_i \vec{x}_i)} \right|^2 . \tag{1.4}$$

If we assume that neutrinos are ultra-relativistic with a speed close to c, and they travel a distance L in time t, then the propagation term can be simplified by assuming all neutrinos are created with the same energy, E, as

$$-i(E_i t - \vec{p}_i \vec{x}_i) \approx \frac{m_i^2 L}{2E}. \tag{1.5}$$

A proper derivation of the neutrino oscillations using wave-packets that does not rely on this assumption is derived in [22], but ultimately results in the same oscillation probability as that shown in Equation (1.11), so is neglected here. The survival, $P(\nu_e \to \nu_e)$, and dissappearance, $P(\nu_e \to \nu_\mu)$, probabilities for electron neutrinos can therefore be expanded from Equations (1.4)

and (1.11) to be

$$P(\nu_e \to \nu_e) = 1 - \sin^2 2\theta \sin^2 \left(\frac{\Delta m^2_{21} L}{4E} \right), \tag{1.6}$$

$$P(\nu_e \to \nu_\mu) = \sin^2 2\theta \sin^2 \left(\frac{\Delta m^2_{21} L}{4E} \right). \tag{1.7}$$

The sinosuidal nature of these probabilities is why the neutrinos are considerred to "oscillate". In an electron neutrino beam with fixed energy, the contribution from muon neutrinos in the beam oscillates as a function of the distance travelled. The effect of these oscillations is maximal when $\frac{\Delta m^2_{21} L}{4E} = \pi/2$. Since the mass splittings are goverened by nature, the experimental choices of E and L (reffered to as the baseline), dictate an experiments sensitivity to a particular mass splitting region.

Of course if the PMNS matrix is diagonal (the mixing angle θ is zero in Equation (1.2)) then the neutrino flavour does not oscillate and an electron-type neutrino will always be detected in that flavour state. The introduction of non-diagonal terms to the PMNS matrix however allows neutrinos to oscillate between available flavour states. As is clear from Equation (1.7) the neutrino oscillations are only sensitive to the squared differences of the mass states, not their absolute masses, and the neutrinos need to have at least one non-zero mass for oscillations to occur.

Equation (1.7) has been derived assuming neutrinos are plane waves travelling through a vaccuum. However, as a neutrino travels through dense matter, it will experience a non-zero potential which can modify the expected oscillation behaviour [23–25]. All neutrinos are sensitive to neutral current elastic scattering, $\nu_x + e^- \to \nu_x + e^-$, however electron neutrinos are also sensitive to charged current coherent forward scattering which produces an identical final state, $\nu_e + e^- \to e^- + \nu_e$. Accounting for the additional interaction channel available to electron neutrinos further modifies their oscillation probabilities in materials with high electron densities, and is referred to as the "MSW-effect".

The introduction of neutrino oscillations provided a perfect explanation for the solar neutrino problem, in which electron neutrinos created in the core of the sun oscillate into other flavours before arriving at terrestrial detectors. The MSW effect results in neutrinos leaving the sun primarily in the second mass eigenstate. Since the ν_e eigenstate sees a smaller contribution from the ν_2 eigenstate (dictated by the magnitude of $\sin\theta$), the observed electron neutrino rate is severely reduced due to the presence of neutrino oscillations. The SNO experiment finally proved this oscillation hypothesis in 2002 using a unique heavy water detector that was capable of observing charged current $\nu_e + {}^2\mathrm{H} \to p + p + e^-$, neutral current $\nu_x + {}^2\mathrm{H} \to p + n + e^-$, and elastic scattering $\nu_x + e^- \to e^- + \nu_x$ interactions [26]. Whilst charged current rate measurements are sensitive to only the electron neutrino component of the flux, elastic and neutral measurements are also sensitive to the muon and tau components, providing a simultaneous verification of the total solar neutrino flux.

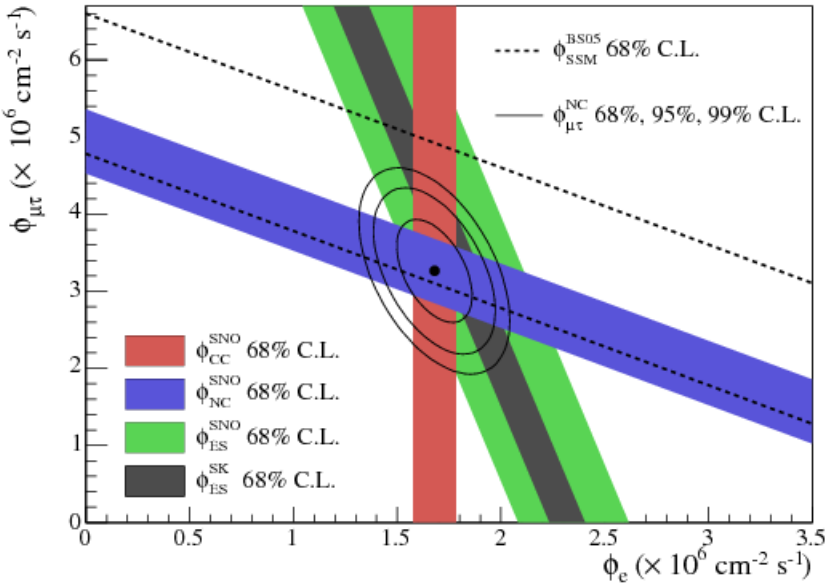

Fig. 1.3 Constraints on the fluxes of electron, and muon and tau neutrinos originating from the sun in the SNO experiment. Bands are obtained from measurements of several different interaction channels. The red band shows the reduction in electron type neutrinos relative to the other flavours, consistent with the Homestake results. The combination of all 3 measurements from SNO is consistent with the SSM prediction for the total solar neutrino flux. Figure take from [27].

A combined analysis of both these channels measured the flux of electron neutrinos and all neutrinos to be

$$\phi^{CC}(\nu_e) = (1.76 \pm 0.10) \times 10^6 \text{cm}^{-2}\text{s}, \tag{1.8}$$

$$\phi^{NC}(\nu_e + \nu_\mu + \nu_\tau) = (5.09 \pm 0.64) \times 10^6 \text{cm}^{-2}\text{s}, \tag{1.9}$$

$$\phi^{ES}(\nu_e + \nu_\mu + \nu_\tau) = (2.39 \pm 0.26) \times 10^6 cm^{-2}\text{s}, \tag{1.10}$$

producing a strong confirmation that only the electron neutrino component was reduced, and the total flux of solar neutrinos was still consistent with theory, as shown in Figure 1.3. This proved that John Bahcall's early flux experiments were correct and the reduction in electron neutrinos was consistent with $\nu_e \rightarrow \nu_x$ neutrino oscillations.

In addition to the SNO result, in 1998 the upgraded Super-Kamiokande (SK) detector, armed with a boost in statistics, was able to bin its atmospheric neutrino measurement as a function of both neutrino energy and zenith angle [28]. This showed that there was a clear up-down asymmetry in the detector as shown in Figure 1.4. If two cosmic ray neutrinos are observed travelling in opposite directions at sea level, and are assumed to have both been created at similar altitudes on exactly opposite sides of the earth, then the difference in travelled distance between the two is equal to the diameter of the earth. This assumption can be extended to all angles to derive a relationship between a cosmic ray neutrino's reconstructed direction and the its total propagation distance.

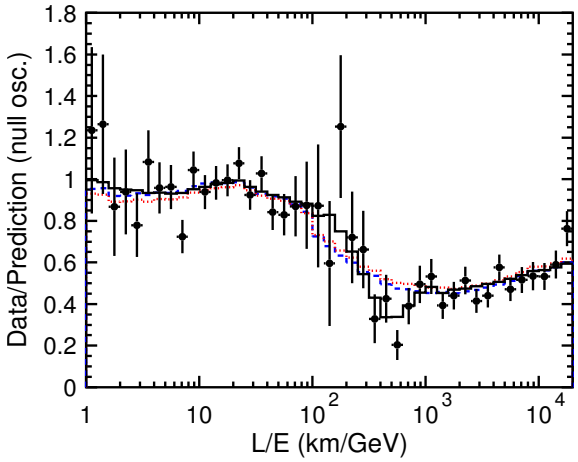

Fig. 1.4 Experimental data from Super-Kamiokande on atmospheric neutrino oscillations. The angle of the incoming neutrino is used to infer an oscillation baseline distance, L, from its assumed trajectory through the earth. The data shows a reduction at high L/E which is consistent with upward going neutrinos undergoing $\nu_\mu \rightarrow \nu_\tau$ oscillations (black solid line). The blue and red lines show predictions from alternative neutrino decoherence and decay solutions respectively which were also suggested at the time but have a worse goodness of fit with the data. Figure taken from from [29].

When applying this assumption, the SK result was found to be consistent with muon-neutrinos oscillating into tau-neutrinos as they passed through the Earth, producing a larger reduction at high neutrino angles, where the total oscillation distance was greatest. This result lead to a Nobel prize alongside the SNO result in 2015 for the discovery of neutrino oscillations.

Since then the picture of neutrino oscillations has advanced significantly with constraints placed on a number of the parameters that govern how neutrinos mix. We know that oscillations must occur between all three of the active flavour and mass states. In a N neutrino mixing scenario, the probability of a neutrino in flavour state α to be observed in another flavour state β is given by

$$P_{\alpha\beta} = \delta_{\alpha\beta} - 4\sum_{i>j}^{N} Re\left(U^*_{\alpha i}U_{\beta i}U_{\alpha j}U^*_{\beta j}\right) sin^2\left(\frac{\Delta m^2_{ij}L}{4E}\right) \pm 2\sum_{i>j}^{N} Im\left(U^*_{\alpha i}U_{\beta i}U_{\alpha j}U^*_{\beta j}\right) sin^2\left(\frac{\Delta m^2_{ij}L}{2E}\right), \quad (1.11)$$

where the mass splitting $\Delta m^2_{ij} = m^2_i - m^2_j$. The $\pm$ term denotes neutrino and anti-neutrino oscillations respectively since the complex conjugate of U must be taken in Equation (1.1) when dealing with antineutrinos. For three neutrinos, the mixing matrix must be defined by at least three rotation

matrices as

$$U = \underbrace{\begin{pmatrix} c_{12} & s_{12} & 0 \\ -s_{12} & c_{12} & 0 \\ 0 & 0 & 0 \end{pmatrix}}_{\text{solar}} \underbrace{\begin{pmatrix} c_{13} & 0 & s_{13}e^{-i\delta_{CP}} \\ 0 & 0 & 0 \\ -s_{13}e^{i\delta_{CP}} & 0 & c_{13} \end{pmatrix}}_{\text{accelerator+reactor}} \underbrace{\begin{pmatrix} 0 & 0 & 0 \\ 0 & c_{23} & s_{23} \\ 0 & -s_{23} & c_{23} \end{pmatrix}}_{\text{atmospheric}}, \tag{1.12}$$

where $c_{ij} = \cos\theta_{ij}$, $s_{ij} = \sin\theta_{ij}$, and each matrix is labelled by the experimental regimes where they have the dominant effect. Solar neutrino oscillation experiments set a strong constraint on θ_{12}, accelerator and reactor driven experiments observe θ_{13}, and atmospheric experiments can probe θ_{23}. In practice, due to the correlated nature of the PMNS matrix, global fits between multiple experimental regimes have provided the best constraints on each of these parameters. In the three neutrino mixing case an additional complex phase, δ_{CP}, must be added that accounts for CP violation introducing differences between the neutrino mixing and antineutrino mixing sectors[1]. This means mixing between the three active neutrinos can be fully described by a total of three mixing angles, two mass splittings (because $\Delta m^2_{13} = \Delta m^2_{23} \pm \Delta m^2_{12}$), and one complex phase.

Global fits to the Daya Bay, Double Chooz, and RENO reactor experiments by the particle data group have led to the constraint of $\sin^2\theta_{13} = 0.0219 \pm 0.0012$ eV^2 [30]. The best constraint on θ_{12} currently comes from a combined fit to both solar neutrino data and reactor neutrino data from the KamLAND experiment, measuring neutrino oscillations from 53 different reactor sources at Kamioka mine [31]. This places the constraint of $\tan^2\theta_{12} = 0.436 \pm 0.029$ and $\Delta m^2_{21} = \left(7.53 \pm 0.18 \times 10^{-5}\right)$ eV^2. The MSW effect, whilst negligible in reactor experiments, must be taken into account when considering the propagation of neutrinos through dense solar material. Since the effect is sensitive to the sign of the mass splitting, the joint fit also places the constraint that $m_2 > m_1$.

In accelerator neutrino experiments, both L and E in Equation (1.11) can be tuned by changing the neutrino beam properties and experimental baseline. These experimental parameters are chosen such that the combined L/E ratio sits at the maximal mixing value for the given mass splitting of interest (so that $(\Delta m^2_{ji} L/E) \sim \pi/2$) to maximise an experimental sensitivity. For long baseline neutrino experiments, an additional near detector is also usually placed close to the beam source so that the flux can be constrained at the production point assuming the dominant oscillations occur over the much larger oscillation baseline L. Current experiments like T2K sit at baselines such that neutrinos do not propagate through enough matter for the MSW effect to introduce sensitivity to the mass ordering of the m_2 and m_3 states. As a result, current accelerator and atmospheric neutrino experiments have only been sensitive to the absolute value of $|\Delta m^2_{32}|$, with both a normal hierarchy (NH, $m_1 < m_2 < m_3$), and an inverted hierarchy (IH, $m_3 < m_1 < m_2$) being allowed by the experimental data. Note that whilst the MSW effect is small for current accelerator neutrino

[1] A complex phase must actually be considered in each of the rotation matrices, but in two-neutrino mixing this is constrained to be zero, and in three-neutrino mixing the unitarity constraint can be used to rotate the matrix into a basis where only one phase must be considered.

oscillation analyses, it can introduce a CP-violating like effect when comparing neutrino and antineutrino oscillations that must be taken into account when trying to constrain δ_{CP}.

Since oscillation experiments observe only the oscillated event rate, they are only sensitive to the non-trivial combination of all relevant angle and mass splitting terms in Equation (1.11). This means that the extraction of the individual mixing parameters usually results in highly correlated best fit parameters which depend on the mass hierarchy assumption. The parameters $\sin^2\theta_{23}$ and Δm^2_{32} are are often quoted together because of this, as the assumption of normal or inverted hiearchies can modify their values. Most recently T2K has placed the constraint of $\sin^2\theta_{23} = 0.55^{+0.05}_{-0.09}$ for normal hierachy ($0.55^{+0.05}_{-0.08}$ for IH), and $|\Delta m^2_{32}| = 2.54 \pm 0.08 \times 10^{-3}$ eV^2 ($2.51 \pm 0.08 \times 10^{-3}$ eV^2 for IH), using both T2K data and the reactor constraints on θ_{13} [32].

With the angles and mass splittings that govern neutrino oscillations constrained to a better than 10% level, the remaining uncertainty on the PMNS matrix comes from the mass hierarchy problem and the unknown value of δ_{CP}. Both the T2K and NOvA experiments have produced the first hints that δ_{CP} may be non-zero [32, 33], a finding that would help to explain the baryon asymmetry in the universe. Unfortunately these experiments currently only place weak constraints on the CP violating phase. The future generation of long baseline neutrino oscillation experiments such as the liquid argon based Deep Underground Neutrino Experiment (DUNE) [34], and Hyper-Kamiokande Experiment [35], hope to place more stringent limits on δ_{CP}, alongside measuring the parameters in the PMNS matrix to an unprecedented level of precision. In DUNE, this will be achieved by measuring neutrino oscillations in a long baseline experiment with a wide band neutrino energy beam capable of sampling multiple oscillation peaks. In addition the use of liquid argon, with excellent muon to electron discrimination will reduce systematics. In HyperK this will be achieved by using a kiloton scale near and far detector to significantly reduce statistics, and potentially a gadolinium doped water tank to reduce background systematics by tagging final state neutrons in events. The improved statistics of these experiments may also allow them to probe the mass hierarchy of the m_2 and m_3 states through observation of the subtle MSW effect over their long baselines.

Whilst there are still details requiring further investigation, the discovery of neutrino oscillations provides direct evidence that neutrinos have a non-zero mass, and the standard model, which includes them as massless, requires extension. If right handed neutrinos are added to the standard model then it becomes possible for the neutrino to acquire a Dirac mass in the same way the other charged leptons do. However, this procedure does not explain why the neutrino masses are so much smaller than their charged counterparts.

In the Type 1 See-Saw model [36] this is addressed by introducing right handed Majorana neutrinos ($\nu = \bar{\nu}$) so that both Dirac and Majorana terms contribute to the Lagrangian. Assuming the presence of only a single neutrino flavour, the mass term can be described in terms of the left and right

handed neutrino fields, ν_L and ν_R, and the Dirac and Majorana masses, M_D and M_R, as

$$L = \frac{1}{2}\begin{pmatrix}\nu_L & \nu_R\end{pmatrix}\begin{pmatrix}0 & M_D\\ M_D & M_R\end{pmatrix}\begin{pmatrix}\nu_L\\ \nu_R\end{pmatrix} + h.c. \tag{1.13}$$

The eigenvalues of the mass matrix then give the possible neutrino masses as

$$m_{1,2} = \frac{1}{2}|M_R + \sqrt{4M_D^2 + M_R^2}|, \tag{1.14}$$

and if the Majorana mass is assumed to be much larger than the the Dirac mass, $M_R \gg M_D$, then the mass eigenvalues become

$$m_1 \approx \frac{M_D^2}{M_R}, \quad m_2 \sim M_R. \tag{1.15}$$

Typically values on the order of the GUT scale are chosen for the Majorana mass of $M_R \sim 10^{15}$ GeV. With Dirac masses on the order of 100 GeV the first mass eigenstate can then be shown to be in agreement with current constraints on the active neutrinos of $m_1 \sim 10^{-2}$ eV^2.

Whilst providing a good explanation of the small neutrino masses, this model requires the addition of at least 3 right handed Majorana neutrinos (although additional see-saw models exist where Majorana neutrinos are not needed [37, 38]). Currently a number of experiments such as EXO are actively searching for signs that the neutrino is a Majorana particle by looking for neutrinoless double beta decay reactions, $0\nu\beta\beta$, in isotopes in which standard beta decays are energetically forbidden [39]. This decay is shown in Figure 1.5 compared to the standard Feynman diagram for two neutrino beta decay. For this decay to occur, the neutrino must be a Majorana particle that can annihilate with itself. The observation of this channel therefore provides a clear signature to determine whether the neutrino is a Dirac or Majorana particle. Whilst many of these experiments have set lower limits on the $0\nu\beta\beta$ decay lifetime [40], no clear experimental signature that the neutrino is a Majorana particle has been observed to date.

Since the weak force interacts only with left-handed particles, adding any kind of right-handed neutrino could mean introducing a particle that only experiences the gravitational force and would therefore not interact at all in existing detectors. However, if such a particle still participates in neutrino mixing it would mean that the standard (3×3) component of the PMNS matrix would be non-unitary, and its presence would leave signatures in precision neutrino oscillation experiments. Currently a number of anomalous mixing results observed at short base line oscillation experiments have shown to disagree with the three neutrino mixing paradigm, and adding more neutrinos that do not couple to the weak force has been suggested as a possible solution [41].

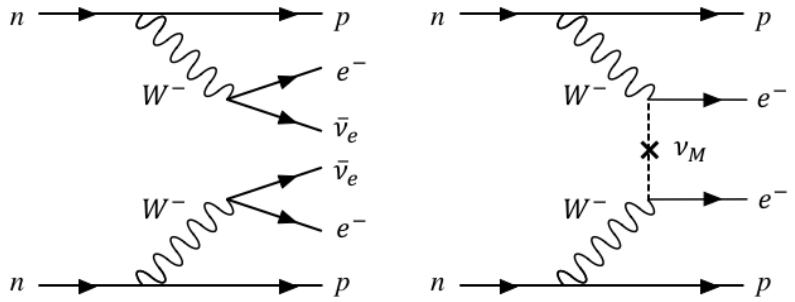

(a) $2\nu\beta\beta$ Decay (b) $0\nu\beta\beta$ Decay

Fig. 1.5 Feynman diagrams for standard and neutrinoless double beta decay. (a) Diagram for standard double beta decay. The neutrinos remove energy from the interaction producing a large spread in the electron energies. (b) Diagram for neutrinoless double beta decay. The Majorana neutrino annihilates with itself, producing only two back-to-back electrons in the final state with a fixed centre of mass energy.

1.3 Sterile Neutrinos

LSND was a liquid scintillator experiment that used pion decay at rest to study an antineutrino beam with $E_\nu < 50$ MeV. With a baseline of only 30 m ($L/E \sim 1$) LSND observed a 3.8σ excess of electron-like events [42]. This signal is consistent with short baseline $\bar{\nu}_\mu \rightarrow \bar{\nu}_e$ oscillations only if a mass splitting on the order of 1 eV^2 is present. Since the ALEPH data sets a strong constraint on the number of neutrinos coupling to the Z boson, this additional mass splitting can only be explained by $3+N$ models which include N additional neutrinos that do not interact with the weak force. These are often referred to as "sterile" neutrinos (ν_s) as they would only show up in detectors through how they modify the oscillation properties of the three active neutrinos. The addition of extra mass splittings and mixing angles to the PMNS matrix (making it a $(3+N)\times(3+N)$ matrix) could result in additional oscillation signals being observable in neutral current interactions (due to $\nu_{e,\mu,\tau} \rightarrow \nu_s$ oscillations), and oscillations between the three active flavours occurring on a much shorter baseline than expected (like in the LSND result).

Whilst the LSND experiment provides a hint that Short BaseLine (SBL) oscillations may occur, the KarMEN experiment (a similar pion decay at rest study) found no evidence for $\nu_\mu \rightarrow \nu_e$ appearance [43], and several additional causes for the LSND anomaly have been suggested, such as the incorrect modelling of neutrino interactions. In addition, at much higher energies the NOMAD experiment [44] found no evidence for neutrino oscillations, excluding $\Delta m^2 > 5.9$ eV^2 at $\sin^2 2\theta_{e\tau} = 1$ for$\nu_e \rightarrow \nu_\tau$ oscillations and $\Delta m^2 > 0.7$ eV^2 for $\nu_\mu \rightarrow \nu_\tau$ oscillations. Unfortunately these results do not fully exclude sterile neutrino mixing region offered by LSND, so the MiniBooNE

experiment [45] was designed to probe the LSND anomaly at a higher energy regime where the dominant systematics would be different but the chosen L/E would be the same.

The MiniBooNE experiment searched for sterile neutrino oscillations by looked for charged-current quasi-elastic interactions, $\nu_\mu(e) + n \to \mu(e) + p$, in a mineral oil target. Selection of either π^+ or π^- before their decay in flight allowed the Booster neutrino beam to run in both neutrino and anti-neutrino mode so that MiniBooNE could probe oscillations in both. When running in anti-neutrino mode MiniBooNE observed an excess of electron-like events in the $0.2 < E_\nu < 1.25$ GeV region, consistent with the LSND result [46]. When running in neutrino mode MiniBooNE saw an excess of electron like events below 0.475 GeV, but there is a mild tension between the neutrino and antineutrino results as shown in Figure 1.6.

In the limit of one relatively large mass splitting the oscillation formula in Equation (1.11) reduces to the simple two neutrino mixing probability shown in Equation (1.7) (since $\Delta m^2_{42} \gg \Delta m^2_{32} \gg \Delta m^2_{21} \approx 0$). In the two neutrino mixing case CP phases are not present so that $P(\nu_\mu \to \nu_s) = P(\bar{\nu}_\mu \to \bar{\nu}_s)$. Because of this, there is significant tension when trying to fit both MiniBooNE datasets at once within a $3+1$ framework, with additional neutrinos needing to be added to the model to explain the observed $\nu_\mu/\bar{\nu}_\mu$ differences. This tension is one of the reasons the MiniBooNE and LSND results are still debated, with some suggesting that the low energy excess could arise from misidentified low energy NC$\gamma\gamma$ interactions in the detector. The MicroBooNE experiment [47] hopes to understand this problem by using a liquid argon detector to further probe the MiniBooNE low energy excess.

Several other experiments have also hinted that sterile neutrino oscillations may exist. An updated prediction of the reactor antineutrino flux has suggested the theoretical prediction needs to be enhanced by around 3% at approximately 5 MeV [48], which has prompted the reanalysis of a number of short baseline reactor neutrino oscillation experiments (< 100 m). A number of these experiments, that rely on a predetermined neutrino flux, now observe a deficit in the neutrino rate when compared to the new theoretical prediction. A combined analysis of the short baseline reactor experiments has yielded the ratio $N_{\text{measured}}/N_{\text{expected}} = 0.927 \pm 0.023$ [49], and short baseline sterile neutrino oscillations have been suggested as a possible solution to this so called "reactor neutrino anomaly".

The gallium based solar neutrino experiments, SAGE, and GALLEX, have also suggested neutrino oscillations may occur on extremely short baselines. When using intense radioactive ^{51}Cr and ^{37}Ar sources to calibrate detector response, both experiments observed a $14 \pm 5\%$ reduction in the rate of neutrinos when comparing to the known activity of each source [50]. This 2.8σ deficit is referred to as the "Gallium Anomaly" and has been shown to agree with $3+N$ mixing models where the introduction of a larger mass splitting on the order of 1 eV^2, similar to the LSND result, causes the neutrinos to oscillate over an extremely short baseline on the scale of the size of each detector.

Whilst the experiments outside of the few GeV range do not suffer from the problems of cross-section modelling, several solutions that do not involve sterile neutrinos have also been suggested for

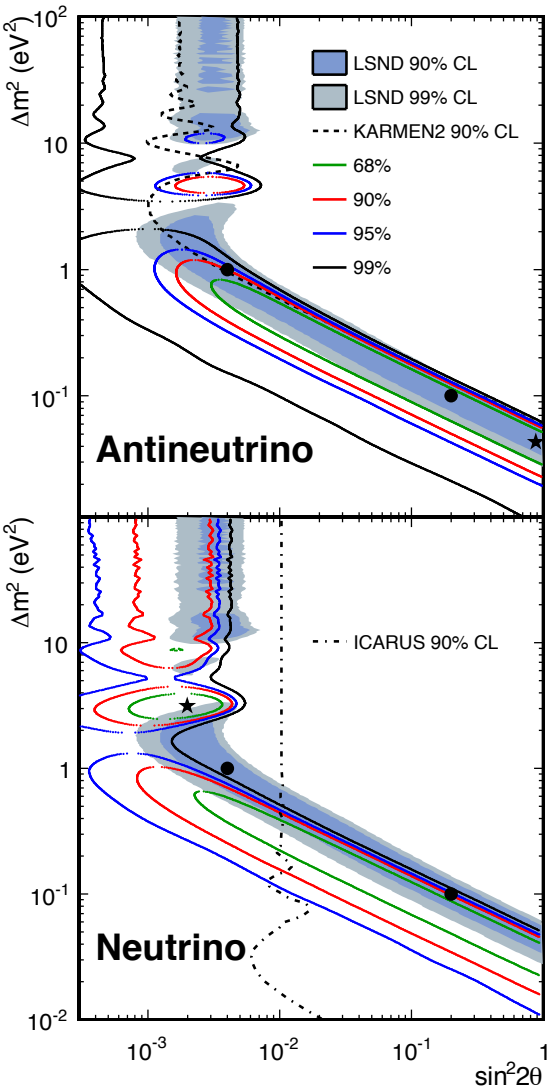

Fig. 1.6 Comparison of the mixing parameter contours extracted from the individual MiniBooNE neutrino and anti-neutrino results to the LSND allowed regions of parameter space. The coloured contours show allowed regions of the mixing space. The LSND result can be seen to agree with the MiniBooNE data, whilst the KARMEN experiment can be seen to exclude the high mass splitting region of the anti-neutrino analyses. Figure taken from [46].

them. It is possible that the reactor flux systematics are underestimated and that further reanalysis of the models will give uncertainties that are consistent with a no sterile oscillation hypothesis [51]. Similarly, problems with the calculation of transitions to excited states in Gallium experiments could explain their observed deficit [52]. These arguments are compounded by several experiments failing to find strong evidence for sterile neutrino oscillations. Analyses of Super-K data have shown that the observed atmospheric oscillations cannot be fully explained by mixing with a sterile state [53], although admixtures of sterile and τ neutrino oscillations have not yet been ruled out [54]. The IceCube experiment has also found no evidence for atmospheric neutrino oscillations consistent with sterile neutrino models, placing strong exclusion limits on a $3+1$ model extending down as low as $\sin^2(2\theta_{24}) \leq 0.02$ [55].

Neutral Current (NC) interactions have the potential to provide stringent constraints on sterile neutrino mixing as they are sensitive to sterile disappearance oscillations ($\nu_\alpha \rightarrow \nu_s$) for any active flavour α. Recently an analysis of NC events at the NOvA near and far detectors found no evidence of sterile neutrinos, placing limits on a $3+1$ mixing space [56]. The MINOS experiment has also observed no evidence for $\nu_\mu \rightarrow \nu_s$ oscillations in a near and far detector simultaneous fit that included both charged-current and NC interactions [57], and a joint fit of the MINOS and reactor data has been shown to exclude the regions of parameter space allowed by MiniBooNE and LSND at a 95% confidence limit [58].

If sterile neutrinos were brought into thermal equilibrium in the early universe then their presence would affect a number of cosmological features such as the Cosmic Microwave Background (CMB) power spectrum and large scale structure formation [59]. Observation of these cosmological properties therefore allows limits to be placed on their properties, being sensitive to both the effective number of neutrinos, N_{eff}, that are affected by the gravitational field (unlike the ALEPH result), and the combined neutrino mass. In 2015, analysis of the Planck measurements of the CMB spectrum were used to set the constraints $N_{\text{eff}} = 3.13 \pm 0.32$ and $\sum m_\nu < 0.68$ eV^2 using Planck data alone [60], whilst combinations of the Planck data and other cosmological observations have been shown to further reduce this limit to $\sum m_\nu < 0.023$ eV^2 and $N_{\text{eff}} = 3.04 \pm 0.18$. Recently a combined analysis of cosmological and accelerator constraints was also used to translate the cosmological constraints into a sterile neutrino oscillation parameter space, excluding mixing angles as low as $\sin^2\theta_{24} > 10^{-4}$ in some cases [61], but this limit is strongly dependent on the effective number of sterile neutrinos.

Trying to account for all available constraints is a significant challenge for sterile neutrino models (especially in a $3+1$ framework) but it is clear that understanding the effect these oscillations could have will play an important role in the future, for both short-baseline and long-baseline oscillation experiments. Importantly our existing knowledge of neutrino interactions in the few-GeV region are a result of direct measurements using short baseline experiments assuming no oscillations are present. Whilst some inputs to neutrino cross-section modelling come from electron scattering experiments, there remain parts of the weak interaction that can only be constrained by accelerator

neutrino experiments. Therefore, if sterile neutrino oscillations with $\Delta m^2_{14} \sim 1$ eV^2 are shown to exist, then their effect on both short baseline oscillation *and* cross-section analyses needs to be fully understood when trying to study the mixing behaviour in the active (non-sterile) neutrino sector.

1.4 Current/Future Oscillation Programs

Neutrino experiments observe oscillations by measuring the total event rate of a given neutrino flavour, N_α. Therefore, a good knowledge of the cross-section σ_α, detector efficiency, ε_α and flux contributions, Φ_α, for each neutrino flavour, $\alpha(\beta)$, is needed to extract the oscillation probabilities between all available flavours, $P(E_\nu, \nu_\beta \to \nu_\alpha)$, from the rate,

$$N_\alpha(E_\nu) = \sigma_\alpha(E_\nu) \times \varepsilon_\alpha(E_\nu) \times \left(\sum_\beta P(E_\nu, \nu_\beta \to \nu_\alpha) \Phi_\beta(E_\nu) \right). \tag{1.16}$$

The current and future generation of neutrino oscillation experiments are entering a regime where statistical uncertainties are no longer dominant, and the systematics on σ_α, ε_α, and Φ_α, need to be minimal so that experimental sensitivity to the oscillation probabilities is maximised.

Provided an experiment has matching near and far detectors (or the propagation between them is sufficiently well understood) then the ratios of event rates can be used cancel the dependence on the neutrino cross-section and detector efficiency, suppressing the effect these systematics can have on the extraction of $P(\nu_\alpha \to \nu_\beta)$. In a perfect disappearance oscillation measurement this ratio is given by

$$R_\alpha^{near/far} = \frac{N_\alpha^{far}}{N_\alpha^{near}} = \left(\frac{\sum_\beta P(E_\nu, \nu_\beta \to \nu_\alpha) \Phi_\beta(E_\nu)}{\Phi_\alpha(E_\nu)} \right), \tag{1.17}$$

where N_α^{near} is the event rate at the near detector before oscillations, and N_α^{far} is the oscillated event rate at the far detector. This relies only on the understanding of the flavour composition of the beam and the oscillation probabilities. In practice however the use of identical near and far detectors is limited by a severe reduction in neutrino flux at a far detector site, meaning a larger detector with modified acceptance is required to achieve the same sensitivity. When using different nuclear targets the effectiveness of this ratio is further reduced as the propagation of the neutrino cross-section between each target must be well understood.

When expanding the oscillation formula in Equation (1.11) it can be shown that the sensitivity to δ_{CP} only shows up in the appearance probabilities. In a dissappearance oscillation scenario taking the complex conjugate of the PMNS matrix in Equation (1.11) removes all dependence on δ_{CP}. Unfortunately neutrino appearance measurements do not benefit as much from this ratio since the cross-section and acceptances of different neutrino flavours are not necessarily the same. Therefore, oscillation experiments searching for $\nu_\mu \to \nu_e$ must still have a good understanding of

the differences between muon and electron neutrino interactions, and these systematic uncertainties can significantly reduce an experiment's ability to probe the CP-violating phase.

1.5 NUISANCE : A Neutrino Generator Tuning Tool

In the recent T2K and NOvA oscillation analyses neutrino interaction uncertainties contributed approximately 10% of the total uncertainty. For future experiments like DUNE and Hyper-K [35] to meet their physics goals these uncertainties need to be pushed down even further, to below 3%. As the statistics increase in neutrino cross-section measurements, it is becoming clear that the simple modelling assumptions that once found reasonable agreement with data are insufficient. For example, in [62] it was found that the default model in the NEUT generator [63] preferred very different best fit parameters when being tuned to data from the MiniBooNE and MINERvA experiments respectively. Tensions such as this in the global dataset suggest more theoretically consistent interaction models need to be adopted by future neutrino experiments. In the meantime, however, current experiments will have to rely on empirical data-driven corrections to ensure that conservative systematics are used that account for these observed tensions. To support this, a rigorous validation procedure also needs to be developed to help experiments understand in what regions of phase space the models need to be improved.

NUISANCE was developed to aid this community effort by providing a flexible framework in which various neutrino interaction generators can be validated and/or empirically tuned [64]. This project began as an internal fitting package used to tune the free parameters in the NEUT event generator and provide model inputs for the T2K oscillation analysis. NUISANCE built on the design principles in this original package, expanding it to become a flexible tuning framework that could cater to neutrino experiments outside of T2K. A significant amount of work during my PhD was spent developing the NUISANCE package [64] alongside Luke Pickering, Clarence Wret, and Callum Wilkinson. The software aims to address the tensions between Monte-Carlo generators and data by providing an extendable framework in which the five main neutrino interaction generators, NUANCE [65], GENIE [66], NuWro [67, 68], NEUT [63], and GiBUU [69], can be validated and empirically tuned. Prior to its release as a public software tool I developed a significant portion of the core structure of the NUISANCE package that allows it to interface with each generator, and the top level routines that allow it to be used for sophisticated systematic analysis.

At the core level NUISANCE reads in different neutrino event generator formats and converts them to a common neutrino interaction event ready for analysis. Direct interfaces with each generators reweighting package is maintained when events are loaded so that Monte-Carlo (MC) predictions can be easily updated using reweighting techniques throughout the framework. This common event format allows any subsequent analysis code to be applied to all of the possible generators equally, ensuring that differences observed between generators are because of their underlying physics assumptions and not due to an incorrect interpretation of how to analyse their output. The rest of

the NUISANCE analysis code builds on these generator input handlers to support validation and systematic studies. A set of measurement classes are provided which allow neutrino cross-section data to be easily added to a central database from which all generators can be compared to. These classes will automatically select all Monte-Carlo events from an input that match a defined signal definition, meaning a single inclusive event file can be used to generate predictions for many different possible signal channels at once. When comparisons are made between a generator and the data, goodness of fit tests are automatically calculated using all information available so that a user can reliably quantify a models performance. Finally, a set of analysis routines are provided that use each generators available reweighting packages and the automated goodness of fit tests to support the automatic extraction of systematic uncertainties and error bands.

Emperical generator tunings, by their vary nature, are extremely model dependent. When faced with large data/MC differences, ad-hoc corrections can always be used to find agreement with the data, but that does not necessarily mean these corrections can be easily propogated to other datasets or applied to other models. Because of this, empirical model tunings can quickly become obsolete as model improvements or new measurements become available. The NUISANCE framework addresses this problem by ensuring that any tuning analysis performed with one generator can easily be repeated by simply rerunning the analysis with only small tweaks to the input configurations.

Already, the NUISANCE framework is in use by analysers on the T2K, NOvA, DUNE, and MINERvA experiments. As models develop in the coming years we hope the NUISANCE framework will allow systematics to be quickly evaluated by these experiments and others in the neutrino community, ensuring they have reliable uncertainty estimates for any model in use at the time.

This thesis focuses on several empirical tuning studies performed for the T2K and MINERvA collaborations, most of which relied on the NUISANCE framework. Whilst each study can be considered a single self contained analysis, each of them was performed inside the NUISANCE framework and have been setup so they can easily be repeated in the future using different generators or experimental data.

1.6 Thesis Structure

The structure of this thesis is as follows:

- In chapter 2 the physics of neutrino interactions on both nucleons and nuclei is introduced, before discussing the assumptions made by each of the Monte-Carlo generators when simulating neutrino events.
- In chapter 3 a number of neutrino cross-section experiments are reviewed, focusing on those whose public data releases are used in this thesis.

- In chapter 4 the possible correlation between neutrino cross-section measurements and sterile neutrino oscillations is addressed, and a method to understand the systematic bias from sterile neutrino oscillations is developed.
- In chapter 5 alternative models for the axial form factor of the nucleon are implemented into NEUT, before data from deuterium filled bubble chamber experiments is used to extract uncertainties for the T2K 2017 oscillation analysis.
- In chapter 6 an ad-hoc model correction is empirically tuned to charged-current inclusive data to fill in an observed data/MC discrepancy seen in both the MINERvA and NOvA experiments. This ad-hoc model is then propagated to T2K energies to understand its potential impact on the T2K oscillation analysis.
- In chapter 7 the GENIE pion production model is tested by simultaneously comparing it to a range of measurements performed by MINERvA, and the possible causes of several tensions are addressed. To account for observed disagreements at low momentum transfer an ad-hoc suppression model is extracted from the data for use as an additional systematic in future MINERvA analyses.
- Finally, in chapter 8 concluding remarks are given on each of these studies.

Chapter 2

Neutrino Scattering

The development of neutrino interaction generators has been accelerated in recent years as new measurements have repeatedly suggested that the simplistic models used by many experiments are incapable of properly describing neutrino-nucleus scattering [70]. Whilst these models were effective in the past to describe low mass target data, such as neutrino-deuterium scattering, the presence of additional nucleons around the vertex is thought to modify the cross-section in a non-trivial way. This, coupled with an inability to easily describe weak interactions in the transition region ($0.5 - 10$ GeV) where additional particles such as pions can be produced, means the derivation of a single consistent cross-section theory that describes all available data, even within a very limited energy range, is yet to emerge.

There are a number of generators in use by current neutrino experiments: NUANCE [65], NEUT [63], GENIE [66], NuWro [67, 68], and GiBUU [69]. This thesis focusses primarily on the comparison and tuning of NEUT and GENIE for accelerator neutrino oscillation studies, so the available model ingredients in each of these generators are discussed in this chapter. At the energies considered in accelerator neutrino beams the dominant interactions can be separated into three different channels as shown in Figure 2.1: Quasi-Elastic scattering (QE), Resonant Excitation Scattering (RES), and Deep Inelastic Scattering (DIS). The turn-on of each of these interactions is dictated by the energy transfer, q_0, of the interaction. As shown in Figure 2.2, at very low energy transfers elastic and giant resonances in which the scattering occurs of the entire nucleus are dominant. As the energy transfer increases however these interactions are quickly overpowered by QE scattering from individual nucleons. At even higher energies enough energy is imparted to the nucleus that additional particles can be produced, resulting in both deltas and other excited nucleon states being produced (RES). Finally at extremely high energy transfers the deep inelastic interaction is dominant, producing multiple particles in the final state. The transition region is considered as the regime between the QE and delta peaks. Since the available energy transfer is dictated by the initial neutrino energy, experiments in different energy regimes are sensitive to

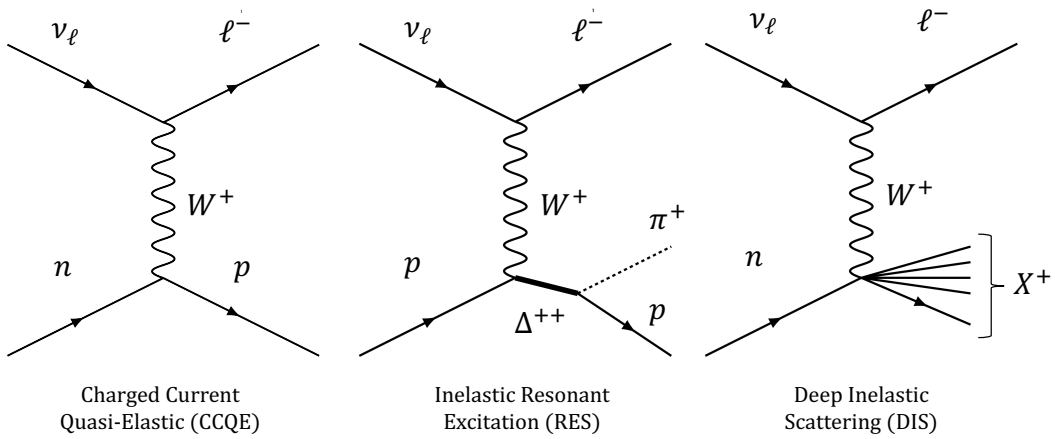

Fig. 2.1 The three main charged-current neutrino-nucleon interaction channels. Similar neutral current diagrams exist in which the interaction is mediated by the exchange of a Z boson. In the case of deep inelastic scattering, X denotes the production of a multiple hadron shower leaving the interaction vertex.

different proportions of these interactions. The turn-on of each these interactions as the neutrino energy increases can be seen in Figure 2.3.

The following sections first focus on the basic theoretical arguments used to model the cross-section in each interaction regime on free nucleons, before considering additional ingredients that are required to predict neutrino interaction rates on nuclei.

2.1 Neutrino Interactions

Deriving a formula for neutrino interaction cross-sections on free nucleons requires in depth knowledge of the nucleon structure. A number of experiments using deuterium to approximate free nucleons provided tests of theory calculations in the 1970-80's, finding each of the following models to be reasonable descriptions of the low statistics data available at the time (for just a few examples, see [73–75]). As a result, many generators include implementations of these models in some form or another, on which more complete models of neutrino interactions are built.

In the following subsections the notation

$$\nu_l(k_0,\vec{k}) + N(p_0,\vec{p}) \rightarrow l(k'_0,\vec{k'}) + A(p'_0,\vec{p'}) \tag{2.1}$$

is used, where $k = (k_0,\vec{k})$ is the neutrino Lorentz four-vector, $p = (p_0,\vec{p})$ is the initial nucleon four-vector, $k' = (k'_0,\vec{k'})$ is the outgoing charged-lepton four-vector, and $p' = (p'_0\vec{p'})$ is the total

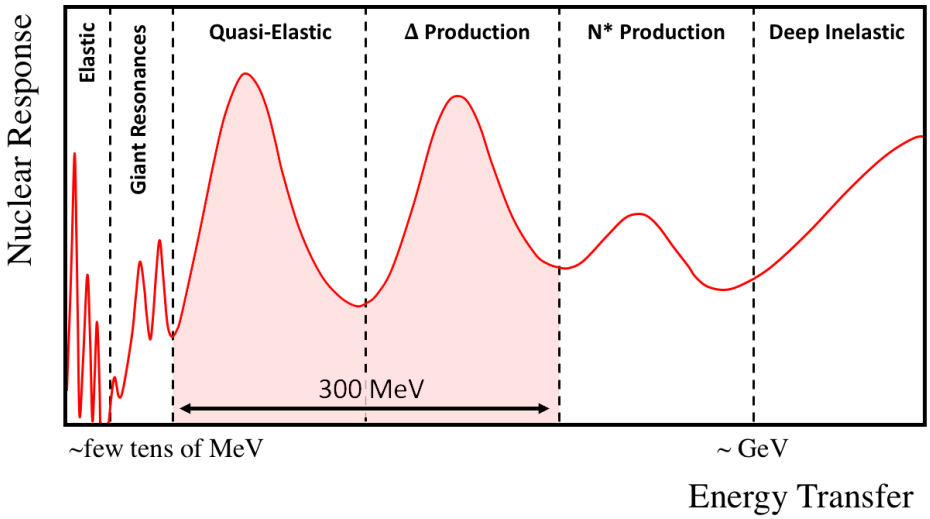

Fig. 2.2 Scattering regimes as a function of energy transfer. The red region shows the significant interaction regime for the T2K experiment. At low energy transfers elastic and giant resonances are dominant but these have little effect in accelerator neutrino experiments. At higher energy transfer the QE peak is dominant until enough energy is imparted to start producing one pion (Δ production or N^* production), or multiple pions (DIS). The transition region is between the QE and Δ regimes and is non-trivial to model. At the very lowest energy transfers in the QE region the simple kinematic assumptions often used begin to break down as the scattering occurs off some fraction of the entire nucleus. Figure adapted from [71].

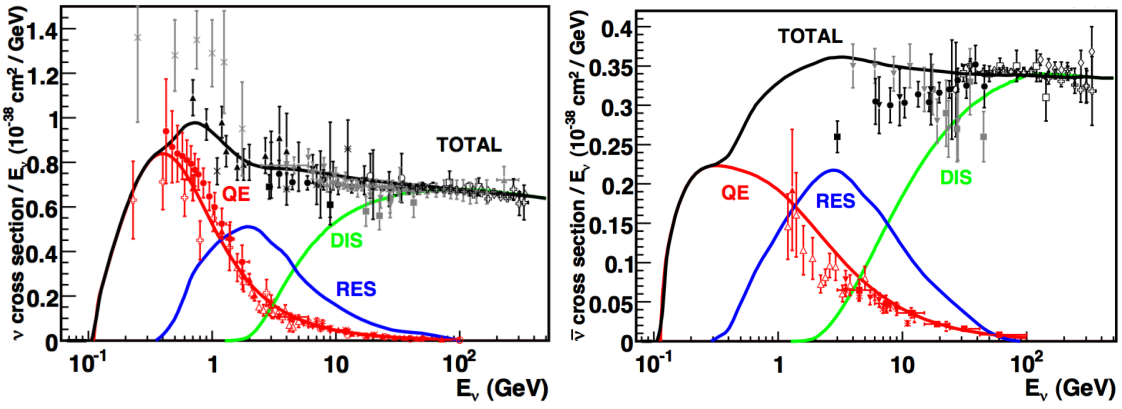

Fig. 2.3 NUANCE cross-section predictions compared to global experimental data for both neutrino scattering (left) and anti-neutrino scattering (right). As the neutrino energy increases so does the available energy transfer, and different interaction channels become dominant as a result. Figures taken from [72].

four-vector of the outgoing hadronic system. In all cases the four-momentum transfer is calculated as $q = (q_0, \vec{q}_3) = k' - k$, with q_0 and $\vec{q}_3$ corresponding to the energy and absolute momentum transfer respectively.

2.1.1 Charged-Current Quasi-Elastic scattering

The dominant signal channel for the T2K experiment is CCQE scattering. Through the exchange of a W boson the interaction converts a neutron into a proton, producing a one proton, one muon final state ($1p1\mu^-$) as shown in Figure 2.1. In the case of anti-neutrino scattering a one neutron, one anti-muon final state ($1n1\mu^+$) is produced. The Llewellyn-Smith (LS) model [76] is often used to describe this interaction, with the differential cross-section being written in terms of the 4-momentum transfer squared, $Q^2 = -q^2$, as

$$\frac{d\sigma}{dQ^2} = \frac{M^2 G_F^2 \cos^2\theta_C}{8\pi E_\nu^2}\left(A(Q^2) \mp \frac{s-u}{M^2}B(Q^2) + \frac{(s-u)^2}{M^4}C(Q^2)\right) \tag{2.2}$$

where M is the nucleon mass, θ_C is the Cabibbo angle, m is the final lepton mass, G_F is the Fermi constant, $(s-u) = 4Mk_0 - Q^2 - m^2$, and the change in sign corresponds to neutrino or anti-neutrino scattering respectively.

The functions $A(Q^2), B(Q^2)$ and $C(Q^2)$, are defined as

$$\begin{aligned} A(Q^2) = {} & \frac{m^2+Q^2}{M^2}((1+\tau)F_A^2 - (1-\tau)F_1^2 + \tau(1-\tau)F_2^2 + 4\tau F_1 F_2) \\ & - \frac{m^2}{4M^2}((F_1+F_2)^2 + (F_A+2F_P)^2 - (\frac{Q^2}{M^2}+4)F_P^2)), \end{aligned} \tag{2.3}$$

$$B(Q^2) = \frac{Q^2}{M^2}F_A(F_1+F_2), \tag{2.4}$$

$$C(Q^2) = \frac{1}{4}(F_A^2 + F_1^2 + \tau F_2^2). \tag{2.5}$$

where $\tau = Q^2/4M^2$. The four form factors F_1, F_2, F_A, and F_P are the fourier transforms of the different charge distributions as seen by the interaction probe. They represent the distributed nature of the nucleon, depending on the Q^2 imparted to the nucleon via the interaction probe. If the scattering was in fact taking place on a point-like charge, the form factor would be constant as a function of Q^2.

The BBBA05 model [77] is used by many generators to write the vector form factors, F_1 and F_2, in terms of the neutron and proton electric and magnetic form factors, G_i^f, as

$$F_1 = F_1^p - F_1^n = \frac{(G_E^p - G_E^n) + \tau(G_M^p - G_M^n)}{1+\tau} \tag{2.6}$$

$$F_2 = F_2^p - F_2^n = \frac{(G_M^p - G_E^p) - (G_M^n + G_E^n)}{1+\tau} \tag{2.7}$$

The functional forms of each G_i^f term are obtained from fitting polynomials to selections of electron-scattering data. (BBBA07 parameters that consider higher order polynomial form factors are also available but are less widely used [78]).

Additional assumptions are required to reduced the number of free parameters in the axial component of the interaction. Imposing the Partially Conserved Axial Current (PCAC) hypothesis [79] and assuming that the divergence of the axial current is dominated by a single pion state allows the Goldberger-Treimann relation to be derived [80], linking F_A and F_P through

$$F_P(Q^2) = \frac{2M^2}{Q^2 + m_\pi^2} F_A(Q^2)\,, \tag{2.8}$$

where m_π is the pion mass. This leaves just a single axial form factor, F_A, that must be determined experimentally from weak interaction measurements. A dipole approximation is commonly assumed, namely

$$F_A(Q^2) = \frac{F_A(0)}{\left(1 + \frac{Q^2}{M_A^2}\right)^2} \tag{2.9}$$

where $F_A(0)$ is the axial coupling constant, $F_A(0) = -1.27$, extracted from the rate of beta decay, and M_A is a free parameter that must be obtained through fits to neutrino-deuterium scattering and pion electroproduction data. Global fits of this dipole model have yielded values typically close to 1.0 GeV for the nucleon axial mass (e.g. $M_A = 1.026 \pm 0.021$ GeV in [81]), although recent studies have suggested that these fits are incomplete as the simple dipole model has insufficient freedom to fully describe the data at high Q^2 (this is discussed in more detail in Chapter 5).

2.1.2 Pion Production

As the neutrino energy increases so does the available Q^2 phase space, moving into a regime where enough energy is imparted to the nucleon that it can be excited into a higher energy resonant state. These resonances can eventually decay back down to the ground state, accompanied by the production of extra particles such as pions, kaons, and photons. If the invariant mass of the nucleon and probe, W, is close to the centre of the mass peak of one of these resonances, the probability of producing one of these states is high.

Modelling of inelastic resonant excitation on nucleons has in the past been done using the Rein-Sehgal (RS) model [82]. Since its derivation a number of more consistent modifications and theoretical pictures of resonant production have been developed, like the MAID form factors [83] used by GiBUU. Despite this, NEUT, NuWro, and GENIE all use the RS model to describe resonant production because of its simplicity in implementation.

The model is derived in the limit of zero lepton mass by considering the leptonic and hadronic currents in the rest frame of the specific resonance (the centre of mass for outgoing hadrons). For CC interactions the differential cross-section, for the production of a given resonance of mass W, is given by

$$\frac{d\sigma}{dQ^2 dv} = \frac{G_F \cos\theta_C}{4\pi^2}\left(\frac{Q^2}{|\vec{q}|^2}\right)(u^2\sigma_+ + v^2\sigma_- + 2uv\sigma_0) \tag{2.10}$$

where σ represents different contributions from left transverse $(-)$, right transverse $(+)$, and longitudinal (0) polarizations of the propagator, $u = k_0(k_0 + k_0' + Q)/2$, and $v = k_0(k_0 + k_0' - Q)/2$. The polarization contributions are calculated as

$$\sigma_\pm = \frac{\pi M}{2M_N}\sum_{j_z} |\langle N, j_z \pm 1| J_\pm |N*, j_z\rangle|^2 \delta(W - M), \tag{2.11}$$

$$\sigma_0 = \frac{\pi M_N}{2M}\frac{|\vec{q}|^2}{Q^2}\sum_{j_z} |\langle N, j_z| J_0 |N*, j_z\rangle|^2 \delta(W - M), \tag{2.12}$$

where J are the hadronic currents for different propagator polarisations, δ is the Dirac-delta function, and the sum runs over all available resonance spin states. M is the true centre of mass energy for the resonance, which in reality has a finite width. This can be accounted for by replacing the δ term in each calculation with the Breit-Wigner factor. The advantage of writing the cross-section in this way is that the form factor bra-ket terms can be expressed as the nuclear transition amplitudes for each of the resonances. Rein-Sehgal use a relativistic harmonic oscillator quark model [84] to pre-calculate the form of these amplitudes for resonances up to $M = 2$ GeV in terms of the experimentally measured vector and axial form factors for the nucleon. The $\Delta(1232)$ resonance has the strongest individual contribution to the measured cross section [85], but in reality the study of a single resonance is almost impossible due to contributions from overlapping nearby resonances. In the full model the amplitudes for one resonance including possible interferences must be calculated, before multiplying by the probability that the given resonance will decay into the final state topology of interest [86]. The NEUT implementation of this model performs this calculation considering 18 possible resonances whilst GENIE considers only the 16 lowest mass resonances and does not include interference terms, instead choosing to add each resonance incoherently before emperically tuning the model to data [87]. NuWro only calculates contributions from the $\Delta(1232)$ resonance as this is the dominant resonance channel.

Validation of a reliable pion production model is complicated by the fact that DIS channels discussed in the next section can produce final states indistuingishable from resonant excitation [88]. Each generator handles this by including a fraction of DIS events at $W < 2.0$ GeV, the magnitude of which is tuned to pion production data. These contributions are referred to as non-resonant pion production events. The NuWro generator uses this to approximate pion production for all resonances above the $\Delta(1232)$ resonance.

2.1.3 Deep Inelastic Scattering

At higher momentum transfer the weak probe can resolve individual quark-partons within the nucleus. Interactions of this kind are referred to as deep inelastic scattering, and result in the production of hadronic jets from the vertex. Whilst this is the dominant process at $E_\nu > 10$ GeV, the turn-on for DIS is much lower, at approximately 1 GeV, and DIS therefore contributes to the total measured cross-section in lower energy experiments [72]. The description here follows the derivations given in [89].

To simplify the model of DIS two invariant variables can be formed from the momentum of the initial neutrino, k, and the initial nucleon, p. These are the Bjorken x (the fractional momentum of the nucleon), and the Bjorken inelasticity, y.

$$x = \frac{Q^2}{2p\cdot q}, \qquad y = \frac{p\cdot q}{p\cdot k}. \tag{2.13}$$

The double differential cross-section in terms of y and x is then given by

$$\frac{d^2\sigma^{\nu(\bar{\nu})}}{dxdy} = \frac{G_F^2 M k_0}{\pi(1+Q^2/M_W^2)^2}\left(A(x,y)F_1(x,Q^2) + B(x,y,k_0)F_2(x,Q^2) + (-)C(y)xF_3\right) \tag{2.14}$$

where M is the nucleon mass, M_W is the boson propogator mass, and $F_1(x,Q^2)$, $F_2(x,Q^2)$, and $F_3(x,Q^2)$ are functions that describe the parton structure in the nucleon, and

$$A(x,y) = y^2 x; \tag{2.15}$$

$$B(x,y,k_0) = 1 - y - \frac{Mxy}{2k_0}; \tag{2.16}$$

$$C(y) = y\left(1 - \frac{y}{2}\right). \tag{2.17}$$

A further simplification is made to Equation 2.14 by relating F_1 and F_2 to the ratio of the longitudinal σ_L and transverse σ_T response functions:

$$R_L(x,Q^2) = \frac{\sigma_L}{\sigma_T}; \tag{2.18}$$

$$2xF_1(x,Q^2) = \frac{F_2(x,Q^2)(1+4M^2x^2/Q^2)}{R_L(x,Q^2)+1}. \tag{2.19}$$

The longitudinal and transverse response functions describe the cross-section along and transverse to the initial beam direction respectively, and can be extracted from comparisons of neutrino and antineutrino scattering as a function of both x and y. In the quark-parton model $R_L = 0$ for a virtual photon interacting with point-like spin half particles [90]. Including this relation simplifies the

cross-section calculation by transforming the structure function coefficients to

$$A(x,y) \to 0; \tag{2.20}$$

$$B(x,y,k_0) \to B'(x,y,k_0) = \left(\frac{y^2 + (2Mxy/Q)^2}{2 + 2R_L(x,Q^2))} + 1 - y - \frac{Mxy}{2k_0} \right); \tag{2.21}$$

$$C(y) \to C(y). \tag{2.22}$$

This reduces the cross-section to a form dependent only on F_2 and F_3 and measurements of $R_L(x,Q^2)$.

At tree level the structure functions are calculated as sums of the fractional momentum of each parton for a given Q^2, multiplied by the probability density functions, $P(\bar{P})$, of the probe resolving a parton(anti-parton) with that specific momentum for a given Q^2 value:

$$F_2(x,Q^2) = 2 \sum_{i=u,d,c,s} (xP(x,Q^2) + x\bar{P}(x,Q^2)); \tag{2.23}$$

$$xF_3(x,Q^2) = 2 \sum_{i=u,d,c,s} (xP(x,Q^2) - x\bar{P}(x,Q^2)). \tag{2.24}$$

Taking the sum and then difference of P and $\bar{P}$ in Equations 2.23 and 2.24 respectively results in $F_2(x,Q^2)$ being sensitive to the total quark-antiquark Probability Density Functions (PDFs) and $xF_3(x,Q^2)$ being sensitive to the total valence quark PDFs in the nucleon. A large amount of theoretical and experimental work goes into extracting these PDFs for the proton from fits to deep-inelastic lepton scattering data [91, 92].

At higher orders the presence of transverse momenta, quark masses and other corrections cause R_L to tend away from zero, so the double differential cross-section shown and the PDFs that accompany it are only of use at tree level. To extend the model to higher orders these effects are commonly folded into $R_L(x,Q^2)$ or the PDF's themselves to create effective dynamic form factors for the cross-section [93].

To simulate a DIS shower in event generators a hadronization model must be included. Each generator relies on the Pythia framework [94] to predict the outgoing particles and their kinematics for a given value of x and Q^2, which is based on the Lund string fragmentation model [95]. GENIE is the exception, relying on the AGKY model [96] for low invariant masses $W < 2.3$ GeV before a smooth transition into using Pythia for higher masses $W > 3.0$ GeV.

2.2 Neutrino-nuclear scattering

No model exists capable of simultaneously describing the exclusive neutrino-nucleus cross-section (including all outgoing particle kinematics) across the three interaction channels discussed pre-

viously. Instead generators must employ a factorisation scheme that handles the nuclear system before and after the interaction, and pieces together different model components incoherently. The steps of this factorisation are the ground state describing the initial distribution of the nucleons before the interaction, the interaction itself and how the surrounding nuclear medium can modify it, and the final state interactions applied to particles as they leave the nucleus. In the following subsections the available models for each of these stages are discussed.

2.2.1 Ground State

The Impulse Approximation assumes that at sufficiently high energy transfer the probe interacts with a single nucleon, and therefore the surrounding nuclear medium can be effectively ignored when determining the inclusive cross-section. This allows an interaction to be written in terms of the scattering of a free nucleon, like that given in Equation (2.1). Whilst simplifying the model implementation, the impulse approximation breaks down at low momentum transfer.

The Pauli exclusion principle prevents any two nucleons from occupying the same momentum/spin state within the nuclear potential well. It is therefore unrealistic to simulate this interaction as the scattering of free nucleons at rest. Instead each nucleon is likely to have an initial non-zero momentum, and an associated binding energy required to free it from the nucleus. Models that describe the probability of a nucleon having a given initial momentum, $S(\vec{p})$, are referred to as "spectral functions", and are described further below.

The total cross-section on the nucleus for a given neutrino energy is calculated by integrating over all possible initial nucleon kinematics described by $S(\vec{p})$, and the outgoing nucleon and lepton kinematics,

$$\begin{aligned}\sigma^A(k,k',p'_1\dots p'_N) = \int d^4p \times S(\vec{p}) \times\ \sigma^n(k,k',p,p'_1\dots p'_N) \\ \times\ \delta\left((k_0-k'_0)+p_0-\sum_i^N (p'_i)_0\right),\end{aligned} \tag{2.25}$$

where σ^n is the interaction cross-section on a free nucleon, and δ is the Kronecker delta. In neutrino event generators this integral is performed using Monte-Carlo methods by drawing a nucleon from $S(\vec{p},E_b)$ and using it to assign the particle 4-vectors for the initial state. Spectral functions available in each of the generators are discussed in brief below, with their probability distributions as a function of nucleon momentum shown in Figure 2.4.

Smith-Moniz Relativistic Fermi Gas (RFG): This is one of the first models to be used widely in neutrino scattering and is still considered the default option in some generators. The nucleons are treated as a collection of non-interacting fermions which form plane-waves in a nuclear potential. Successive states are filled up to a Fermi-momentum level, p_F^{RFG}, above which all states are left

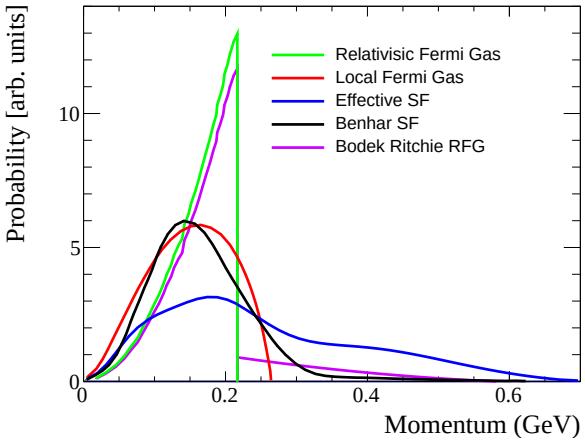

Fig. 2.4 Momentum probability distributions comparisons for a number of the spectral functions available in NuWro. The sharp peak in the RFG models are due to the Fermi momentum. Figure reproduced from [97].

empty. This produces a spectral function given by

$$S(\vec{p}) = \frac{6\pi^2 A}{(p_F^{RFG})^2}\Theta(p_F^{RFG} - |\vec{p}|), \tag{2.26}$$

where A is the nucleon atomic number, and Θ is the Heaviside step function. For particles to escape the potential they must gain sufficient momentum to be knocked into a state above p_F^{RFG}. This choice of potential results in a constant binding energy applied to each nucleon, and an over-exaggeration of Pauli blocking at low energy transfers. The Smith-Moniz quasi-elastic model is an analytical derivation of the total QE cross-section, using an integral over this spectral function and the Llewelyn-Smith QE definition for scattering of free nucleons.

Local Fermi Gas Model (LFG): The nucleus is simulated as a Fermi gas where p_F^{LFG} depends on the local nucleon density, $\rho(\vec{r})$, at the interaction vertex [98]. This leads to a position dependent spectral function given by

$$S(\vec{p}) = \frac{6\pi^2 A}{(p_F^{LFG}(\vec{r}))^2}\Theta(p_F^{LFG}(\vec{r}) - |\vec{p}|), \tag{2.27}$$

and a more natural approximation of Pauli blocking. When drawing from the initial momentum distributions the value of p_F^{RFG} obtained from an RFG approximation is still used as an upper limit on p_F^{LFG}.

Benhar Spectral Function: This is a 2-dimensional spectral function that is calculated using both a mean field potential and an additional term describing the behaviour of short-range correlated pairs of nucleons [99]. This additional term makes up 20% of the total probability distribution, producing a tail at high momentum that extends beyond the constant p_F of the Fermi gas models. Whilst this approach effectively accounts for the scattering of correlated nucleon pairs when calculating

the total cross-section, it is simulated in generators using a simple impulse approximation and only a single nucleon is ejected on the hadronic side of the interaction. The spectral function must be calculated explicitly for a given target distribution of initial nucleon momentum and removal energy.

Effective Spectral Function: Behaviour has been observed in electron scattering experiments where the response for interactions that include longitudinally polarized virtual photons when plotted against a "super-scaling" function, can describe available data across all nuclear targets and all momentum transfers [100]. The effective spectral function takes advantage of this behaviour by following a similar derivation to the Benhar-Fantoni spectral function to produce an empirical model that can describe electron scattering data at $Q^2 > 0.3$ GeV [101]. This is achieved by taking a parametrisation of the initial state nucleon momentum distribution and tuning the free parameters until the model produces a good fit to the super-scaling data.

Bodek-Ritchie Relativistic Fermi Gas: This is an extension of the RFG model at higher energies to account for both the turn on of DIS and correlations between nucleons. The result is a high momentum tail in the probability distribution (smaller than the Benhar spectral function tail) and a slight increase in the total cross-section [102].

2.2.2 Interaction

The impulse approximation breaks down at low energy transfers where the probe is capable of resolving more than one nucleon whilst it interacts. Correlations between nucleons can significantly modify the quasi-elastic cross-section, and can also lead to the ejection of multiple nucleons from the interaction vertex. Fits to MiniBooNE Charged Current QE (CCQE) measurements found that large values for the axial mass in Equation (2.9) are required to describe $\nu - \mathrm{C}$ scattering, in direct contradiction with similar studies performed on $\nu - {}^2\mathrm{H}$ data. It has been suggested by a number of groups that these disagreements are due to the lack of nucleon-nucleon correlations present in the simple QE RFG models used.

The quasi-elastic tree level diagram shown in Figure 2.1, where a single nucleon is knocked out of the nuclear potential well are sometimes referred to as 1-particle-1-hole (1p-1h) processes, whilst interactions with a higher number of correlated nucleons ejected are referred to as n-particle-n-hole (2p-2h, 3p-3h, etc) processes. Proper treatments of such effects are important to neutrino oscillation experiments, since attributing observed data/MC disagreements to 1p-1h or 2p-2h channels has been shown to systematically shift the extracted absolute mass splitting by as much as 8% [103]. A number of empirical and theoretical models that try to account for this have been implemented in generators and found to improve agreement with both MiniBooNE and MINERvA data, by increasing the predicted CC0π cross-section without having to inflate the axial mass [104, 105].

The Transverse Enhancement Model (TEM) is motivated by studies performed in the electron scattering community. An excess has been repeatedly observed at low Q^2 in the QE transverse response function (transverse to the direction of momentum transfer) when scattering off bound nucleons [101]. The TEM model is a purely empirical model in which the observed excess is fit with the form

$$R_T = 1 + AQ^2 e^{-Q^2/B}, \tag{2.28}$$

where A and B are treated as free parameters. This result is then folded into the neutrino cross-section model via a modification of the nuclear magnetic form factors for the proton and neutron as

$$G'^{p(n)}_M(Q^2) = G^{p(n)}_M(Q^2) \times \sqrt{1 + AQ^2 e^{-Q^2/B}}. \tag{2.29}$$

where $G_{M(p,n)}$ are the original magnetic form factors obtained from fits to electron-scattering data shown in Equations 2.6 and 2.7. This enhancement is then attributed to 2p-2h processes, and generators use it to simulate events with 2 nucleons ejected from the interaction vertex for a given Q^2.

The Dytman Empirical 2p-2h model accounts for multi-nucleon effects by drawing values from a 2D Gaussian in (q_0, q_3) and using them to calculate the kinematics for the lepton and nucleon-pair. The normalisation, position, and width of the Gaussian, which defines the normalisation of 2p-2h events, is then empirically tuned to both MiniBooNE and NOMAD data simultaneously [106].

The Nieves [107] and Martini-Marteau models [108], in contrast, are both microscopic calculations of np-nh interactions that assume a LFG nuclear model. Cutkosky cut rules take all intersected particles and put them on-shell in the calculation, allowing many possible contributing vertex diagrams (like those shown in Figure 2.5) to be included in the response. Both the Nieves and Martini-Marteau models express the cross-section in terms of a set of hadronic responses that are obtained by applying Cutkosky cut rules to one of the possible boson self-energy diagrams shown in Figure 2.5. The choice of both bare propagator and vertex diagrams considered can significantly change the predictions and applicability of the model. This summation framework used by the Nieves and Martini-Marteau models is referred to as the Random Phase Approximation (RPA) framework.

When extracting the 1p-1h response in the first diagram (Figure 2.4 (a)), the effect of long-range nucleon correlations is included by introducing an effective nucleon-nucleon field (labelled v_t in Figure 2.6) which can be used to dress the propagator in additional particle loops [109]. This results in a modification of its self-energy in the nuclear medium and a quenching of the electroweak coupling strength. Commonly this 1p-1h model feature is referred to as simply "RPA" despite the fact that the RPA framework can be used to calculate np-nh processes. It yields a correction

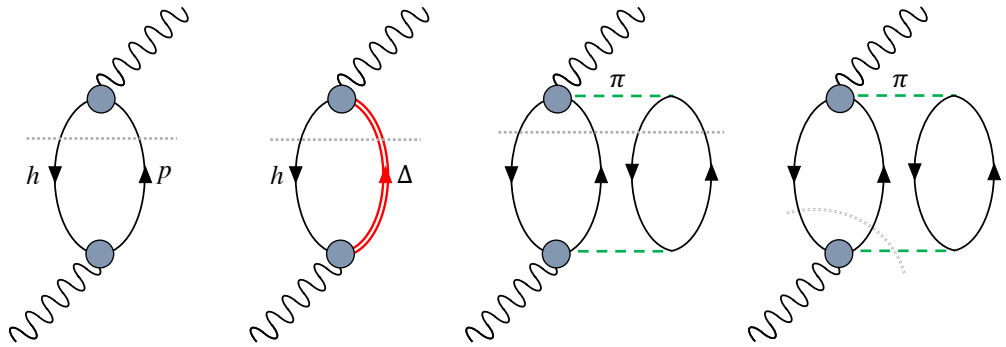

(a) 1p-1h (b) Δ Resonance (c) 2p-2h (d) 1p-1h-1π

Fig. 2.5 First four bare propagator self-energy diagrams used in the Nieves/Martini-Marteau calculations. p and h are particle and hole states respectively. π and Δ refer to pions and Delta resonances. Cutkosky lines shown dashed in grey define a possible interaction final state. Figure (a) produces a 1-particle 1-hole state, (b) a 1-Delta 1-hole state, (c) a 2p-2h state, and (d) a 1p-1h-1π state. Possible contributions to the responses are summed over by including many different vertex diagrams within the grey-blue circles. Figure reproduced from [111].

which noticeably suppresses the bare 1p-1h interaction model as a function of q_0 and q_3 as shown in Figure 2.7 [110].

To account for 2p-2h interactions in these models, the diagram in Figure 2.4 (c) is considered when calculating the responses. In this case the many possible diagrams shown in Figure 2.8 are included when dressing the vertex, allowing the model to describe a range of nuclear effects that fall under the umbrella term of "2p-2h", such as pionless delta decay where the pion is re-absorbed by the nucleus before it decays. Original calculations of the Nieves/Martini 2p-2h models were limited to a validity region of $E_\nu < 1.2$ GeV since only the lowest delta resonance was included in the expansion. Later calculations have shown that the models can be extended up to neutrino energies of 10 GeV provided the 3-momentum transfer is limited to $|q_3| < 1.2$ GeV [107]. This cut-off is clear in Figure 2.9.

It is important to point out that whilst the Nieves (or Martini-Marteau) 1p-1h and 2p-2h models discussed here are implemented as separate optional models in neutrino event generators, they are actually pieces taken from a single consistent model which calculates all interactions shown in Figure 2.5 within a consistent random phase approximation framework. The two models differ from one another in the choice of diagrams considered, with the Martini-Marteau model predicting approximately twice as large a 2p-2h contribution than the Nieves model. The MiniBooNE data unfortunately offers no clear discrimination between models in this case, since both are consistent within the reported flux uncertainties of the experiment [104].

Comparisons of some of the available 2p-2h models in the NuWro and GENIE generators are shown in Figure 2.9 convolved with the MINERvA flux. Each model gives very different $(q_0 - q_3)$

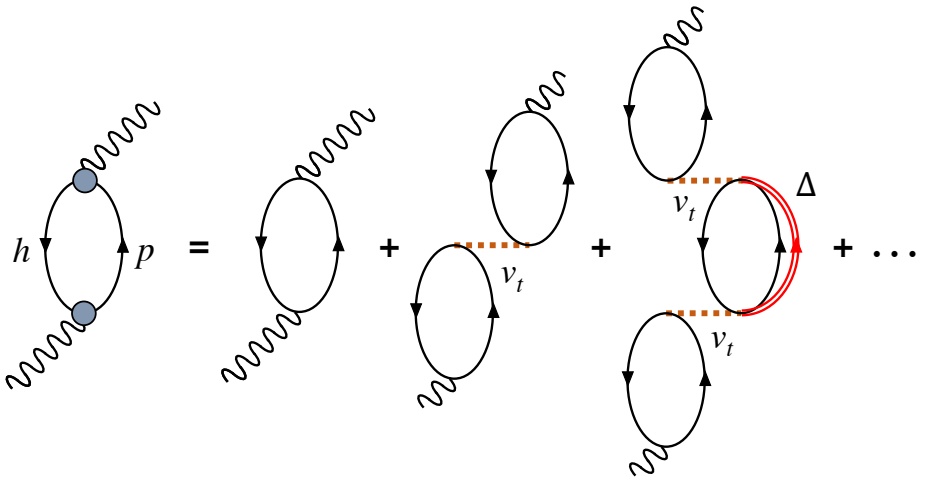

Fig. 2.6 Example diagrams contributing to the 1p-1h W-boson self energy in the nuclear medium. p and h are particle and hole states respectively. Δ refers to the production of Delta resonance states. v_t is an effective nucleon-nucleon force added to account for long range correlations. Figure reproduced with permission from [109].

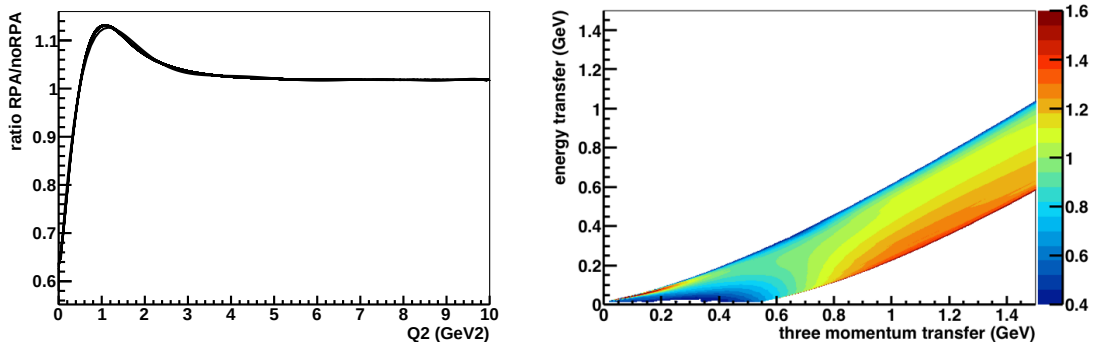

Fig. 2.7 Ratio of 1p-1h predictions as a function of different kinematics with (RPA) and without the Nieves RPA correction (noRPA) included. These correction functions can be applied as weights to simulated neutrino events to approximate the effects of RPA on an interaction model. (left) Effect of the corrections as a function of Q^2. In NEUT this function is applied to an RFG based CCQE model to include RPA effects. (right) Effect of the same corrections as a function of $q_0 - |\vec{q}_3|$. The Z-axis describes the correction ratio. Both figures are taken with permission from [110].

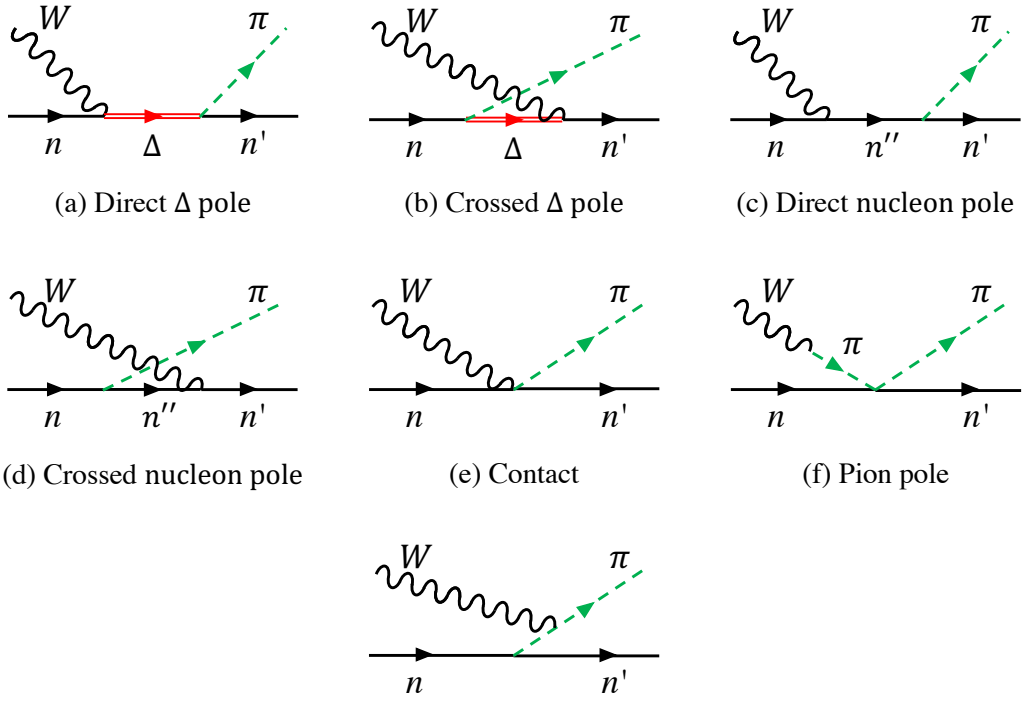

(a) Direct Δ pole (b) Crossed Δ pole (c) Direct nucleon pole

(d) Crossed nucleon pole (e) Contact (f) Pion pole

(g) Pion in flight

Fig. 2.8 Pion production diagrams considered by the Nieves model when calculating the responses for Figure 2.5 (c) and (d) . Figure reproduced from [111].

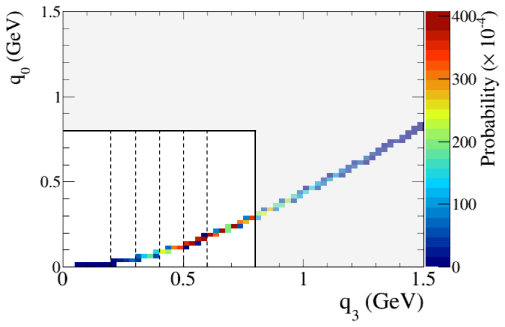

(a) Transverse Enhancement Model (NuWro)

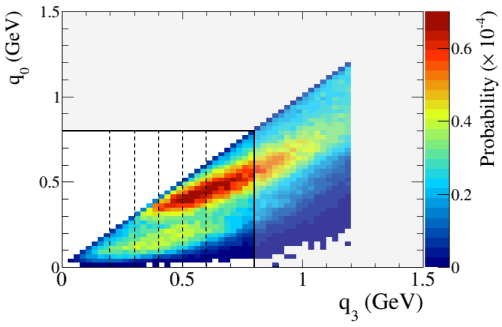

(b) Nieves Model (GENIE)

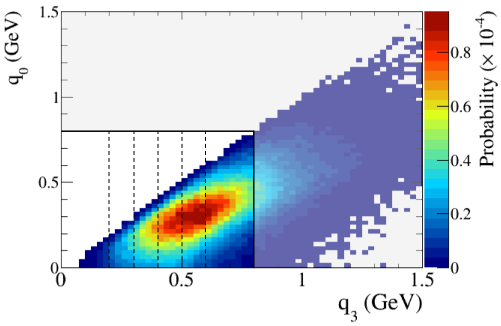

(c) Dytman Empirical MEC (GENIE)

Fig. 2.9 Comparisons of the Transverse Enhancement, Nieves, and Dytman Empirical MEC 2p-2h predictions available in neutrino event generators shown as a function of $q_0 - q_3$. Distributions were produced using NUISANCE. The area not masked in gray indicates approximate kinematic ranges currently accessible by experiments that use hadronic kinematics to estimate q_3. Dashed vertical lines show binning used by the MINERvA experiment when probing q_3 in [113].

responses, which can lead to different estimates of the systematic bias when reconstructing the neutrino energy from final state lepton kinematics. Despite this, measurements of purely lepton kinematics such as p_μ and θ_μ are unable to clearly distinguish between each of these models, therefore additional 2p2h shape uncertainties are required to account for the projected model envolope. Measurements of hadronic kinematics, such as those discussed later in this thesis may be able to discriminate between these models in the future.

As with all of these models, both effective and microscopic, the calculations account for the increase in the measured cross-section when considering np-nh interactions, but little information on the kinematics of the outgoing hadrons is provided. In both NEUT and NuWro a multi-nucleon ejection model is implemented to handle this by ensuring energy conservation and imposing Pauli blocking on the outgoing nucleons [112].

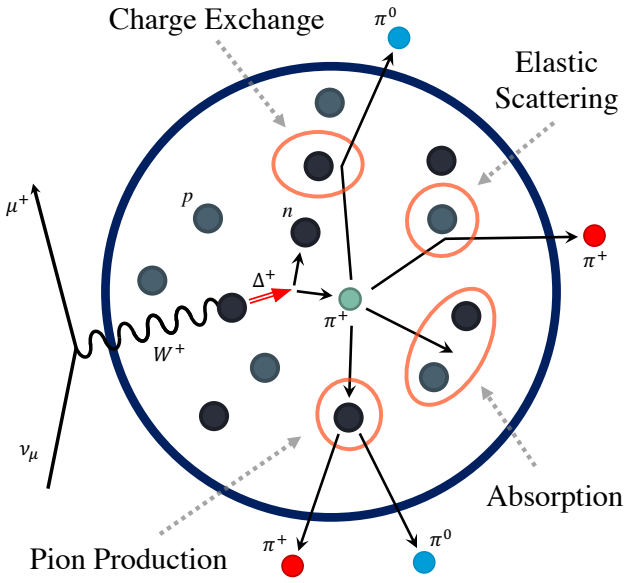

Fig. 2.10 Possible re-interactions that pions can undergo whilst leaving the nucleus after a Δ decay. The neutrino-lepton vertex is pictured outside the nucleus since the outgoing muon is not included in the cascade.

2.2.3 Final State Interactions (FSI)

As particles traverse the nuclear medium they have a finite chance of re-interaction with the remaining nucleons. As shown in Figure 2.10, pions can scatter both elastically and inelastically, can be absorbed by a pair nucleons, and can undergo charge exchange. Such re-interactions, referred to as FSI, can significantly modify the spectrum and multiplicities of hadrons observed in the final state after all particles have left the nucleus [114]. It is therefore impossible to reliably determine the interaction that occurred on individual nucleons inside the nucleus purely from the hadrons observed in a detector. This has led to experiments publishing measurements in terms of final state topologies such as CC0π instead of CCQE to remove model dependence in their data [115, 116].

NEUT and NuWro both use implementations of a classical intra-nucleus cascade model [117] in which the outgoing particles are stepped through the nucleus in small time increments. At each step the probability of interaction is calculated from the total scattering cross-section for each of the outgoing particles in the cascade. If the simulation decides an interaction must occur, one of the possible channels shown in Figure 2.10 is randomly chosen according to their relative cross-sections and the particles created are added to the list of already cascading particles. This process is repeated until the particles in the list have all either been absorbed or leave the nucleus. The Oset model [117] describes pion and nucleon interaction probabilities on single nucleons in a nuclear medium, and both generators use this model as an input when determining the rate of re-interaction for each particle as a function of energy. In the NEUT FSI model these inputs have undergone further

tuning to $\pi - A$ scattering data to provide uncertainty estimates for the T2K oscillation analysis [118].

In contrast GENIE uses its own effective cascade model in which a single step is approximated for each particle leaving the neutrino interaction. Given a particle's initial kinematics the final states are estimated, including any extra particles that may be ejected. This has the advantage that only a single step is simulated and can be easily reweighted. However, due to its approximate nature, the model must be tuned to data from both pion and nucleon scattering over a broad range of targets to ensure the reinteraction rates and final state multiplicities are suitable descriptions of nature [96].

It is expected that when hadronic showers have a low transverse size (e.g. during hadronization) interactions take place coherently on the shower as a whole, leading to a suppression of the re-scattering cross-section for each individual particle [119]. This is reflected in cascade generators by introducing a "formation zone" around the vertex in which the particles are not allowed to interact with the nucleon medium.

The GiBUU generator implements a far more sophisticated semi-classical cascade model by simultaneously solving the Boltzmann-Uehling-Uhlenbeck (BUU) equation [69] for all possible particles produced by the neutrino interaction [120]. The BUU equation is given by

$$\left[\partial_\mu + (\Delta_p H_i)\Delta_r - (\Delta_r H_i)\Delta_p\right] f_i(\vec{r},t,\vec{p}) = C[f_i, f_j] \tag{2.30}$$

where i, j correspond to different particle types (π, δ, N), f is a distribution function for the given particle, H is a mean field potential describing the nuclear ground state, and C is a collision term that handles all possible interaction/decay modes. Since the collision term also handles interactions with other particles the full series of equations for every species must be solved simultaneously. Calculating this solution for each event is computationally expensive, so GiBUU trades efficiency for completeness, providing the most sophisticated modelling of FSI interactions available in current neutrino interaction generators at the cost of an increase in computation time. Whilst GiBUU has been shown to provide good agreement with several pion production measurements [121], it is currently not possible to reweight events to account for cross-section systematics. As a result, it has not been adopted as the primary event generator in any T2K oscillation analyses.

Chapter 3

Neutrino Interaction Experiments

Since the neutrino couples only to the weak field, its detection is possible only by indirect means, usually via the outgoing charged lepton in a charged current interaction. Since the true neutrino energy is not known a priori, it must be reconstructed from the interaction products. This makes the neutrino cross-section as a function of the true neutrino energy difficult to extract without some inherent model dependence. An alternative approach being followed by modern experiments is the measurement of the neutrino cross-section as a function of final state observables (e.g. reconstructed muon momentum, pion kinetic energy). This method assumes that any model capable of describing a broad range of interaction kinematics data can also reliably predict the neutrino cross-section as a function of E_ν. To fully constrain the cross-section in this way a number of measurements are required to cover all possible regions of phase-space probed by oscillation experiments.

There is currently an extensive effort in the community to measure the neutrino scattering cross-section over a broad range of targets, energy ranges, and kinematic variables. This is being achieved both by dedicated cross-section experiments (e.g. Bubble Chambers, MINERvA) and also as spin-off measurements made at near detectors in neutrino oscillation experiments (e.g. MiniBooNE, ND280, NOvA). The strengths and weaknesses of a number of these detectors are reviewed in this chapter, focussing on the experiments whose data is used in later chapters of this thesis.

3.1 Bubble Chamber Experiments

Neutrino scattering in the few GeV region was first studied by a number of bubble chamber experiments based at Argonne (ANL) [122–128], Brookhaven (BNL) [129–131], Fermilab (FNAL)[132–134], and CERN (BEBC) [135, 136] in the 1970s-90s. All of these experiments relied on using pion decay in flight, produced by impinging high energy protons on a fixed target, to produce an intense beam of high energy muon neutrinos. For the experiments considered in this thesis, the energy of

Experiment	ANL	BNL	FNAL	BEBC
Flux Range	0.0 – 6.0 GeV	0.0 – 7.0 GeV	0.0 – 200.0 GeV	0.0 – 260.0 GeV
Flux Peak	0.6 GeV	1.0 GeV	20.0 GeV	2.0 GeV
Measurements	Inclusive [124, 125]	Inclusive [130]	Inclusive [133]	
	QE [123, 125]	QE [130, 131]	QE [134]	QE [137]
	1π [122, 126, 127]	1π [138]	1π [132]	1π [135–137]
	2π [128]	2π [138]		

Table 3.1 Review of bubble chamber measurements on deuterium only. Data was taken from the Durham HepData project [139].

the flux peaks range from 0.5 GeV to 20.0 GeV, with the ANL and BNL experiments being closest to the T2K beam, at around 0.6 GeV and 2 GeV respectively. In bubble chamber experiments ionising particles form microscopic bubbles as they traverse the superheated liquid detector medium. These tracks can then be photographed by multiple cameras to produce stereoscopic images of particle trajectories.

The studies performed by these experiments covered a series of different target fills (from Deuterium to Neon), but most notable are their measurements of ν – D scattering channels. Since the neutrino cross-section is so small, the use of low density deuterium as a target severely limits the number of observed interactions. With only two nucleons in the initial state, scattering of this kind leads to the disintegration of the target nucleus, resulting in the ejection of both the struck and spectator nucleon into an observable final state. Detection of both of these nucleons, combined with minimal nuclear binding effects, allows the neutrino energy to be reconstructed reliably for deuterium targets, and for the datasets to be easily approximated as the scattering of free nucleons. This ability significantly outweighs the current statistical limitations of the available datasets, and a number of these measurements are still in use today. A brief overview of the bubble chamber experiments discussed later in this thesis is shown in Table 3.1.

3.2 The T2K Experiment

T2K studies long baseline neutrino oscillations by measuring electron neutrino appearance in a muon neutrino beam fired from Tokai to Kamioka (T2K) in Japan [140]. As shown in Figure 3.1, the experiment uses two near detectors (INGRID and ND280) to study the unoscillated neutrino flux, before using the Super-Kamiokande (SK) experiment [141] as a far detector to probe the oscillated neutrino spectrum at a baseline of 295 km.

The T2K beam is created by firing 30 GeV protons at a graphite target [142]. The resultant hadron showers are focused using two magnetic horns to select positive or negative pions and direct them down a 96 m long decay pipe. Pions that decay in flight produce a high intensity neutrino beam which passes through a beam dump at the end of the decay volume. The beam dump is designed

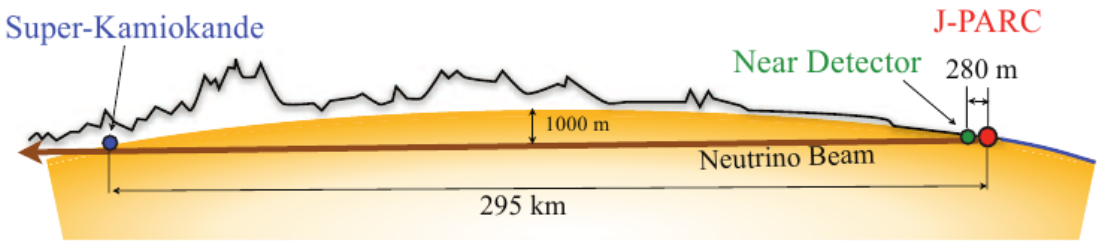

Fig. 3.1 Diagram of the T2K oscillation beamline. Figure taken from [140].

to absorb the majority of particles other than neutrinos remaining in the beam. A muon monitor (MUMON) that sits further downstream is used to place a constraint on the beam direction and intensity by measuring the remaining muons that pass through the beam dump.

Along the axis of the beam the spread in the neutrino energy from meson decays is significant. At increasing angles off-axis, the neutrino spectrum narrows and moves to lower energy as shown in Figure 3.2, a direct result of the simple two-body kinematics of the pion decay. T2K takes advantage of this effect by situating the detectors 2.5° off-axis, placing the peak neutrino energy close to the oscillation maximum for the long baseline. This also results in the majority of events observed in ND280 and SK being quasi-elastic and resonant interactions.

The near detectors are both located approximately the same distance away from the beam source in the T2K near detector hall as shown in Figure 3.2. The primary purpose of INGRID is to measure the beam flux profile through quasi-elastic scattering events, whilst the purpose of ND280 is to measure the ν_μ and ν_e spectrum of neutrino induced quasi-elastic and resonant scattering on carbon and oxygen. Alongside providing constraints for the T2K oscillation analysis, ND280 has also been used to make a number of publicly released measurements of neutrino-nucleus cross-sections.

As shown in Figure 3.3, ND280 consists of a central tracker region surrounded by an Electromagnetic Calorimeter (ECal) [144]. Upstream of the tracker region is a water based π^0 Detector (P0D) [145] designed to constrain the neutrino-induced π^0 production cross-section which is a signficant background at Super-Kamiokande. The entire tracker and P0D region is enclosed in the UA1 magnet and the 0.2 T magnetic field it generates is orientated perpendicular to the neutrino beam direction. To reduce backgrounds originating from neutrino interactions inside the magnet the Side Muon Range Detector (SMRD) [146] sub-detector was created by inserting plastic scintillator modules between segments of the magnet return yoke. Hits in the SMRD are then used to veto magnet interaction backgrounds.

The tracker region is separated into two Fine Grained Detectors (FGD) [148] which serve as the main interaction targets, and three argon gas Time Projection Chambers (TPC) [149]. The most upstream FGD (FGD1) is constructed from $9.6 \times 9.6 \times 1860$ mm^3 bars of plastic scintillator (CH) which provide active tracking of particles leaving the nucleus in a neutrino scattering event. 192 separate bars are instrumented to form a layer, and 30 layers are placed with alternating horizontal

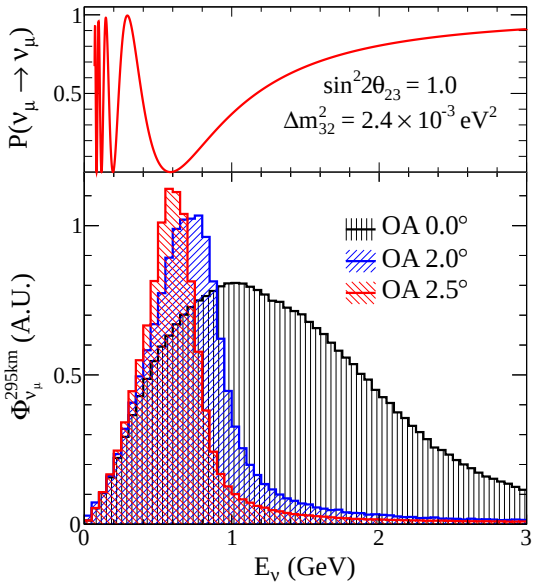

(a) The effect changing the off-axis angle of T2K's detectors has on the shape and normalisation of the neutrino flux distribution. The top curve shows the position of the first oscillation maxima at SK. The bottom plot shows the flux predictions 295 km from the source for several Off-Axis (OA) angles. Figure taken from [142].

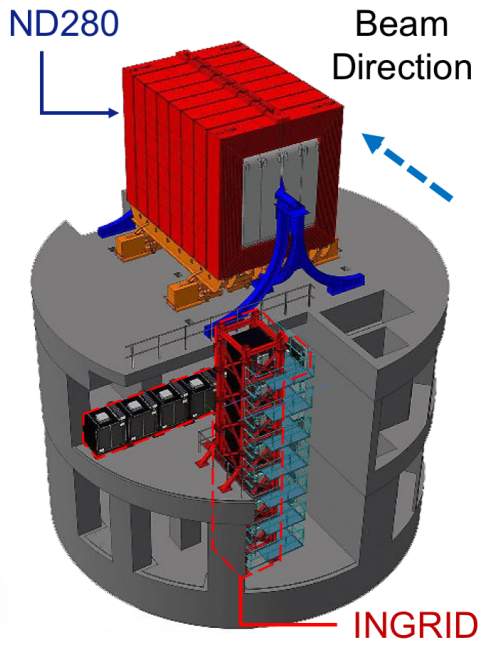

(b) The T2K near detectors ND280 and INGRID's positions relative to one another in the near detector hall, 280 meters downstream of the beam target. Figure taken from [143].

Fig. 3.2 (a) The effect varying the off-axis angle in T2K has on the flux spectrum, and (b) the ND280 detector hall layout.

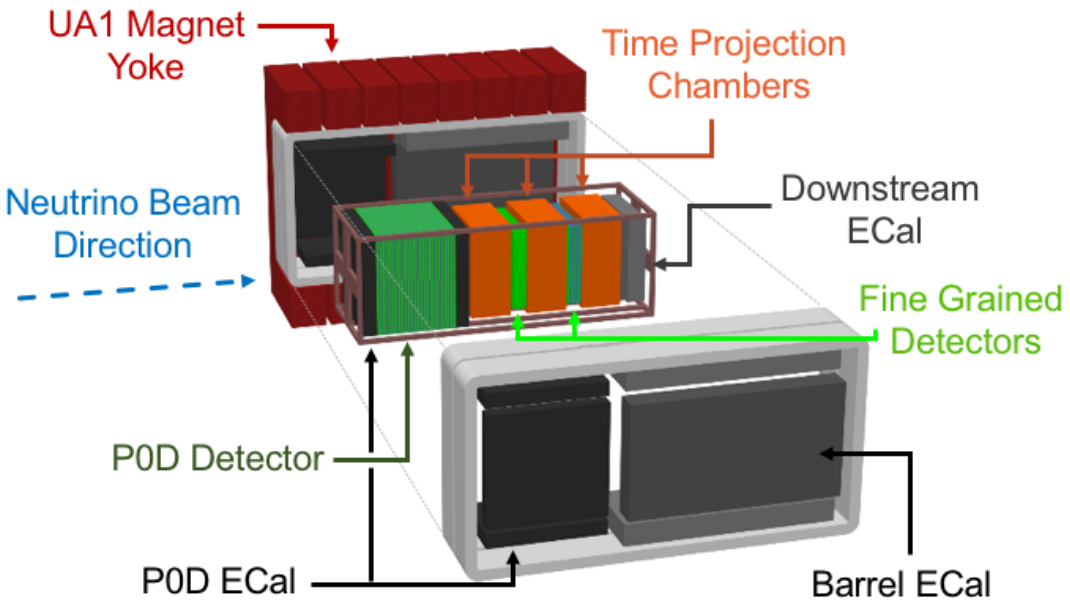

Fig. 3.3 Exploded half-view of the ND280 detector showing the position of each of its sub-detectors. Figure taken from [147].

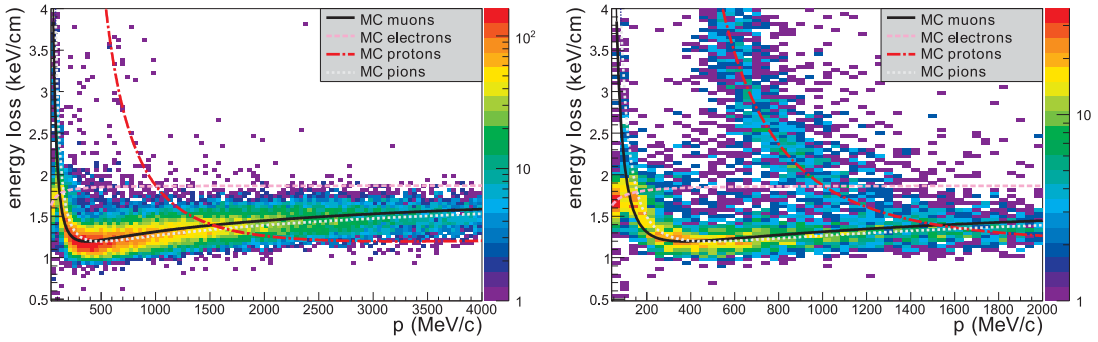

Fig. 3.4 Energy loss as a function of momentum for negatively charged (left) and positively charged (right) particles in the T2K TPC. Comparisons between the observed and expected energy loss for each particle hypothesis (MC curves) are used to discriminate particle species. Figure taken from [150].

and vertical orientations to allow 3-dimensional reconstruction of the interaction vertex. The downstream FGD (FGD2) uses a similar design to FGD1 but replaces 16 of the active scintillator layers with layers of passive water target so that comparisons between FGD1 and FGD2 can be used to extract the cross-section on water alone.

If a charged particle escapes the FGD it can pass up or downstream into one of the surrounding TPCs. As the charged particle traverses the TPC, ionisation electrons created in the argon gas drift in the TPC electric field from a central cathode to individual micro-megas readouts. The 3D trajectory of the particle can be reconstructed by looking at the time each hit arrives on the readout pad. The curvature of this track in the magnetic field is used to estimate the momentum of the particle, which combined with the energy lost as a function of momentum can be used to discriminate between different particle species as shown in Figure 3.4.

The ECals are also constructed from plastic scintillator strips, but are interleaved with 1.75 mm of lead between each layer. This increases the total number of radiation lengths and optimises the sub-detectors for calorimetric reconstruction of electrons and photons. Since the ECal surrounds the entire tracker region it can also be used as a veto to remove additional out-of-fiducial-volume backgrounds in a similar way to the SMRD. Hits in the ECal are reconstructed using a shower clustering algorithm to form isolated objects which can then be matched to particle trajectories reconstructed in the tracker.

The use of TPCs in a magnetic field means ND280 analyses can achieve good charge discrimination of muons and pions leaving the interaction vertex, unmatched by experiments without a magnetic field. Unfortunately, since the TPCs are located up and downstream of the FGDs many analyses have poor angular acceptance and have been restricted to only looking for tracks with angles less than $\sim 60^{\circ}$ with respect to the beamline axis. The combination of targets allows the ND280 detector to make cross-section measurements on carbon and oxygen necessary to propagate studies at ND280 to predictions at SK.

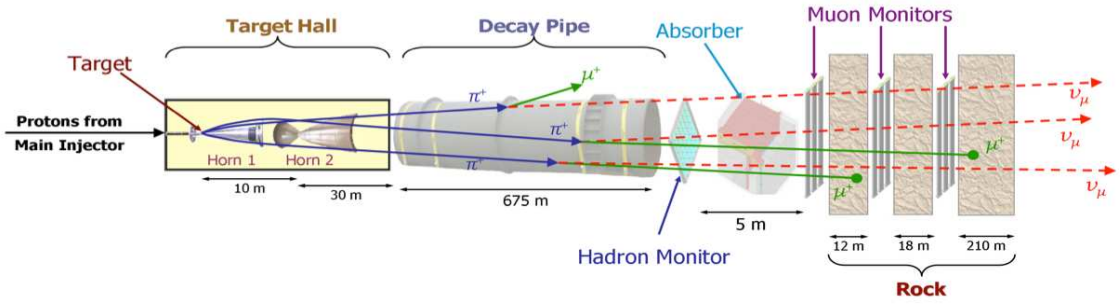

Fig. 3.5 NuMI Beamline Schematic. Figure taken from [154].

3.3 The MINERνA Experiment

MINERvA is a neutrino cross-section experiment studying neutrino interactions in the 0.1 – 100.0 GeV energy range [151]. The MINERvA detector is situated 2.1 m upstream of the MINOS near detector in the NuMI beamline at Fermilab [152, 153].

The NuMI neutrino beam is created using a similar method to T2K by firing 120 GeV protons at a graphite target [152] as shown in Figure 3.5. The mesons created in the target hall produce a high intensity neutrino beam with a flux peak of 3 GeV when NuMI is running in low-energy mode. Since MINERvA sits on-axis in this beam it is capable of measuring high statistics event samples that probe the quasielastic, pion production, and deep inelastic scattering regimes. Future MINERvA analyses aim to study neutrino interactions in the NuMI medium-energy beam with a flux peak of 7 GeV.

The inner detector volume consists of an active target region of 127 plastic scintillator (CH target) bars with a triangular cross-section placed into hexagonal scintillating planes perpendicular to the beam direction as shown in Figure 3.6. The triangular bars ensure that particles have a high chance of striking more than one bar as they pass through a single plane, as shown in Figure 3.7. The total inner detector consists of 64 of these planes, with each layer rotated 60° to the previous one, providing good 3-D reconstruction of tracks that cross multiple planes. The fully active target design allows analyses to make a good measurement of the total hadronic energy in an event by summing all energy deposited around the interaction vertex. This quantity can then be unfolded back to the true hadronic energy for an event by correcting for the detector response of different particle species.

The outer detector region consists of both electromagnetic and hadronic calorimeters to provide accurate reconstruction of particles that were not contained within the inner detector region as shown in Figure 3.6. The electromagnetic calorimeters are formed by alternating 0.2 cm layers of lead between 10 scintillator layers similar to those used in the active tracker region, and the hadronic calorimeters by alternating 2.54 cm layers of steel. This combination provides good containment of all hadrons originating from the interaction vertex.

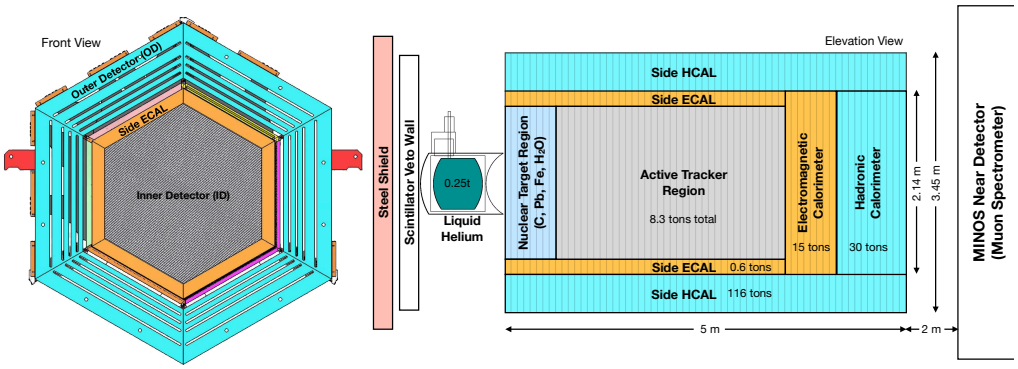

Fig. 3.6 MINERvA detector cross-sections. (left) Hexagonal plane layout. (right) Inner tracker region layout. Figures taken with permission from [151].

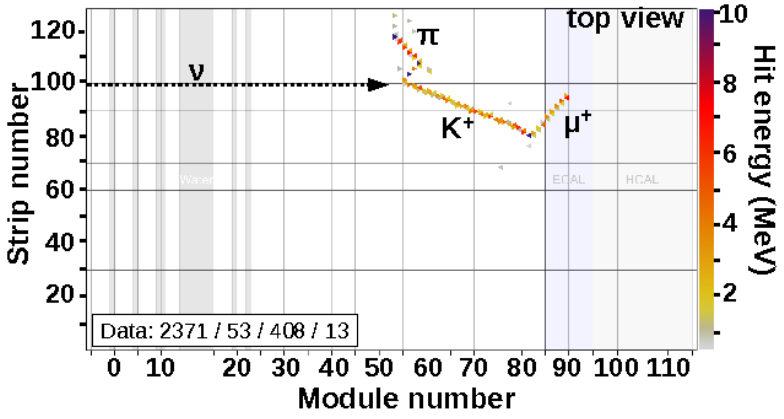

Fig. 3.7 Example event display showing neutral current kaon production inside the MINERvA tracker region. Particles passing through the detector leave hits in multiple scintillating bars within a single plane. Hits are combined across multiple planes to form particle tracks. Figure taken from [155].

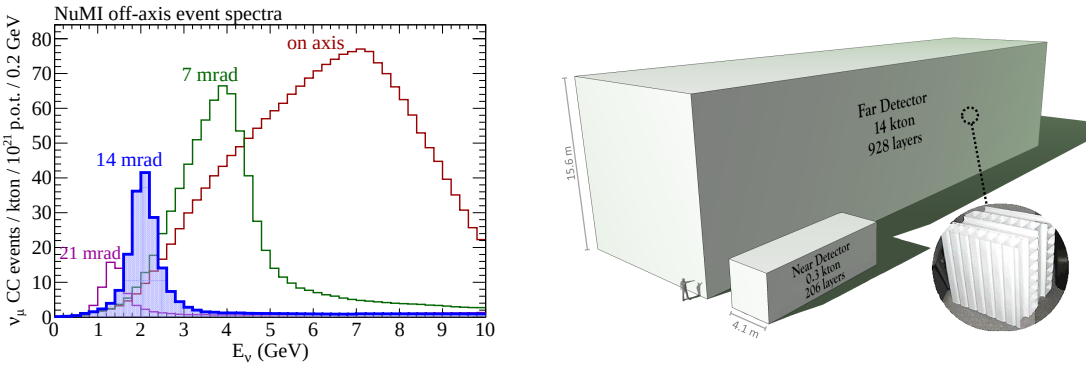

(a) (b)

Fig. 3.8 The NOvA experimental flux and detector dimensions. (a) NuMI flux predictions at varying off axis angles. The NOvA experiment sits at 14mrad, with a narrower peak than if it was placed on-axis. (b) Comparison of the size of the NOvA near and far detectors. To cancel cross-section uncertainties the near and far detectors are almost identical, varying only in size. Figures taken from [156, 157].

Since MINERvA has no magnetic field it is difficult to perform track-by-track charge identification of particles. Instead it uses the MINOS detector, which is magnetised, to tag muons, introducing a limit on some analyses that the angle between the outgoing muon and the beam axis must be less than 25° to ensure it propagates into the MINOS spectrometer.

The nuclear target region and liquid helium cryo-vessel at the front of the detector allow MINERvA to make measurements on a range of nuclear targets (He, O, Fe, CH, Pb). This region consists of five layers of passive targets interspersed with additional scintillator tracker modules to allow vertices to be extrapolated back to a given region. This allows MINERvA to make multiple measurements with the same flux profile so that flux uncertainties can be reduced when determining ratios of cross-sections on different targets.

3.4 The NOvA Experiment

NOvA is a long baseline neutrino oscillation experiment operating between Fermilab and Minnesota with a baseline of 810 km [156]. Both the near and far detectors are designed to be as identical as possible to reduce systematic uncertainties in the near/far event rate ratios. The target material and instrumentation method are the same in both, the two differing only in their size, with the near detector being 222 t and the far detector 15 kt. Both detectors are placed 14 mrad off-axis to the NuMI neutrino beam which centres the beam peak at 2 GeV as shown in Figure 3.8.

The NOvA detectors are formed by extruding titanium-loaded PVC into hollow bars which are filled with liquid scintillator (CH). Titanium dioxide in the bars helps increase internal reflection of scintillation light, which is picked up by a wavelength shifting fibre connected to a photodiode

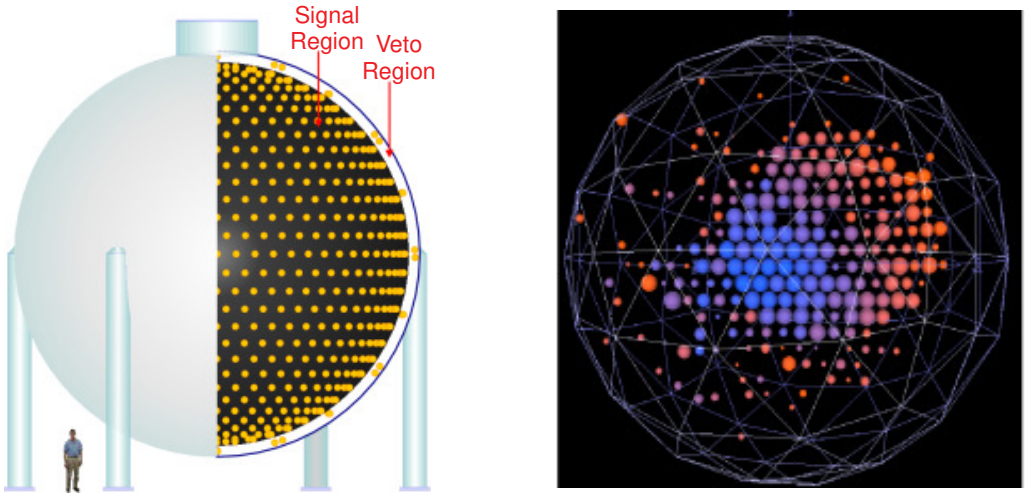

Fig. 3.9 MiniBooNE Experimental Setup. (left) MiniBooNE detector tank design. (right) MiniBooNE Cerenkov ring event display example. Each circle represents a struck photomultiplier tube. Figures taken from [45, 159].

readout. The bars are arranged in parallel to form planes perpendicular to the beam, and each plane is rotated 90° to the previous plane to allow 3D track reconstruction. Separation of muon neutrino and electron neutrino events is achieved by the observation that muons leave cleaner MIP-like tracks in the detector. Since the NOvA near detector is a fully active liquid scintillator target it is possible to reconstruct the total hadronic energy by separating energy deposits around the interaction vertex, as is done in MINERvA.

3.5 The MiniBooNE Experiment

The MiniBooNE experiment was designed to study short baseline neutrino oscillations using quasi-elastic neutrino interactions with a typical energy of 0.55 GeV [45]. MiniBooNE used a 8 GeV proton beam impinging on a beryllium target to produce the booster neutrino beam (BNB) at Fermilab [158]. A single magnetic focussing horn was used to select positive or negative pions in the meson shower produced from the target, which were then allowed to decay in a 50 m decay volume. The neutrinos produced from these decays passed through 474 m of dirt before reaching the MiniBooNE detector, 541 m downstream from the beam production point.

The MiniBooNE detector was a 12.2 m spherical tank, separated internally by a thin opaque sphere to define two regions, a main tank and an outer tank, as shown in Figure 3.9. The main tank was lined uniformly with 1280 photo-multiplier tubes (PMT) facing inwards, providing 4π coverage, and the outer tank was lined with 240 photo-multipliers that let the outer region be treated as an external veto. The spherical tank was filled with a long polymer chain mineral oil (CH_2) with a high refractive index, which provided better background discrimination and lower energy thresholds than a water Cherenkov detector.

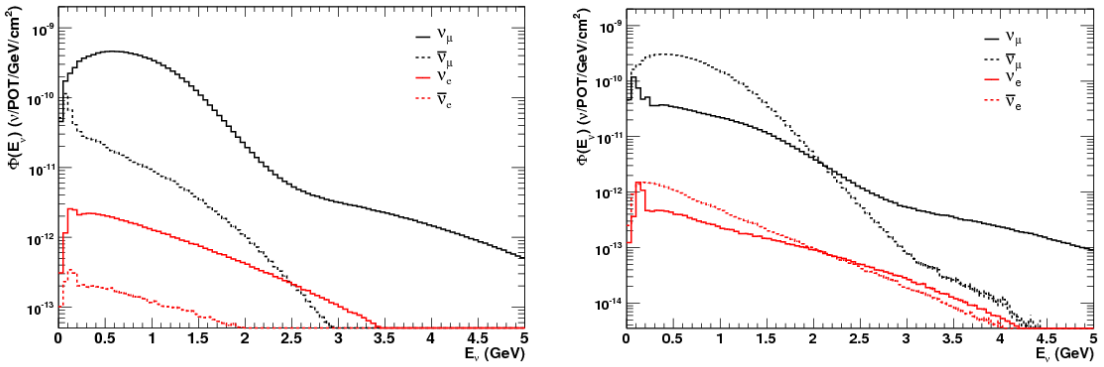

Fig. 3.10 MiniBooNE flux predictions for forward horn current (left), and reverse horn current (right). Figures are taken from [158].

Neutrino events were selected by identifying Cherenkov rings with the PMT's in the main tank, whilst rejecting events with PMT hits in the outer tank. In general since muons are minimum-ionising particles they produce clearer rings of PMT hits than electrons. Muon and electron track discrimination was therefore performed by feature analysis of the Cherenkov rings, allowing the MiniBooNE detector to discriminate between the two particles with a 99% accuracy. Pion production events were identified by detecting an additional ring from the michel-electron produced in the pion decay. The un-magnetised nature of the detector unfortunately means it had poor charge discrimination. This was a significant issue when performing quasi-elastic measurements in anti-neutrino mode where the wrong-sign contamination in the beam as shown in Figure 3.10 resulted in a significant contribution from quasi-elastic neutrino scattering in the selected event sample [158].

3.6 Future Neutrino Experiments

The Hyper-Kamiokande (Hyper-K) experiment is the proposed successor to Super-K, with an increased target mass of approximately one megaton of water [35]. A number of cross-section measurements have already been performed on $\nu - \mathrm{O}$ interactions by the K2K [160], and T2K experiments [116], and Hyper-K will benefit from the extensive model improvements developed during their lifetimes. Additionally, it has been proposed that gadolinium-loaded water could be used as a detector medium. This would allow Hyper-K to tag neutrons produced in a neutrino interaction, reducing backgrounds and allowing for higher precision measurements of $\nu - \mathrm{O}$ interactions.

In contrast, the DUNE long baseline oscillation experiment relies on the use of Liquid Argon TPC (LArTPC) technology to measure $\nu - \mathrm{Ar}$ interactions [34]. In LarTPC's the ionization tracks from charged particles are drifted towards a number of wire collection planes, and the readout from each

plane can be combined to create 3D reconstructed tracks of individual particles exiting a vertex. Liquid argon provides a good medium for neutrino experiments as it has a high density, and large drift distances can be achieved, allowing large fully active detector volumes to be constructed for use in high statistics measurements. However, since LArTPC's are still being developed, to date only the ArgoNeuT experiment has published measurements of $\nu - \mathrm{Ar}$ interactions in a few-GeV neutrino beam [161]. Therefore, our current simulations of interactions on argon are derived with a large uncertainty from constraints on lower atomic mass targets, such as carbon and oxygen.

For DUNE and Hyper-K to meet their required physics goals, the systematic uncertainties on neutrino interactions need to be reduced to less than 3%. An extensive cross-section measurement program will be required in the coming years to achieve this goal. The Short Baseline Neutrino Detector (SBND) [162] experiment at Fermilab plans to constrain the $\nu - \mathrm{Ar}$ cross-section, by measuring interactions in the booster neutrino beam, at a baseline of approximately 110 m.

As discussed in Chapter 1, the presence of sterile neutrinos can impact long baseline oscillation experiments by further modifying the observed oscillation probability, and introducing unaccounted for biases in cross-section measurements. The Fermilab SBN program aims to place a constraint on these oscillations by observing the booster neutrino beam at multiple baselines. Alongside SBND, the MicroBooNE [47] and ICARUS [163] detectors will be used to monitor the beam composition 470 m and 600 m from the source respectively. All three of these detectors also contribute towards the DUNE long baseline program by providing additional tests of the implementation of large scale LarTPCs. Furthermore improved e/γ shower discrimination offered by LarTPCs will be used by the MicroBooNE detector to probe the MiniBooNE low energy excess.

3.7 Experimental Summary

Alongside providing generator tuning tools, the second aim of the NUISANCE project is to collect and consolidate the entire collection of neutrino cross-section data from multiple experiments into a single repository. Achieving this goal will then allow neutrino interaction models to be consistently compared against one another and to a broad range of different interaction channels at varying experimental energy ranges. To summarise the experiments considered so far, and to support the analyses discussed in the remainder of this thesis, a review of each of their strengths is provided in Table 3.2.

Experiment	Flux	Target	Strengths	Published Analyses
Bubble Chambers	0.6 – 260 GeV	D	Good E_ν reconstruction Small nuclear effects	Inclusive QE 1π $N\pi$ (See review in [139])
T2K	0.6 GeV	CH (H2O, Pb, Ar)	Magnetised Carbon-vs-Oxygen Measurement Fine TPC Tracking	Inclusive [164] 0π [116] 1π [165]
MINERvA	3 GeV (LowE_ν) 5 GeV (Medium E_ν)	CH (C, Fe, Pb, H)	Hadronic Calorimety High Statistics	Inclusive [113] 0π [166] 1π[167] $N\pi$ [168] DIS [169]
MiniBooNE	0.6 GeV	CH	4π acceptance	QE/0π [170] 1π [171]
NOvA	2 GeV	CH	High statistics Identical near/far detector	
DUNE	3 GeV	Ar	Excellent $e-\mu$ discrimination High resolution tracking Sample multiple oscillation peaks	
SBND	0.6 GeV	Ar	Excellent $e-\mu$ discrimination High resolution tracking	
Hyper-K	0.6 GeV	H2O (Gd)	High statistics Neutron tagging	

Table 3.2 Overview of neutrino experiments relevant to the work presented in this thesis. The MINERvA experiment can operate in two different beam modes, therefore has two possible energy peaks. The targets collum shows the composition of the primary detector target, with possible secondary targets shown in brackets. Experiments measuring cross-sections on CH and H2O targets are most important when constraining the T2K interaction model. Only a selection of the most recent official publications for each of the main interaction topologies are shown. For a review of the extensive publications on measurements of neutrino itneractions in bubble chamber experiments, see [139].

Chapter 4

Short Baseline Neutrino Oscillations

As discussed in Chapter 1, neutrino oscillation experiments have established the absolute values of the three angles, and two mass splittings that describe mixing between the active neutrino flavours. However, experimental evidence from the LSND [42], MiniBooNE [46], and gallium experiments [50] have all suggested that oscillations with a much larger Δm^2 may occur over short baselines. Since observations of Z^0 decays already place a strong constraint on the number of active neutrinos, introducing a mass splitting of this size requires the addition of one or more 'sterile' neutrinos to the standard model that do not couple to the weak force. These models are referred to as $3+N$ models. Various sterile neutrino analyses have been performed in the past 15 years, however there is still no clear consensus on whether sterile neutrinos exist. This is because there are still several unresolved tensions between measurements of short baseline oscillation parameters. As discussed in Chapter 1, the KARMEN experiment found no signs of sterile neutrino mixing, excluding a large region of the mixing space preferred by the LSND and MiniBooNE experiments.

When trying to resolve tensions between accelerator experiment results the current uncertainty surrounding how to model the neutrino cross-section on a nuclear target poses a big issue. Often these accelerator sterile neutrino analyses have no additional near detector to constrain the unoscillated flux. As a result, the extracted flux spectrum after oscillations can be heavily dependent on the choice of cross-section model. This is a significant problem for global fitters attempting to combine data from multiple experiments. Since a number of cross-section models are in use by different groups, it is possible that including datasets that use two conflicting cross-section models in their extraction could lead to biases in a global fit. Understanding these biases and how cross-section modelling can affect a sterile neutrino oscillation analysis is paramount for the next generation of short baseline neutrino experiments.

This chapter focuses on understanding the effect sterile neutrino flux biases may have when model builders place constraints on neutrino interaction generators. In Section 4.1 the effect of short baseline oscillations on published cross-section measurements is discussed. In Section 4.2 a method

is outlined to check how well a set of model uncertainties cover sterile mixing biases in cross-section data fits. In Section 4.3 this procedure is applied to T2K's tuning of the NEUT 5.1.4.2 interaction model to MiniBooNE data [63]. Finally, in Section 4.4 the results are used to produce error inflation estimates for ND280 short baseline analyses.

4.1 Relation between Cross-section Measurements and Sterile Neutrino Searches

If Short BaseLine oscillations (SBL) do indeed exist in nature, it is possible that they may have already been observed at a number of other accelerator neutrino cross-section experiments. If we consider the simple case of active neutrino disappearance, sterile neutrino mixing would introduce a deficit in the number of observed neutrino interactions as a function of both distance and energy. Since the deficit depends on the neutrino propagation and not the type of weak interaction in the detector (QE, RES, DIS), a reduction in the rate would be observed at the same true neutrino energy across all interaction channels at once. Cross-section experiments often neglect the existence of short baseline oscillations, assuming the predicted flux has not changed in any way between the beam production point and the detector. In the limit of a perfect detector, and assuming no neutrino oscillations, the total cross-section for a given channel can be extracted as

$$\sigma_{\text{null}} = \frac{N}{T\Phi_{\text{null}}}, \tag{4.1}$$

where N is the observed number of signal events, T is the number of targets (commonly the total number of target nucleons is used), and Φ_{null} is the integrated flux prediction in a null-hypothesis (no sterile mixing) scenario.

The presence of sterile neutrino oscillations should be considered an additional flux systematic in Equation (4.1), capable of reducing the total flux by an unknown amount. If some fraction of the beam has oscillated into sterile non-interacting states, then the published flux prediction, Φ_{null}, used to extract the cross-section, is an incorrect overestimation of the total active neutrino flux. This leads to a biased underestimation of the cross-section in the published dataset, the strength of which is dependent on the given experimental baseline. Since the true event rate is the combination of the active flux, Φ_{osc}, and true cross-section, σ_{true}, the biased result can be expressed as

$$\sigma_{\text{bias}} = \frac{N}{T\Phi_{\text{null}}} = \frac{\sigma_{\text{true}} T \Phi_{\text{osc}}}{T\Phi_{\text{null}}}. \tag{4.2}$$

This can be expanded to evaluate the shift in the published cross-sections for a given experiment after the data has already been released as a a function of the null-to-oscillated fluxes as

$$\sigma_{\text{true}} = \sigma_{\text{bias}} \times \left(\frac{\Phi_{\text{null}}}{\Phi_{\text{osc}}} \right) \tag{4.3}$$

where Φ_{osc} is calculated assuming a given sterile neutrino mixing hypothesis.

Understanding these biases is of great importance to groups attempting to place constraints on the properties of sterile neutrinos or on cross-section models. Constraints are often extracted by comparing some reference model prediction (such as those from the NEUT event generator) to the detected event rates, assuming any difference outside of all other systematic uncertainties is a result of sterile neutrino mixing. These reference models are commonly referred to as a "null hypothesis prior". Many of the reference cross-section models available in current neutrino generators have been chosen because they fit some selection of the available scattering data. Furthermore, the free parameters in these models are often tuned by iterating over the available parameter space and choosing a set of values that maximise the models agreement with data whilst assuming a null mixing hypothesis. If the best fit parameters in any of these model tunings are found to significantly shift when sterile mixing is taken into account, then they should be considered too unreliable for use in a subsequent sterile neutrino oscillation analysis. Because of this, any sterile neutrino oscillation fit to short baseline data should be treated with caution before it is verified that the model that was used is insensitive to these possible biases. In addition, if the presence of sterile neutrino oscillations is confirmed in the coming years, many cross-section fits will need to be redone to understand if these oscillations could have impacted them in any way.

4.2 Extracting Residuals

The easiest way to avoid external mixing biases in short baseline oscillation fits is to take a conservative approach in which any cross-section parameters not already constrained by electron/pion-scattering data are left entirely free. Unfortunately, large variations in cross-section parameters are capable of introducing changes in the event spectrum that can resemble neutrino oscillations, reducing the expected sensitivity to sterile mixing parameters.

A more thorough approach would be to include comparisons to many cross-section datasets when constructing a joint likelihood. This has the advantage that it could be extended to include a range of different experimental baselines and energy ranges. This would require the cross-section models agreement with available scattering data to be evaluated for every choice of mixing parameters considered in the oscillation analysis, performing a simultaneous global cross-section and sterile neutrino oscillation fit. Unfortunately, a global cross-section fit of this kind has yet to be performed even under a null mixing hypothesis, and is likely to be too computationally expensive for current analyses given the large number of datasets that would need to be included.

If a sterile neutrino analysis has already been performed with a cross-section model that was tuned to data assuming a null hypothesis, it may be too difficult to update the results to account for additional biases in the cross-section model. In this case, a compromise is to check if the tuned cross-section model uncertainties used in the fits provided good coverage of the possible biases in

the region of mixing space investigated. If it can be proven that a cross-section tuning is insensitive to sterile mixing, then the model is safe to be used in a subsequent oscillation fit and the analysis is still valid. Thankfully the formalism defined in Section 4.1 can be used to understand if this is the case. Assuming different choices of mixing hypotheses, Equation (4.3) can be used to extract the 'true' cross-section data points for any of the datasets originally used to tune the cross-section model. The model tuning can then be repeated using these updated data points and the results compared with the original values used in the sterile oscillation analysis. If the re-extracted model parameters show little variation under different mixing hypotheses then they can be deemed reliable for use in a short baseline oscillation fit.

For a given data distribution the correction shown in Equation (4.3) must be folded into each bin individually, assuming some spectrum for the event rate as a function of energy in a bin. If events are generated according to the published flux distribution for a dataset, then Monte-Carlo (MC) events can be used to infer this spectrum in each kinematic bin. In MC events, the neutrino kinematics that led to a specific set of event kinematics are known, making it easy to include such a correction. In a given bin with kinematic constraints, x, the ratio of null-to-oscillated fluxes can be approximated by looping over all events and calculating a short baseline oscillation probability for each event inside the bin. The correction factor for a single bin, $C(x)$, is then given by

$$C(x) = \frac{\sum_i^N r(x^i)}{\sum_i^N r(x^i) P(\nu_\ell \to \nu_\ell, E_\nu^i)} \tag{4.4}$$

where the sum i runs over the entire event sample of size N, r is a boolean function that returns true if the event kinematics x^i lie within the kinematic restrictions of the bin, and $P(\nu_\ell \to \nu_\ell, E_\nu^i)$ is the survival probability for the neutrino in the event. In the studies discussed later in this chapter a simple two neutrino mixing muon survival probability is considered such that

$$P(\nu_\mu \to \nu_\mu, E_\nu^i) = 1 - \sin^2 2\theta_{\mu\mu} \sin^2 \left(\frac{1.27 \times \Delta m^2[eV^2] \times L[km]}{E_\nu^i[GeV]} \right), \tag{4.5}$$

where $\sin^2 2\theta_{\mu\mu}$ and Δm^2 are free mixing parameters defining the strength and frequency of oscillations, and L is the experimental baseline. This oscillation probability was chosen to match that used in an ongoing T2K short baseline oscillation analysis, but in theory any oscillation probability can be used in Equation (4.4)[1]. To approximate L on an event-by-event basis, without the full detector simulation, a random value was thrown for each event according to the average decay point of the neutrino's parent particle.

The factor C can be used to correct published cross-section data points and errors assuming the presence of sterile neutrino mixing. It must be stressed however that at this point C itself is model dependent, as we have used a cross-section model to evaluate the integrated neutrino rate in a chosen kinematic bin as a function of energy. It is therefore not possible to simply correct the data

[1] The chosen probability should match what analysis the model intends to be used for. A model tested by folding in a two-neutrino correction factor may still be inappropriate for a three-neutrino oscillation analysis.

to the 'true' value and release the updated results, instead analysers need to explicitly re-evaluate the bias correction for their own model. A simpler approach is to apply the inverse of this correction to the MC prediction when tuning a model to data, as this is functionally identical but avoids having to constantly re-update the data and its errors for each cross-section parameter set considered in a fit. This is shown when writing the test-statistic, χ^2, between the data and the MC as

$$\chi^2 = \sum_i \left(\frac{C^i D^i_{\text{bias}} - M^i_{\text{true}}}{C^i \Delta D_{\text{bias}}} \right)^2 = \sum_i \left(\frac{D^i_{\text{bias}} - (M^i_{\text{true}}/C^i)}{\Delta D_{\text{bias}}} \right)^2, \tag{4.6}$$

where D^i_{bias} is the released data central value for the i^{th} bin, ΔD_{bias} is the released data error, M^i_{true} is the MC prediction, and C^i is the correction factor for the bin.

Since C is just the inverse of the average oscillation probability, the value M^i_{true}/C^i evaluates to the sum over survival probabilities for all events in a bin. Therefore a Monte-Carlo generator tuning study can be repeated assuming any short baseline mixing hypothesis bias by simply weighting each event in the MC sample according to the survival probability. The extracted cross-section parameters from this updated fit will then be an approximation of the results obtained if the experiment had assumed the given mixing hypothesis when extracting their published results.

To test the validity of a reference model all one then needs to do is check whether the errors on the reference model cover the systematic shifts in parameters observed under different mixing hypotheses. This residual is calculated as

$$R(p) = \frac{p_{\text{ref}} - p_{\text{osc}}}{\Delta p_{\text{ref}}} \tag{4.7}$$

where p_{ref} and Δp_{ref} is a parameter and its associated error in the reference model (usually the null hypothesis prior), and p_{osc} is the best fit parameter choice that would have been made if sterile neutrino biases were accounted for in the fit. For each set of mixing parameters, a value $R(p)$ can be calculated for a given free cross-section model parameter. If $|R(p)| > 1.0$ at any point, then it is possible the prior uncertainty Δp_{ref} is underestimated and must be inflated to provide appropriate coverage of all systematic shifts possible when considering sterile neutrino biases.

This form of $R(p)$ naturally provides guidance on the level of error inflation that may be required. If the model errors, Δp_{ref}, are scaled by the maximum value of $R(p)$ observed for all the mixing hypotheses considered, then the updated model parameter uncertainties definitely provide 1σ coverage of the sterile biases when used as a prior in a subsequent sterile neutrino fit.

4.3 Sterile Neutrino Oscillations at T2K

This issue of short baseline biases in the external data fits was one of the main concerns in an early T2K study that attempted to use an older tuning of the NEUT 5.1.4.2 interaction model as a null

hypothesis prior when extracting limits on sterile neutrinos [172]. The reference model used in this analysis was tuned by the T2K Neutrino Interactions Working Group (NIWG) [173] by varying free model parameters in NEUT until a goodness of fit with respect to MiniBooNE data was maximised [171, 174–176]. These tunings were developed to be used as inputs for the 2012 appearance and disappearance oscillation analysis, but, since it was not their primary focus, no sterile neutrino mixing biases were included at the MiniBooNE baseline ($\sim$ 541 m) in the tunings.

It was unclear whether these model constraints were then valid for use in a more recent short baseline oscillation study being performed at ND280. These oscillation sensitivity studies (referred to as the “ND280 SBL Analysis") had already been performed within the analysis framework. To avoid having to redo this analysis for a wide range of different cross-section model tunings, it was decided that first, the validity of the reference model should be tested. The methods derived in the previous section were used to assess whether the uncertainties assigned to each of the free cross-section model parameters provided sufficient coverage of the sterile mixing biases that could be present.

4.3.1 NEUT Interaction Model

NEUT 5.1.4.2 was the default model of choice for all T2K oscillation analyses between 2012 and 2014. Version 5.1.4.2 uses the Smith-Moniz RFG spectral function model, with Quasi-Elastic (QE) and RESonant (RES) pion production interaction modes described by the Llewellyn-Smith and Rein Sehgal models respectively. These models are described in detail in Chapter 2. Notably, this older version of NEUT does not contain the microscopic Nieves model for multi-nucleon interactions. A number of free parameters are available in NEUT that can be used to reweight the event predictions to alternate model settings without having to regenerate new event samples. In this analysis, we consider all free cross-section parameters that were included in the ND280 SBL Analysis. Each of the free parameters considered are discussed in brief below.

- M_{A}^{CCQE} : Choice of dipole axial mass in Charged-Current Quasi-Elastic (CCQE) scattering events. Changes the normalisation and shape of the CCQE cross-section.
- **CCQE Norm.** : Total normalisation scaling applied to the overall CCQE cross-section.
- M_{A}^{RES} : Choice of the dipole axial mass in the axial form factor for resonant events. Changes the normalisation and shape of the cross-section for all the resonant pion production channels.
- W **Shape** : Ad-hoc parameter that changes the shape of the W distribution in the pion production cross-section. Affects RES events.
- **CC Oth. Shape** : Shape parameter affecting CC channels other than QE and RES. Affects mostly DIS pion production.

- **CC Coh. Norm.** : Total normalisation of the CC coherent pion cross-section.
- **CC 1π Norm.** : Total normalisation scaling applied to the CC single pion production cross-section.
- **NC Coh. Norm.** : Total normalisation scaling applied to the Neutral Current (NC) coherent pion production cross-section.
- **CC $1\pi^0$ Norm.** : Total normalisation scaling applied to the NC single neutral pion production cross-section.
- **NC Oth. Norm.** : Total normalisation scaling applied to NC channels other than QE and RES. Affects mostly DIS pion production.

4.3.2 NIWG Generator Tuning

To place initial constraints on the parameters in NEUT, the NIWG Tuning Package was developed [2]. This software package uses quasi-elastic and pion production data from the MiniBooNE experiment to constrain free parameters in a model. It achieves this by scanning an available parameter space to find a model parameter set whose predictions best fit a selection of the MiniBooNE data. For a given choice of alternative model parameters, the package calculates a weight in NEUT that evaluates the change in the cross-section between two discrete model choices. These weights are then binned into histograms that match the data to produce reweighted MC predictions for direct comparison so that goodness of fit statistics can be calculated.

MiniBooNE does not provide full correlations between bins for their datasets, instead only releasing uncorrelated shape-only uncertainties, alongside a total fractional flux normalisation uncertainty. Therefore, to evaluate the goodness of fit for a given model choice in the NIWG Tuning Package, the shape of the MC was compared to the data and a test statistic was calculated from the difference in shape plus the difference in absolute normalisation. This is given by

$$S = \frac{\sum_i d_i}{\sum_j m_j}, \tag{4.8}$$

$$\chi^2 = \left[\sum_i \left(\frac{d_i - (Sm_i)}{\Delta d_i}\right)^2\right] + \left(\frac{1-(1/S)}{\Delta\phi}\right)^2, \tag{4.9}$$

where S is a factor that normalises the MC to match the data, d_i is the data in the i^{th} bin, Δd_i and m_i are the shape uncertainty and MC prediction for the corresponding bin, and $\Delta\phi$ is the absolute fractional normalisation uncertainty for the chosen dataset. These χ^2 statistics are calculated for each dataset under consideration and added together incoherently (neglecting any cross-correlations between distributions) to form a joint likelihood that can be used to tune the model. An interface

[2] This cross-section tuning tool ultimately lead to the creation of the NUISANCE framework

Model	Datasets	Publication
CCQE	CCQE 2D $T_\mu - \cos\theta_\mu$	[174]
CC1π-νD	CCπ^+ 2D $E_\nu^{rec} - Q^2$	[175]
	CCπ^0 1D Q^2	[171]
	NC 1D π^0 $\lvert\vec{p}_{\pi^0}\rvert$	[176]
CC1π-νA	CCπ^+ 1D Q^2	[175]
	CCπ^0 1D Q^2	[171]
	NC 1D π^0 $\lvert\vec{p}_{\pi^0}\rvert$	[176]

Table 4.1 Choice of MiniBooNE datasets chosen to constrain each of the NEUT models in the T2K 2012 NIWG model tunings.

with MINUIT [177] allows the NIWG Tuning Package to iterate through possible model choices and scan the parameter space until a joint χ^2 statistic is found. This automatic tuning procedure allows the NIWG Tuning Package to be used in the systematic tuning of different cross-section models in NEUT.

In the NEUT 5.1.4.2 tunings, three separate fits were considered using the NIWG Tuning Package. The quasi-elastic component of the interaction model was first tuned to measurements of ν_μ CCQE interactions. For the pion production model, two separate tunings were then performed, intended to produce two seperate models as inputs for the T2K long baseline appearance and disappearance analyses. These are therefore referred to as the CC1π-νA (Appearance) and CC1π-νD (Disappearance) tunings respectively. The exact datasets included in each of the tunings considered in this chapter are discussed on the following pages. Note that to obtain a complete model constraint, both a quasi-elastic tuning (CCQE) and a pion production tuning (either CC1π-νA or CC1π-νD) was required. The cross-section model parameter constraints used in the ongoing ND280 SBL Analysis were derived from the CCQE+CC1π-νA tuning results. The full list of the dataset projections considered in each tuning study is reviewed in Table 4.1.

Parameter	NIWG Tuning	SBL Model	Updated Tuning	Residual
"CCQE"				
M_{A}^{CCQE} (GeV)	1.64 ± 0.11	1.21 ± 0.45	1.62 ± 0.03	0.91
CCQE Norm.	0.88 ± 0.02	1.00 ± 0.11	0.87 ± 0.11	-1.18
"CC1π-νD"				
M_{A}^{RES} (GeV)	1.41 ± 0.12	1.41 ± 0.11	1.41 ± 0.08	0.04
W Shape (MeV)	26 ± 12	88 ± 46	25 ± 12	-1.37
CC Oth. Shape	0.36 ± 0.39	0.00 ± 0.40	0.51 ± 0.38	1.29
CC Coh. Norm	1.42 ± 0.46	1.00 ± 1.00	0.77 ± 0.34	-0.23
CC 1π Norm	1.15 ± 0.09	1.15 ± 0.45	1.19 ± 0.08	0.09
NC Coh. Norm	0.99 ± 0.29	1.00 ± 0.30	0.99 ± 0.29	-0.03
NC $1\pi^0$ Norm	0.96 ± 0.13	0.96 ± 0.43	0.91 ± 0.12	-0.09
NC Oth. Norm	0.98 ± 0.29	1.00 ± 0.30	0.99 ± 0.30	-0.04
"CC1π-νA"				
M_{A}^{RES} (GeV)	1.16 ± 0.05	1.41 ± 0.11	1.23 ± 0.06	-1.64
W Shape (MeV)	42 ± 12	88 ± 46	30 ± 12	-1.28
CC Oth. Shape	0.36 ± 0.39	0.00 ± 0.40	0.22 ± 0.39	0.55
CC Coh. Norm	0.66 ± 0.35	1.00 ± 1.00	0.92 ± 0.46	-0.08
CC 1π Norm	1.63 ± 0.16	1.15 ± 0.45	1.35 ± 0.10	0.46
NC Coh. Norm	0.96 ± 0.29	1.00 ± 0.30	0.99 ± 0.29	-0.02
NC $1\pi^0$ Norm	1.19 ± 0.14	0.96 ± 0.43	1.08 ± 0.14	0.27
NC Oth. Norm	0.99 ± 0.30	1.00 ± 0.30	0.99 ± 0.30	-0.03

Table 4.2 Best fit parameters for the NIWG external MiniBooNE tunings (NIWG Tuning), compared to the null hypothesis priors used in the ND280 SBL Analysis (SBL Model). In some cases, the parameters and uncertainties in the SBL Model were left at their theoretical value and obtained a large uncertainty instead of being updated to match the extracted values in the "NIWG Tuning" column. The latest tuning results presented in this thesis, obtained by repeating the original NIWG tunings, are shown in the "Updated Tuning" column as a cross-check. The residuals shown in the final column are obtained using Equation (4.7) and taking the difference between the "SBL Model" and the "Updated Tuning" model parameters.

NIWG CCQE Tuning

Since the overlap between the CCQE and pion production channels at MiniBooNE is small, the quasi-elastic parameters were separated from the rest of the free model parameters in the NIWG CCQE Tuning study. CCQE-corrected interaction data [174], published as a double differential cross-section in reconstructed muon kinetic energy, T_μ, and scattering angle, $\cos\theta_\mu$, was used to constrain both M_{A}^{CCQE} and CCQE Norm. This MiniBooNE measurement used a selection of events with only a single muon in the final state to extract the CCQE cross-section[3]. The results for these tunings are shown in Table 4.2 under the "NIWG Tuning" column. Large enhancements of M_{A}^{CCQE} were found ($\sim$ 1.6 GeV) relative to the nominal ($\sim$ 1.2 GeV) in the NIWG tunings due to the lack of multi-nucleon effects in NEUT 5.1.4.2.

NIWG CC1π-νD Tuning

The MiniBooNE CC1π^+ [175], CC1π^0 [171], and NC1π^0 [176] data releases were used in a joint tuning to constrain the remaining pion production parameters in NEUT for the T2K long baseline disappearance analysis. Including multiple interaction channels was necessary to fully constrain the model's many free parameters. To avoid the problem of neglecting cross-correlations between distributions, a single dataset was chosen from each of these publications. In the CC1π^+ case, events with a single charged pion and a muon in the final state were selected by MiniBooNE to produce a double differential cross-section as a function of the neutrino energy, E_ν, and the four momentum transfer, Q^2. This distribution was used in the NIWG tunings to constrain the charged current pion production parameters in NEUT, and was chosen to ensure that ν_μ induced pion production had the correct energy dependence when propagated between the ND280 and SK detectors in the long baseline disappearance analysis. For the $CC1\pi^0$ channel, a similar selection was applied by MiniBooNE, requiring one muon and one neutral pion in the final state to extract the cross-section as a function Q^2. Finally, the $NC1\pi^0$ data release required a single neutral pion in the final state with no observed muon. Since a Q^2 distribution was not also released with this data, instead, comparisons to the NC π^0 $|\vec{p}_{\pi^0}|$ distribution were used to place a constraint on the NC Oth. Norm. and NC Coh. Norm. parameters in the NIWG tunings. The W Shape parameter was found to pull far away from nominal theoretical value in these tunings (see Table 4.2), producing a close to unphysical result of 26 ± 12 MeV compared to the theoretical value of 88 MeV. Therefore, at the time, it was suggested that in all subsequent T2K oscillation analyses the parameter should be left at a starting value of 88 MeV and have a large conservative uncertainty assigned to it.

[3] It is important to highlight that the use of this model dependent CCQE data in modern tuning efforts is strongly discouraged. The MiniBooNE CCQE-corrected data contains an inherent model dependence. The data was extracted using a tuned NUANCE prediction to subtract CC1π interactions where the pion is absorbed before it leaves the nucleus. Instead the MiniBooNE CC0π distributions contained in the same data release should be used to properly account for correlations between CCQE and CC1π channels.

NIWG CC1π-νA Tuning

In the appearance analysis pion production model tunings, a similar approach was taken as that in the NIWG CC1π-νD tunings. A single distribution was chosen from each of the MiniBooNE CC1π^+, CC1π^0, and NC1π^0 data releases when constructing a likelihood. The only notable difference being that instead of comparing the model to the double differential $E_\nu - Q^2$ distribution in the MiniBooNE CC1π^+ data release, comparisons were made to the published single differential Q^2 cross-section data. This avoided the problematic model dependence that is inherent in E_ν data releases that could potentially bias a long baseline ν_e appearance analysis. Moving to use this dataset instead in the NIWG tunings resulted in a slight shift in some of the extracted parameter values (see Table 4.2), with a slightly higher value for W Shape being extracted.

Updated Tunings

For the studies presented in this chapter it was necessary to first check that similar results to the original NIWG tunings could be extracted when repeating the studies using the latest version of the NIWG Tuning Package. 2×10^6 CC-inclusive NEUT events were generated using the MiniBooNE flux and a CH_2 target. These events were loaded into the NIWG Tuning Package and each individual tuning study was repeated to produce three sets of parameter constraints (one for CCQE, CC1π-νA, and CC1π-νD respectively). These "Updated Tunings" are shown in Table 4.2. Small differences were found between this updated study and the original NIWG tunings ("NIWG Tuning" column in Table 4.2) , but almost all parameters were found to be in agreement within errors from the fit.

The NEUT model tunings used in the ND280 SBL Analysis were derived from the CC1π-νD NIWG tunings (SBL Model in Table 4.2). For the M_{A}^{RES}, CC 1π Norm, and NC 1π^0 Norm parameters, the central value in the SBL Model was changed to exactly match the outputs of the NIWG tunings. In all other cases however, when faced with large shifts of the parameters away from their theoretical values, the remaining parameters were left at their theoretical values, with a large uncertainty assigned to them to cover the observed pulls in the NIWG tunings. For example, instead of adopting an extreme M_A^{CCQE} value of 1.64 GeV^2, the nominal NEUT value of 1.21 GeV was chosen with a large uncertainty that would cover the difference. This approach is justified when the model is being used only as an initial estimate, on top of which further constraints will be applied using T2K near detector data before being used in a long baseline oscillation analysis. However, in the SBL Analysis, where no effective near detector is available, this is not the case, and it is vital that proper uncertainties are applied to the cross-section model's central values before being used in the oscillation analysis.

The prior parameter constraints in the cross-section model used by the ND280 SBL analysis are shown in the "SBL Model" in Table 4.2. Whilst the uncertainties on many parameters have been chosen to cover the central values obtained in the NIWG CCQE and CC1π-νD tunings, the large uncertainties extracted in the NIWG tunings have not been accounted for. When the tunings are then repeated with the latest version of the NIWG tuning package, best fit results are found that

are within the NIWG Tuning uncertainty ranges, but are not within the uncertainty ranges of the SBL Model. When using Equation (4.7) to calculate error residuals for the null hypothesis this is clear. Treating the values and uncertainties from the "SBL Model" as p_{ref} and Δp_{ref}, and the values from the "Updated Tuning" as p_{osc} in Equation (4.7) shows that a number of parameters lie outside of the valid 1σ coverage, $|R(p)| < 1.0$ range. The residual for CCQE Norm. is at -1.18 due to the choice of 0.11 as the prior uncertainty instead of 0.12. The W shape parameter was left at the default theoretical value in the SBL model of 88 ± 46 MeV and as such the W shape residuals calculated using Equation (4.7) are always expected to be large. Large residuals are also observed for the CC Oth. shape parameter in the updated CC1π-νD tuning. Since the CC Other contributions in each sample were small, this parameter is very sensitive to statistical fluctuations in the MC in when repeating the tunings.

4.4 Bias Residual Scans

After the latest version of the NIWG Tuning Package was shown to reproduce the original NIWG tunings within error, a modification was made to the package to allow sterile induced biases to be easily folded into the MC cross-section prediction.

To calculate the oscillation probability a value of L is required in the MC simulation on an event-by-event basis. Limited information is provided on the distance between the parent meson decay point and the neutrino interaction point, outside of running the full MiniBooNE simulation, so an approximation was derived from the experimental details available. In cases where no exact value for L and its error is provided, the decay point can be approximated from the length of the decay tunnel, l_T, the thickness of the shielding between the decay tunnel and detector, l_S, and the total active width of the detector, l_D. Assuming a large Gaussian spread in L, gives

$$L = \frac{l_T + 2l_S + l_D}{2} \quad , \quad \Delta L = \sqrt{\frac{l_T^2 + l_D^2}{4}} \tag{4.10}$$

The experimental distances evaluated from the MiniBooNE experimental setup are shown in Table 4.3. In Ref. [45] a mean oscillation distance of ~ 520 m is quoted by the MiniBooNE collaboration but no exact uncertainty is provided. To account for possible variations in this quoted L a conservative error was chosen that covered the difference between the quoted value and the value using Equation 4.10 of 10 m. Variations to the MiniBooNE decay length were found to have a negligible effect on the results, as considering the extreme case of assuming the neutrino source is at the near or far end of the decay volume still only resulted in a $\sim 10\%$ variation in L. A discussion on Equation (4.10) is presented in Appendix A for use in cases where no value of L is provided by an experimental collaboration.

For each event, a value of L was randomly thrown within the chosen uncertainties for use in the oscillation probability calculation. The random seed was kept fixed so that each event obtained

Decay Volume (l_V)	50 m
Muon Shield (l_V)	479 m
Chamber Width (l_B)	12.2 m
Quoted L	520.00 m
Calculated L	510.10 ± 51.50 m
Chosen L	520 ± 10 m
Chosen L/E	$\sim$0.86 km GeV^{-1}

Table 4.3 MiniBooNE baseline specifications. A central value of L is chosen with errors that cover the difference between the calculated value and that quoted by the MiniBooNE collaboration [45].

a unique oscillation distance that remained constant for that event across different tuning studies. Using this value, and the true neutrino energy of the event, Equation (4.5) was used to calculate a sterile disappearance probability, which was assigned as a weight to the event. Binning these weights into the MC histograms when comparing the model predictions to the MiniBooNE data was then sufficient to produce MC predictions with sterile bias corrections folded in.

Since this correction method was implemented into the NIWG tuning package, it was possible to easily repeat the tuning studies under any arbitrary mixing hypothesis by simply updating the mixing parameters in Equation (4.5) before the sterile oscillation event weights were calculated. The rest of the cross-section model tuning procedure could be repeated as before to produce updated best fit tunings for any arbitrary set of mixing parameters. It was found that sterile neutrino mixing was capable of introducing large changes to some distributions which significantly pulled the best fit parameters. Examples of how the sterile bias correction has modified the distribution of the best fit prediction for some representative mixing values are shown in Figures 4.1 and 4.2.

Applying the sterile bias correction factor can reduce the overall normalisation of the MC prediction significantly when the average neutrino energy of the selected bin sits close to a maximum oscillation deficit. In the T_μ datasets, large variations are observed for some hypotheses due to the strong correlation between T_μ and E_ν as shown in Figure 4.3. A similar but weaker effect is also present in the p_{π^0} dataset.

4.4.1 Residual Scans

To properly assess whether a model is insensitive to sterile mixing biases, it is not enough to check a single mixing hypothesis. The stability of the model's central values must be checked for all possible mixing hypotheses that will be considered in the subsequent sterile oscillation analyses. However, since a single generator tuning study like the examples shown in the previous section take approximately 24 hours, fine scanning of many different mixing hypotheses is not always feasible. In this study, a grid search method was used to scan the range of different mixing hypotheses. A binning in $\sin^2\theta_{\mu\mu} - \Delta m^2_{24}$ was chosen to exactly match the coarse binning used in the ND280 SBL

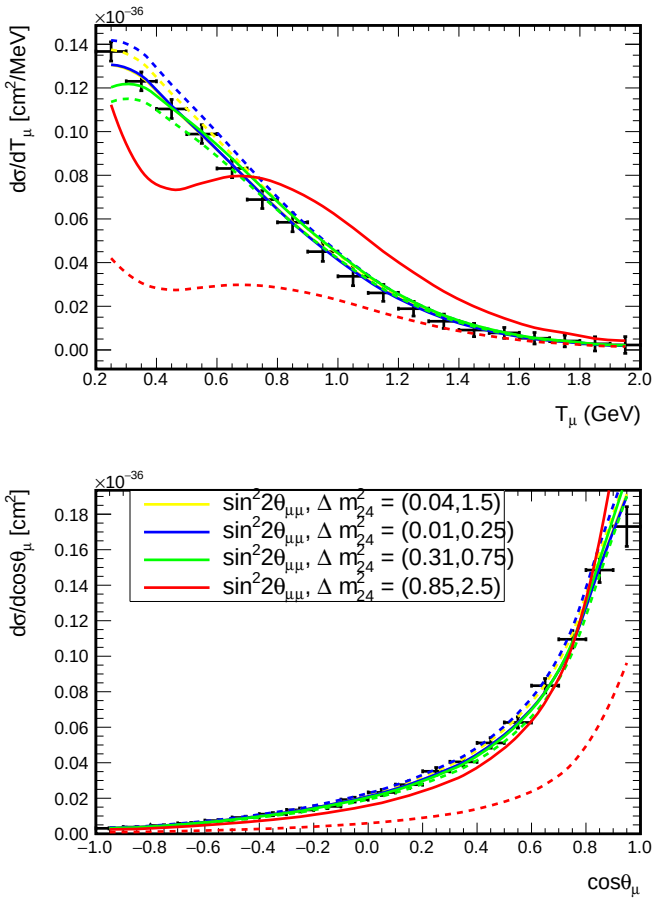

Fig. 4.1 MiniBooNE 2D $T_\mu \cos\theta_\mu$ dataset compared to best fit predictions when sterile induced biases are included for several examples of possible mixing parameter sets. Dashed lines on the projected distributions show the predicted cross-section before the MC model has been scaled by the CCQE normalisation factor. The MiniBooNE T_μ distribution is far more sensitive to sterile mixing, as E_μ strongly correlates with E_ν.

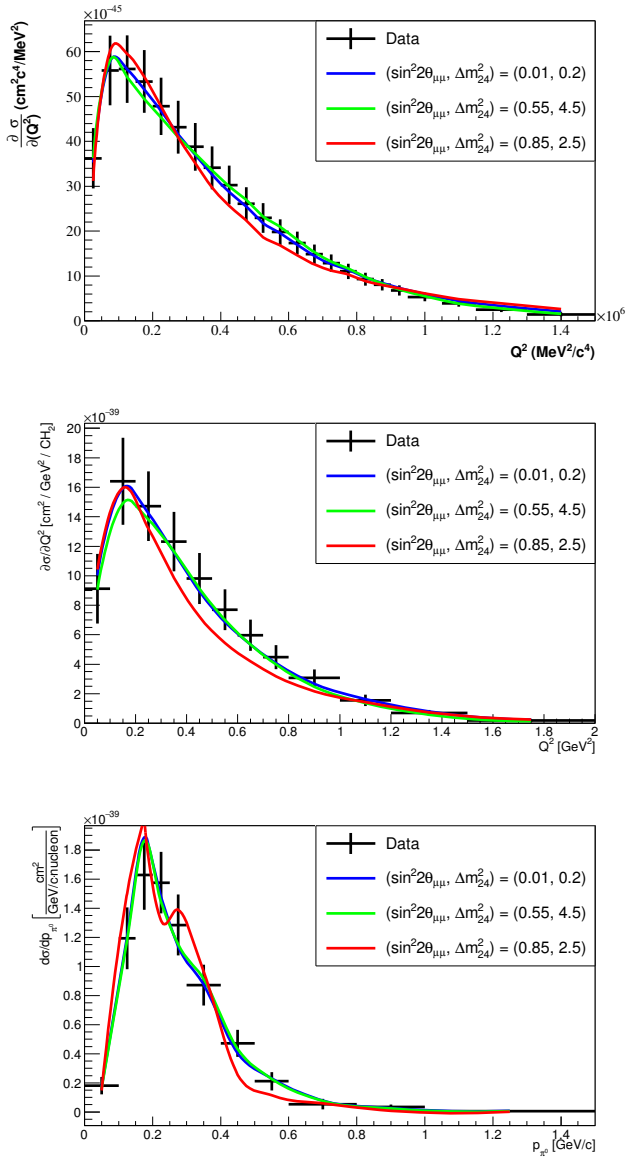

Fig. 4.2 MiniBooNE pion production datasets compared to best fit predictions at a range of mixing parameters. At larger mixing angles the shape of the NC1π^0 P_{π^0} prediction shows the strongest shape modification, whilst the normalisation change induced by sterile oscillations was corrected by the free parameters that handle individual cross-section channel normalisations.

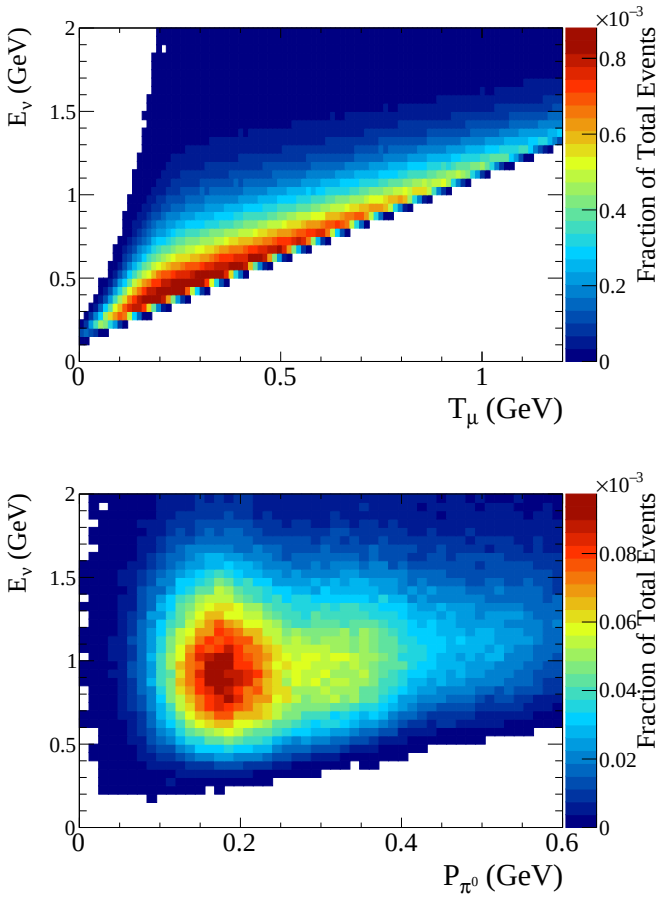

Fig. 4.3 2D projections of NEUT event samples as a function of neutrino energy and data kinematics. CCQE (left) and NC1π^0 (right) event selections were applied to a sample of CC-inclusive NEUT events generated with the MiniBooNE flux to produce both distributions. The kinematic limits mean that higher neutrino energies are required to produce events with high energy pions or muons in the final state. This deficit of events in the lower right quadrant of both T_μ and $|p_{\pi^0}|$ results in sterile neutrino mixing as a function of E_ν inducing shape variations in the 1D projections.

Bin	$\sin^2 2\theta_{\mu\mu}$	Δm^2 / eV^2
1	0.000 – 0.025	0.0 – 0.5
2	0.025 – 0.050	0.5 – 1.0
3	0.050 – 0.075	1.0 – 2.0
4	0.075 – 0.100	2.0 – 3.0
5	0.100 – 0.125	3.0 – 4.0
6	0.125 – 0.150	4.0 – 5.0
7	0.150 – 0.175	5.0 – 6.0
8	0.175 – 0.200	6.0 – 7.0
9	0.200 – 0.225	7.0 – 8.0
10	0.225 – 0.250	8.0 – 9.0
11	0.250 – 0.275	9.0 – 10.0
12	0.275 – 0.300	10.0 – 20.0
12	0.300 – 0.325	20.0 – 30.0
13	0.325 – 0.350	30.0 – 40.0
14	0.350 – 0.375	40.0 – 50.0
15	0.375 – 0.400	50.0 – 60.0
16	0.400 – 0.500	60.0 – 70.0
17	0.500 – 0.600	70.0 – 80.0
18	0.600 – 0.700	80.0 – 90.0
19	0.700 – 1.000	90.0 – 100.0
20	1.000 – 1.000	100.0 – 100.0

Table 4.4 Coarse grid binning for the sterile neutrino analysis. Possible mixing hypotheses are chosen based on the central value of each bin. The final bin in both dimensions has a negligible width such that the maximum possible Δm^2_{24} and $\sin^2 2\theta_{\mu\mu}$ are both evaluated as potential mixing hypotheses.

Analysis (see Table 4.4), reducing the required CPU hours to scan the entire mixing space whilst still ensuring that all points that would be sampled by the ND280 SBL Analysis were tested.

For each bin, the central values in the $\sin^2\theta_{\mu\mu}$ and Δm^2_{24} dimensions were chosen for the sterile oscillation parameters in Equation (4.5). These values were kept fixed, and a cross-section fit, with sterile bias corrections applied, was performed using the method discussed in Section 4.4. After each individual fit a residual was calculated for each of the different free cross-section parameters using Equation (4.7). In this calculation, the output of the fit was treated as, p_{osc}, whilst the values of p_{ref} and Δp_{ref} were kept fixed at the central value and uncertainty for each parameter in the "SBL Model" column in Table 4.2. This procedure produced 10 individual residual scans in total, one for each of the free parameters under consideration.

4.4.2 CCQE Residual Results

Residual scans for each of the CCQE parameters obtained from fits to MiniBooNE CCQE-corrected data are shown in Figure 4.4. It was found that larger values of both M_A and CCQE Norm were

required to fit the data when a large sterile induced bias was present. The results from these fits were used as p_{osc} in Equation (4.7), whilst the values of p_{ref} and Δp_{ref} were kept fixed at the central value and uncertainty for each parameter in the "SBL Model" column in Table 4.2. Since the prior uncertainty on CCQE Norm was slightly underestimated in the SBL model the residuals lie slightly outside the $|R| < 1.0$ range even at low $\sin^2 2\theta_{\mu\mu}$. At higher mixing probabilities the CCQE Norm. value increases to correct the shift in normalisation, bringing it into an acceptable range. In the regions above $\sin^2 2\theta_{\mu\mu} \sim 0.7$ the parameters were pulled very far out of the range defined by the SBL priors and the residuals were large, with a maximum residual of 11.06 and 2.04 for CCQE Norm. and M_A^{CCQE} observed respectively. The goodness of fit between the MC and MiniBooNE CCQE data was found to be poor in this region of mixing space. This is expected when the sterile mixing has introducted distortions in the shape that cannot be corrected for by changes in the cross-section model (see Figure 4.1).

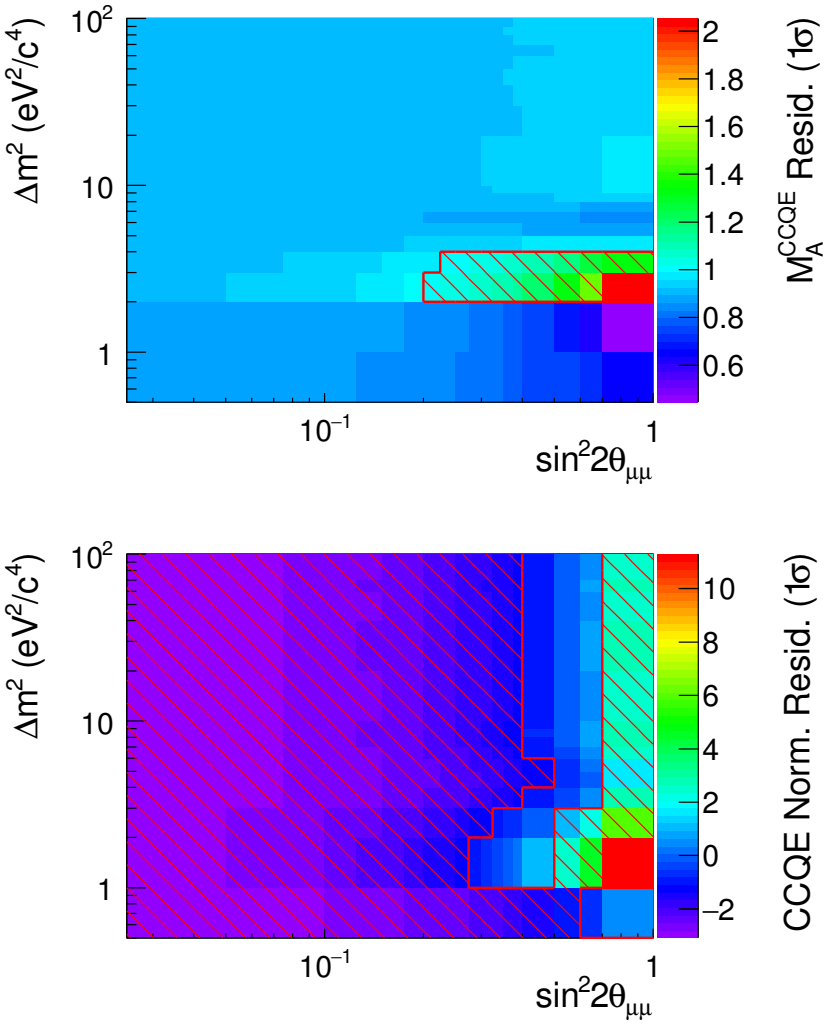

Fig. 4.4 Parameter residuals for each of the NIWG CCQE cross-section fits performed over a range of mixing parameters. The red contours highlight bins with a problematic residual ($|R_{ij}| > 1.0$)

It is possible to use the goodness-of-fit to exclude large residuals in regions where the data-MC agreement is poor. The minimum χ^2 for each fit is shown in Figure 4.5. Results where the p-value, calculated from the best fit χ^2 and number of degrees of freedom for the model tuning in each bin, is less than 68% are shown highlighted in red. Since the MiniBooNE data does not include cross-correlations between bins the number of degrees of freedom ($NDOF$) are likely overestimated in Equation (4.9). As a result, for a large fraction of the fits the minimum $\chi^2/NDOF$ found was significantly less than 1.0 and the p-values for each bin are overestimated. Therefore the lack of correlations produces a conservative exclusion region which is likely to be smaller than what would be observed if full correlation information was provided. Excluding fits in this region reduces the maximum observed residuals (and required error inflation) to 6.0 and 1.2 respectively. It must be stressed, however, that this reduced inflation is only valid outside of the excluded region and any sterile oscillation analyses (like the ND280 SBL Analysis) hoping to perform larger scans of the sterile mixing space must include the maximum residuals observed regardless of their goodness of fit.

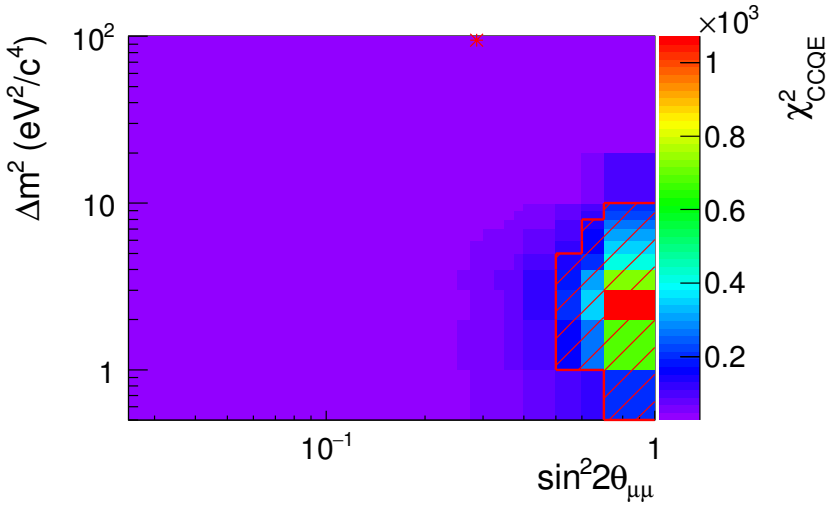

Fig. 4.5 χ^2 values for each NIWG CCQE cross-section fits performed over a range of mixing parameters. The red contours highlight bins where the cross-section fit result has a goodness-of-fit with a confidence of less than 68%. The minimum χ^2 bin is denoted by a red star and was found in the maximum mass splitting bin considered in coarse grid used by the SBL Analysis.

4.4.3 CC1π-νD and CC1π-νA Residual Results

Similar shifts in cross-section model parameters at high mixing were found in the CC1π-νD tunings. Since the CC1π-νD analysis used an E_ν distribution to constrain the cross-section model, this was found to be overly sensitive to oscillations with a number of fits failing to converge to a reasonable set of parameters within a large number of fit iterations. This is shown in Figure 4.6 where the best-fit χ^2 increases with $\sin^2 2\theta$ and Δm^2. Non-converging bins are shown in white in Figure

4.6. These convergence problems made it difficult to extract a full residual scan for the CC1π-νD tunings. In addition the bin with the best goodness of fit was found at one of the maximum $\sin^2 2\theta_{\mu\mu}$ points considered, next to the region of highest instability where non-converging fits were present.

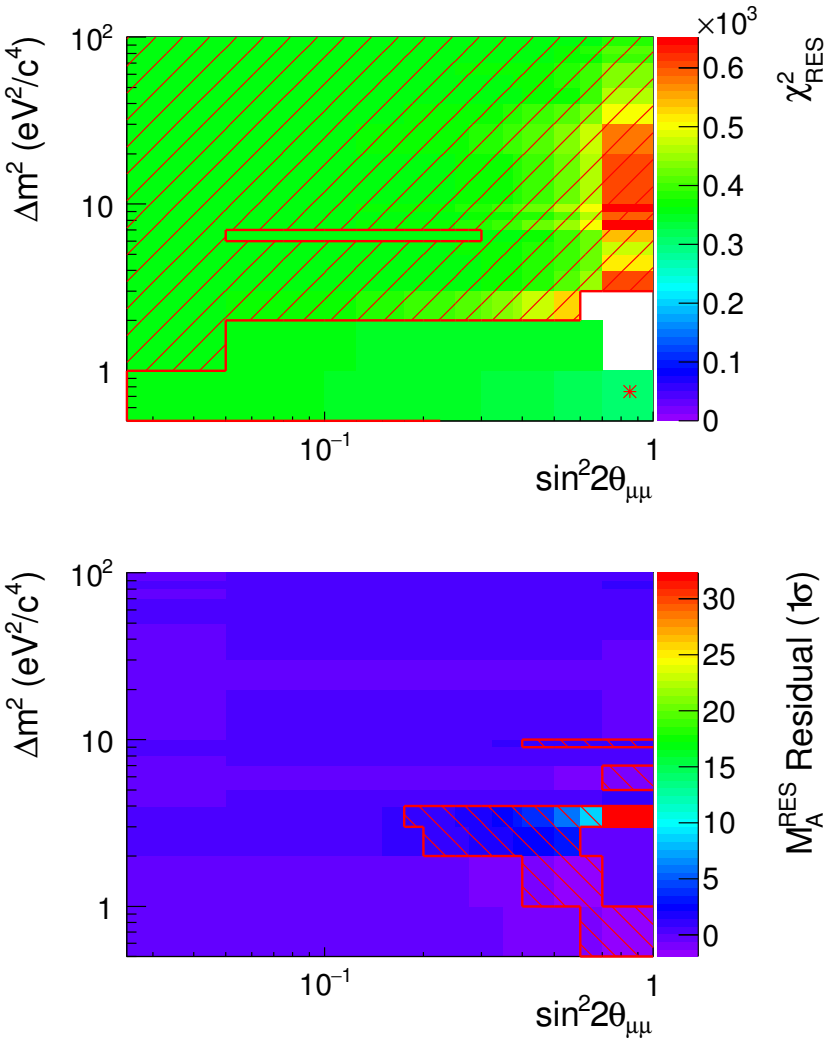

Fig. 4.6 (Top) χ^2 values for each NIWG resonance "disappearance" cross-section fit performed over a range of mixing parameters. The red contours highlight bins where the cross-section result has a goodness-of-fit with a confidence of less than 68%. The minimum χ^2 bin is denoted by a red star, and non-converging bins are filled in white. (Bottom) Example residual scan for the M_{A}^{RES} parameter for a range of mixing different mixing parameters in the NIWG resonance "disappearance" cross-section fits. . White bins in the top plot show fits that did not converge due to sterile mixing significantly modifying the model's spectrum as a function of energy. In addition a large portion of the mixing space has a poor goodness of fit at high $\sin^2 2\theta_{\mu\mu}$ because of the inclusion of E_ν data. This suggests the disappearance model tuning is unfit for use in a sterile neutrino fit.

As discussed earlier, the ND280 SBL Analysis model is derived from the NIWG CC1π-νD tuning results, however, due to the issues with non-converging bins, these tunings were deemed to be unfit for use in a sterile neutrino analysis. However, when performing the residuals scans for the

CC1π-νA tunings, all of the possible mixing hypotheses considered resulted in a converging fit. This was due to the removal of the 2D $E_\nu - Q^2$ CC1π^+ dataset in favour of a single differential in Q^2 which was less sensitive to sterile neutrino oscillations. Poor goodness-of-fit values were only observed at high mixing, as shown in Figure 4.7, so only a small region of mixing space residuals could be excluded based on the model's ability to fit the data.

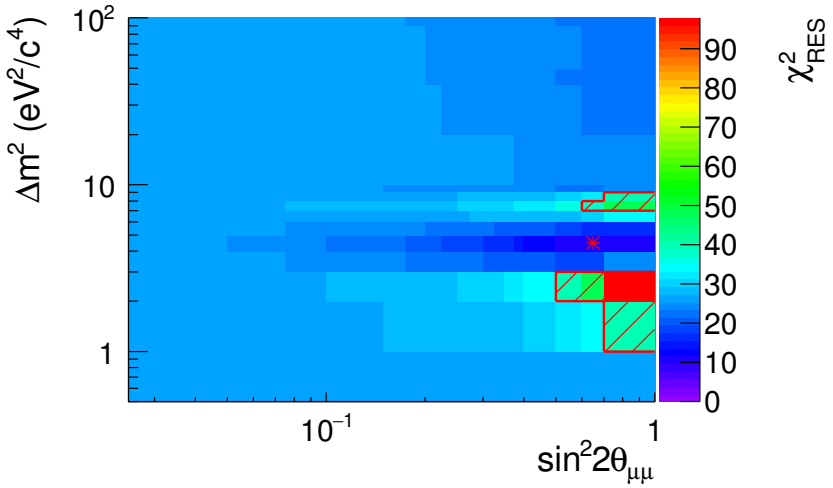

Fig. 4.7 χ^2 values for each NIWG resonance "appearance" cross-section fit performed over a range of mixing parameters. The red contours highlight bins where the cross-section fit result has a goodness-of-fit with a confidence of less than 68%. The minimum χ^2 bin is denoted by a red star.

Since the NIWG CC1π-νA tunings were found to be far more stable when sterile oscillation biases were included it was decided that the errors in the ND280 SBL Analysis should be rescaled to cover all possible biases observed in the CC1π-νA tuning scans. To do this, the results of each of the updated tunings for the CC1π-νA sterile mixing scans were used as p_{osc} in Equation (4.7), whilst the values of p_{ref} and Δp_{ref} were kept fixed at the central value and uncertainty for each parameter in the "SBL Model" column in Table 4.2. This allowed a conservative error scaling to be calculated that covered the difference between the SBL Model (derived from the original CC1π-νD tunings) and the updated CC1π-νA tunings, as well as any extra bias induced from sterile mixing in the external data. Residual scans calculated for each of the resonance parameters using this method can be seen in Figure 4.8. Problematic bins with $|R| > 1.0$ are highlighted with red contours.

Since M_{A}^{RES} and W-Shape both had starting residuals outside the range ± 1 they were considered problematic for almost every bin in the mixing space. All cross-section parameters show the same general behaviour observed in the CCQE fits. At large values of $\sin^2 2\theta_{\mu\mu}$ they are pulled away from the reference model's central values. Fortunately, the conservative errors placed on channel normalisations mean that the possible biases due to sterile mixing for the CC Oth. Norm., NC Coh. Norm., and NC Oth. Norm., are already covered by the prior uncertainties. Unfortunately the CC1π, NC1π^0, and CC Coh. normalisations all require larger prior uncertainties if the SBL Model

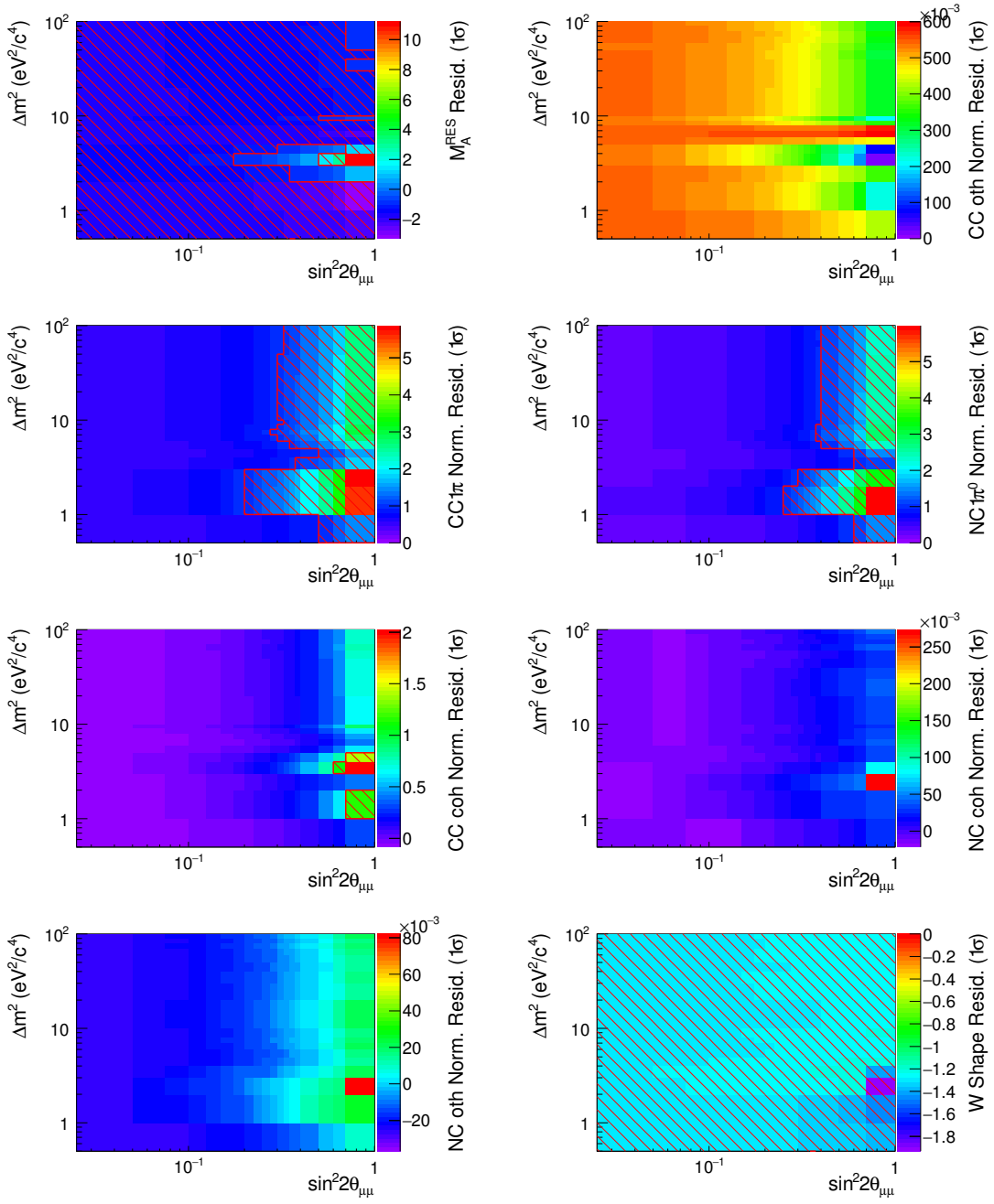

Fig. 4.8 Parameter residuals for each of the NIWG "appearance" cross-section fits performed over a range of mixing parameters. All parameters show some dependence on the sterile mixing hypothesis assumed in the fits. The red contours highlight bins with a problematic residual ($|R_{ij}| > 1.0$). In these regions the uncertainties used in the ND280 SBL Analysis do not provide sufficient coverage of the large biases that may be present in the external data due to sterile mixing. Some parameters, like M_{A}^{RES} and W Shape show large residuals at very low values of $\sin^2 2\theta_{\mu\mu}$ suggesting their uncertainties are underestimated even when sterile mixing effects are weak.

is to be used to probe the $\sin^2 2\theta > 0.7$ region in the ND280 SBL Analysis, as the residuals were found to be large in this region.

4.5 Conclusions

The reference model residuals were used to calculate error inflation tables for each cross-section parameter for use by the ND280 SBL Analysis. Using the residual scans shown previously a scaling matrix, $E(\theta)$, was produced as a 2D histogram for parameter θ, with the i^{th} and j^{th} bins filled from the corresponding residual histogram, $R(\theta)$, according to

$$E_{ij}(\theta) = \max(1.0, |R_{ij}(\theta)|). \tag{4.11}$$

An additional matrix was produced by taking the maximum error scaling residual across all of the residual scans, to form a single error scaling histogram that could be used to de-weight the prior uncertainties on the cross-section model by a single function of $\sin^2 2\theta$ and Δm^2_{24} if required. Figure 4.9 shows the error scaling matrices created for the combined CCQE parameters, combined CC1π parameters, and the total cross-section model (CCQE and CC1π studies combined). Since the maximum error scaling value was large, requiring the initial analysis errors to be scaled by a factor of over 10, it was suggested that completely flat priors (no constraints) should be used on the cross-section model instead to ensure the biases observed in this analysis would not impact subsequent SBL analyses in anyway. This work, and the SBL analysis it was developed for, have laid the groundwork for an updated sterile neutrino oscillation analysis to be performed by T2K in the future that plans to use the latest cross-section models available in NEUT, and severely relaxed parameter constraints, to place a reliable limit on sterile neutrino oscillations.

The analysis discussed in this chapter highlights the need to test model uncertainties used in short baseline oscillation models to avoid possible biases from external data. A general method was developed to evaluate these biases which is easily transferable to external cross-section fits in any neutrino event generator.

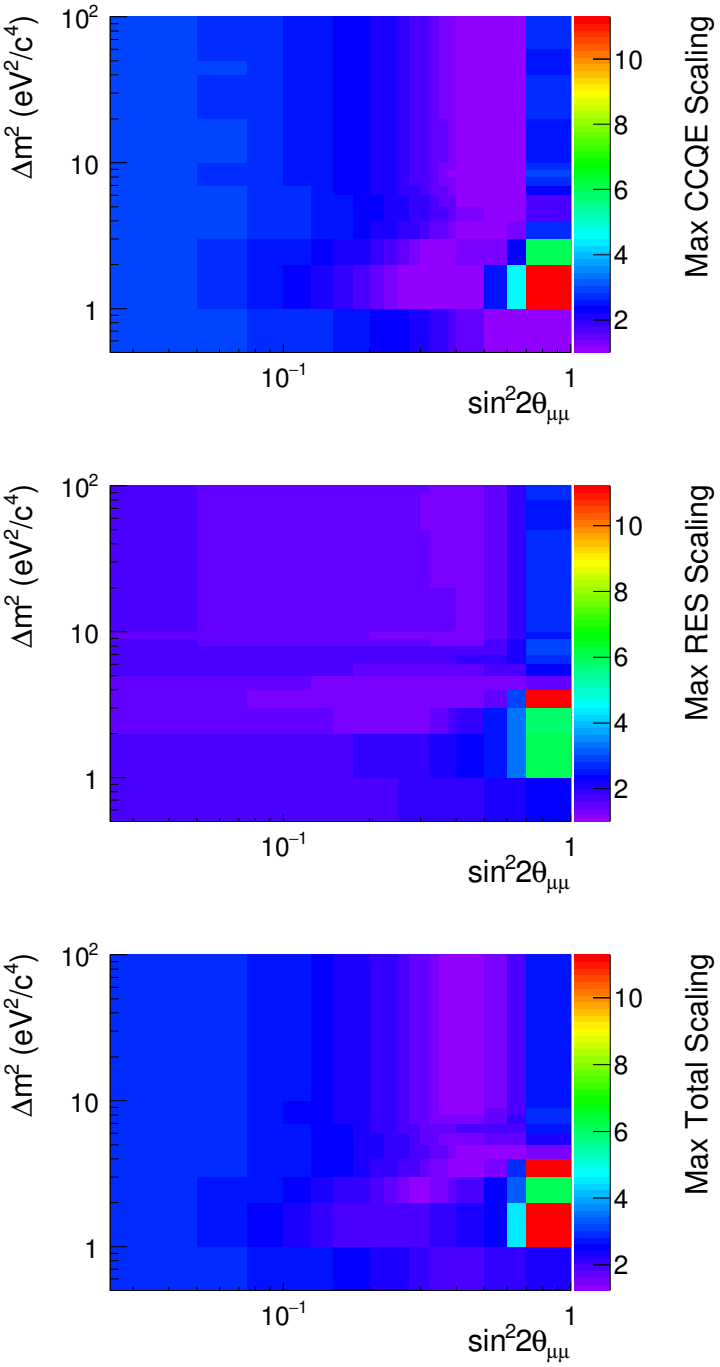

Fig. 4.9 Combined error scaling tables for the CCQE and CC1π (RES) fits. These histograms can be used as lookup tables to evaluate how much the cross-section uncertainties need to be inflated for a given choice of sterile mixing hypothesis to ensure appropriate coverage of the sterile mixing biases in the MiniBooNE data.

Chapter 5

Form Factor Uncertainties for T2K Oscillation Analysis

5.1 Introduction

At T2K energies the dominant interaction topology is charged current zero pion production (CC0π). ND280 has a smaller angular acceptance for final state particles than Super-Kamiokande (SK), therefore a cross-section model is required to extrapolate from restricted to full angular phase space in the Oscillation Analysis (OA). Because of this it is vital that appropriate uncertainties are placed on the CC0π model used in the extrapolation, especially in the high lepton angle bins that ND280 does not probe.

The CC0π topology is primarily composed of CCQE events with a small fraction of multi-nucleon 2p2h and CCπ-abs events (where a pion is produced but reabsorbed during the nuclear cascade) also contributing. The 2017 T2K OA uses the Smith-Moniz RFG model in NEUT 5.3.3 to describe CCQE interactions. Since many of the electromagnetic nucleon form factors present in Equation (2.2) can be constrainted from electron-scattering data, the dominant uncertainty present in current models of CCQE neutrino-nucleon scattering originates from the axial form factor, F_A.

This form factor is weakly constrained by theory with only two commonly accepted bounds on its shape [81]. The first strong bound, originating from beta decay measurements, requires that the form factor goes to the axial coupling constant at negligible momentum transfer, $F_A(0) = g_A = -1.267$. The second bound is derived from perturbative QCD [178], which states that the form factor must obey an asymptotic scaling law at high momentum transfer of $F_A(Q^2 \gg 0) \sim Q^{-4}$. Note that $Q^2 < 2$ GeV^2 can still be considered below the asymptotic regime, so does not place an exact limit in the given Q^2 regions considered in this work, only requiring that the form factor eventually tends towards zero at ever increasing momentum transfers. Since the choice of form factor is arbitrary

between these bounds, the shape of F_A is often further constrained by comparing different models to experiments.

Commonly a dipole form has been used to describe F_A as it provides reasonable agreement with available data and has only one free parameter, the axial mass M_A. This assumes a roughly exponential distribution for the axial charge in the nucleon as a function of the radius. There is no exact theoretical justification for this choice, other than it is a model that has been shown to agree with bubble chamber with the minimal number of parameters. A number of historical global fits placed constraints on the axial mass to be $M_A = 1.026 \pm 0.021$ GeV using neutrino-deuterium data and 1.069 ± 0.016 GeV using pion electropoduction data [81]. Reanalyses of the pion electroproduction data have shown that additional loop corrections are capable of reducing this result by 0.055 GeV, bringing the two datasets in line with one another.

Recently it has been proposed that the dipole assumption is not well motivated and lacks sufficient freedom to fully describe all available data [179–182]. The majority of data used to constrain M_A originates from measurements with $Q^2 < 1.0$ GeV^2, with much weaker constraints placed at $Q^2 > 1.0$ GeV^2 since the data is statistically limited in this region as shown in Figure 5.1. Since the dipole model has only one free parameter it has limited freedom to modify its shape so that it can reliably fit both regions simultaneously. Instead tunings to both regions at once often place a strong constraint on M_A at low Q^2 whilst failing to capture the known statistical uncertainty in the tail. There are no theoretical constraints on what the shape of the form factor should be in the region between the low momentum transfer, beta decay bound, and the high momentum transfer, QCD scaling law bound. Therefore, it is expected that the limited shape freedom of the dipole model does not fully represent the known uncertainty in this region. Whilst choosing the simplest model that fits the data was deemed acceptable when comparing CCQE models to bubble chamber data in the past, the axial form factor is now a dominant systematic uncertainty for many experiments. Underestimating this cross-section model uncertainty has the potential to overexaggerate experimental sensitivy to different mixing parameters. This high Q^2 tail region is of significant importance for the ND280 to SK propagation stage of the T2K OA since high Q^2 events correlate with high muon scattering angle events in both detectors. It is during this propagation that underestimated uncertainties on the axial form factor could lead to problems, since the ND280 detector can only constrain the forward going (low Q^2) region of the CCQE model.

The nominal NEUT model currently uses a simple dipole model to describe the axial form factor with a conservative choice of $M_A = 1.21 \pm 0.20$ GeV, that covers the differences between values extracted from deuterium (1.03 GeV) and carbon (1.35 GeV). This chapter describes the extraction of more reliable axial form factor shape uncertainties at high Q^2 for use by the T2K OA, by building an enveloping error band frmo a number of available form factor models. Section 5.1 describes the development of several alternatives to a simple dipole model. Section 5.2 describes the tuning of these forms to bubble chamber deuterium data, and finally Section 5.3 discuss the creation of

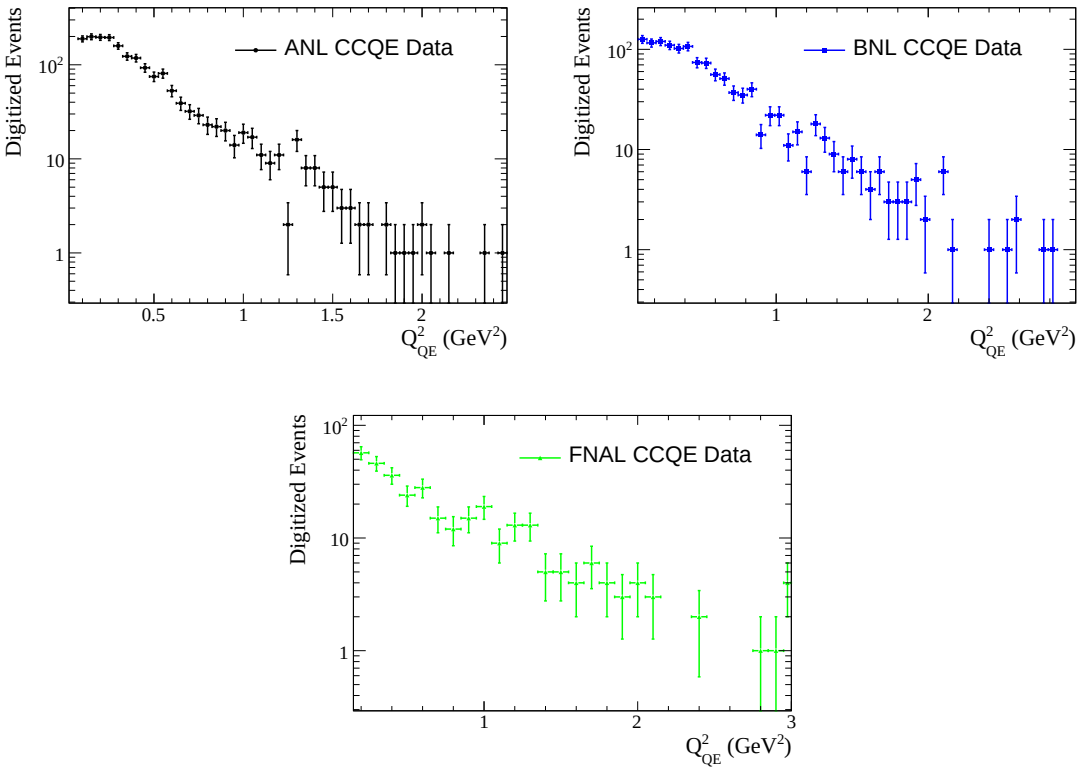

Fig. 5.1 Bubble chamber events as a function of Q^2 digitised from [123, 130, 132]. Since no normalisation information is provided for the raw event rate distributions in the original publications, these rates cannot be compared directly to one another, instead requiring a common Monte-Carlo model to be compared to each one.

ND280 fake dataset predictions to estimate the impact such models could have on the neutrino oscillation parameters.

5.2 Non-dipole Axial Form Factors

Recently a number of alternative parametrisations have been suggested [181, 183] that provide better shape uncertainties and stronger theoretical motivation than the simple dipole axial form factor model. These models and their motivations are presented briefly in the following subsections.

5.2.1 2-component Model

This model was originally introduced to describe the electromagnetic structure of the nucleon and reflect the shape of the form factor predicted by higher order QCD perturbation theory at high Q^2. It moves away from simple dipole models for the nucleon, instead trying to describe form factors in terms of different vector contributions in the nucleus. In Ref. [183] the same model was extended to describe axial form factor data probed in pion electroproduction measurements. The axial form factor is described in terms of two contributions:

$$F_A^{2-Comp}(Q^2) = g_A(1+\gamma Q^2)^{-2} \times \left(1-\alpha+\alpha\frac{m_a^2}{m_a^2+Q^2}\right), \tag{5.1}$$

where g_A is the axial coupling constant, $g_A = -1.267$, m_a is an axial meson mass term, and α and γ are free parameters to be extracted from data. The first term, with parameter γ, represents contributions to the form factor from the valence quark core of the nucleon. Values for γ are obtained from studies of the electromagnetic nucleon form factors ignoring the axial contribution, and are found to be 0.25 GeV and 0.515 GeV in [184] and [185] respectively. These differences arise from the choice of electromagnetic form factor data used to extract each value, highlighting a clear model dependence in their extraction. Since there is no clear theoretical preference for each parameter set, both are considered in this work with their envelope treated as the total uncertainty of the two-component model. The second component, depending on α and m_a, represents the contribution from the axial meson quark-antiquark cloud. m_a is taken to be the mass of the lowest contributing axial meson, which is the $a_1(1260)$ with a mass of $m_a = 1.230$ GeV. In [183], values for the free parameter α are extracted from fits to the pion electroproduction data shown in Figure 5.2. A resonance production framework is required to express the pion electroproduction data in terms of the axial form factor, with different framework choices predicting very different form factor shapes. It is clear from Figure 5.2 that whilst pion electroproduction data can be used to constrain F_A, large uncertainties will still be present due to the many available resonance production frameworks. Since variations in these frameworks are not considered in this work, they are not discussed in detail here, and instead the reader is directed to [183] for a more thorough review. In [183], all

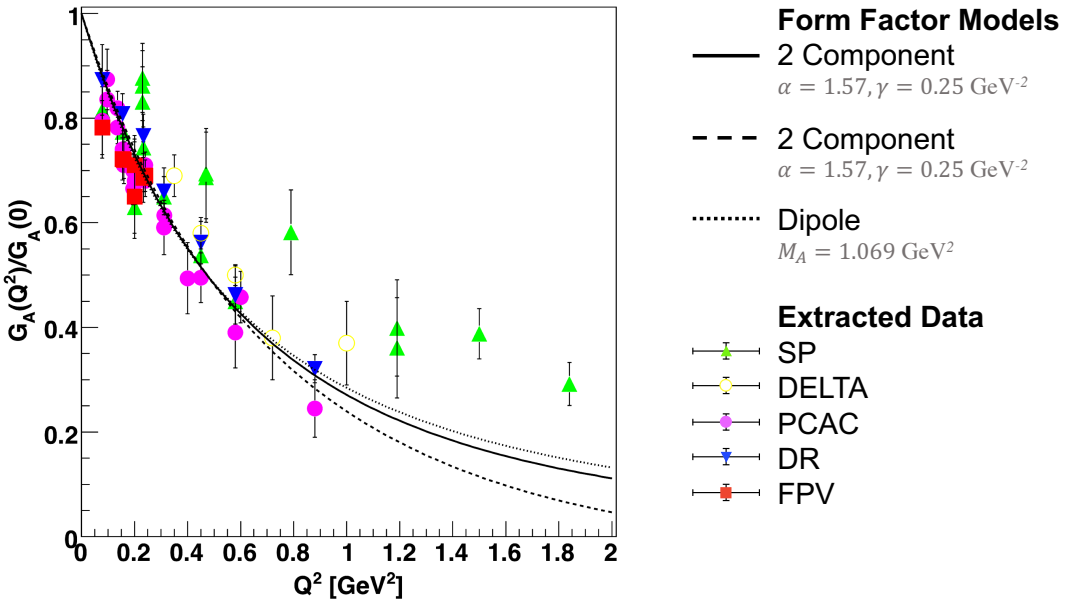

Fig. 5.2 2-Component form factor predictions compared to pion electro-production measurements. The data points show pion electro-production measurements translated into form factor space. The colours show the varied results when using different model choices for resonance interactions in the extraction. The black line shows the prediction for a dipole form factor ($M_{\mathrm{A}} = 1.069$ GeV), whilst dashed and dotted lines show the two-component model predictions for $\gamma = 0.25$ GeV^{-2} and 0.515 GeV^{-2} respectively. Figure taken with permission from [183].

these different shapes are considered to produce a constraint on α for a given choice of γ. This method resulted in two constraints of $\alpha = 1.57 \pm 0.04$ for $\gamma = 0.25$ GeV^{-2} and $\alpha = 0.95 \pm 0.05$ for $\gamma = 0.515$ GeV^{-2}. The effect of varying α within the extracted uncertainties for each of these best fit results is shown in Figure 5.3 compared to a simple dipole model.

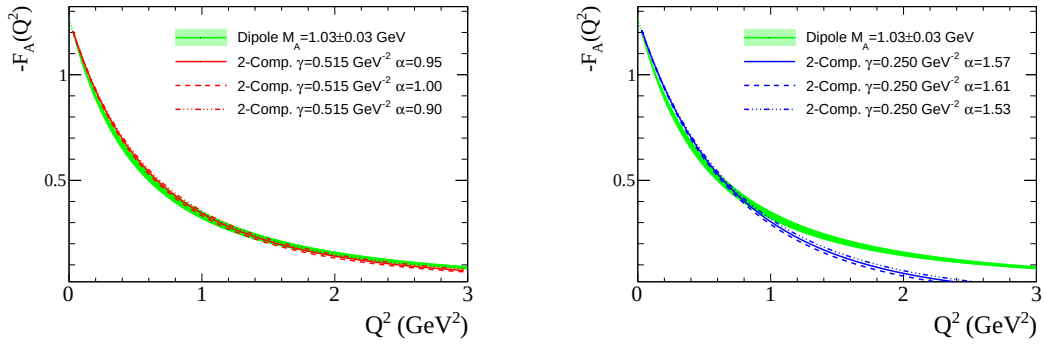

(a) α Variations, $\gamma = 0.515$ GeV^{-2} (b) α Variations, $\gamma = 0.25$ GeV^{-2}

Fig. 5.3 Variations of the 2-component form factor within the provided global fit uncertainties on α for both choices of γ considered in Ref. [183].

Early studies of the 2-component model found that a similar problem as for the dipole model occurred when tuning to data. Strong constraints were placed at low Q^2 and there was insufficient freedom to inflate the model uncertainty at high Q^2 to reflect the lack of data in that regime. Even when varying both γ and α freely it was found to be too difficult to vary the prediction at high Q^2 without simultaneously modifying the model's shape at low Q^2 as shown in Figure 5.4. Because of this it was decided that the 2-component model was insufficient for use by the T2K OA, and an improved model with significantly increased shape freedom was required.

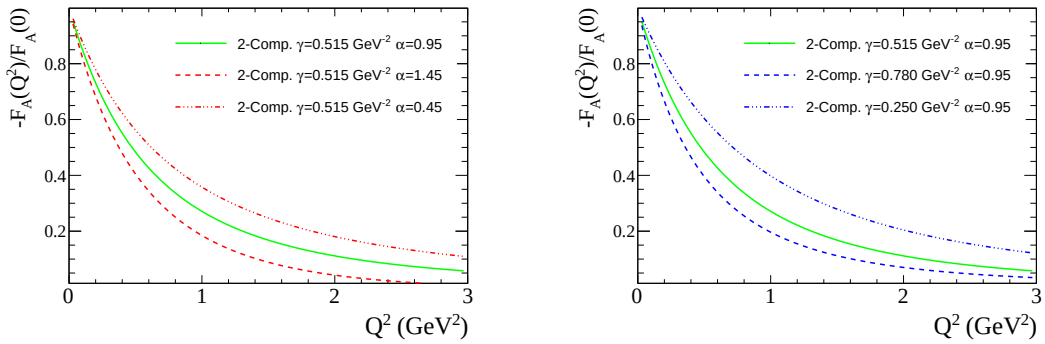

(a) α Variations (b) γ Variations

Fig. 5.4 Large variations of the α and γ parameters in the 2-component form factor model. In each plot the example parameter sets lie far outside the 1σ uncertainty ranges quoted in Ref. [183].

5.2.2 3-component Model

The 3-component model was developed to provide an alternative form factor model for use in the T2K long baseline oscillation analysis. A priority was placed on developing a model that contained enough degrees of freedom that it could produce an ad-hoc uncertainty band that covered the possible predictions of a dipole model, and both of the possible two-component model parameter sets. In addition it needed to account for the observed statistical uncertainty present in the bubble chamber CCQE data. This would ensure that conservative shape uncertainties were placed on the axial form factor to avoid any underestimation potentially biasing the oscillation analysis results. Since the 2-component model was also capable of describing a dipole model with appropriate choice of γ this was chosen as the basis for an improved model. The 3-component model was created by extending the base model with an additional exponential term which decays at high Q^2. This exponential term provides the freedom to vary the gradient of the form factor at low Q^2, leaving the free parameters in the original 2-component part of the model to set the shape at higher momentum transfer. The model is given by

$$F_{\mathrm{A}}^{3-Comp}(Q^2) = \left[g_A (1+\gamma Q^2)^{-2} \times \left(1 - \alpha + \alpha \frac{m_a^2}{m_a^2 + Q^2} \right) \right] + \left[\lambda g_A Q^2 e^{\lambda - \beta Q^2} \right], \tag{5.2}$$

where α, γ, λ and β are free parameters. In early studies of the model λ and β were varied freely, however fits of this kind were found to have trouble converging since very small values of β could introduce large unphysical fluctuations in the tail of the distribution. To avoid this issue λ was defined to be $\lambda = (-\sqrt{|\theta|\beta})$, and θ was instead treated as a free parameter in the model. Making this substitution does not modify the possible form factor shapes (since any choice of β affecting the normalisation can be counteracted with an appropriate choice of θ), but does correlate the two parameters in a fit, resulting in a reduction of the absolute exponential term when the exponential extends to high Q^2. This removes the ability for the correction to try and produce unphysical narrow peaks to correct a single bin, making the fits converge faster. Taking the square root of both terms also caused the variation each parameter could introduce to be strongly suppressed when approaching $\lambda = 0.0$, making the fit more stable when scanning near the parameter boundaries.

Nominal values of $(\alpha, \beta, \theta, \gamma) = (0.95, 0.515, 2.0, -0.15)$ were arbitrarily chosen for the 3-component model. β is required to be positive and greater then 1.0 and $|\theta|$ must be appropriately chosen to ensure the exponential does not cause the model to significantly disagree with the QCD scaling law by producing large deviations from a $\sim Q^{-4}$ behaviour above $Q^2 > 1$ GeV^2 . The functional form of each contribution can be seen in Figure 5.5.

Appropriate choices of each parameter allow the model to transition continuously between the dipole, 2-component, and 3-component models, allowing fits to data to extract uncertainties that cover the possibilities of all 3 models. The effect that varying each free parameter has on the axial form factor is shown in Figure 5.6.

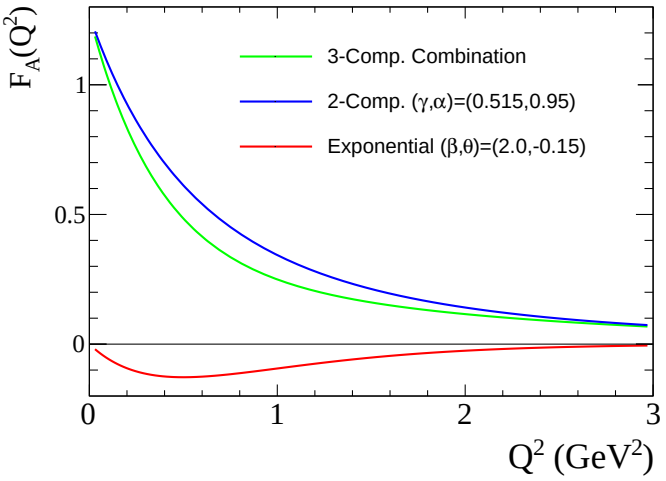

Fig. 5.5 Comparison of the 2-component and exponential contributions to the total 3-component model. The total exponential term is always considered to be negative, suppressing the form factor at low Q^2.

5.2.3 Z-Expansion Model

Introduced in Ref. [181], the Z-expansion form factor is a model-independent parametrization of the nucleon structure. The aim of the Z-expansion model is to describe the form factor as a simple Taylor expansion in a dimensionless variable with minimal assumptions on its shape. Only the beta decay bound at low Q^2, and the QCD scaling law constraints at high Q^2 are applied to the model, with every part in between left entirely free to be constrained by data. By mapping the kinematically allowed regions of Q^2 onto a dimensionless variable z in the range $|z| < 1$ it allows the form factor to be expressed using a Taylor expansion as

$$F_{\mathrm{A}}(Q^2) = \sum_{k=0}^{N} a_k z(Q^2)^k, \tag{5.3}$$

where a_k are free parameters obtained from empirical tunings. The function z that applies the Q^2 mapping is given by

$$z(Q^2) = \frac{\sqrt{t_c + Q^2} - \sqrt{t_c - t_0}}{\sqrt{t_c + Q^2} + \sqrt{t_c - t_0}}, \tag{5.4}$$

where t_c is the momentum-transfer cut-off for particle production, and t_0 is an optional parameter that defines what value of Q^2 corresponds to $z = 0.0$. The cut-off corresponds to the production mass threshold in $N\bar{N} \to n\pi$ interactions, since the axial form factor is related to the $N\bar{N}\pi$ form factor through the Partially Conserved Axial Current hypothesis [79]. 1π production is forbidden by kinematic constraints, and 2π production is forbidden by G-parity, therefore, the 3-pion production mass threshold is used, $t_c = 9m_\pi^2$. The choice of t_0 depends on the application since the form of

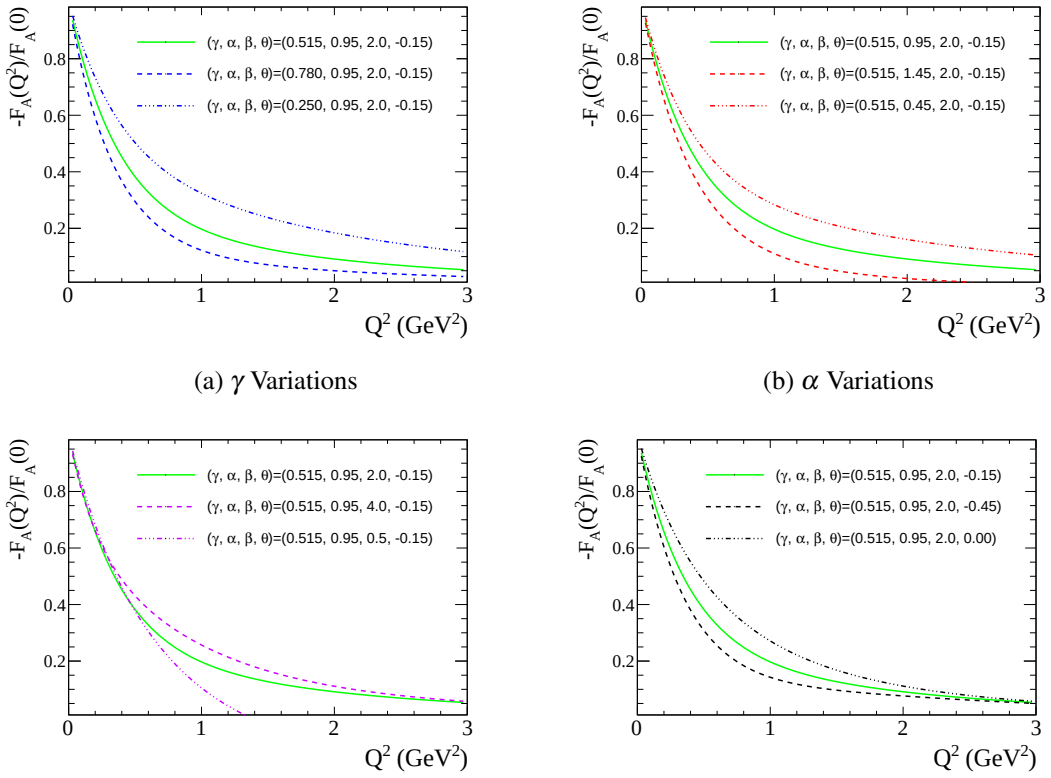

(a) γ Variations

(b) α Variations

(c) β Variations

(d) θ Variations

Fig. 5.6 The effect varying each of the free parameters in the 3-component model has on the shape of the axial form factor. An extreme value of β is shown in the bottom left plot to highlight the breakdown of the model if $\beta < 1.0$, producing a form factor that goes below zero.

Equation (5.4) ensures that any value of $t_0 < t_c$ will result in values of z within the unit circle. An appropriate choice for t_0 is therefore one that distributes the majority of data points of interest within the smallest $|z|$ range so as to optimise the convergence in Equation (5.3). For a given maximum momentum transfer, Q^2_{max}, this is

$$t_0^{optimal}(Q^2) = t_c(1 - \sqrt{1 + Q^2_{max}/t_c}). \tag{5.5}$$

For CCQE neutrino scattering the majority of data points sit below approximately $Q^2 < 1$ GeV^2, corresponding to $t_0 = -0.28$ GeV^2. This is the nominal value suggested in the Z-expansion model Ref. [180] and so is also the choice considered here.

With an appropriate $Q^2 \to z$ mapping, the a_k coefficients in Equation (5.3) are left as free parameters that can be empirically tuned to describe the structure of the nucleon. Since the optimal choice of t_0 minimises the range of $|z|$ it is expected the higher order coefficient terms contribute at less than 10%. As a result the shape of the form factor is approximately linear as a function of z and is most sensitive to variations in a_0 and a_1.

In the implementation suggested in Ref. [180] a nominal model using $N = 8$ in Equation (5.3) is suggested. Several constraints must be placed on the many Z-expansion form factor coefficients to ensure it maintains the correct shape and agrees with the beta decay and perturbative QCD form factor bounds. These two constraints are enforced in the model by applying a series of QCD sum rules to the coefficients $a_{0,5,6,7,8}$ which expresses them in terms of the coefficients parameters $a_{1,2,3,4}$, reducing the number of free parameters in the model from nine to four [180].

Coefficients for $a_{1,2,3,4}$ are extracted in Ref. [180] by tuning the model to reanalysed deuterium CCQE data from ANL, BNL, and FNAL. To further constrain the model during the fits, Gaussian bounds were placed on the coefficients in the form of likelihood penalty terms. The QCD scaling law was further enforced by applying a Gaussian bound of

$$|a_k/a_0| \leq 25/k \quad \text{for} \quad k > 5, \tag{5.6}$$

after the sum rules have been applied to the coefficients $a_{0,5,6,7,8}$. Analyses of different spectral function models in Ref. [181] motivate the additional constraint of

$$|a_k/a_0| \leq 5, \tag{5.7}$$

for all coefficients. In the Z-expansion tunings in Ref. [180] further studies showed that relaxation of these additional bounds in the tunings produced small shifts in the extracted shape of the axial form factor and approximately a 50% increase in the total extracted uncertainties for each a_k term.

Two separate parameter sets were published from these studies, one from tuning to $Q^2 < 1$ GeV^2 data and another more inclusive tuning to $Q^2 < 3$ GeV^2 data. In the $Q^2 < 1$ GeV^2 tuning additional errors were included in the final result to account for differences in deuteron corrections and acceptance corrections. In the $Q^2 < 3$ GeV^2 it was not possible to properly include these corrections as the lower statistics bins do not follow Gaussian distributions, so instead, the published results have reduced systematic errors which neglect these corrections. The best fit values, V, and associated correlations, C, for each of the published studies are given by

$$V(Q^2 < 1 \text{ GeV}^2) = \begin{bmatrix} a_1 \\ a_2 \\ a_3 \\ a_4 \end{bmatrix} = \begin{bmatrix} 2.30 \pm 0.13 \\ -0.60 \pm 1.00 \\ -3.80 \pm 2.50 \\ 2.30 \pm 2.70 \end{bmatrix}, \tag{5.8}$$

$$C(Q^2 < 1 \text{ GeV}^2) = \begin{bmatrix} 1 & 0.350 & -0.678 & 0.611 \\ 0.350 & 1 & -0.898 & 0.367 \\ -0.678 & -0.898 & 1 & -0.685 \\ 0.611 & 0.367 & -0.685 & 1 \end{bmatrix}, \tag{5.9}$$

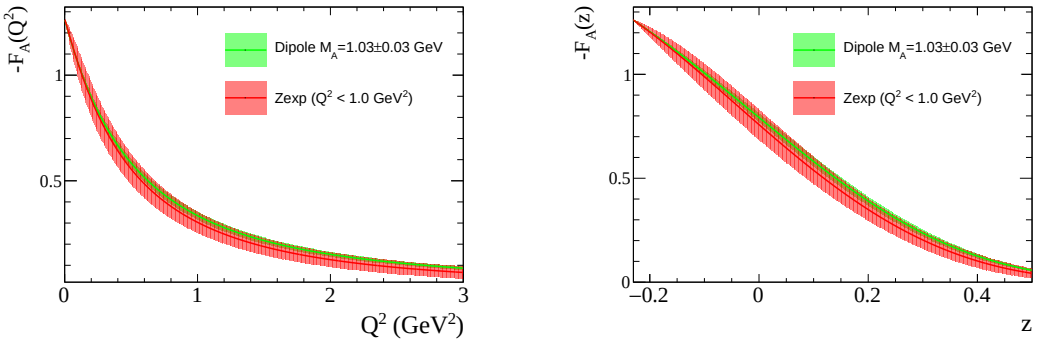

Fig. 5.7 Z-Expansion form factor uncertainties from Ref [180]. (left) Uncertainties shown when the form factor is expressed as a function of Q^2. (right) The same uncertainties expressed as a function of the expansion variable z, where the form factor can be seen to be closer to a linear function at low z.

and

$$V(Q^2 < 3\ \text{GeV}^2) = \begin{bmatrix} a_1 \\ a_2 \\ a_3 \\ a_4 \end{bmatrix} = \begin{bmatrix} 2.28 \pm 0.08 \\ 0.25 \pm 0.95 \\ -5.20 \pm 2.30 \\ 2.60 \pm 2.70 \end{bmatrix}, \tag{5.10}$$

$$C(Q^2 < 3\ \text{GeV}^2) = \begin{bmatrix} 1 & 0.321 & -0.677 & 0.761 \\ 0.321 & 1 & -0.889 & 0.313 \\ -0.677 & -0.889 & 1 & -0.689 \\ 0.761 & 0.313 & -0.689 & 1 \end{bmatrix}. \tag{5.11}$$

The extracted uncertainty bands on the axial form given by (5.8) and (5.9) are shown in Figure 5.7. Initial variation studies found that the $a_{1,2,3}$ parameters are capable of significantly modifying the shape of the form factor when varied within their extracted 1σ uncertainties in the Q^2 range shown in Figure 5.8. In contrast the a_4 term produced much smaller modifications in this range and extreme variations were required to produce modifications comparable to the other parameters.

5.2.4 Form Factor Comparisons

To provide additional form factor choices to the T2K OA the functional forms discussed previously were implemented into the NEUT and NuWro event generators. NEUT was modified to allow events to be generated on free nucleon targets by assuming the scattering took place on a RFG with negligible Fermi-momentum and binding energy. For each alternative form factor, a reweight parameter was added to NEUT's internal reweighting package so that weights could be calculated

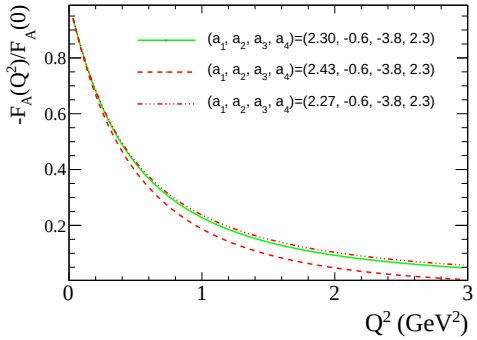

(a) a_1 Variations

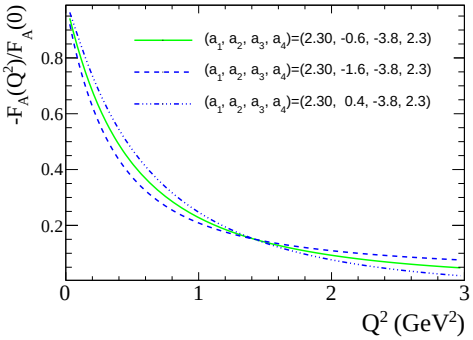

(b) a_2 Variations

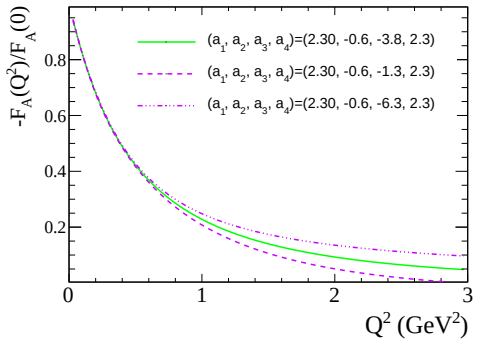

(c) a_3 Variations

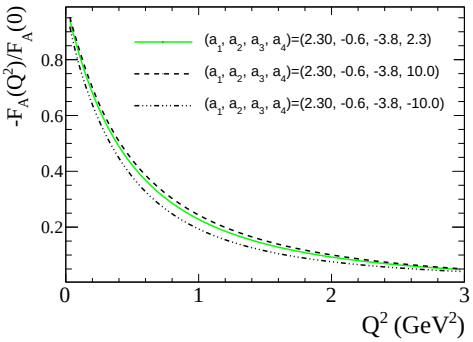

(d) Extreme a_4 Variations

Fig. 5.8 The effect each of the free parameters ($a_1 - a_4$) in the Z-expansion model has on the predicted shape of the axial form factor. Variations of each parameter were based on uncertainties given in Equation (5.8). The pinching effect shown in the a_2 variations is a result of the application of the sum rules. Variations in a_4 are known to produce the smallest variations since its contribution is multiplied by z^4 and $-1 < z < 1$.

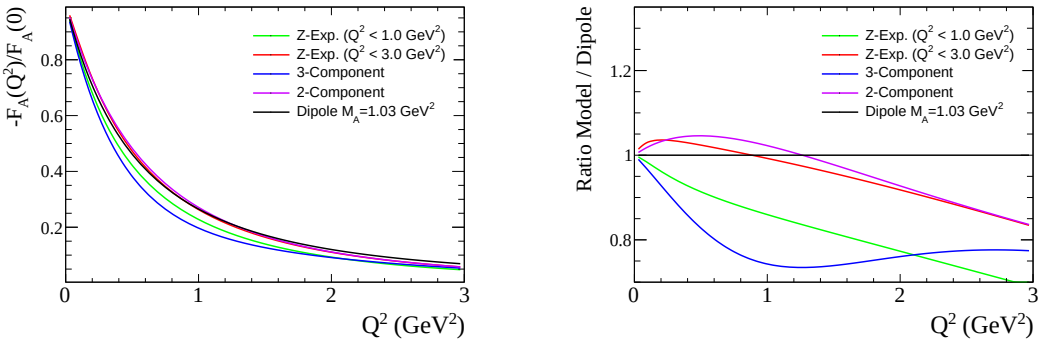

Fig. 5.9 Each of the alternative form factor models compared to a simple dipole model before being tuned to bubble chmaber deuterium data. (left) Form factor shape as a function of Q^2. (right) Ratio of alternative form factors to the simple dipole model, highlighting the large shape differences between the nominal predictions of each model.

relative to a dipole model. This made it possible to generate one large event sample using a dipole model, which could then be reweighted afterwards to any of the alternative models considered in this study without having to regenerate events. This was achieved by calculating the ratio between the cross-section for the alternative form over the cross-section for the dipole form for a given set of event kinematics.

Both the Z-expansion and 3-component model were chosen as possible models for the T2K OA; the ad-hoc 3-component model because of its ability to transition between multiple models, and the Z-expansion because of its minimal model dependence. Comparisons of the shape of each form factor model are shown in Figure 5.9. To compare the form-factors at very low Q^2 where the cross-section is high it is also useful to calculate the squared radius of the axial charge distribution as

$$\frac{< r_A^2 >}{(\hbar c)^2} = -6 \left. \frac{dF_A(Q^2)}{dQ^2} \right|_{Q^2=0}. \tag{5.12}$$

For each of the models considered this gives

$$r_A^2 = \frac{12}{M_A^2} \quad \rightarrow \quad \text{Dipole} \tag{5.13}$$

$$r_A^2 = 6(2\gamma + \frac{\alpha}{m_A^2}) \quad \rightarrow \quad \text{2-Comp.} \tag{5.14}$$

$$r_A^2 = 6(2\gamma + \frac{\alpha}{m_A^2}) + 6\sqrt{|\theta|\beta} \quad \rightarrow \quad \text{3-Comp.} \tag{5.15}$$

$$r_A^2 = \frac{\partial z}{\partial Q^2} \left(a_1 + \sum_{k=1}^{8} a_k k z^{k-1} \right) \Bigg|_{Q^2=0} \quad \rightarrow \quad \text{Z-expansion} \tag{5.16}$$

where the Z-expansion summation must be made over all a_k terms after the QCD sum rules have been applied for a given choice of $a_{1,2,3,4}$. Larger values of r_A^2 are approximately correlated with

Model	r_A^2 (fm^2)
Dipole (Global $M_A = 1.03 \pm 0.03$ GeV^2)	0.45 ± 0.03
Dipole (ND280 $M_A = 1.21 \pm 0.20$ GeV^2)	0.35 ± 0.13
2-Component ($\gamma = 0.25$)	0.38 ± 0.01
2-Component ($\gamma = 0.515$)	0.35 ± 0.01
3-Component ($\pm 20\%$)	0.50 ± 0.09
3-Component ($\pm 70\%$)	0.50 ± 0.21
Z-Expansion (1 GeV)	0.46 ± 0.22
Z-Expansion (3 GeV)	0.40 ± 0.19

Table 5.1 Comparison of the predicted axial radius and its associated uncertainty for each of the form factor models considered.

smaller CCQE cross-sections (or lower values of M_A). The introduction of the exponential term in the 3-component model allows θ and β to modify the axial radius, with larger choices for the absolute value of θ increasing the axial radius (reducing the cross-section at low Q^2).

To evaluate the central values and uncertainties on r_A^2 for each model, gradients were calculated computationally at $Q^2 \to 0$ by repeatedly throwing the free parameters within their uncertainties (using associated correlations for the Z-expansion models). Gaussians were then fitted to the resultant r_A^2 distributions. Initial arbitrary uncertainties of $\pm 20\%$ were placed on each of the 3-component parameters since starting uncertainties were not known. Results for each model are shown in Table 5.1. The largest fluctuations observed for the axial radius were seen in the Z-expansion models, whilst similar uncertainties were found for the 3-component only when starting with nominal uncertainties of 70% for all parameters instead of 20%. Such a large variation in the 3-component model parameters is not excluded given that a large uncertainty must already be applied to the model when considering the range of best fit α values obtained when using different central values for γ in [183]. Since the 3-component form is an ad-hoc model, there are no constraints that can be derived from theory on its free parameters, beyond those provided in [183]. It was therefore necessary to develop a tuning procedure that could constrain the form factor models implemented in NEUT through comparisons to data on CCQE scattering of a deuterium target.

5.3 Tuning NEUT to bubble chamber data

To test their implementations and extract prior constraints on the free parameters a number of the available form factor models in NEUT were empirically tuned to data. Bubble chamber CCQE deuterium scattering measurements from the ANL [123, 125], BNL [131], BEBC [137], and FNAL [134] experiments were selected for this since nuclear effects in the data are minimal. The event rate histograms in the original papers were digitised and implemented as individual measurements within the NUISANCE generator tuning framework. For some measurements insufficient information was

Exp.	Format	Ref.	Likelihood	Norm.
ANL	Cross-section : $\sigma(E_\nu)$	[123]	Least-squares	Rate+Shape
ANL	Event Rate : $R(Q^2)$	[125]	Poisson	Shape-only
BNL	Cross-section : $\sigma(E_\nu)$	[131]	Least-squares	Rate+Shape
BNL	Event Rate : $R(Q^2)$	[131]	Poisson	Shape-only
FNAL	Event Rate : $R(Q^2)$	[134]	Poisson	Shape-only
BEBC	Differential Cross-section : $d\sigma/dQ^2$	[137]	Least-squares	Shape-only

Table 5.2 Likelihood types used for each dataset in the joint CCQE fit. The ANL and BNL distributions were treated with floating flux normalizations.

provided to properly normalise MC predictions for direct comparison to the published rates. In these cases only shape comparisons were possible. The ANL, BNL experiments also published $\sigma(E_\nu)$ measurements which were implemented as flux-unfolded measurements in NUISANCE. In the case of the original BNL paper a value of M_A in a simple dipole approximation was extracted for each bin and published as a function of E_ν. For this dataset the Llewellyn-Smith model was used to correct the data points back to approximate $\sigma(E_\nu)$ data points that could be used in NUISANCE. The full list of datasets considered when evaluating the models is shown in Table 5.2.

Four large MC samples each containing 1×10^6 quasi-elastic scattering events were generated using the nominal dipole model in NEUT for each experiment. Since it was not possible to simulate bound deuterium in NEUT a free neutron target was simulated instead with a weighted correction factor applied later. The NEUT MC outputs were read into the NUISANCE framework which subsequently calculated the reconstructed energy, E_ν^{QE}, and four-momentum transfer, Q^2_{QE} from the muon kinematics for each event as

$$E_\nu^{QE} = \frac{2M_n E_\mu - M_n^2 - m_\mu^2 \pm M_p^2}{2\left(M_n - E_\mu + \sqrt{E_\mu^2 - m_\mu^2}\cos\theta_\mu\right)}; \tag{5.17}$$

$$Q^2_{QE} = -m_\mu^2 + 2E_\nu^{QE}\left(E_\mu - \sqrt{E_\mu^2 - m_\mu^2}\cos\theta_\mu\right). \tag{5.18}$$

where, M_n is the nucleon mass, E_μ is the muon energy, m_μ is the muon mass, M_p is the proton mass, and θ_μ is the scattering angle of the muon with respect to the incoming neutrino. These reconstructed quantities, used in the original bubble chamber experimental measurements, assume quasi-elastic scattering of a free nucleon at rest with negligible binding energy. In a deuterium target this is a reasonable assumption as the nucleon binding energy is low, and Pauli blocking only affects the very lowest Q^2 events. The event kinematic quantities were binned into the relevant histograms in NUISANCE for direct comparison to the experimental data points.

To account for the lack of a deuterium model in NEUT the Singh model was used to correct for final state effects in deuterium [186]. A starting weight for each event was calculated as a function of Q^2 by interpolating the correction factor shown in Figure 5.10. These weights were applied to the histogram fill for each event to produce an updated MC prediction that included the correction.

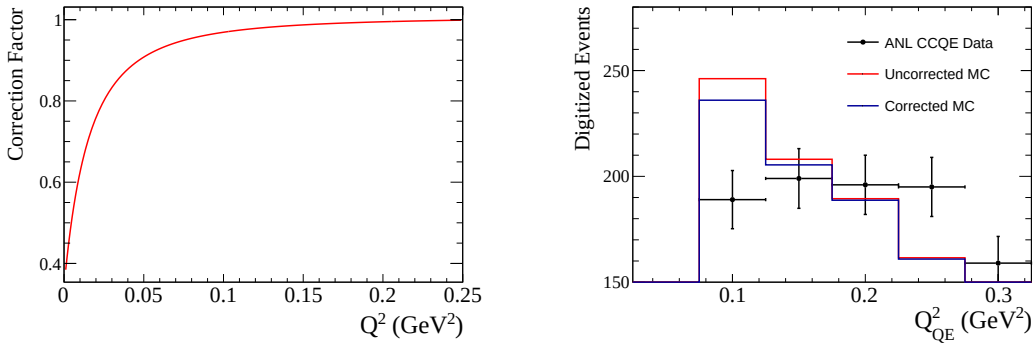

Fig. 5.10 Free nucleon to Deuteron corrections. (left) Singh et. al. correction factor [186]. (right) Effect of applying the correction factor as a weight on an event by event level has on the nominal MC prediction. Whilst it is necessary to include deuteron binding effects when considering measurements of QE scattering that probe extremely low Q^2 regions, the Singh correction becomes negligible above 0.2 GeV^2, having little effect on the fit results in this work.

Since no data points were considered below $Q^2 < 0.025$ GeV^2 and the correction tends to unity above 0.2 GeV^2, the effect on the fit results was small. Regardless it was applied in all tunings to remain consistent with earlier form factor extraction studies performed by ANL and BNL [125, 131].

To avoid biases to any single kinematic distribution the model predictions were compared to both Q^2 and E_ν distributions simultaneously where available. Since insufficient information was available to properly normalise the MC predictions to the published event rates, $\sigma(E_\nu)$ distributions were used to set a constraint on the overall normalization of the cross-section, leaving the Q^2 event distributions to constrain the shape. The inclusion of these E_ν datasets ensured that the normalisation of the results was kept within reason, avoiding cases where extreme, unphysical QE normalisations may result in better agreement with the Q^2 spectrums. Normalization information was available for the BEBC 1DQ^2 dataset, but this was still treated as a shape-only constraint in the fit so that normalisation constraints came entirely from the lower energy E_ν datasets. The ANL or BNL MC distributions were drawn from the same event samples ensuring correlations between E_ν^{QE} and Q^2_{QE} in the model were naturally included in the likelihood when calculating the data-MC differences.

A joint chi-square test statistic (χ^2) for all experimental datasets was calculated by adding together the individual χ^2 calculations for each distribution shown in Table 5.2. The uncertainties were assumed to be fully uncorrelated between the bins since no correlations were provided by the experiments. This gave a Poisson chi-square for the event rate datasets of

$$\chi^2_{poisson} = 2\sum_i^N Sm_i - d_i + d_i \log\left(\frac{d_i}{Sm_i}\right), \tag{5.19}$$

where d_i is the data in the i^{th} bin and Δd_i and m_i are the data uncertainty and MC prediction for the corresponding bin respectively, and $S = \frac{\sum_i d_i}{\sum_j m_j}$ is a factor that normalises the total MC event rate to match the data. Similarly the least-squares test statistics were calculated as

$$\chi^2_{least} = \sum_i^N \left(\frac{d_i - S m_i}{\Delta d_i} \right)^2 \tag{5.20}$$

For the ANL and BNL datasets the normalisation factor was fixed at $S = 1.0$ so that differences in the total rate between the data and MC were also included in the likelihood. Initial studies of these likelihoods found that 1×10^6 was the minimum number of MC events required to ensure the statistical fluctuation in the MC prediction in each bin was small enough to give reliable χ^2 calculations for all models under consideration.

To tune the alternative models the implemented reweight dials discussed in the previous section were used to convert the nominal dipole MC event predictions to the predictions for a 3-component or Z-expansion model. This provided event weights to NUISANCE that could update the model predictions whilst keeping the procedure to calculate the total χ^2 exactly the same. Parameters in each of the alternative models could then be varied freely within the NUISANCE framework to evaluate the effect they had on the goodness of fit. To find a best fit parameter set the NUISANCE-MINUIT interface was used to scan the model parameter space using a gradient descent method until the joint test-statistic was minimised [177, 187]. Errors on each of the fit parameters were evaluated using MINUIT's HESSE functionality by finding regions in which $\Delta\chi^2 = 1$ around the minimum.

Three different models were considered for tuning. First the dipole model was tuned to extract a value for M_A. This helped validate the fit procedure by checking it did not produce values for M_A that significantly disagreed with historical tunings. Second, the 3-component model was tuned using the same procedure to extract prior constraints on each of its free parameters. Finally, the Z-expansion model was tuned to validate its implementation in NEUT. The Z-expansion model already had prior constraints available in Ref. [180], so the purpose of this tuning study was to check similar results could be obtained using the NEUT implementation, and to understand how differences in the fitted datasets or coefficient bounds may impact the extracted Z-expansion coefficient uncertainties.

For each model the free parameters (see Figures 5.6 and 5.8) were varied to increase agreement with the data. In the 3-component model an additional weak Gaussian constraint of 0.0 ± 0.8 GeV^{-2} was applied to θ during the fit to avoid the form factor moving into unphysical regions causing the fits to fail. In the original Z-expansion tunings similar Gaussian constraints were placed on a_k to further constrain the form factor shape. Such bounds were difficult to implement within the rigid NEUTReWeight interface so instead the NEUT Z-expansion fits were performed without them (the QCD sum rules relating $a_{0,5,6,7,8} \rightarrow a_{1,2,3,4}$ were still applied).

To consider the effect of flux uncertainties an additional set of tunings were performed for each model, where the ANL and BNL flux normalisations were allowed to float freely within a 15% prior Gaussian uncertainty. This is motivated by the fact that the integrated ANL cross-section above 1 GeV is approximately 10% higher than BNL. The likelihood for the ANL and BNL χ^2 calculations was modified in the free fits to be

$$\chi^2(ANL\ E_\nu) = \left[\sum_i \left(\frac{d_i - (\Phi_{ANL} \times m_i)}{\Delta d_i}\right)^2\right] \tag{5.21}$$

$$\chi^2(BNL\ E_\nu) = \left[\sum_i \left(\frac{d_i - (\Phi_{BNL} \times m_i)}{\Delta d_i}\right)^2\right] \tag{5.22}$$

$$\chi^2(PENALTY) = \sum_{k=ANL}^{BNL} \left(\sum_{l=ANL}^{BNL} (1-\Phi_k)\left(M^{-1}\right)_{kl}(1-\Phi_l)\right), \tag{5.23}$$

where d_i is the data in the i^{th} bin and Δd_i and m_i are the data uncertainty and MC prediction for the corresponding bin respectively. Φ_{ANL} and Φ_{BNL} were treated as free parameters in the fit and $\chi^2(PENALTY)$ was an additional penalty term accounting for the correlated flux uncertainty between each experiment. M is the flux correlation matrix. Assuming a non-zero correlation allowed the fits to consider cases where both experiments had very strongly correlated sources of flux uncertainties. Initial studies found varying the correlation between 0% and 75% introduced little change in the final fit result. The 75% correlated case produced the largest extracted uncertainties, albeit only by 3% in total, so this correlation was chosen for all floating flux normalisation studies, with M being defined as

$$M = \begin{bmatrix} 0.0225 & 0.0169 \\ 0.0169 & 0.0225 \end{bmatrix} \tag{5.24}$$

Additional studies were performed with different correlations applied between the floating flux parameters. These were found to have a minimal effect on the final fit results. In all cases 'free fit' refers to the tuning with floating flux normalizations and an assumed correlation of 75% between the two normalizations as this was found to introduce a very small inflation of the parameter errors ($\sim 0.5\%$) compared to results using weaker correlations.

5.3.1 Discussion of Parameter Results

The extracted model parameters for each of the tuning studies are shown in Tables 5.3-5.6. Comparisons of the models after tuning to bubble chamber data are shown in Figures 5.11 and Figures 5.12. In each fit it was possible for MINUIT to converge on a reasonable set of parameters with a good fit to the data. The best fit χ^2/NDOF values were in the range $1.04 - 1.10$. After fitting the difference between the central value MC predictions for each of the models was small when projected onto the experimental kinematics Q^2 and E_ν. Despite the similarity in their best fit shapes, each model

Parameter	Fixed	Free
M_A^{CCQE} [GeV]	1.06 ± 0.03	1.10 ± 0.03
ANL Norm.	1.0	1.11 ± 0.05
BNL Norm.	1.0	1.01 ± 0.06
$\chi^2/NDOF$	164.47/150	159.74/149

Table 5.3 NEUT Dipole Model F_A model fit results obtained from joint fits to bubble chamber data. 'Fixed' means that the flux normalizations are left fixed while 'Free' means that the flux normalizations are left free with 15% Gaussian uncertainty and 75% correlation between ANL and BNL. The NDOF is reduced by 1 in the free fit as an additional flux uncertainty variation is included in the fit.

predicts significantly different error bands on the axial form factor in the high Q^2 region despite an almost identical fit procedure being applied. These differences arise purely from the additional freedom to modify the shape in the alternate form factor choices.

The dipole form factor produced the worst fit to the data in both the "fixed" and "free" tunings. However, the difference in χ^2 between the dipole and alternative models was insignificant given the large number of degrees of freedom in the fit. When the ANL and BNL normalisations were kept fixed a value of $M_A = 1.06 \pm 0.03$ GeV^2 was obtained. In general the Q^2 distributions were found to prefer increased values of M_A as this slightly improved agreement in the tail of the Q^2 distributions. In contrast the E_ν distributions preferred smaller axial masses due to inclusion of normalisation information in their χ^2 contributions. Since the Q^2 distributions dominated the fit, contributing over 90% of the total data points, the weighted average of M_A output by the fit was higher than previous studies by other groups where the E_ν distributions and total cross-section normalisation had a more equal weighting in the fits. Despite the slightly higher extracted axial mass, the fixed tuning results were found to be in agreement with the previous fits to neutrino scattering data and pion electro-production data, obtaining 1.06 ± 0.03 GeV^2, compared to 1.03 ± 0.03 GeV^2 in [81].

When the ANL and BNL experiments were allowed to float within their assigned 15% flux uncertainties larger values of M_A were extracted. In this case MINUIT could easily correct for changes in normalisation introduced by the Q^2 datasets preference for larger values of M_A by simply scaling the ANL and BNL normalisation terms. This is further reinforced by the $40-50\%$ correlations observed between M_A and Φ_{ANL} and Φ_{BNL} shown in Figure 5.13. In these tunings a reduction of the ANL flux by approximately 10% was preferred, which effectively enhances the extracted cross-section as a function of energy by the same amount (in Figure 5.11 the correction is applied by scaling the MC down instead). After the ANL data has been corrected the correlation between the two experimental normalisations is then extracted to be approximately 30%. Such a correlation was extracted for all models. It is expected that if additional constraints were applied from pion electroproduction studies the extracted value of M_A may be decreased slightly in the floating flux normalisation fits. These additional constraints would need to be applied for each possible pion electroproduction data extraction method (see Figure 5.2) therefore it was not feasible to include such constraints in the NEUT tunings.

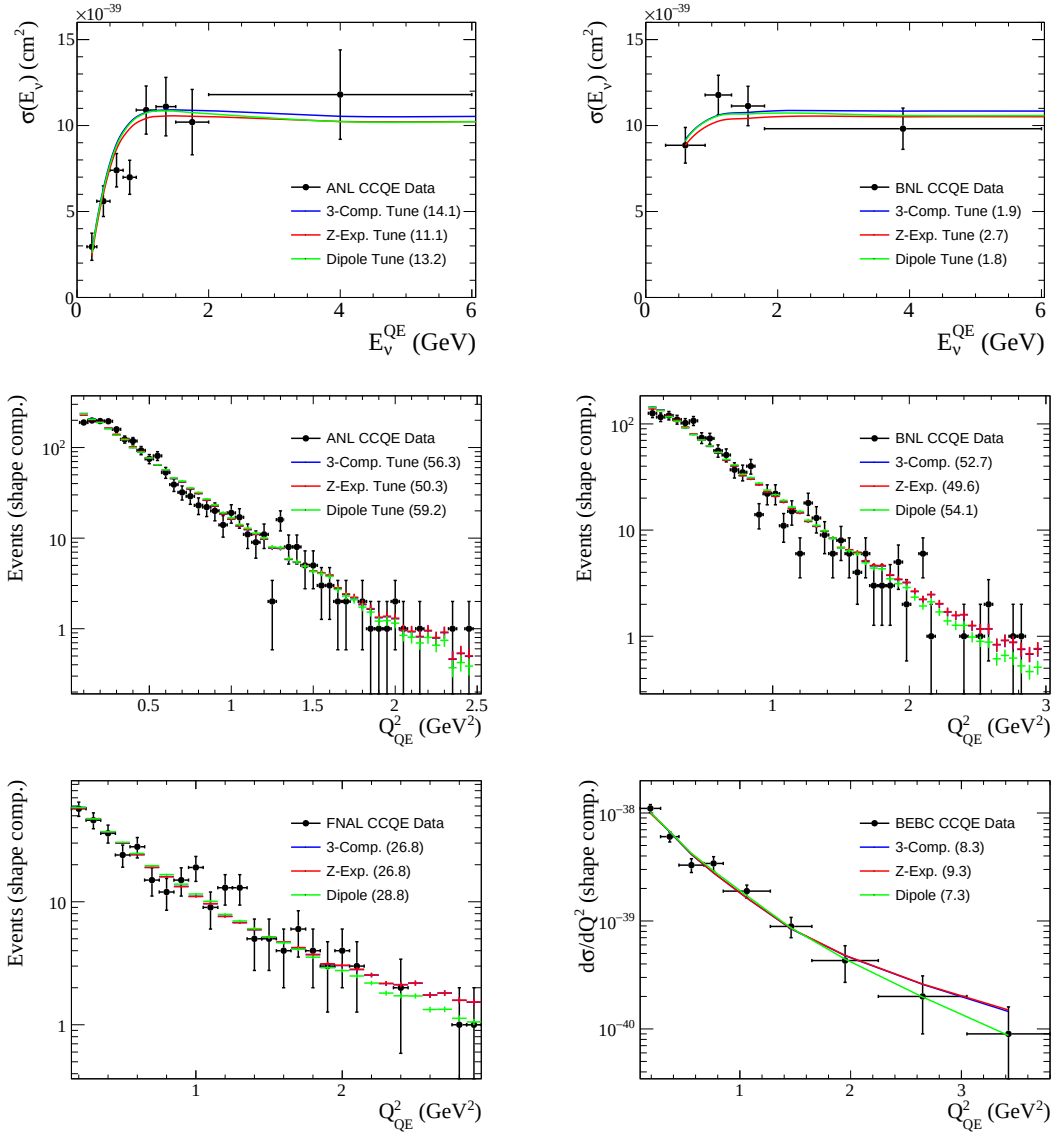

Fig. 5.11 Best fit results compared to data for each model for the fixed normalisation tunings. Each model prediction is evaluated using reweighting from a single set of events generated with a dipole form factor. This model reweighting procedure is the same as that used in the T2K OA. Because of this the statistical fluctuations between bins in the MC predictions are common between models. At high Q^2 the statistical fluctuation is higher as NEUT generates less events in this region, but this was not found to significantly affect the fit results. Each model prediction is almost identical at low Q^2, with only a slight divergence at high Q^2 in the 3-component and Z-expansion models due to their enhanced shape freedom.

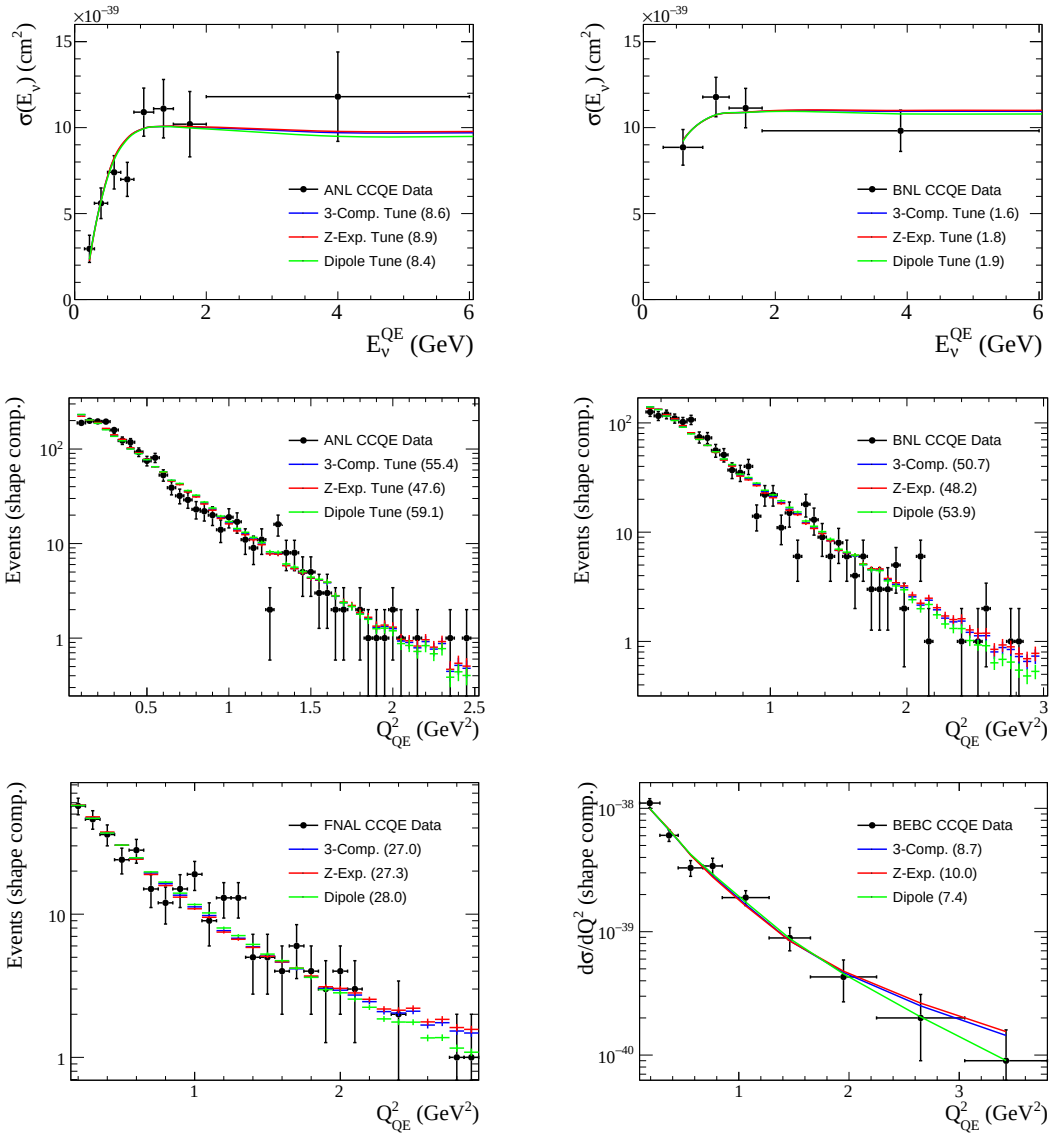

Fig. 5.12 Best fit results compared to data for each model for the floating normalisation tunings. The normalisation of the E_ν predictions for ANL and BNL were floated freely in the tunings that produced these results, so each one shows slightly different overall normalisation compared to the fixed normalisation tunings. Each model prediction is evaluated using reweighting from a single set of events generated with a dipole form factor. Each model prediction is almost identical at low Q^2, with only a slight divergence at high Q^2 in the 3-component and Z-expansion models due to their enhanced shape freedom.

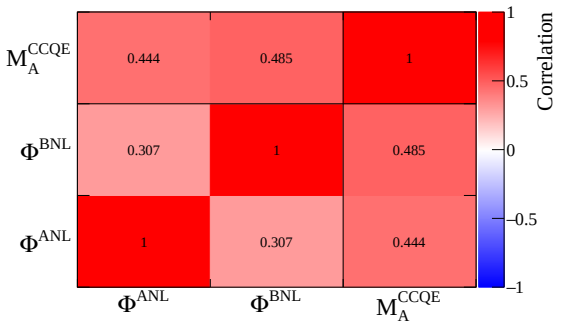

Fig. 5.13 Dipole fitted correlations for the joint bubble chamber tuning.

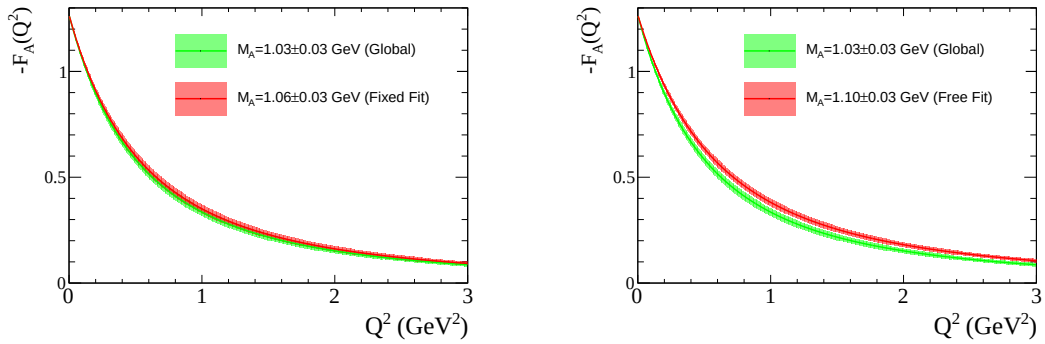

Fig. 5.14 Comparison of various dipole form factor uncertainty error bands assuming different values for M_A^{CCQE} and its uncertainty.

Since the understanding of the Q^2 shape was of most importance to these studies and the floating flux tunings produced improved agreement with the Q^2 distributions it was decided that the free tuning method was the most appropriate to extract conservative form factor priors for use by the T2K OA. The form factor uncertainties given the extracted values of M_A compared to the global fit values taken from [81] are shown in Figure 5.14.

The 3-component form factor was found to perform similarly well to a dipole model, but produced a much larger uncertainty on F_A at high Q^2 as expected (see Figure 5.15). There was a preference for the absolute exponential terms to be enhanced in the fit relative to its starting shape as shown in Table 5.4. The best fit choices of θ and β strongly modify the slope of the form factor at $Q^2 \sim 0.75$ GeV^2. The presence of local minima was checked by starting MINUIT at different points in the parameter space and checking the extracted parameter values were stable. Even when starting the fit in a region where the exponential term did not contribute (a nominal value of $\theta \sim 0.0$) the fits still converged on the central values shown in Table 5.4 with values for α and γ in strong disagreement with the nominal 2-component model parameters.

The addition of the exponential term to the 2-component model, strongly modifies the shape at low Q^2, meaning the 2-component contribution can be adjusted in the fit to extend the tail to a higher

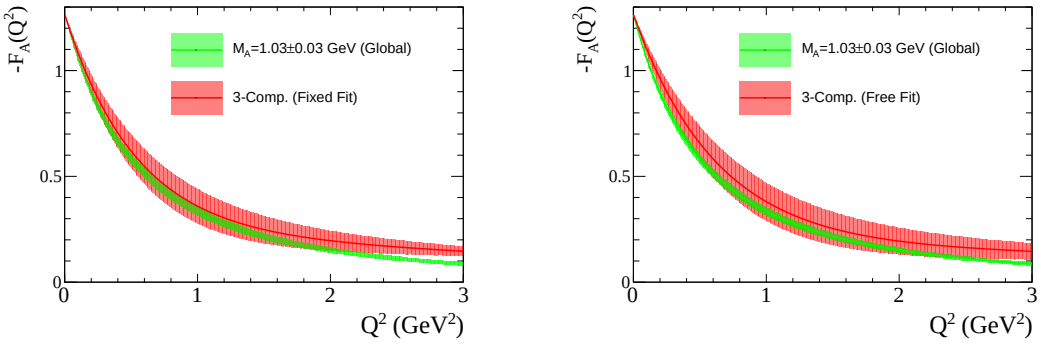

Fig. 5.15 Comparison of the extracted 3-component form factor uncertainties to a simple dipole model. (left) Uncertainty bands on F_A extracted from the fixed 3-component tunings. (right) Uncertainty bands on F_A extracted from the free 3-component tunings.

Q^2. Changing between fixed and floating flux normalisations in the fit was found to produce a similar shape shift to that seen in the dipole model tunings, increasing the overall normalisation of the form factor at high Q^2 even further. A value of $(\alpha = 0.11, \gamma = 0.41)$ corresponds to an approximately dipole model with $M_A \sim 1.56$ GeV in this region. Since the tail extends to extremely large Q^2 this feature of the 2-component model is in conflict with the QCD scaling law, suggesting a deficiency in tuning the α and γ terms without prior constraints. It is likely this does not manifest in the 2-component model tunings in Ref. [183] because of the strong constraints at low momentum transfer and the restricted shape of the model used, suggesting a shape restriction defficiency in the model similar to that of the dipole model.

The shift in the correlations of the 3 component model when moving to a free normalistion tuning shows that the χ^2 surface in the tuning is non-linear, with the correlations at the altered best fit point between α and the other parameters being very different compared to those at the fixed normalisation tunings parameter set. Each tuning was repeated with a number of randomly chosen parameter values, but there was no significant divergence from the fit results, reinforcing that in this particle case a global best fit was found. However, because of this behaviour, and the fact that the 3 component form factor is an emperical model designed to provide ad-hoc conservative error bands, care should be taken when using the model in subsequent fits to other datasets, always ensuring that a reliable global best fit is found.

Since the 3-component model was developed to provide an ad-hoc conservative error band on F_A, it was decided that the weak agreement with the QCD scaling law should be considered an extreme case that was worth investigating in the T2K OA.

The Z-expansion model tunings were found to produce the best $\chi^2/NDOF$ values of all the fits to the bubble chamber data, but only by a very small amount. This was expected given the Z-expansion model had the most freedom out of all form factors considered. When comparing the axial radius at the best fit, this model was also found to produce the largest uncertainty, as shown in Table 5.5. The

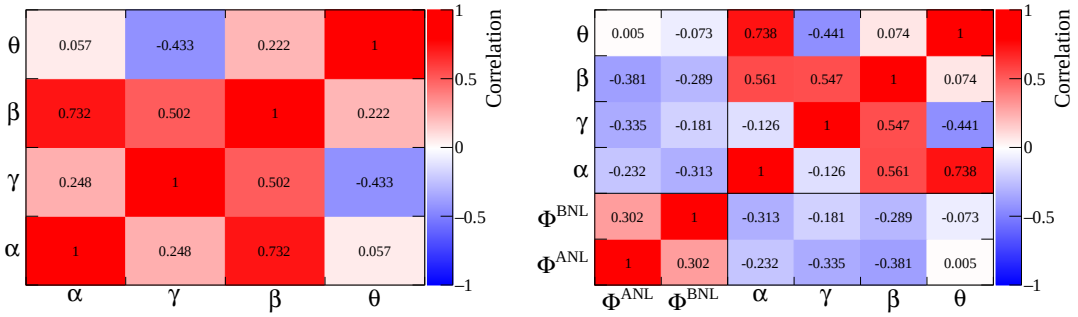

Fig. 5.16 Extracted correlations for the 3-component model from the bubble chamber tunings. (left) Results from the fixed normalisation tunings. (right) Results from the free normalisation tunings. The large shift in correlations between α and the other parameters is a result of the large shift in α when moving to the free fit, finding a new best fit solution in a different part of the χ^2 surface.

Parameter	Fixed	Free
α	0.23 ± 0.08	0.11 ± 0.10
γ [GeV^{-2}]	0.44 ± 0.02	0.41 ± 0.03
β [GeV^{-2}]	1.22 ± 0.14	1.04 ± 0.13
θ [GeV^{-2}]	-0.26 ± 0.18	-0.26 ± 0.16
ANL Norm.	1.0	1.13 ± 0.05
BNL Norm.	1.0	1.03 ± 0.05
$\chi^2/NDOF$	160.15/147	153.99/146

Table 5.4 NEUT 3-Component Model F_A model fit results obtained from joint fits to bubble chamber data. 'Fixed' means that the flux normalizations are left fixed while 'Free' means that the flux normalizations are left free with 15% gaussian uncertainty and 75% correlation between ANL and BNL.

Model	Axial Radius (fm^2)
Dipole	0.38 ± 0.02
3-Component	0.32 ± 0.13
Z-Expansion	0.34 ± 0.23

Table 5.5 Comparison of the predicted axial radius and its associated uncertainty for each of the form factor models considered at their best fit point from the 'free' tunings.

Parameter	Fixed	Free	Original $< 1\text{GeV}^2$	Original < 3 GeV^2
a_1	2.19 $\pm$0.13	2.25 $\pm$0.10	2.30 $\pm$0.19	2.28 $\pm$0.12
a_2	0.93 $\pm$0.58	2.00 $\pm$0.86	-0.60 $\pm$1.60	0.26 $\pm$1.32
a_3	-7.67 $\pm$3.35	-10.77 $\pm$2.04	-3.80 $\pm$3.84	-5.20 $\pm$3.17
a_4	-4.67 $\pm$1.52	-4.66 $\pm$2.94	2.30 $\pm$4.08	2.60 $\pm$3.90
ANL Norm.	1.0	1.15 $\pm$ 0.06	-	-
BNL Norm.	1.0	1.05 $\pm$ 0.05	-	-
$\chi^2/NDOF$	158.58/150	152.72/146	-	-

Table 5.6 NEUT Z-Expansion Model F_A model fit results obtained from joint fits to bubble chamber data. 'Fixed' means that the flux normalizations are left fixed while 'Free' means that the flux normalizations are left free with 15% Gaussian uncertainty and 75% correlation between ANL and BNL. Since the tunings presented here use data up to $Q^2 \sim 3$ GeV^2 comparisons with the "Original< 3 GeV^2" results are of greatest concern when validating the model. Good agreement is found for the dominant a_1 parameter, whilst poorer agreement is found for the higher co-efficients due to the lack of Gaussian constraints applied to these parameters in the fit.

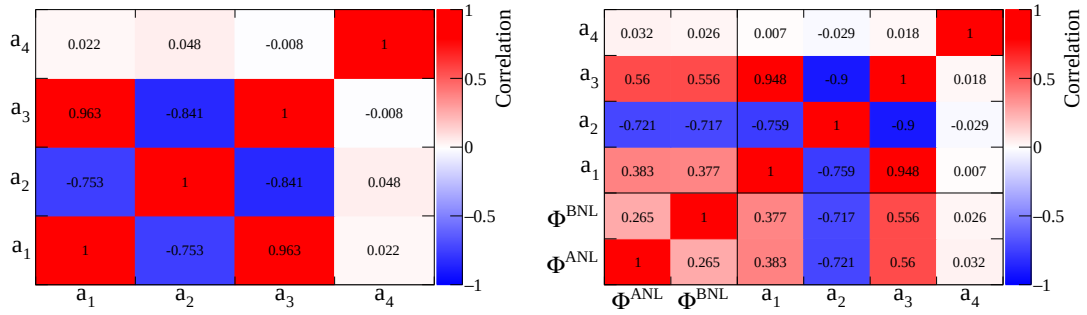

Fig. 5.17 Extracted correlations on the Z-expansion model from the bubble chamber tunings. (left) Correlations from the fixed normalisation tunings. (right) Correlations from the free normalisation tunings.

extracted parameter results were found to agree within errors for the coefficients $a_{1,2,3}$ extracted in Ref [180] using $Q^2 < 3$ GeV^2 data, as those tunings best match the bubble chamber tunings performed here. The a_4 parameter was the only coefficient found to be in disagreement with the previous tunings.

In the original Z-expansion tunings Gaussian bounds were placed on all coefficients, but no such constraints were applied in the NEUT tuning studies. Since the $Q^2 < 3$ GeV^2 data has only a weak sensitivity to the a_4 coefficient this parameter is weakly constrained in the fits when no additional bounds are included. This is shown by the weak correlations MINUIT extracts between a_4 and the other coefficients in Figure 5.17, reinforcing the statement that the correlations observed in Equation (5.9) between a_4 and the other parameters could originate from the combination of the sum rules and the Gaussian bounds applied in Ref [180].

The agreement between extracted a_1 coefficients shown in Table 5.6 was taken as an additional sign that the NEUT implementation of the Z-expansion model was correct, since the form factor is mostly sensitive to this parameter. The uncertainties extracted for a_1 were found to be of comparable magnitude to the original $Q^2 < 3$ GeV^2, but approximately 50% smaller than the $Q^2 < 1$ GeV^2 tunings since those studies included deuteron modelling and acceptance correction uncertainties.

The published Z-expansion form factor uncertainties were found to have a lower normalisation than the NEUT tunings. This was because they neglected higher energy BEBC data in the fit and the MC comparison method meant the cross-section normalisation had a higher weighting in the fits. Floating the flux normalisations in the fits caused significant increases in the a_2 coefficient and reductions in a_3. This had the combined effect of increasing the overall cross-section, which could then be corrected for by modifying the flux parameters. Despite these shifts the form factor uncertainty bands between both NEUT tunings and original $Q^2 < 3$ GeV^2 tunings in Ref [180] were still found to overlap with one another as shown in Figures 5.18 and 5.19.

5.3.2 Propagation of uncertainties in the T2K Oscillation Analysis

The models tuned in the previous section were all implemented into the latest version of NEUT 5.3.6. An additional patch was added to NEUT 5.3.3 so that each of the reweightable dials could be used to reweight the standard T2K MC production to the alternative form factor predictions in the T2K Oscillation Analysis (OA).

In cases where full event reweighting cannot be used to capture a known model uncertainty, due to phase space restrictions or time constraints[1], alternative methods are required to ensure the oscillation analysis is not biased by the known uncertainty. In the T2K OA this is achieved through a series of fake data studies in which a number of alternate model predictions are generated for ND280 and SK which can be treated as alternative simulated datasets.

To evaluate the systematic bias for a given fake dataset, first an “Asimov” model tuning study is performed [188] in which fake data is generated from the nominal MC prediction including some arbitrary chosen set of oscillation parameters. The standard MC model is then tuned to this "Asimov" data to ensure the known input oscillation parameters can be reliably re-extracted. Afterwards similar fake datasets are also generated using the alternative model predictions and the procedure is repeated. A comparison of the extracted oscillation parameter contours between the "Asimov" and the alternate fake data studies can then be used to quantify the level of bias present due to the nominal MC model lacking the sufficient freedom to describe the alternate prediction.

The axial form factor uncertainties discussed in this chapter were used to generate fake datasets for the T2K OA. For the 3-component model the "free" tuning was chosen as this provided a large

[1] The move to using alternative cross-section parameters requires an extensive validation procedure to ensure stability in the OA fits.

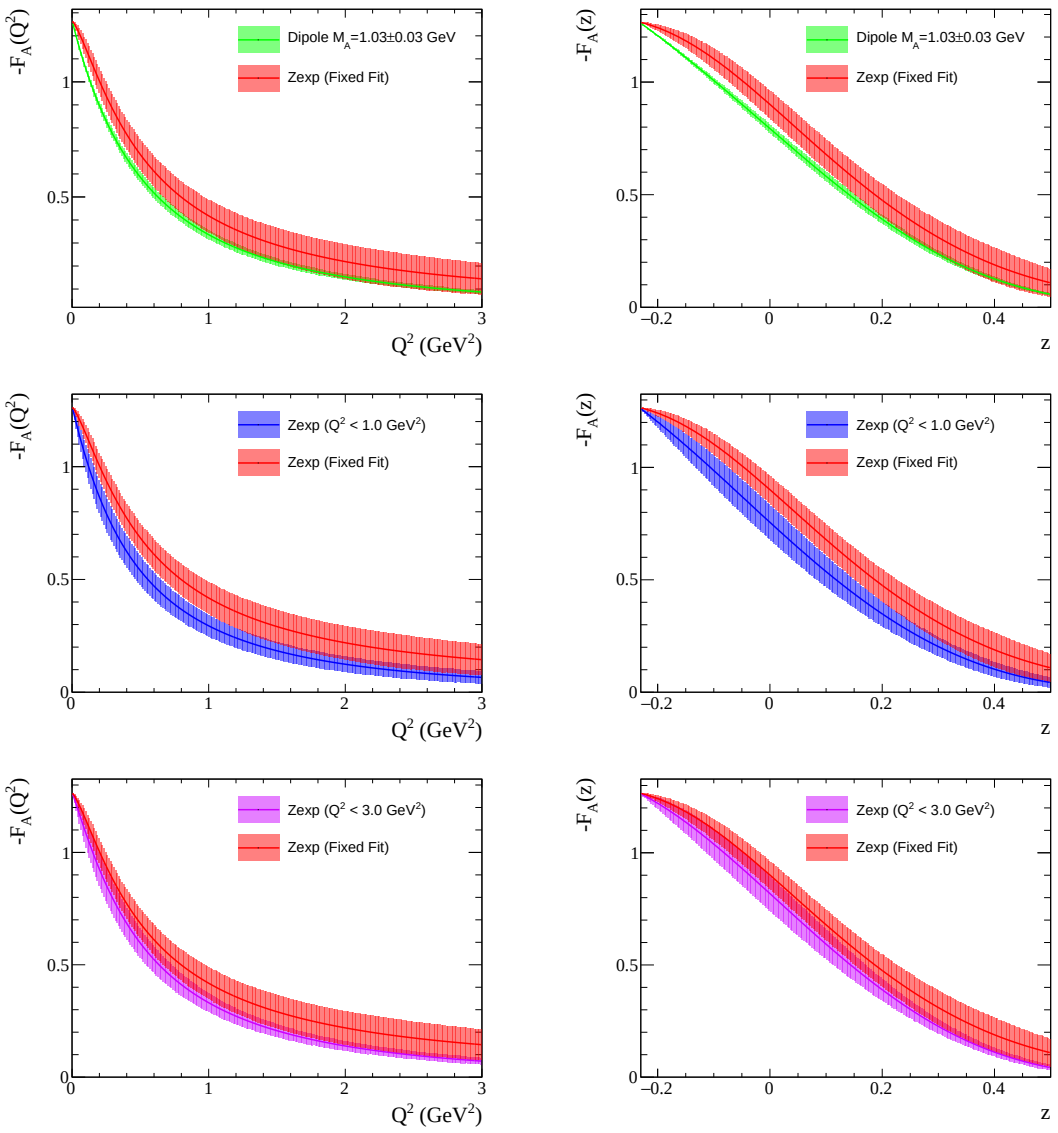

Fig. 5.18 Comparison of the extracted Z-expansion form factors from the fixed normalisation NEUT tunings to the original tunings given in [180]. The form factors are shown both as a function of Q^2 (left) and z (right).

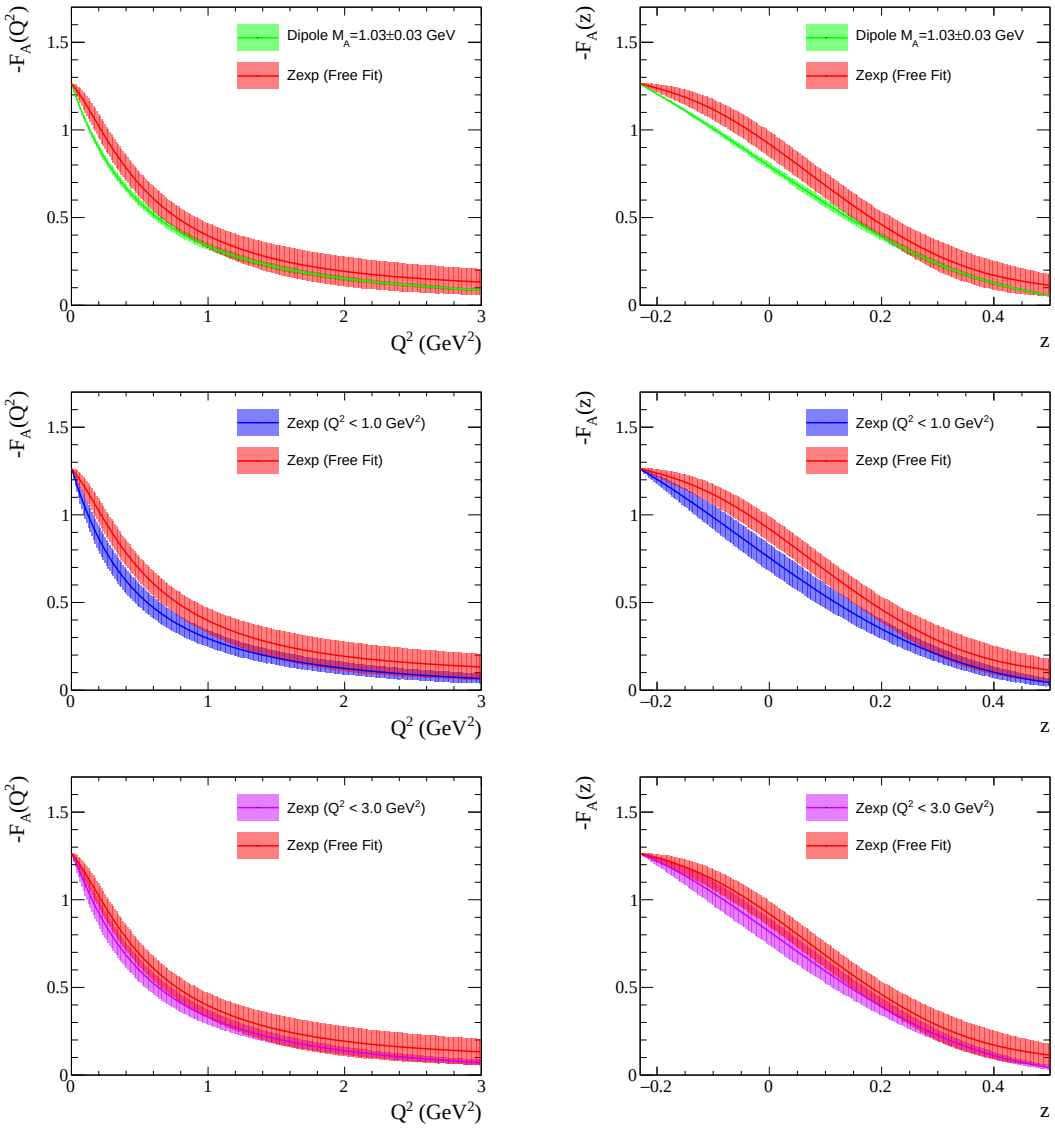

Fig. 5.19 Comparison of the extracted Z-expansion form factors from the free normalisation NEUT tunings to the original tunings given in [180]. The form factors are shown both as a function of Q^2 (left) and z (right). When the flux normalisation is floated in the fits, the extracted form factor is higher at high Q^2 compared to the one extracted from the fixed normalisation fits.

shape uncertainty at high Q^2. For the Z-expansion model the original $Q^2 < 3$ GeV^2 model tunings from Ref [180] were chosen since they included the additional Gaussian constraints on the a_k coefficients that were not included in these studies. In Ref [180] it was shown that relaxing the constraints on a_k and adding in efficiency corrections inflated the errors by approximately 30-50%. To account for this each of the errors in the chosen tunings in Equation (5.11) were also inflated by 50% to ensure T2K was using a conservative systematic error band.

A total of six fake datasets were passed to the T2K Beam And ND280 Flux extrapolation task Force (BANFF), that attempted to capture the $\pm 1\sigma$ uncertainties on the chosen 3-component and Z-expansion models. To minimise the total number of fake datasets a stochastic throw method was used to extract parameter sets from the highly correlated fit results. A random vector R was created by drawing randomly from a Gaussian with width equal to 1.0 centred on 0.0. This vector was then combined with the Cholesky decomposition[2] of the model covariance matrix to produce a set of parameter modifications that could be applied to the central values, v, to produce a new randomly thrown parameter set v' that accounts for the correlation between parameter errors.

$$v' = v + R(\text{Gaus}) \times M^{\text{Cholesky}} \tag{5.25}$$

This method was repeated 10000 times to randomly throw parameter sets within the associated model uncertainties whilst also accounting for parameter correlations. For each throw the form factor prediction as a function of Q^2 was drawn and the entire collection of form factor shapes was used to produce a $\pm 1\sigma$ error band. Finally, out of the 10000 throws two discrete throws were chosen that were closest to the central value, plus upper and lower 1σ uncertainty band edges in a region of interest. This could be used to produce three fake dataset parameter predictions for each model, regardless of the total number of free parameters in the original model. Since the high Q^2 region was of particular interest to T2K the region with $Q^2 > 1.0$ GeV was chosen to extract the error bands, resulting in the chosen parameter sets shown in Table 5.7. These choices of model parameters produced the upper and lower error bands shown in Figure 5.20.

The different cross-section predictions as a function of Q^2 and E_ν for each of these models is shown in Figure 5.21 for the ND280 flux predictions. These weightings were applied to both ND280 and SK weights identically so that fake data sets could be made from the T2K Production MC. The resultant fake datasets were found to introduce small variations in the extracting oscillation mixing contours for the T2K 2017 analysis, varying the position and width of δ_{CP} contours by up to 2.7% and 5.3% respectively [188]. Future T2K analyses plan on using the full implementation of the Z-expansion model to ensure the shape freedom is fully captured in the oscillation analysis.

[2]The Cholesky decomposition effectively takes the square root of the covariance, $M^{\text{Cholesky}} M^{\text{Cholesky}} = M$. This provides an estimate on the errors on each parameter including correlations between other parameters.

Fake Dataset	Parameter	1	2	3	4
	Z-Expansion Model	a_1	a_2	a_3	a_4
1	Central	2.28	0.26	-5.20	2.60
2	Lower	2.25	1.19	-7.18	4.87
3	Higher	2.30	-1.24	-2.63	2.08
	3-Comp. Model	α	γ	β	θ
4	Central	0.110	0.410	1.040	-0.260
5	Lower	0.132	0.406	1.090	-0.101
6	Higher	0.155	0.413	0.968	-0.378

Table 5.7 Fake dataset parameters derived from the stochastic throw method for use by the T2K OA.

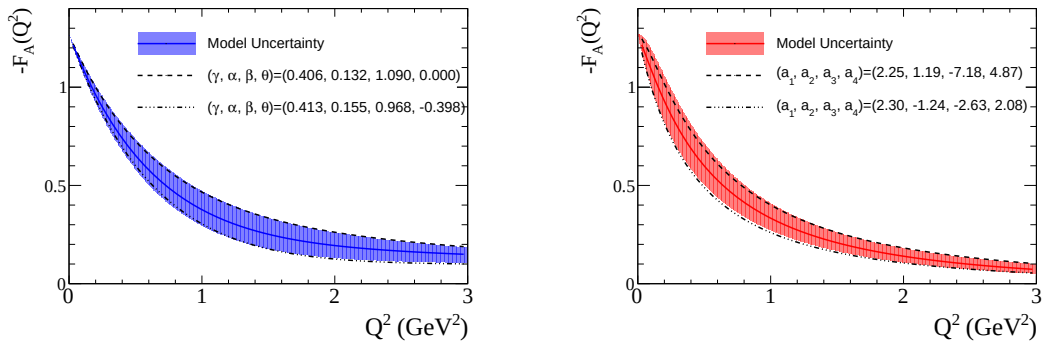

Fig. 5.20 Comparison of the chosen $\pm 1\sigma$ fake data parameter sets to the true uncertainty bands for each model obtained from the full set of stochastic parameter throws. (left) 3-component model. (right) Z-expansion model.

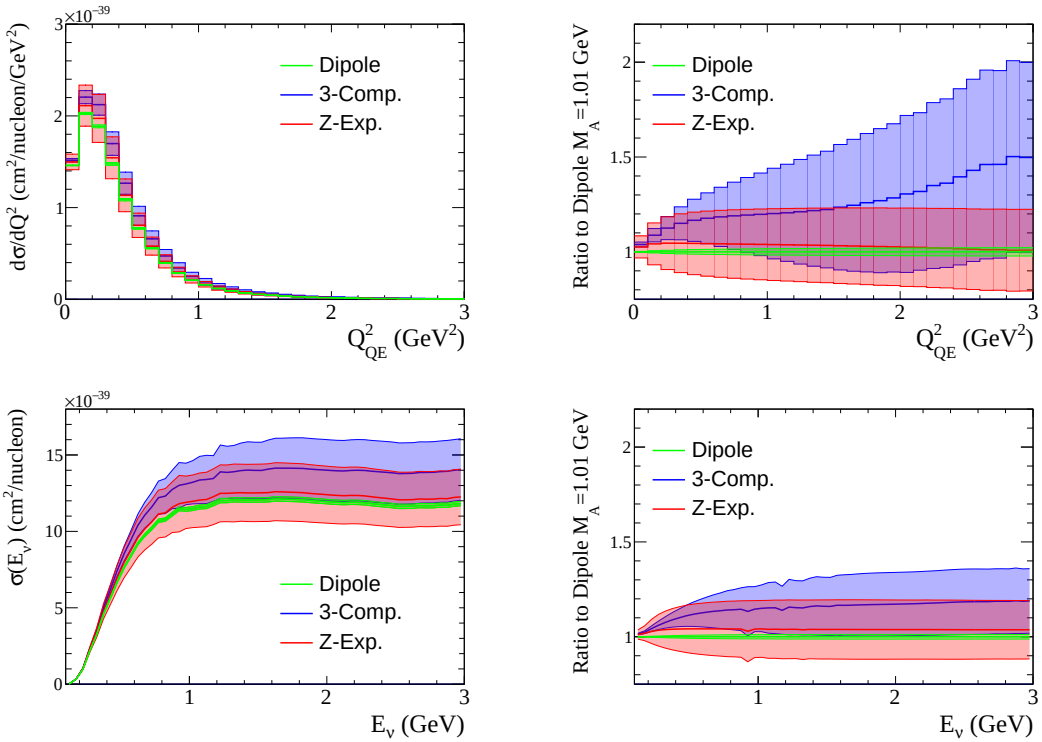

Fig. 5.21 Comparison of the different form factor $\pm 1\sigma$ error band predictions when simulated with the ND280 flux on a CH target. Since the upper and lower error bands on each model are considered in the T2K fake data, the envolope of models is effectively considered in the T2K OA.

Chapter 6

CC-inclusive Gaussian Corrections

6.1 Introduction

Experiments with fully active scintillator targets allow precise measurement of hadronic energy deposits in the final state of neutrino interaction events. This is of significant advantage in neutrino experiments as the neutrino energy is not known *a priori*. It is possible to extract a proxy for E_ν using energy conservation by looking at the total energy deposited in a detector for a given event. However, since nuclear effects and detector acceptances can modify the observed kinematics of final state particles a model is required to extrapolate back to the true neutrino energy from the measured event information. The choice of nuclear models introduces a large systematic uncertainty in this extrapolation and there is currently a strong community effort to make measurements of final state hadronic kinematics to help constrain such models. One experimental goal is an attempt to estimate the true energy and momentum transfer, q_0 and q_3, on an event by event basis for neutrino interactions as these kinematic quantities have already been extensively mapped in e-A scattering experiments and are the natural kinematics many theoretical models are expressed in.

Recently a MINERvA measurement [113] showed that in a region of low momentum transfer systematic uncertainties are reduced when extrapolating from the observed event kinematics to the three-momentum transfer q_3 . This has made it possible to extract a CC-inclusive cross-section measurement as a function of both q_3 and the hadronic energy observed in their detector, referred to as the 'available energy', E_{av}, an approximation of the true energy transfer for the event q_0. The MINERvA analysis has therefore provided one of the first high statistics measurements of neutrino interactions in quantities similar to those already probed by e-A experiments. The cross-section published by the MINERvA collaboration is shown in Figure 6.1.

When comparing the nominal GENIE 2.8.4 model to the data it was shown that there were large data/MC disagreements: an overestimation of the data in the QE dominated low recoil region

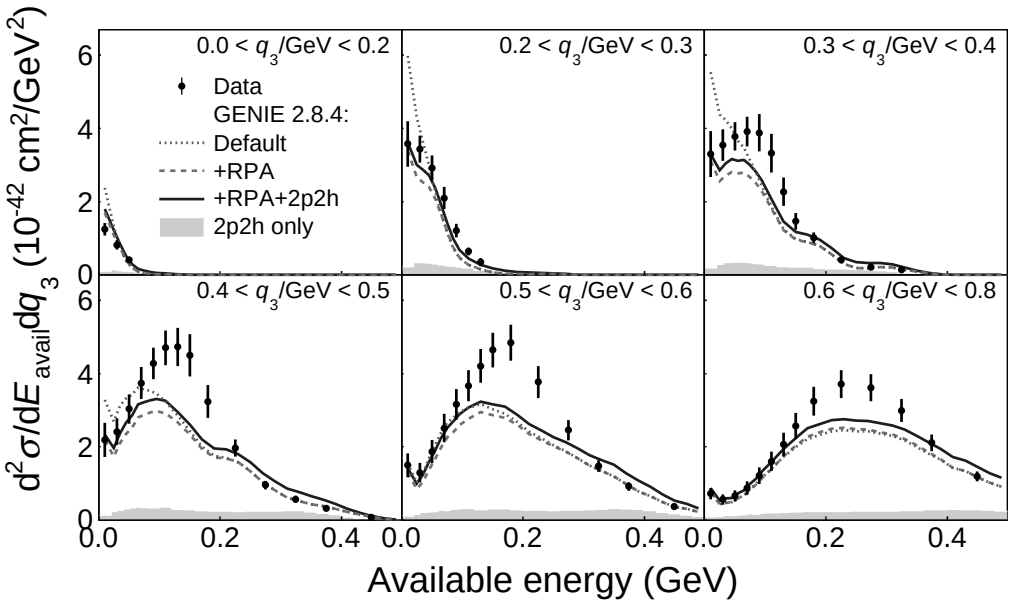

Fig. 6.1 MINERvA ν_μ CC-inclusive low recoil measurement as a function of q_3 and E_{av}. RPA and 2p2h refer to the addition of the Nieves RPA and 2p2h models to the Default GENIE model. RPA introduces a supression effect at $E_{av} \sim 0.0$ GeV, whilts 2p2h increases the cross-section at $E_{av} \sim 0.1 - 0.3$ GeV. Figure taken with permission from [113].

($q_3 < 0.4$ GeV, $E_{av} < 0.05$ GeV), and an underestimation in the dip region between the QE and RES peaks ($q_3 > 0.4$ GeV, $E_{av} \sim 0.2$ GeV). This is evident when comparing the dotted gray line to the data points in Figure 6.1. Disagreements at low recoil are believed to be due to the lack of RPA corrections in the GENIE 2.8.4 model. In Figure 6.1 it is shown that the inclusion of the Nieves RPA model improves agreement with the data in this region. The addition of the Nieves 2p2h predictions (filled in grey) to the GENIE model also slightly increases agreement with the data in the dip region, but the contributions from multi-nucleon events are relatively flat as a function of E_{av} and a more peaked prediction is needed if the disagreement in the dip region is assumed to be entirely from a deficiency in the 2p2h model.

To consider the effect of these possible model deficiencies in future analyses, the MINERvA collaboration perform a tuning of the GENIE 2.8.4 model to the data. Since no information is given on the source of the disagreement in the CC-inclusive measurement they consider four possible sources, attributing the disagreement to the 1p1h model, the entire Nieves 2p2h model, or two of the distinct initial states for the Nieves 2p2h model (pn or nn pairs). An ad-hoc Gaussian weighting is used to enhance one of these possible model components and the shape of the Gaussian is tuned until satisfactory agreement with the data is found in the dip region. Later comparisons have found that these Gaussian modifications derived from the neutrino CC-inclusive data also improve agreement with CC0π and $\bar{\nu}_\mu$ CC-inclusive measurements made by the MINERvA experiment.

The NOvA experiment, at similar energies to MINERvA, has also made measurements of CC-inclusive neutrino interactions as a function of E_{av} and has observed similar discrepancies between

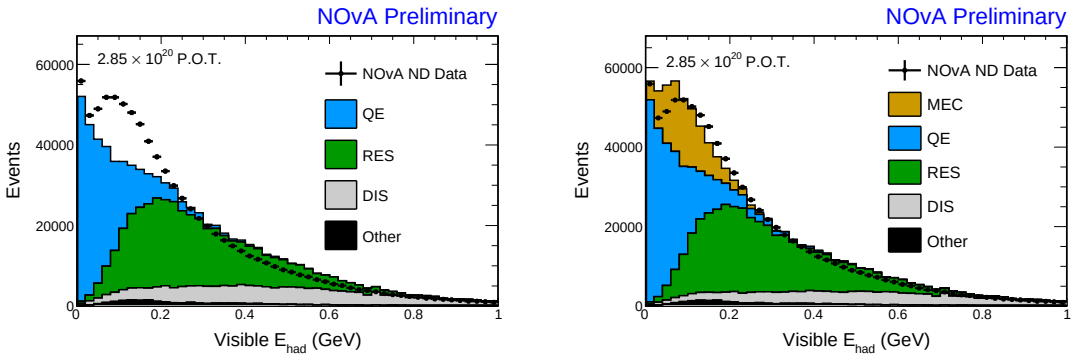

Fig. 6.2 NOvA CC-inclusive measurements of q_3 and E_{av} compared to GENIE 2.10.4 simulations. The "MEC" prediction refers to GENIE's empirical MEC multi-nucleon interaction model after it has been tuned with a Gaussian correction to better fit the data. Figures taken from [189].

GENIE and the data as shown in Figure 6.2 [189]. To account for this in the NOvA oscillation analysis the GENIE Empirical MEC model was added to their MC prediction before being tuned as a function of q_3 using a similar procedure to MINERvA to account for the data/MC discrepancy.

These complementary measurements suggest a deficiency in the GENIE CC0π models studied that has only come to light when observing neutrinos with detectors that can reliably probe the total energy deposited around the interaction vertex. NEUT uses a very similar interaction model to the GENIE simulation used in the MINERvA and NOvA studies so there was a concern that not accounting for these known deficiencies could introduce a bias to the T2K OA. This chapter describes the modification of NEUT's CC0π model through the tuning of ad-hoc Gaussian corrections to the MINERvA CC-inclusive data. Section 6.1 discusses in detail the MINERvA CC-inclusive data. Section 6.2 discusses initial comparisons of NEUT and NuWro to the MINERvA data. Section 6.3 discusses the implementation of a 2D Gaussian correction and the tuning of these corrections. Section 6.4 compares the tuned MINERvA enhancements to public ND280 data before Section 6.5 discusses the implications these studies could have on future T2K oscillation analyses.

6.2 MINERvA CC-inclusive Comparisons

MINERvA extracts a ν_μ CC-inclusive measurement by selecting events with a forward going muon that has been tagged in the MINOS spectrometer. With a reliable measurement of the muon energy the event's remaining energy can be extracted from the energy deposited in the MINERvA detector. This reconstructed quantity is related to the "available energy" for the event by correcting for the known efficiencies and acceptances for different particles. The available energy for a true event is defined as the sum of kinetic energies, T_i, of final state protons and charged pions, and the total

Index	Cut
1	$\theta_\mu < 20^\circ$
2	$E_\mu < 1.5$ GeV
3	1 Initial State ν_μ
4	1 Final State μ
5	$2.0 < E_\nu /$ GeV < 6.0

Table 6.1 Cuts applied to select MINERvA CC-inclusive events in the NUISANCE framework.

energy of final state electrons, photons, and neutral pions. This can be written as

$$E_{av} = \sum_{i=p,\pi^\pm} T_i + \sum_{i=e^\pm,\gamma,\pi^0} E_i, \tag{6.1}$$

where the seperation of total and kinetic energy for different particles is performed to best match the detectors response. Protons and charged pions are expected to deposit only their kinetic energy in the calorimeters. The other particles are observed as clusters of energy deposits that closely matches their total energy. With a known E_{av} the momentum transfer squared for the event can be extracted by taking advantage of the known muon kinematics. A quasi-elastic assumption is used to reconstruct Q^2_{rec} for the event as

$$E_\nu^{rec} = E_{av} + E_\mu \tag{6.2}$$

$$Q^2_{rec} = -m^2_\mu + 2E_\nu^{rec}\left(E_\mu - \sqrt{E^2_\mu - m^2_\mu}\cos\theta_\mu\right), \tag{6.3}$$

where the definition of E_ν^{rec} assumes the available energy is a good proxy for the true energy transfer. The three-momentum transfer is then simply a function of the total momentum transfer squared and the energy transfer

$$q_3 = \sqrt{Q^2 + q_0^2}. \tag{6.4}$$

To extract q_3 a nuclear model is used to correct E_{av} back to q_0 on an event by event basis. This extrapolation is inherently model dependent, but given small differences in $q_0 - E_{av}$ the model dependence is expected to be small in the low recoil region [113].

To make comparisons with NEUT the MINERvA dataset was added to the NUISANCE framework. For each CC-inclusive event passing the signal definition cuts, shown in Table 6.1, values for E_{av} and q_3 were extracted from the simulated final state particles and binned into histograms matching the MINERvA data. The published data points and associated correlations were then used to automatically calculate a χ^2 value for each MC prediction considered.

To judge how well the NEUT model compared to the MINERvA data, 2×10^6 events were generated in NEUT 5.3.6. The Smith-Moniz model [190] was used to simulate CCQE 1p1h interactions with a dipole form factor and axial mass of $M_A = 1.01$ GeV. The Nieves RPA model was applied to

1p1h events through a Q^2 dependent event weighting [107]. The Nieves 2p2h model was also used to simulate multi-nucleon interactions assuming 60% of such interactions occur on pn pairs [107]. Resonant production is simulated using the Rein-Sehgal model with updated form factors tuned to bubble chamber pion production data[82]. Coherent pion production was simulated using the Berger Sehgal coherent model [191] and final state interactions were treated in an intranuclear cascade based on the Oset cascade model [117]. This model combination in NEUT was chosen to reflect the model being used in the T2K OA at the time. The use of a RFG model with Nieves RPA and 2p2h predictions makes the underlying CC0π interaction simulation similar to the GENIE model used in the MINERvA tunings, with the main difference being the treatment of Final State Interactions (FSI) in each generator.

The NEUT model prediction, separated by different true interaction topologies, is shown in Figure 6.3. It is clear that the same disagreement seen in the dip region for GENIE is also present for the NEUT model considered here. Both generators use a base RFG model with Nieves RPA and 2p2h simulations added, so it is likely the disagreement seen in both originates from this CC0π model combination. The χ^2 calculated from the published covariance and the NEUT MC prediction was $\chi^2/NDOF = 3519/67$ when considering all bins. Large χ^2 values of similar magnitude were also found by the MINERvA collaboration when comparing GENIE to both the reconstructed and unfolded distributions. This is a result of the high statistics in the CC-inclusive sample and the clear inability of the models to describe the shape of the distribution across all the q_3 slices considered.

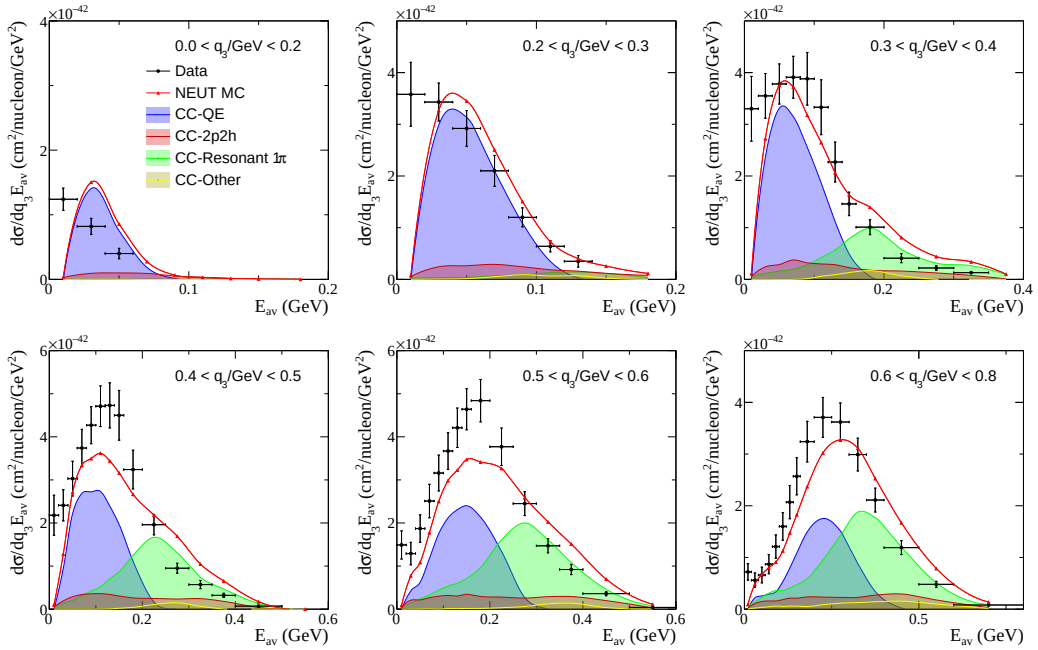

Fig. 6.3 MINERvA inclusive charged-current neutrino cross-section measurement on carbon [113] as a function of transferred momentum and available neutrino energy (after unfolding) compared to the T2K reference model in NEUT.

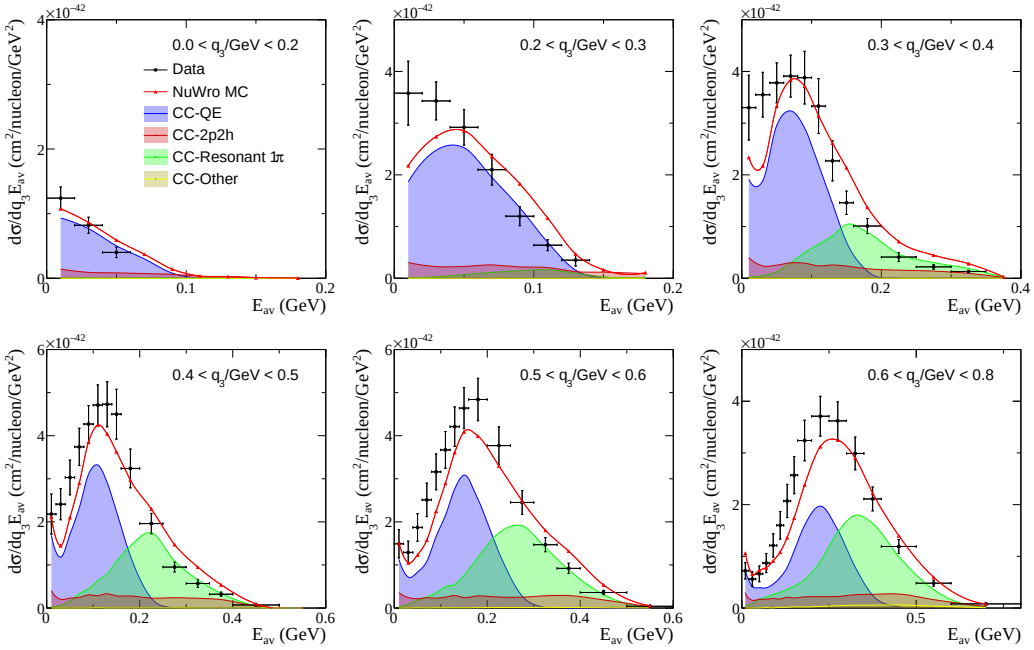

Fig. 6.4 MINERvA inclusive charged-current neutrino cross-section measurement on carbon [113] as a function of transferred momentum and available neutrino energy (after unfolding) compared to the T2K reference model in NuWro.

To study the effect that moving to a local Fermi gas might have, an additional MC event sample was generated in NuWro using a LFG and the same Nieves RPA and 2p2h models. When this was used to produce the equivalent plot in NUISANCE shown in Figure 6.4 it was found that the change in nuclear model had a significant effect on the shape of the 1p1h model. This suggests that the use of a simple RFG for the 1p1h model in NEUT could be to blame for the disagreement in the dip region. However, since the data is CC-inclusive and multiple interaction channels contribute in this region it is extremely difficult to reliably disentangle the exact cause of the discrepancy. The 2p2h contribution is relatively flat in both distributions, but could be significantly shifted if the relative contributions from pn and nn pairs are shifted, or the response of the 2p2h model was changed as a function of true energy transfer.

In addition to these problems an event deficit was observed in the lowest E_{av} for each q_3 slice only in NEUT. In both NuWro and GENIE it is possible for CCQE interactions to produce events with only a single low energy nucleon exiting the nucleus as a result of final state interactions. If a proton undergoes a charge exchange interaction it is also possible for this to produce single neutron final states which do not contribute to the E_{av} total. In the NEUT version considered in this work however, an exagerated implementation of Pauli blocking is applied in which the nucleon must be above the chosen nucleus binding energy after it leaves the nucleus, introducing a sharp cut-off in q_0 as shown in Figure 6.5.

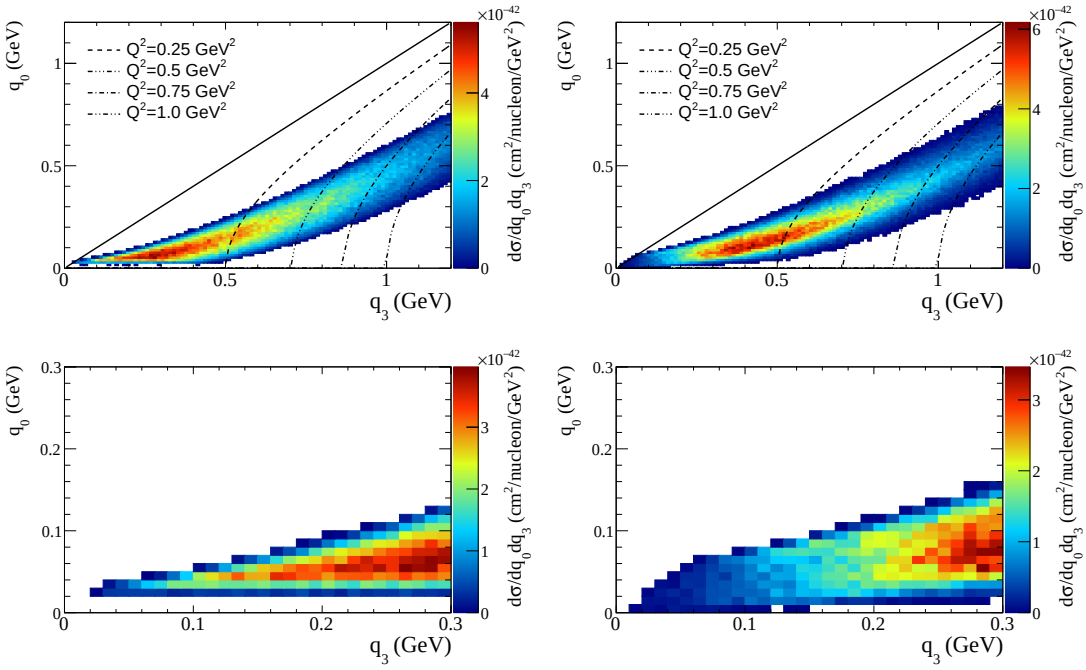

Fig. 6.5 Comparison of NEUT and NuWro's QE cross-section as a function of (q_0, q_3) for very low recoil events. (left) The sharp cut off at low q_0 is introduced by a strong Pauli blocking implementation. Turning off Pauli blocking completely fills in this missing region of phase-space but significantly modifies the neutrino-nucleus CCQE cross-section and can be considered an unphysical modification. (right) The missing region of phase space is filled when using a local Fermi gas in NuWro that has a much more relaxed binding energy. The lines correspond to regions of different Q^2. The lower plots, show an enlarged region at low momentum transfer ($Q^2 < 0.09$ GeV^2), to highlight the harsh cut off in events due to the binding energy issue in NEUT. The solid line is the kinematic limit.

The effects of binding energy choices in NEUT were already handled by a set of ND280 fake data studies in the T2K 2017 OA, therefore a stronger focus was put on understanding the dip region problems in these studies. Future versions of NEUT will adopt a local fermi gas implementation by default, avoiding this problem. To avoid the problematic lowest E_{av} bins, a masking feature was implemented into NUISANCE that could remove the data points and corresponding correlations when evaluating the total data-MC χ^2 test statistic. This procedure reduced the nominal NEUT $\chi^2/NDOF$ from $3519/67$ to $2224/61$. Other than the dip region the next largest contribution to the χ^2 was then the high E_{av} tail dominated by 2p2h and CC1π events.

MINERvA sits at a higher energy range than T2K and therefore sees a large contribution of pion production events. The comparisons shown here suggest that the nominal parameters in NEUT's CC1π model (tuned to lower energy bubble chamber data) also do a poor job of describing the high E_{av} region at higher neutrino energies. Similar tensions have also been found when comparing directly to exclusive MINERvA CC1π data. For the purpose of these CC0π studies, however, NEUT's pion production model was left fixed at its nominal values.

Through comparisons of the different interaction channel contributions shown in Figure 6.3, two possible methods to improve the data-MC difference were identified:

- The RFG CCQE model performs poorly at higher q_3 in the dip region. When comparing to the LFG model in NuWro, both contributions drop off at $E_{av} > 0.2$ GeV but NEUT requires an additional enhancement in to shift the peak into the dip region and bring it in line with the data.
- The Nieves 2p2h model provides a very flat contribution to the total cross-section across the E_{av} space. If the model were strongly enhanced in the dip region and suppressed at high E_{av} this would improve the agreement with the data.

It is impossible to know exactly which part of the model is deficient since these are the first measurements of their kind in the neutrino sector. It is also possible that a modification or distortion of the pion production model is also needed at low E_{av} in the dip region in NEUT, although preliminary investigations of this possiblity suggested large unphysical modifcations would be needed, in conflict with other constraints on the model. Both the 1p1h and 2p2h have different energy dependencies which need to be considered. To ensure both possibilities were accounted for, two separate model corrections were extracted, the first assuming the CCQE model alone needs an enhancement to be applied, and the second assuming the 2p2h model needs both an enhancement and a suppression. We consider cases where we keep the rest of the model fixed, although really the only way to truly account for this is to build towards one large CC-inclusive model tuning for neutrino interactions.

6.3 Extracting Gaussian Corrections

To parametrise the data-MC difference a 2D Gaussian weighting function in (q_0, q_3) space was chosen with the hope that defining the correction in terms of true interaction kinematics would allow modifications to be easily propagated to different energy ranges. The function was defined as

$$\Delta_0 = q_0 - q_0^{mean}, \tag{6.5}$$
$$\Delta_3 = |q_3| - q_3^{mean}, \tag{6.6}$$

$$a = \frac{\cos^2\theta}{2(q_0^{width})^2} + \frac{\sin^2\theta}{2(q_3^{width})^2}, \tag{6.7}$$
$$b = \frac{-\sin 2\theta}{4(q_0^{width})^2} + \frac{\sin 2\theta}{4(q_3^{width})^2}, \tag{6.8}$$
$$c = \frac{\sin^2\theta}{2(q_0^{width})^2} + \frac{\cos^2\theta}{2(q_3^{width})^2}, \tag{6.9}$$

$$G(q_0, |q_3|) = A^{Norm} exp\left(-a\Delta_0^2 + 2b\Delta_0\Delta_3 - c\Delta_3^2\right) \tag{6.10}$$

where $q_{0,3}^{mean}$ denotes the Gaussian central value, $q_{0,3}^{width}$ defines its width, A^{norm} defines its total normalisation, and θ its angular tilt away from the $q_0 - q_3$ axes. This function was added to NUISANCE as an event weighting lookup function that could be varied freely by MINUIT. When applied to a given event, the true $q_0 - q_3$ values were extracted from the neutrino and lepton kinematics and used to calculate a weight

$$W(\vec{e}(q_0, |q_3|)) = G(q_0, |q_3|) \times S(\vec{e}(q_0, |q_3|)), \tag{6.11}$$

where $S(\vec{e}(q_0, |q_3|))$ is a boolean signal classification that ensures the Gaussian weights are only applied to certain chosen event classifications. This allowed the weighting to be applied to any arbitrary part of a generator MC model provided a signal classification could be derived from the information contained in the event.

To reflect the possible model deficiencies identified earlier, two Gaussian signal definitions were considered. The first assumed the observed deficiency came entirely from the 1p1h interaction model (shown in blue in Figure 6.3) with the definition

$$S_{CCQE}(\vec{e}(q_0, |q_3|)) = \text{Any true 1p1h event.} \tag{6.12}$$

Since only an enhanced 1p1h CCQE model was being considered the Gaussian event weights were truncated as

$$W_{CCQE} = max[1.0,\ G(q_0, |q_3|) \times S_{CCQE}]. \tag{6.13}$$

In the 2p2h tuning case a similar signal definition was used to select only true 2p2h interactions for weights to be applied to. These are shown in red in Figure 6.3. Since it appeared the 2p2h model also needed to be suppressed, event weights were instead only truncated to be above zero, allowing the prediction away from the centre of the Gaussian to be strongly supressed if necessary.

MINUIT [177] was used to tune both the Gaussian corrections separately, assuming only one of them was the appropriate correction to apply. The free parameters shown in Equation 6.10 $(q_{0,3}^{mean}, q_{0,3}^{width}, A^{norm}, \theta)$ were allowed to vary until the masked chi-square test statistic was minimised and a set of best fit parameters were found. All other free parameters in NEUT were left fixed at their nominal values. Initial data/MC comparisons of the NEUT model in Figure 6.3 motivated starting Gaussian central values of $(q_0, q_3) = (0.2\ \text{GeV}, 0.5\ \text{GeV})$, which helped the fit converge on an acceptable set of parameters within 1000 iterations ($\sim$ 24 CPU hours).

6.3.1 CCQE Gaussian Corrections

The best fit CCQE tuning parameters and likelihoods compared to the nominal values can be found in Table 6.2. As shown in Figure 6.6 an enhancement in the dip region is preferred in the $(0.4 < q_3/\ \text{GeV} < 0.6)$ slice and the introduction of a Gaussian correction reduces the total $\chi^2/NDOF$ down to $1124/55$. The data places a strong constraint on each of the free parameters, but it is likely that if other degenerate cross-section parameters were varied (such as M_A^{CCQE}) the uncertainties would be inflated as a result. The inability to suppress the 1p1h cross-section in the tune results in a large χ^2 contribution still coming from the lowest q_3 data points, and it is possible enhanced RPA suppression factors could relieve this tension. The disagreements at higher E_{av} however, suggest the additional need for a modified 2p2h or CC1π model.

An enhancement at higher q_3 than the starting assumption was extracted from the 1p1h fits, leading to a total MC prediction that looks offset relative to the data in Figure 6.6. When slicing the data as a function of E_{av} instead it is clear that the covariance information provides a much stronger shape constraint within each individual E_{av} slice as shown in Figure 6.7, whilst deviations from the shape when comparing neighbouring E_{av} bins provide smaller increases to the total χ^2. The fits therefore converge on a result which predicts the correct shape for each $d\sigma/dq_3$ distribution at the cost of producing a slightly different total normalisation in each E_{av} slice. This leads to a best fit distribution that appears to have an offset peak in Figure 6.6.

	Nominal	CCQE Correction	2p2h Correction
A^{norm}		4.83 ± 0.09	15.96 ± 0.11
q_0^{mean} (GeV)		0.36 ± 0.03	0.22 ± 0.02
q_0^{width} (GeV)		0.13 ± 0.01	0.03 ± 0.02
q_3^{mean} (GeV)		0.43 ± 0.02	0.48 ± 0.03
q_3^{width} (GeV)		0.21 ± 0.02	0.13 ± 0.02
θ (rad)		2.35 ± 0.08	-0.46 ± 0.15
Allow $W < 1.0$		No	Yes
χ^2	2224	1124	941
$NDOF$	67	67	67
$\chi^2/NDOF$	33.2	16.8	13.1

Table 6.2 Nominal, and Best-fit likelihood comparisons and extracted Gaussian parameters for the 1p1h and 2p2h correction tuning studies. The Nominal column shows the results before any correction is applied. Allow W < 1.0 refers to whether weights are truncated below 1 or suppression of the nominal prediction is allowed. The large $\chi^2/NDOF$ is a result of the models lack of a ability to fully recreate the shape of the data at high E_{av}.

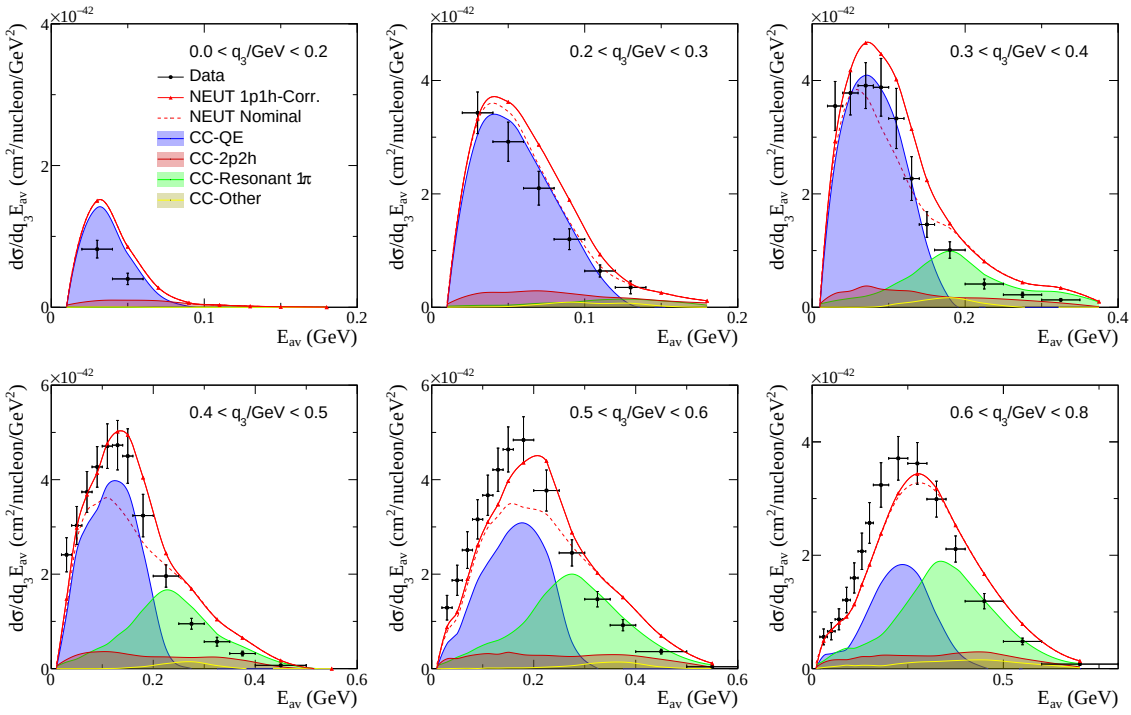

Fig. 6.6 Best fit CCQE Gaussian correction compared to MINERvA CC-inclusive data for all 6 slices of q_3 the data is published in. The best fit distribution (solid red) appears to be slightly offset due to a preference for the fit to ensure the shape in each E_{av} slice is correct.

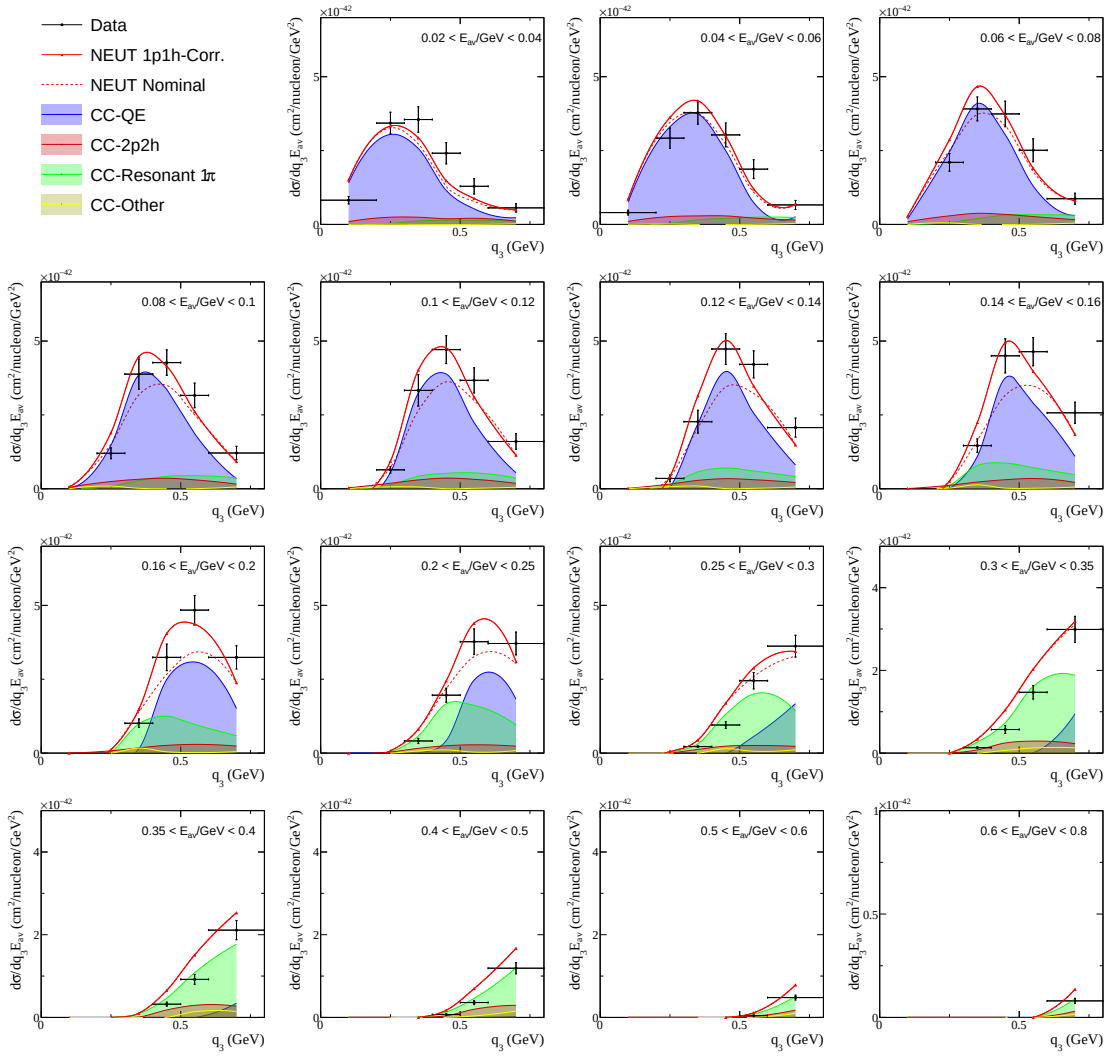

Fig. 6.7 Best fit CCQE Gaussian correction compared to MINERvA CC-inclusive data for all 16 slices of E_{av} the data is published in. It is clear that the shape of each slice is correct, although the overall normalisation when comparing different slices to one another, varies, over-predicting or under-predicting in different slices. At high E_{av}, the uncertainties on the data points are significantly smaller. In this region the larger energy deposits are more spread out in the MINERvA calorimeters, making it easier to reconstruct the total energy in the event, and to seperate the muon track from other particles. This reduces the systematic uncertainty on the data points in this region.

Due to kinematic constraints on the CCQE model the choices of $q_{0,3}^{mean}$ result in only half of the Gaussian occupying a region of kinematically allowed phase space for the 1p1h model as shown in Figure 6.8. This large enhancement at high q_0 extends the 1p1h cross-section tail out into the dip region. The convolution of the Gaussian correction with NEUT's 1p1h interaction model results in a kinematic distribution that peaks closer to $q_0 \sim 0.2$ GeV similar to the NuWro LFG model shown in Figure 6.5. Whilst comparisons of different spectral function models to e-A data already set strong constraints on the shape of 1p1h interactions as a function of (q_0, q_3) there is currently a large variation between models in the dip region, and the RFG model has been shown to drop off at much lower q_3 than other more theoretically consistent interaction models in this region. Therefore the Gaussian enhancements to NEUT's 1p1h model derived from the MINERvA data are not completely disallowed by e-A comparisons and appear to want to bring the model in line with more theoretically motivated interaction models.

6.3.2 2p2h Gaussian Corrections

Parameter results extracted when applying the Gaussian correction to true 2p2h events are shown in Table 6.2. Weights for the 2p2h correction case were allowed to be below 1.0 since the 2p2h model extends to much higher E_{av} and the model could be making the agreement worse in the delta region where CC1π interactions dominate. Since the small 2p2h model contributions are flat across the E_{av} space a very large enhancement factor is required to fill in the dip region, with a maximum weighting factor of 15.96 extracted in the tunings.

The extracted enhancement leads to a distribution which looks offset to higher E_{av} relative to the data in each q_3 slice as shown in Figure 6.9. Again this offset is less obvious when slicing the data as a function of E_{av} instead of q_3. Since in these tunings the total 2p2h cross-section can be suppressed, there is a reduction in the cross-section away from the dip region at high E_{av}. As a result only the CC1π model contributes above E_{av} and the agreement with the data is improved in this region as well.

As shown in Figure 6.10 the tunings have completely removed the Delta component (band at high q_0 and q_3) of the model from the fits leaving only a sharp Gaussian centered at $(q_0, q_3) = (0.2\text{ GeV}, 0.5\text{ GeV})$. Interestingly the resultant 2p2h distribution in (q_0, q_3) space is similar to the GENIE Empirical 2p2h model obtained from tunings to MiniBooNE and NOMAD data which follows a Gaussian distribution with a peak at $(q_0, q_3) = (0.3\text{ GeV}, 0.6\text{ GeV})$. It is possible that the nominal NEUT model's overestimation of the data in this region may be due to over counting between the Delta contributions in the 2p2h interaction model and the Delta resonance in the Rein-Sehgal CC1π model, and that the discrepancies may be resolved if a single consistent model was used in the generator.

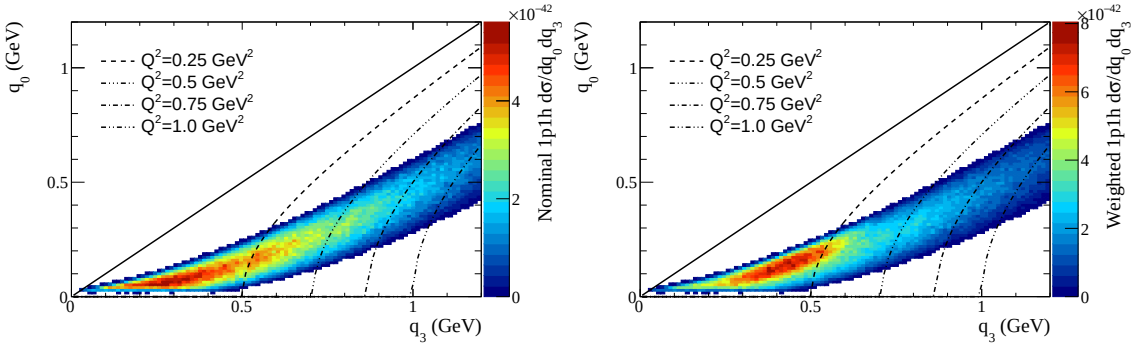

(a) Nominal NEUT 1p1h prediction.

(b) 1p1h Gaussian weighted NEUT prediction.

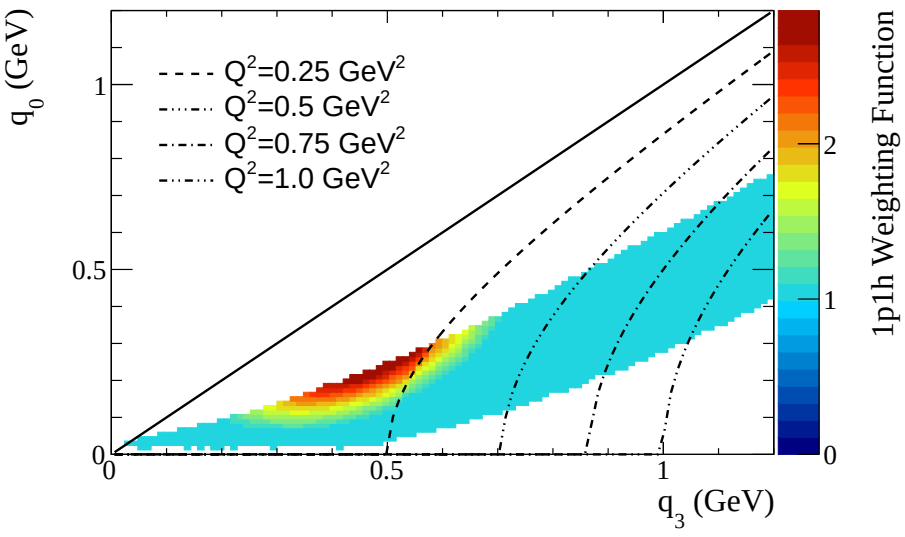

(c) Average event weight per bin.

Fig. 6.8 Best fit CCQE Gaussian correction applied to true CCQE MINERvA events. The average weight plots the shape of the 'Gaussian lookup function'. The average event weight per bin plot is obtained by taking a ratio of figures (b) and (a). This shows that the best fit correction introduces an enhancement at the upper kinematic limit of QE interactions, making the QE model look more like a LFG model than a RFG model.

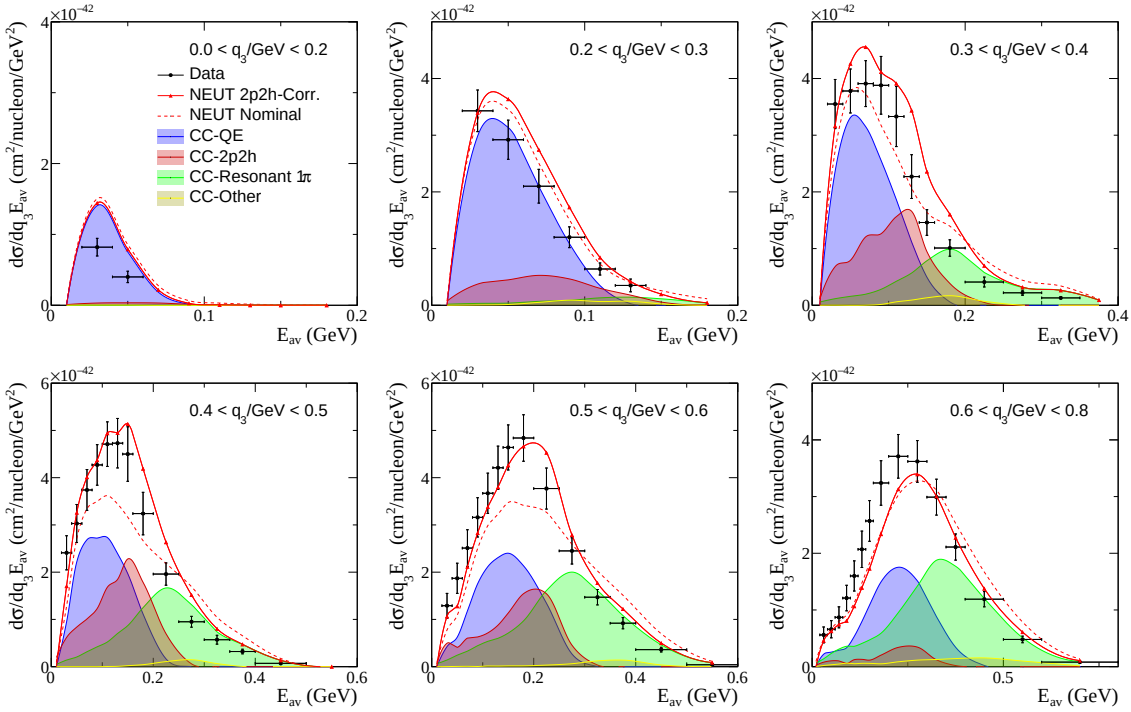

Fig. 6.9 Best fit 2p2h Gaussian correction compared to MINERvA CC-inclusive data for all 6 slices of q_3 the data is published in. Since a large weight is applied to the 2p2h model at the best fit point, statistical uncertainties in the 2p2h MC predictions (shown filled in red) are exaggerated. Again the best fit distribution (solid red) appears to be slightly offset due to a preference for the fit to ensure the shape in each E_{av} slice is correct.

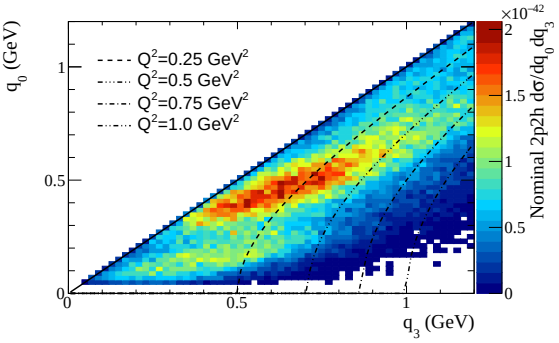

(a) Nominal NEUT 2p2h prediction.

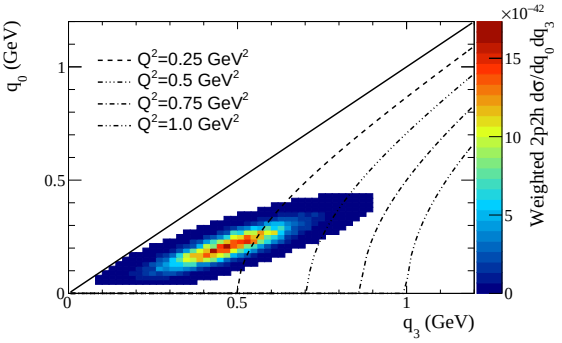

(b) 2p2h Gaussian weighted NEUT prediction.

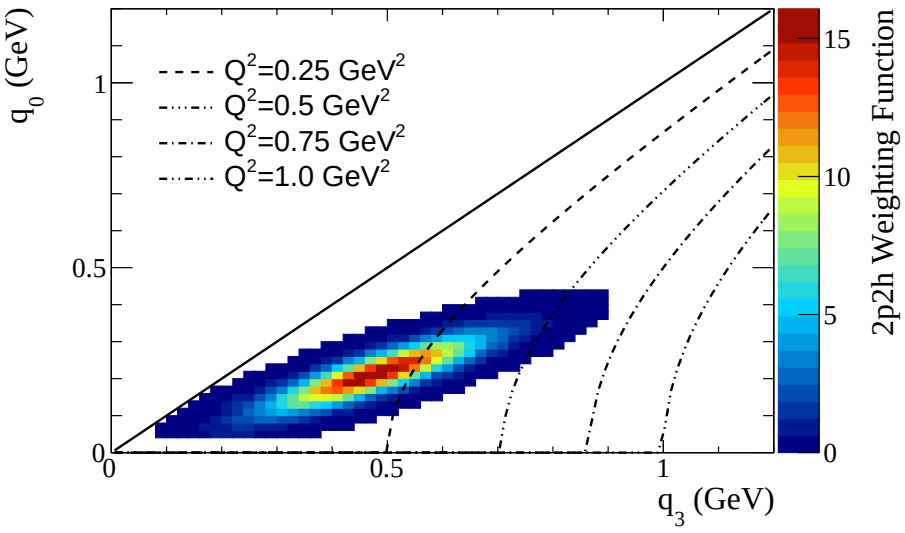

(c) Average event weight per bin.

Fig. 6.10 Best fit 2p2h Gaussian correction applied to true 2p2h MINERvA events. The average weight plots the shape of the 'Gaussian lookup function'. The average event weight per bin plot is obtained by taking a ratio of figures (b) and (a). This shows that the best fit correction severely reduces the upper peak in the 2p2h distribution, preferring a final $(q_0 - q_3)$ spectrum (b) which looks very similar to the Dytman emperical MEC model discussed in Chapter 2.

6.4 Propagating Corrections to ND280

Defining the Gaussian as a function of (q_0, q_3) allowed it to be easily propagated to other selections or experiments. This assumed that applying the correction to the total prediction for 1p1h or 2p2h would give an appropriate E_ν dependence when moving down to lower energy experiments. To understand what the enhancements would look like at T2K, 2×10^6 events were generated with the same NEUT model as before on a CH target using the ND280 ν_μ flux. NUISANCE was used to select ν_μ CC0π events from this sample and bin them as a function of $(p_\mu, \cos\theta_\mu)$. A single bin in these kinematics is strongly correlated with a given Q^2 but is capable of sampling many different (q_0, q_3) combinations. As a result the enhancement to the 1p1h model occupies a band of Q^2 between $0.1 < Q^2/\text{ GeV}^2 < 0.3$ in the $p_\mu - \cos\theta_\mu$ space as shown in Figure 6.11. In contrast the 2p2h modification is capable of introducing a low Q^2 suppression which is visible as a blue band in the top left corner of the average weight distribution shown in Figure 6.12. Since both enhancements are tuned to the dip region discrepancy they both occupy the same regions of Q^2, enhancing the maximum CC0π prediction by a factor of approximately $1.5 - 2.0$.

To quantify whether the corrections were favoured at ND280 the MC was compared to measurements of CC0π $p_\mu - \cos\theta_\mu$ final states in the ND280 carbon FGD1 target, published in Ref. [115]. As shown in Figure 6.13, the largest enhancements are seen in the $0.6 < \cos\theta_\mu < 0.9$ slices and the 1p1h or 2p2h corrections introduce very similar modifications in this region. The largest differences between the two assumptions appear in the very forward going slice (corresponding to low Q^2) where the 2p2h correction can suppress the cross-section prediction at low p_μ.

It is worth pointing out that the data shown in Figure 6.13 is highly correlated, a result of the model independent unfolding procedure used in [115], therefore it is important to compare the models agreement using the full covariance information[1]. The published covariances were used to calculate a total χ^2 for each prediction. The nominal NEUT MC prediction (shown in dashed) was found to be preferred by the data, predicting a $\chi^2/NDOF = 172/66$ compared to $\chi^2/NDOF = 282/66$ and $\chi^2/NDOF = 291/66$ for the 1p1h and 2p2h corrected predictions respectively. Figure 6.14 suggests that in some $\cos\theta$ slices the MC slightly underestimates the data in similar regions of Q^2 that the MINERvA tuned enhancements occupy, but the data/MC discrepancy is of a much smaller magnitude. Similarly a suppression in the very forward going bin in agreement with the 2p2h correction is present, and suggests that the shape of the Nieves 2p2h implementation in NEUT needs to be further suppressed at low Q^2 to agree with the data.

[1] Uncorrelated χ^2 calculations data can be extremely misleading when large correlations are actually present in data. In neutrino measurements this is often the case, so it is recommended that comparisons of a models agreement by eye should never be taken too seriously.

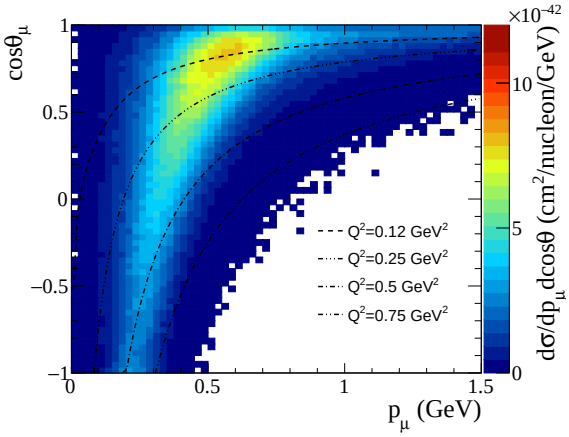

(a) Nominal NEUT prediction.

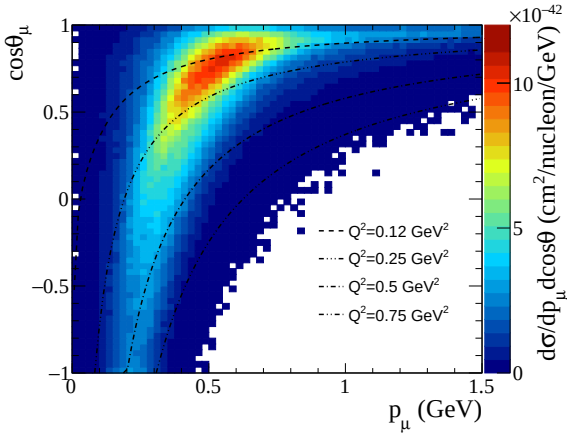

(b) 1p1h Gaussian weighted NEUT prediction

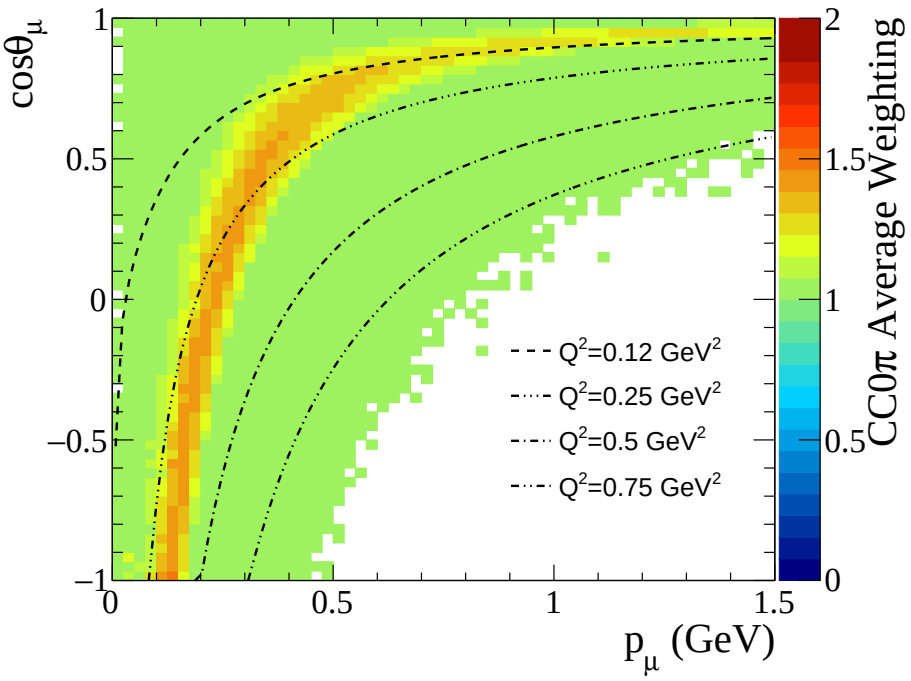

(c) Average event weight per bin.

Fig. 6.11 Best fit 1p1h Gaussian correction applied to True 1p1h ND280 CC0π events and the effect it has on the CC0π cross-section. The average weight per bin plots the shape of the correction applied to the overall CC0π cross-section. The $q_0 - q_3$ weighting maps onto a line of almost constant Q^2 at ND280.

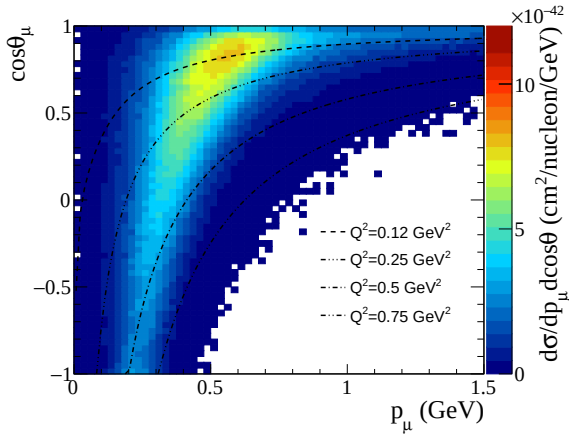

(a) Nominal NEUT prediction.

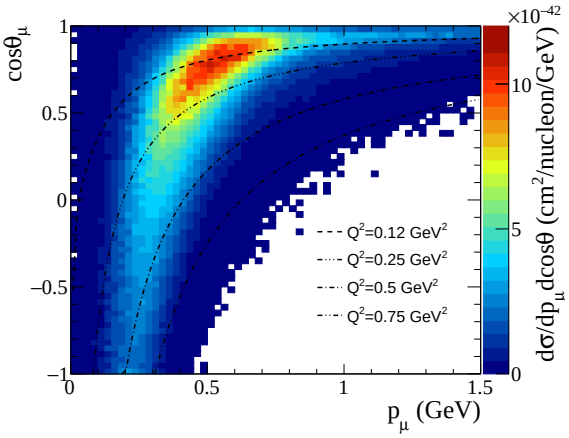

(b) 1p1h Gaussian weighted NEUT prediction

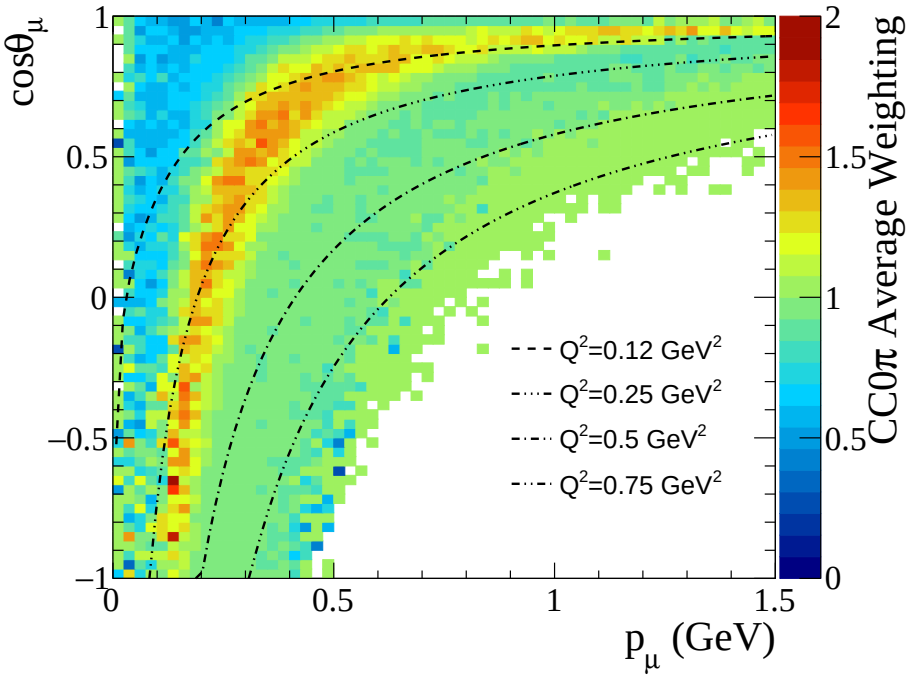

(c) Average event weight per bin.

Fig. 6.12 Best fit 2p2h Gaussian correction applied to True 2p2h ND280 CC0π events and the effect it has on the CC0π cross-section. The average weight per bin plots the shape of the correction applied to overall CC0π cross-section. The $q_0 - q_3$ weighting maps onto a line of almost constant Q^2 at ND280 similar to the CCQE tuning, however an additional suppression is present at very low Q^2 due to the suppression of 2p2h events away from the centre of the Gaussian correction.

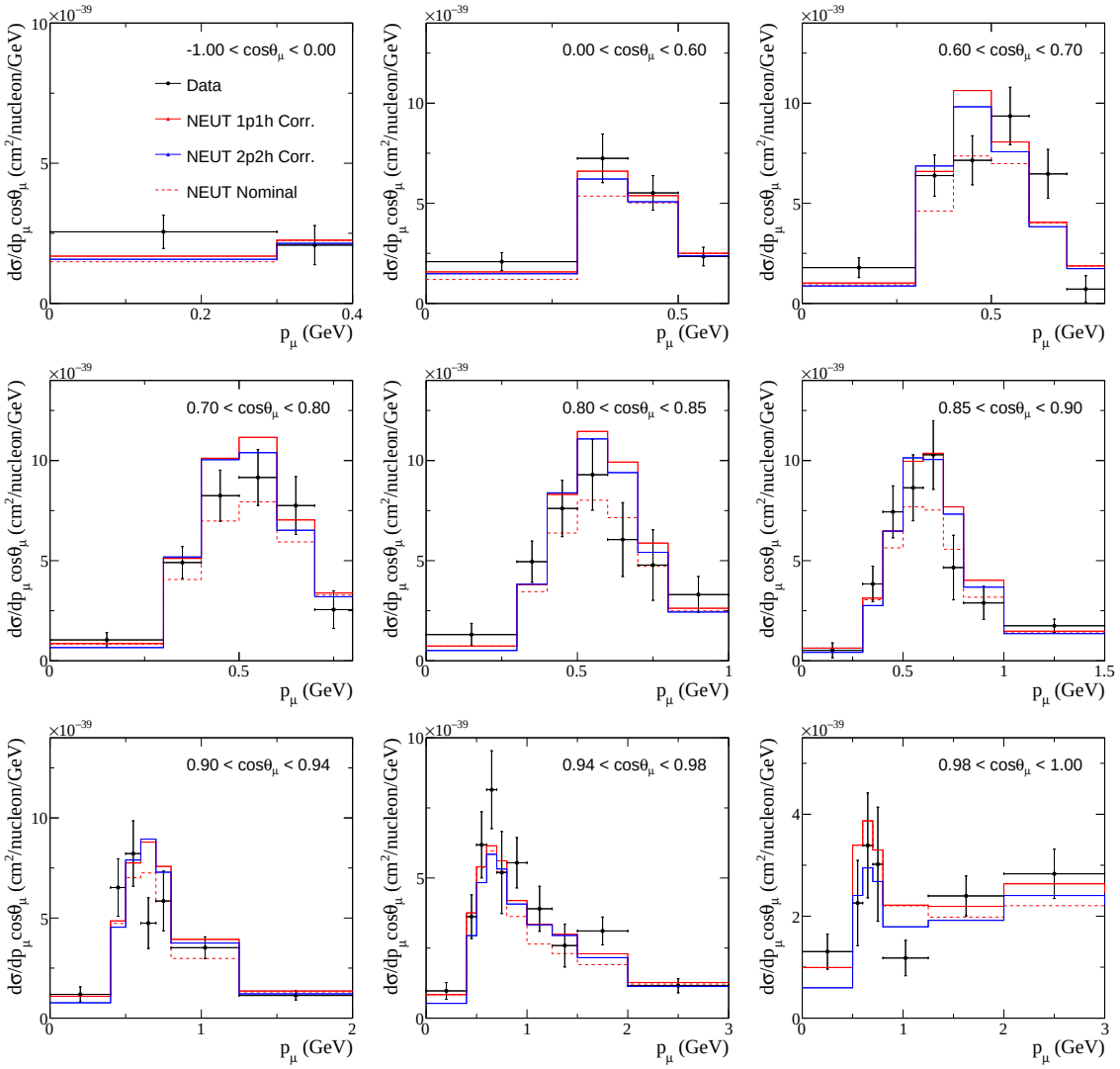

Fig. 6.13 Comparison of the NEUT models considered to T2K CC0π data from published in Ref. [115].

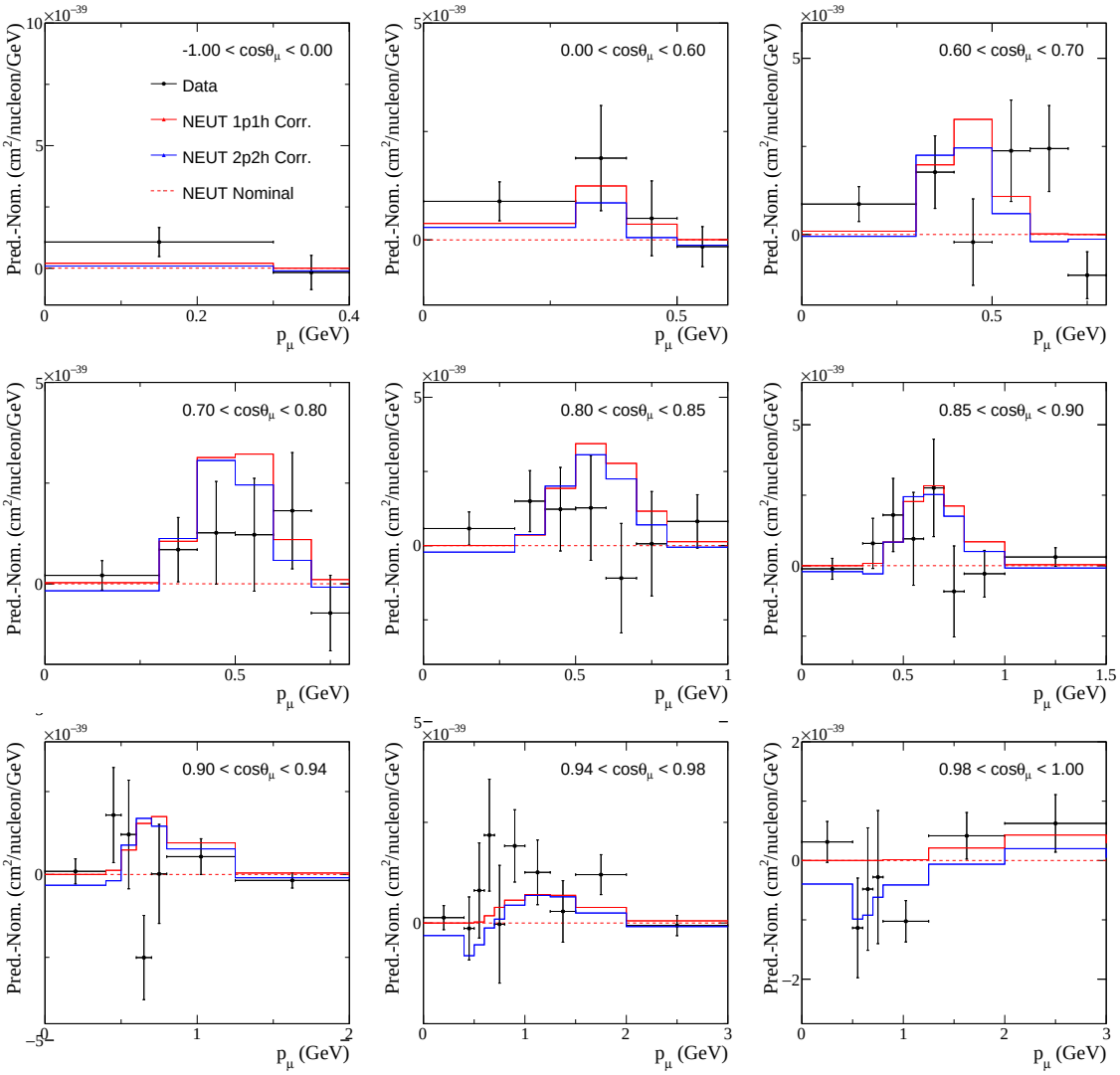

Fig. 6.14 Comparison of the difference between T2K CC0π data and the NEUT nominal MC prediction showing the slight enhancement prefered by some bins at higher angle bins. The difference introduced due to the MINERvA corrections are also shown to highlight the overestimation of the enhancement needed as $\cos\theta$ increases.

6.5 Concluding Remarks

These studies have extracted corrections to the NEUT CC0π model from the $E_{av} - q_3$ CC-inclusive data by following a similar tuning methodology to that used by MINERvA in [113] and NOvA in [189], and have found them to reduce the NEUT models agreement with lower energy T2K data. Whilst a slight enhancement relative to NEUT nominal is observed at similar Q^2 values in ND280, it is of a much smaller magnitude and the nominal NEUT MC is consistent with the published ND280 data within error bands. The enhancements obtained from MINERvA drastically overestimate the enhancement needed at T2K and make the $\chi^2/NDOF$ significantly worse. A likely cause for this is that applying the modification to the entire 1p1h or 2p2h channel does not fully capture the E_ν dependence of the model deficiency being probed.

One possibility to consider is that the data/MC discrepancy at MINERvA originates from some sub-component of the model which may have different energy dependence from the cross-section of the entire model. In the case of the 1p1h model interactions the Smith-Moniz model [190] is used to describe CCQE interactions on a nucleus. It does this by describing the cross-section in terms of five hadronic structure functions, W_i, which contain information on both the nucleon (form factors) and nuclear (spectral functions) structure. It is defined as

$$\chi = \cos^{-1}\left(\frac{p_l \cos\theta}{2E_l}\right) \tag{6.14}$$

$$\begin{aligned}\frac{d^2\sigma}{dp_l d\Omega} = \frac{G_F^2 p_l^2 \cos^2(\chi)}{2\pi^2 m_N}\Bigg[W_2 + \left(2W_1 + W_A\frac{m_l^2}{m_N^2}\right)\tan^2\chi \\ + (W_B + W_8)\frac{m_l^2}{m_N E_l \cos^2\chi} \\ - W_8\frac{2\tan\chi\sec\chi\sqrt{q^2\cos^2\chi + |q_3|^2\sin^2\chi + m_l^2}}{m_N}\Bigg],\end{aligned} \tag{6.15}$$

where G_F is the Fermi constant, p_l is the lepton momentum, E_l is the lepton energy, m_l is the lepton mass, θ is the lepton scattering angle, m_N is the target nucleon mass, q is the four momentum transfer, and W are hadronic structure functions. The hadronic functions encapsulate the nuclear structure, depending on the choice of nuclear spectral function. The form of the Smith-Moniz model means each of the hadronic functions contribute differently as the neutrino energy increases. In the case of antineutrino scattering W_8 changes sign, and as a result its contributions suppress the total 1p1h cross-section. To estimate the fractional contribution from each W_i in a given kinematic bin it is possible to calculate a ratio by setting all but one W_i term to zero in the calculation before dividing by the nominal calculation with all W terms included. These ratios, R_i, have the following

forms

$$R_1 \sim 2W_1 \tan^2\chi \tag{6.16}$$

$$R_2 \sim W_2 \tag{6.17}$$

$$R_A \sim W_A \frac{m_l^2}{m_N^2} \tan^2\chi \tag{6.18}$$

$$R_B \sim W_B \frac{m_l^2}{m_N \varepsilon_2 \cos^2\chi} \tag{6.19}$$

$$R_8 \sim W_8 \left(\frac{m_l^2}{m_N \varepsilon_2 \cos^2\chi} - \frac{2\tan\chi \sec\chi \sqrt{q^2\cos^2\chi + |q_3|^2 \sin^2\chi + m_l^2}}{m_N} \right) \tag{6.20}$$

Therefore R_2 is the only function which does not explicitly depend on the quantity χ. The quantities $\tan^2\chi$ and $1/\cos^2\chi$ become large as the muon scattering angle increases, therefore it is expected that at lower energies and higher scattering angles than the MINERvA data probes the contributions from the structure functions other than W_2 will become important.

The ratios, R_i, can be used as weights when binning histograms to understand each term's contribution to the total 1p1h cross-section and check this assumption. Figure 6.15 shows the relative contributions in the MINERvA $q_3 - E_{av}$ binning. The green line represents contributions from the W_2 structure function, highlighting that at MINERvA energies only a single hadronic term dominates the 1p1h cross-section. Its contribution is relatively flat as a function of E_{av}, contributing $\sim 80-100\%$ of the total cross-section in each bin.

When applying the same analysis to the T2K CC0π predictions it is clear that the separate W contributions vary drastically as a function of $\cos\theta_\mu$ as shown in Figure 6.16. In the very forward going low recoil slices W_2 still dominates but at higher angles the other hadronic structure functions become important and the W_8 function (axial-vector interference contribution) begins to dominate the cross-section.

It is expected that if the Gaussian corrections were applied only to the W_2 structure function the parameters extracted from the MINERvA data are likely to agree with the previously extracted results. Making this assumption would then lead to a natural suppression of the enhancement at ND280 in the higher angle bins, reducing the correction by $\sim 50\%$ in the $0.6 < \cos\theta < 0.9$ slices. This would be a more elegant way to introduce energy dependence to the Gaussian corrections without having to introduce additional ad-hoc energy scaling parameters. The W forms depend heavily on the choice of nuclear spectral function, which reinforces earlier findings shown in Figure 6.5 that the outdated RFG model is rapidly becoming insufficient as higher statistics and better precision data becomes available, and even a move to a simple LFG model could drastically improve NEUT's ability to fit available data.

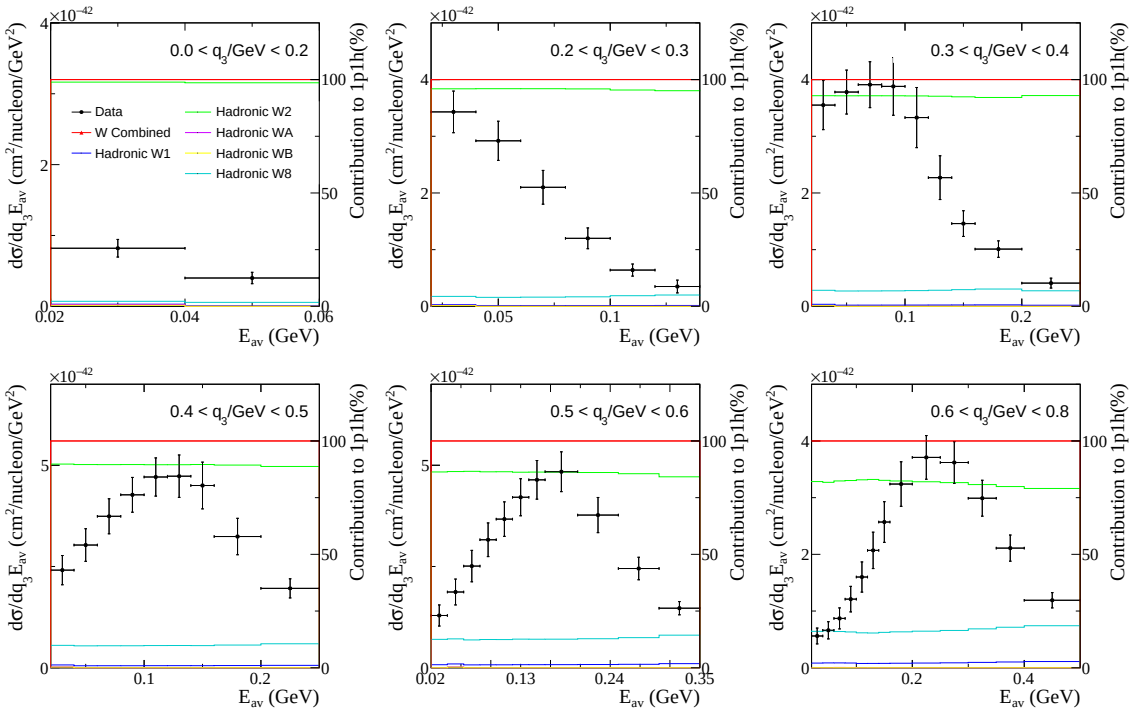

Fig. 6.15 Relative contribution from each of the W_i hadronic structure functions to NEUT's 1p1h Smith-Moniz interaction model shown in the MINERvA CC-inclusive $E_{av} - q_3$ binning. In each slice, the contributions from the W_2 structure function (green line) are dominant, with little variation as a function of E_{av}.

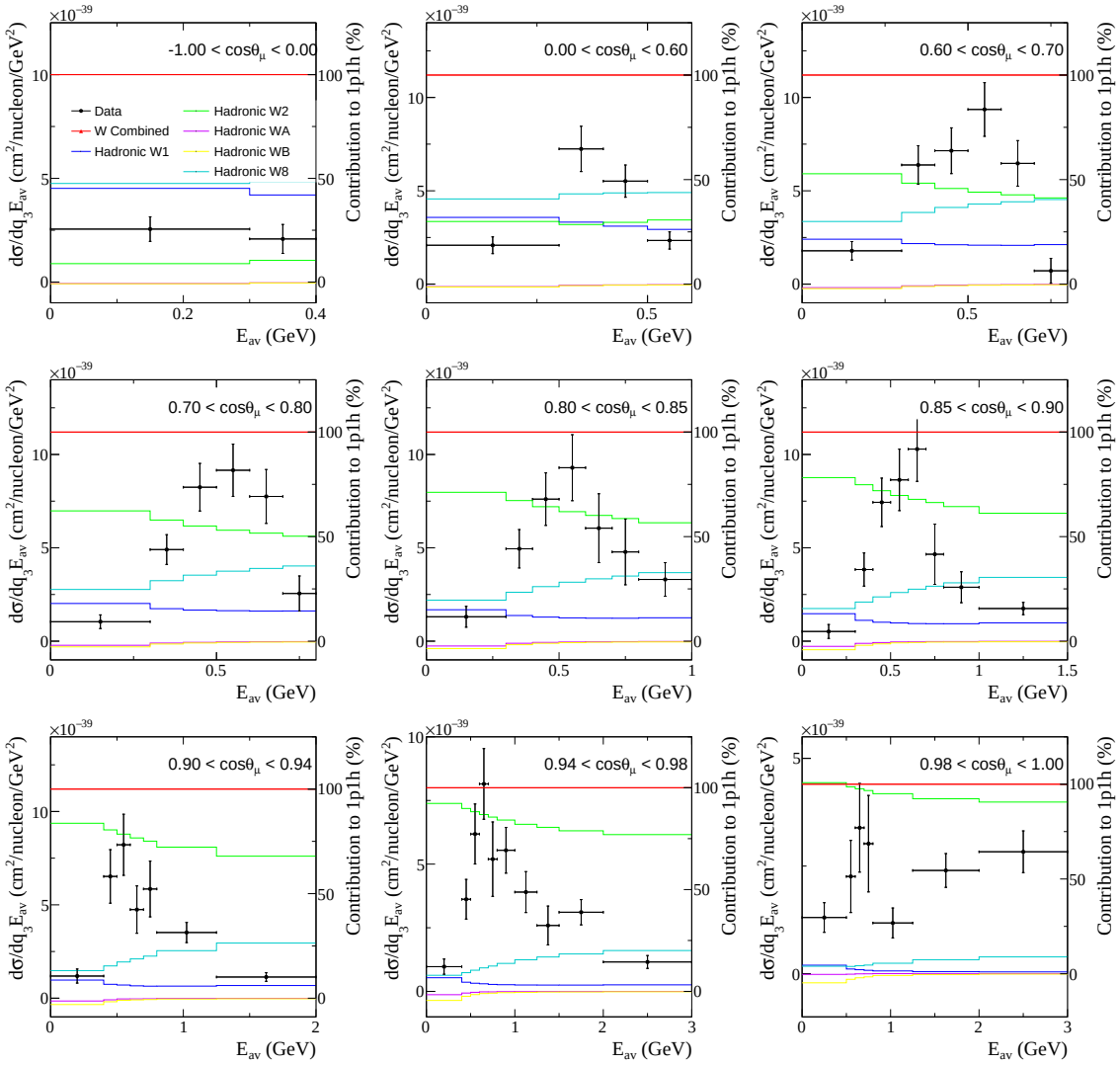

Fig. 6.16 Relative contribution from each of the W_i hadronic structure functions to NEUT's 1p1h Smith-Moniz interaction model shown in the T2K CC0π $p_\mu - \cos\theta_\mu$ binning. Comparison of this plot, to the previous figure shows that the relevance of the structure functions other than W_2 turns off at higher MINERvA energies when considering the low recoil (forward going region). A problem in the W_2 structure function could therefore introduce a large model deficiency in MINERvA that is not observed at T2K energies.

It is also possible that a similar procedure of applying ad-hoc corrections to individual 2p2h hadronic structure functions could suppress the 2p2h modifications at lower energies. Since the Nieves implementation in NEUT 5.3.6 is a simple total cross-section look-up table such a separation of the model was not possible in this analysis, but work is ongoing to implement and validate both the Nieves 1p1h and 2p2h cross-section models in NEUT 5.4.0 which would allow more freedom to develop ad-hoc modifications of this kind.

Due to the large increase in total χ^2 observed when comparing the MINERvA tuned enhancements to ND280 data the corrections extracted in these studies were deemed inappropriate for use in the T2K 2017 OA. It is clear, however, that the observed CC0π data/MC discrepancies occupy very similar regions of phase space to those seen at MINERvA and NOvA, suggesting both may be originating from the same model deficiency. This has strong implications for future T2K-NOvA joint oscillation analyses as it could introduce a correlated uncertainty that needs to be fully understood so that the correct energy dependence can be modelled and appropriate systematics can be applied.

Chapter 7

MINERvA Pion Tunings

7.1 Introduction

In recent years there has been a shift for experimental groups to release neutrino interaction cross-section measurements on nuclear targets in terms of final state topologies such as CC0π or CC1π. Whilst avoiding model dependent nuclear corrections, these releases typically have signal definitions that incorporate many different interaction channels producing the same degenerate final state. Therefore, anyone wishing to compare theoretical models to the data must ensure they also have a good description of all possible contributing channels.

Monte Carlo generators are particularly suited to this task as they can predict the interplay between each channel through the application of final state interaction simulations. The ultimate goal of a generator is to contain a consistent set of physics models whose combination is capable of reliably describing a broad range of the available neutrino scattering dataset. Unfortunately, a number of MC analyses performed on generators across multiple experiments and energy regimes have highlighted that there currently exist tensions between the T2K, MiniBooNE, and MINERvA experiments in both the CC0π and CC1π channels (for example in [62]). Models that have found good agreement with one of these experiments, often find worse agreement when compared to other experiments. A similar problem has been seen in which generator models tuned to specific kinematic regions or interaction channels do not provide adequate predictions for other channels. These issues raise concerns about the predictive powers of these generators, and a currently a model has yet to emerge that can achive a good fit to all experimental data at once [70]. As experiments move into a regime where systematic uncertainties from cross-section models are becoming dominant, these models are being tested more than ever before, and even models that once provided good agreement with a subsection of the experiments, are beginning to beak down when faced with new neutrino-nuclear cross-section data.

Differences in the neutrino flux and scattering targets between experiments make it difficult to diagnose the exact cause of observed tensions in the global data set. In particular, as results are averaged over the neutrino flux distribution, it is difficult to understand the energy dependence of an observed deficiency in any particular model, and decide how uncertainties should be propagated between different experimental energy ranges. Tensions observed when comparing a model to different measurements within a single experiment are a sign that the relative contributions from different channels in the model may be wrong. This can suggest a fundamental problem with an inclusive interaction model that should first be adressed before attempting to tackle the more difficult issue of emperically tuning a cross-section model to data from many different experiments.

This chapter describes the first NUISANCE-MINERvA tuning project aimed at extracting constraints on GENIE model parameters through joint fits to charged current pion production channels. In Section 7.1 the problem of joint fits to many datasets from a single experiment is addressed and a goodness of fit evaluation procedure is defined. Section 7.2 describes the default GENIE 2.12.6 pion production model on which these studies are based before reviewing comparisons of the model to the datasets of interest. In Section 7.3 the reweighting systematics available in GENIE are discussed, before being used to update the GENIE model predictions to reflect the ANL/BNL pion model tunings in Ref. [192]. In Section 7.4 attempts are made to empirically tune additional unconstrained systematic parameters in GENIE to improve agreement with the MINERvA data. In Section 7.5 an additional low Q^2 ad-hoc correction is added to the model to resolve observed tensions between the ANL/BNL datasets and the MINERvA data.

7.2 Defining a test statistic

To quantify how well a given model compares to published MINERvA data a joint χ^2 test-statistic was defined. When tuning to final state signal topologies there is a significant overlap between different neutrino-nucleon interaction channels, but tuning to many distributions from a single experiment at once helps to break this degeneracy and ensure all available data is accounted for when estimating model variations. MINERνA has publicly released a number of pion production datasets in recent years to aid the community in the testing of interaction models. In this work we use 4 charged-current measurements that are dominated by resonant single pion production: a ν_μCC1π^+ measurement [193], a ν_μCC$N\pi^+$ measurement [168], a ν_μCC1π^0 measurement [167], and a $\bar{\nu}_\mu$CC1π^0 measurement [168].

Each of the data releases considered in this study are available for comparison in the NUISANCE framework [194], and are summarised in Table 7.1 . In all cases the latest public release is used for each dataset. When a CC-inclusive generator sample is read by the framework, signal events are automatically selected according to each measurement's signal definition and compared to the data. To reduce biases from large statistical correlations the event selections were run over the same MC

Channel	ν_μCC1π^+	ν_μCC$N\pi^+$	ν_μCC1π^0	$\bar{\nu}_\mu$CC1π^0
N bins p_μ	8	9	8	9
N bins θ_μ	9	9	9	9
N bins T_π	7	7	7	7
N bins θ_π	14	14	11	11
N bins Total	38	39	35	36
Signal	1 FS $\pi^\pm$ 1 FS μ^- $W_{rec} < 1.4$ GeV -	> 0 FS $\pi^\pm$ 1 FS μ^- $W_{rec} < 1.8$ GeV -	1 FS π^0 1 FS μ^- $W_{rec} < 1.8$ GeV $\theta_\mu < 25°$	1 FS π^0 1 FS μ^+ $W_{rec} < 1.8$ GeV -
Ref.	[193]	[168]	[167]	[168]

Table 7.1 Summary of the measurements used in this analysis. FS corresponds to final state particle (after FSI), and W_{rec} corresponds to the reconstructed hadronic mass for the event.

event samples each time so that selected events are fully correlated between kinematic distributions according to the model.

For all these measurements, MINERvA released single differential cross-sections terms of observed kinematic quantities: p_μ, θ_μ, θ_π, T_π. This allows model comparisons to be made purely in terms of detector-level observables with reduced model biases in the data. Due to limited statistics each of these distributions was published as a standalone one-dimensional histogram with associated correlations only available between neighbouring bins in the histogram. Whilst some experiments have previously released correlations between neutrino and anti-neutrino measurements with matching signal definitions [195], at this time no measurements have yet publicly released correlations between different kinematic distributions or event topologies. This presents a serious problem for groups wishing to tune models to available neutrino data as the lack of correlations introduces a bias in the χ^2 statistic that is difficult to quantify. It is worth noting that such a problem still exists when tuning a generator model "channel-by-channel" (e.g. tuning to CC1π^+ data before tuning to CC1π^0 data in a separate fit) since the extracted model constraints will still become inputs to a single combined generator model. Hopefully in the future experiments will move to releasing correlation matrices that span many different kinematic quantities and allow model tuners to place more reliable constraints, but before then, alternative methods must be used to empirically estimate model uncertainties whilst trying to minimise these biases as much as possible.

NUISANCE uses the published data points and covariance information to automatically calculate an individual χ^2 goodness of fit for each MC prediction relative to the data. A joint χ^2 statistic for all datasets considered was calculated by summing each individual χ^2 value assuming no correlations were present between distributions. To avoid significant overcounting of the normalisation systematics in each measurement a modified χ^2 was defined by combining rate and shape-only χ^2 contributions. In each channel, the p_μ distribution was selected to set both a normalisation and a shape constraint using the full covariance provided by MINERvA. The remaining distributions, θ_μ, T_π, and θ_π, were treated as shape-only comparisons by normalising each MC prediction to

match the data's total normalisation before calculating a shape χ^2 contribution using the shape-only covariance matrix in the public data release. In cases where the shape-only covariance was not published, the shape-only covariance was manually extracted from the rate covariance. For the ν_μCC1π^0 dataset an updated covariance was provided by the MINERvA collaboration with suitable precision to extract shape-only covariances that could be reliable inverted. The joint test statistic was defined as

$$\Delta_{p_\mu,i} = d_{p_\mu,i} - m_{p_\mu,i}, \tag{7.1}$$

$$\Delta^S_{k,i} = d_{k,i} - \left(m_{k,i} \times \frac{\sum_j d_{k,j}}{\sum_j m_{k,j}} \right), \tag{7.2}$$

$$\chi^2 = \sum_{i,j}^{N_{p_\mu}} \Delta_{p_\mu,i} (M^{-1}_{p_\mu})_{ij} \Delta_{p_\mu,j} + \sum_{k=\theta_\mu,T_\pi,\theta_\pi} \sum_{i,j}^{N_k} \Delta^{S_k}_{k,i} (S^{-1}_k)_{ij} \Delta^S_{k,j}, \tag{7.3}$$

where $d_{k,i}$ is the bin content for the data in the i^{th} bin of the k^{th} distribution, $m_{k,i}$ is the bin content for the equivalent MC distribution, and N_k is the total number of bins in the k^{th} distribution. M_k and S_k are the full and shape-only covariance matrices for the k^{th} distribution respectively.

This procedure reduces the number of times the flux normalisation systematics are overcounted but does not eliminate the problem entirely. Treating p_μ distributions also as shape-only would reduce it further, at the cost of removing sensitivity to the relative strength of each channel. In addition, including both charged pion channels introduces an unknown systematic correlation bias because the ν_μCC1π^+ signal selection ($N_{\pi^+} = 1, W < 1.4$ GeV) is a subset of the more relaxed ν_μCC$N\pi^+$ selection ($N_{\pi^+} \geq 1, W < 1.8$ GeV). Unfortunately this bias cannot be resolved without additional information on the statistical correlation observed in the data so its effect has to be neglected in the total χ^2 calculation and the uncertainties extracted are likely to be slightly underestimated. Future studies could look at ways to alleviate these issues by placing a single flux constraint using the integrated cross-section of all samples combined, or by trying to estimate the maximum statistical correlations from the analysis of a large range of different generator models. In any case such procedures will ultimately be limited by the lack of sufficient information available in the data and the problem will only be truly resolved by a shift in the experimental community to a data release method that allows statistical and systematic correlations between bins to be reliably tracked across all channels.

7.3 Default Pion Production Model in GENIE

The GENIE event generator is used by a number of experiments to describe neutrino interactions on a broad range of targets [66], and is currently the default Monte-Carlo generator for the MINERvA

experiment. A number of measurements performed by MINERvA have relied on either GENIE version 2.6.2 or version 2.8.4 to simulate signal and background MC events. This study instead focus on GENIE version 2.12.6 as this was the latest official release at the time, benefiting from various generator improvements and new model implementations. Between GENIE 2.6.2 and 2.8.4 a number of different interaction channels were added such as nucleon decay and inverse muon decay, however for the purpose of this pion production tuning analysis, the default model in these versions can be considered almost identical. When moving to GENIE 2.12.6 the default model is again very similar. This version uses a single nuclear spectral function model to describe the nucleon momentum distributions for all interactions. In the default model the Bodek Ritchie RFG distribution [102] is used, including an additional high momentum tail due to short range nucleon correlations.

To simulate pion production an implementation of the Rein-Sehgal (RS) model is used, with an invariant mass cut of $W < 1.7$ GeV [82]. The notable difference between GENIE 2.8.4 and 2.12.6 is that in older version of GENIE pions were ejected isotropically in the rest frame of the nucleon. However, in 2.12.0 onwards pions are ejected based on the angular distribution of the Rein-Sehgal model by default. The effect of the lepton masses is taken into account when calculating the possible phase space but is neglected in the full cross-section calculation. An in depth review of the GENIE single pion production model is given in Chapter 2. In addition to pion production of a single nucleon in a nucleus, it is also possible for a neutrino to produce a pion by scattering coherently off the nucleus as a whole. GENIE uses the Rein-Sehgal coherent model to describe coherent pion production with lepton masses included in the calculation [196]. Note that a newer Berger-Sehgal implementation [191] is available in GENIE 2.12.6 but is not switched on by default; it predicts a smaller cross-section than the default Rein-Sehgal implementation.

A number of models are available to describe CCQE scattering in GENIE 2.12.6, but their choice has little impact on the pion production channels at MINERvA. In these studies we use the suggested "DefaultPlusValenciaMEC" model as this is the closest combination to the modifed GENIE 2.8.4 models considered by MINERvA in their low recoil analysis [113]. This combination, which is referred to as "Nominal" in the text, uses a Bodek-Ritchie RFG distribution, the Smith-Moniz model for 1p1h scattering [190], and the Valencia model for 2p2h interactions [104], alongside the default Rein-Sehgal based GENIE model for pion production.

With each GENIE version a set of pre-generated splines is provided which contains the total cross-section for every possible interaction mode as a function of neutrino energy. These splines, combined with the configurations used to generate them, mean that simulations can be ran with a set of model configurations that have been approved by the GENIE collaboration. In all cases throughout this work, the official GENIE 2.12.6 splines and configuration files were used when generating events for comparison to the data. To compare the default GENIE model to data, 2.5 million events were generated for the MINERvA flux predictions in muon neutrino and antineutrino

mode using the official GENIE splines. These were then processed by NUISANCE so that the model could be overlaid with the MINERvA datasets.

The MC predictions seperated by vertex level interaction topology (before FSI) are shown in Figure 7.1. In the case of the shape-only datasets ($\theta_\mu, T_\pi, \theta_\pi$) the shape-only $\chi^2/NDOF$ calculation is shown in the legend. In the nominal model the shape of the p_μ distributions agree well with the data for all measurements: however, the model overestimates the total cross-section for charged pion production and as a result the $\chi^2/NDOF$ for the CC1π^+ and CCNπ^+ p_μ datasets is large.

When comparing the total rates in the p_μ distributions it is clear that the default model describes the total normalisation of $\bar{\nu}_\mu$CC1π^0 and ν_μCC1π^0 channels well, whilst overestimating the charged pion distributions. For all plots other than the p_μ distributions, the shape of the spectrum (red line) should be compared to the data as this prediction is used to calculate the total χ^2 for those distributions. In the muon angular distributions the shape of the MC model was found to overestimate the data below $\theta_\mu < 5^\circ$ for all channels. When comparing just the shape distributions, however, the ν_μCC1π^+, ν_μCC$N\pi^+$, and $\bar{\nu}_\mu$CC1π^0 channels agree despite still showing a very slight overestimation in the low angle region. In comparison the ν_μCC1π^0 channel has missing strength at high θ_μ that means the shape comparison exaggerates the low angle discrepancy and the channel has a much worse $\chi^2/NDOF$.

The ν_μCC1π^+ pion kinetic energy prediction's shape agrees well with the data, producing the lowest $\chi^2/NDOF$ for the T_π distribution out of all of the samples. Despite encompassing many of the ν_μCC1π^+ events the ν_μCC$N\pi^+$ sample has a worse fit to the data. When separating by true interaction channels it is clear that at high T_μ there is a large overestimation of the data. Since the ν_μCC$N\pi^+$ pion distributions are a summation over all observed pions (one histogram fill for every π^+ in the final state) it is possible that the distribution of kinetic energy in the final state needs to be redistributed for ν_μCC$N\pi^+$ events. The neutral pion channels show a similar disagreement at low T_π which could also be resolved if pions exiting the nucleus had a lower kinetic energy on average.

Finally, when comparing the pion angular distributions it appears that GENIE produces charged pions at too high angles in the ν_μCC1π^+ channel. In contrast the ν_μCC$N\pi^+$ channel does not observe this disagreement, despite their similar signal definitions. A modification of the angular distribution of single pion production would be required to resolve this discrepancy either by greatly enhancing CC1π^+ on n interactions or by modifying the angles that pions are initially ejected at the vertex in the nucleus.

Each of the measurements are overlaid as MC/data ratio distributions in Figure 7.2. So that the distributions better describe the contributions to the total χ^2 the shape-only datasets (θ_μ,θ_π, T_π) were normalised to match the data before the ratio was taken and the error bars reflect the extracted shape-only uncertainties on the data. The shape of the ν_μCC1π^+ and ν_μCC$N\pi^+$ datasets follow similar behaviour to one another, as well as the shape of the ν_μCC1π^0 and $\bar{\nu}_\mu$CC1π^0 datasets. There is a divergence at low θ_μ where GENIE predicts the shape of the neutral pion channels to

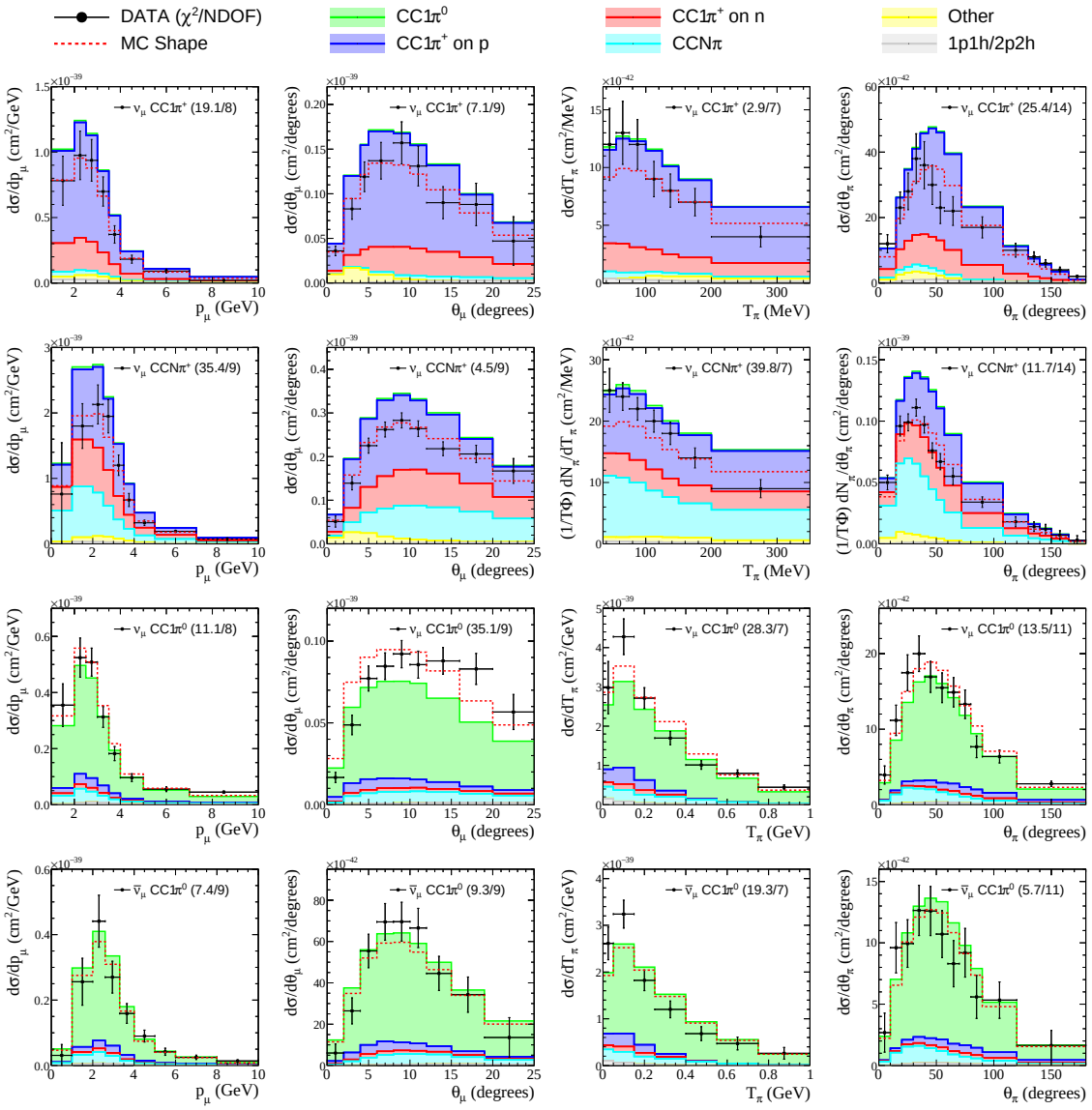

Fig. 7.1 Default GENIE 2.12.6 model predictions compared to MINERvA datasets considered in this analysis. The coloured topologies seperate the events by vertex level interaction types before FSI. "Other" corresponds to a combination of remaining interactions, but is dominated by coherent pion production. Each row corresponds to a single measurement, whilst each column corresponds to a single kinematic distribution. The default GENIE model was found to overestimate the charged pion production channels. Whilst the shape of the p_μ distributions seems to be correct (red dashed line), there are larger shape disagreements in all other plots.

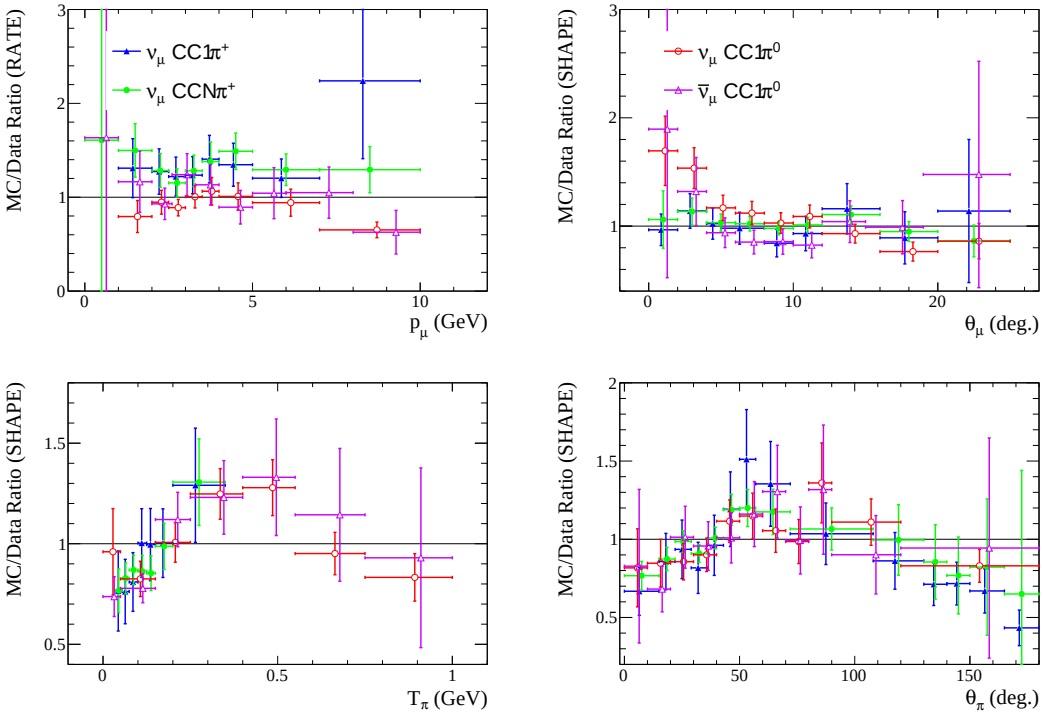

Fig. 7.2 MC/data ratios for the GENIE Nominal model predictions. The p_μ distribution is treated as a rate comparison in the χ^2 comparison so a ratio is taken between the absolute MC prediction and the data. The other distributions are treated as shape-only so the MC is scaled to match the data normalisation before the ratio is taken and the uncertainties are the extracted shape-only data error bars. When comparing the data this way several trends become apparent. An overestimation is seen for all channels at both $T_\pi \sim 0.3$ GeV and at $\theta_\pi \sim 50$ deg. In addition the neutral pion predictions both overestimate the shape of the data at low θ_μ.

peak at lower angles than the data suggests. In the pion kinematic distributions all channels follow a similar trend that suggests the need for the T_π spectrum to be shifted to lower energies in GENIE and for the angular distribution of pions to be shifted to lower angles.

7.4 GENIE Modelling Systematics

One significant strength of the GENIE event generator is its ability to perform sophisticated systematic analysis through the GENIE ReWeight package. A large range of different event weighting 'dials' are included with each release that allow systematics to be evaluated by calculating the shift in the cross-section for a given model change relative to the nominal model prediction.

Experiments often use the charged-current resonant axial mass, M_A^{RES} (*MaCCRES*), as a systematic to vary both the normalisation and Q^2 shape of resonant interactions alongside a total resonant cross-section normalisation dial, NormRES (*NormCCRES*), which approximates the behaviour of

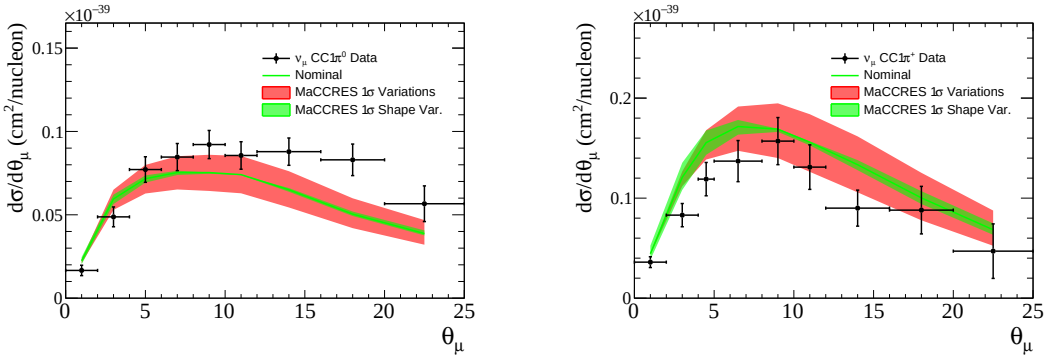

Fig. 7.3 Examples of the effect varying the $M_{\mathrm{A}}^{\mathrm{RES}}$ dial has on the Default GENIE model predictions. The red bands highlight the variation to the MC predictions total rate and shape. The green variation bands are obtained by normalising the reweighted curves to the nominal prediction to highlight the smaller effect the dial has on the shape of the distributions. These error bands were produced using the NUISANCE framework.

varying $F_A(0)$ in the axial form factor within the Rein-Sehgal model. Since low θ_μ correlates with low Q^2, variations in $M_{\mathrm{A}}^{\mathrm{RES}}$ have the largest effect on the shape of the muon angular distributions as shown in Figure 7.3, but also have a small effect on the T_π spectrum.

Several dials are available to vary the normalisation of each of the non-resonant channels in GENIE (e.g. *NonRESBGvnCC1pi, NonRESBGvpCC1pi*) but each dial was found to introduce very similar modifications to the shapes predictions. Therefore, to reduce the number of free parameters in this study, all the dials were grouped into a single background scaling for non-resonant 1π production (NonRES1π) following the approach considered in Ref. [192]. A similar treatment of grouping the dials was also applied to non-resonant 2π production (NonRES2π) and neutrino and antineutrino were assumed 100% correlated in both cases. The effect of varying the non-resonant normalisations is shown in Figures 7.4 and 7.5. A 1σ modification corresponds to a 50% variation of the non-resonant background, but since contributions are relatively small compared to the dominant resonant contributions, the variation in the total rate for each channel is also small, with the neutral pion channels seeing the largest effect. Variations in the NonRES2π dial introduced a large shift in normalisation for the $\nu_\mu \mathrm{CC}N\pi^+$ channel as expected but were also found to introduce small changes in the other single pion channels by modifying the small fraction of multi-pion events present in those samples.

Recently re-analysed data from ANL and BNL was used to empirically tune GENIE's single pion production model on free nucleons [192, 197]. A simultaneous fit to E_ν and Q^2 data for $CC1p1\pi^+$, $CC1n1\pi^+$, and $CC1\pi^0$, channels was used to extract constraints on the $M_{\mathrm{A}}^{\mathrm{RES}}$, NormRES, and NonRES$1\pi$ in GENIE. The studies found that a small shift in $M_{\mathrm{A}}^{\mathrm{RES}}$ was required to model the low Q^2 region and a large suppression of the non-resonant background (by $\sim 50\%$) amplitude was required to predict the strengths of the $CC1n1\pi^+$, and $CC1\pi^0$ channels correctly. The updated

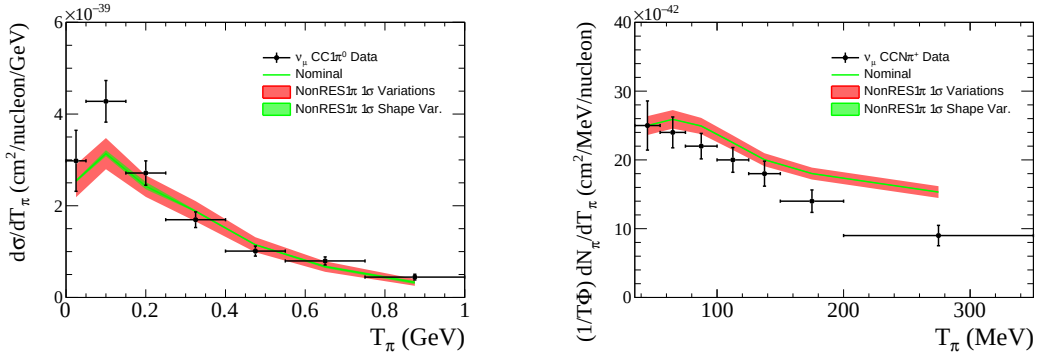

Fig. 7.4 Examples of the effect varying the NonRES1π dials has on the Default GENIE model predictions. The red bands highlight the variation to the MC predictions total rate and shape. The green variation bands are obtained by normalising the reweighted curves to the nominal prediction to highlight the smaller effect the dial has on the shape of the distributions. These error bands were produced using the NUISANCE framework.

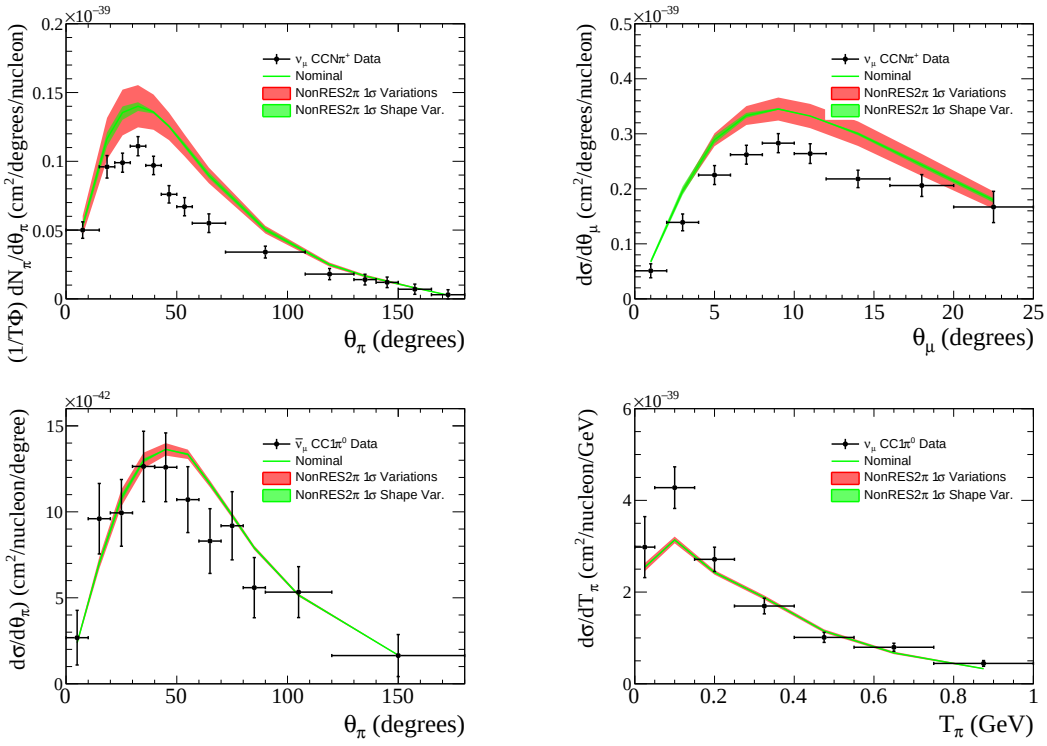

Fig. 7.5 Examples of the effect varying the NonRES2π dials has on the Default GENIE model predictions. The red bands highlight the variation to the MC predictions total rate and shape. The green variation bands are obtained by normalising the reweighted curves to the nominal prediction to highlight the smaller effect the dial has on the shape of the distributions. These error bands were produced using the NUISANCE framework.

Model	GENIE default	ANL/BNL Tune
M_A^{RES}	1.12 ± 0.22	0.94 ± 0.05
NormRES	100 ± 20	115 ± 7
NonRES1π	100 ± 50	43 ± 4

(a) Tuning Results

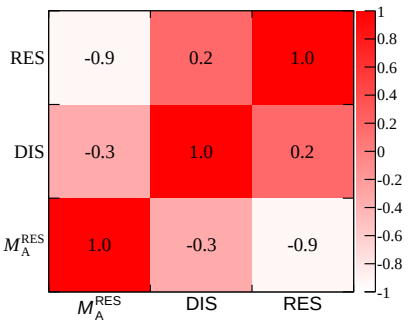

(b) Parameter Correlations.

Fig. 7.6 Results from the ANL/BNL GENIE pion production tunings taken from Ref [192]. A large suppression of the NonRES1π background and M_A^{RES} was required to achieve a good fit to the ANL/BNL data. The correlations were provided so that the results could be included as a χ^2 penalty in subsequent GENIE model tunings. "DIS" refers to the NonRES1π normalisation which, in GENIE, is derived from deep inelastic scattering being propagated down to $W < 2.3$.

parameter tunings obtained in Ref. [192] are shown in Table 7.6a and the associated correlations are shown in Figure 7.6b.

This pion model tuning has been adopted by both MINERvA and NOvA in their ongoing analyses as it has been shown to improve agreement in the delta-dominated region of their CC-inclusive analyses [113, 189]. Historically there have been several tensions become apparent when moving between deuterium scattering data and neutrino scattering on nuclear targets, and disagreements in heavier target experiments are generally taken as a sign that a model is missing additional nuclear effects not present in deuterium scattering measurements. Therefore, care must be taken that the shift to updated model tunings from deuterium data is capable of describing all available interaction data from an experiment.

Figure 7.7 shows the updated MC predictions when the default GENIE model has been reweighted to reflect the parameter changes shown in Table 7.6a. The contributions to the total χ^2 for each distribution are shown in Table 7.9. Since no correlations are available between samples it is likely that the joint test-statistics does not follow a χ^2 distribution with the quoted NDOF. Because of this the total χ^2 is suitable for comparing different models to one another but should not be used to estimate the model's agreement with all datasets at once. The individual contributions calculated from the full or shape-only covariance, however, still give a reasonable idea of the models agreement with a given individual dataset. The CC1π^+1p channel at ANL sees much smaller contributions from non-resonant backgrounds compared to the CC1$\pi 1n$ and ν_μCC1π^0 channels, but at MINERvA the final state topology measurements are insensitive to the type of struck nucleon and all measured channels are sensitive to the suppression of the NonRES1π parameter. In the charged pion case this improves the total normalisation agreement and the χ^2 contributions for p_μ datasets shown in Table 7.9 are improved. For the $\bar{\nu}_\mu$CC1π^0 channel this change improves the χ^2 for the p_μ dataset but surprisingly the same is not true for the ν_μCC1π^0 channel despite the

Distribution	Channel	NBINS	Default χ^2	ANL/BNL Tune χ^2
p_μ (Rate)	ν_μCC1π^+	8	19.1	14.4
	$\bar{\nu}_\mu$CC1π^0	9	7.4	6.1
	ν_μCC$N\pi^+$	9	35.4	20.8
	ν_μCC1π^0	8	11.1	18.9
θ_μ(Shape)	ν_μCC1π^+	9	7.1	16.3
	$\bar{\nu}_\mu$CC1π^0	9	9.3	15.4
	ν_μCC$N\pi^+$	9	4.5	12.0
	ν_μCC1π^0	9	35.1	65.5
T_π (Shape)	ν_μCC1π^+	7	2.9	2.7
	$\bar{\nu}_\mu$CC1π^0	7	19.3	17.9
	ν_μCC$N\pi^+$	7	39.8	36.2
	ν_μCC1π^0	7	28.3	31.5
θ_π (Shape)	ν_μCC1π^+	14	25.4	26.8
	$\bar{\nu}_\mu$CC1π^0	11	5.7	5.8
	ν_μCC$N\pi^+$	14	11.7	11.2
	ν_μCC1π^0	11	13.5	15.9
All	All	148*	275.6	317.6

Table 7.2 χ^2 comparisons values for the nominal GENIE model and the ANL/BNL single pion tuning seperated by each kinematic distribution considered in this analysis. The "Default" column shows the χ^2 results when the Default GENIE model is compared to all datasets. The "ANL/BNL Tune" column shows the χ^2 results when the updated GENIE model, after it has been reweighted to the ANL/BNL bubble chamber pion production tuning parameter set, is compared to all datasets. For all datasets other than the p_μ datasets, the shape-only χ^2 statistic is shown.

ANL/BNL tunings neglecting antineutrino data. The modification of M_A^{RES} distorts the θ_μ spectrum so that now the MC predicts larger contributions at lower angles than the data suggests and the χ^2 contributions from the θ_μ distributions are increased significantly for all channels as shown in Figure 7.8.

The systematic variations considered are capable of modifying the total normalisation of resonant/non-resonant terms and distorting the Q^2-shape of the pion production model, but have no freedom to modify the pion kinematic distributions directly. The small fluctuations in the predictions and total shape χ^2 contributions from θ_π and T_π are a result of the low angle, low pion energy bins having a slightly higher proportion of low-Q^2 events. It is clear from these comparisons that the ANL/BNL tunes are not all that is required to achieve a satisfactory fit to the MINERvA pion production data and actually introducing them as fixed model constraints produces an increase in the total χ^2. It is therefore necessary to introduce additional systematic variations that are unconstrained by the ANL/BNL tunes to try and rectify these issues. A large selection of GENIE reweight dials were studied before candidates for introducing additional freedom were chosen based on their ability to modify the shape predictions and their efficiency.

From version 2.12.0 onwards GENIE has simulated the non-isotropic ejection of pions in delta decays using calculations from the Rein-Sehgal model by default. A systematic dial, Theta$-\pi$

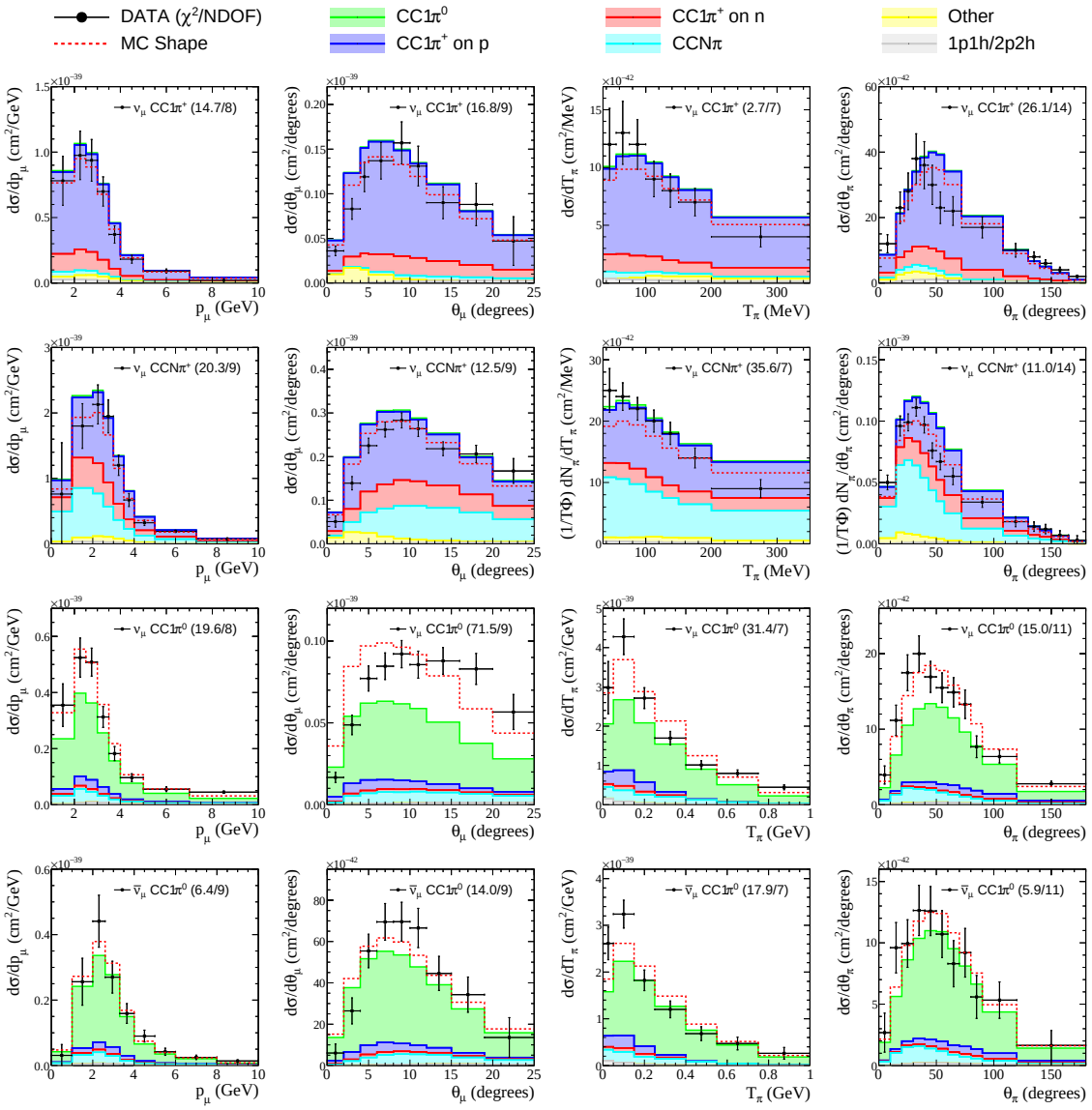

Fig. 7.7 GENIE ANL/BNL single pion tuning model predictions compared to MINERvA data. The distributions have been weighted to the ANL/BNL tuning parameter set before being overlaid with the NUISANCE framework. When comparing these predictions to that shown in Figure 7.1, the updated bubble chamber tuning parameters are not a significant improvement over the Default GENIE model. Whilst the updated parameters improve agreement in the charged pion channels, the total normalisation, and in turn the agreement with the data, for the neutral pion channels is severely reduced.

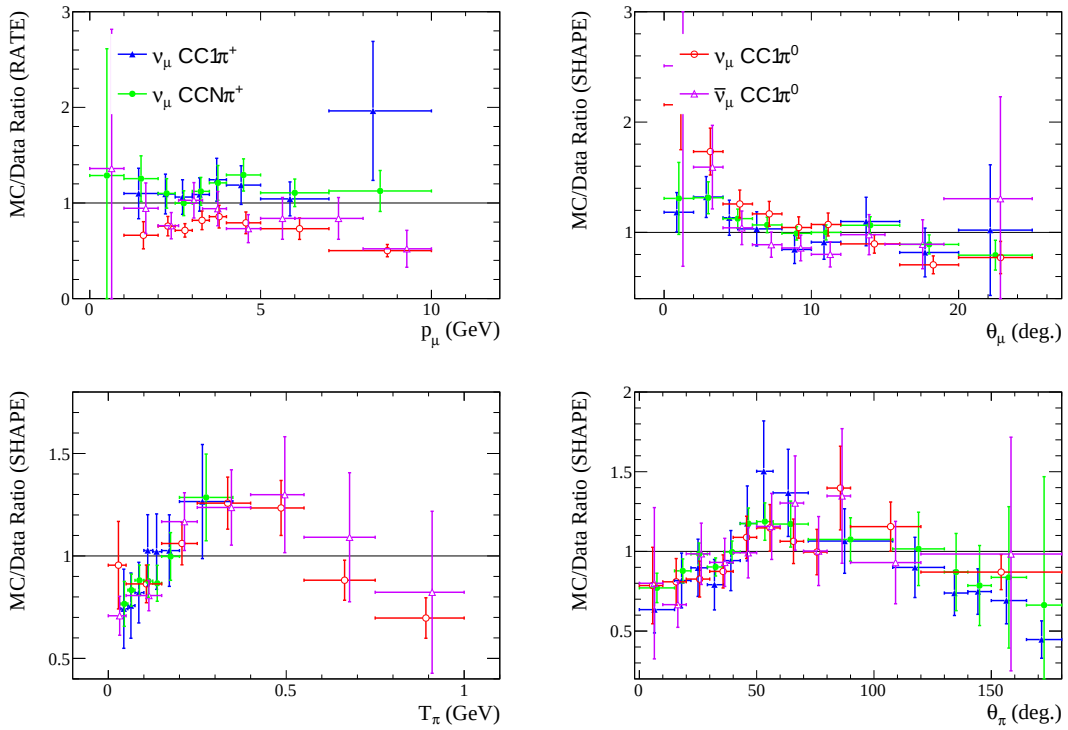

Fig. 7.8 GENIE ANL/BNL Tuning MC/data ratios. Each MC distribution was reweighted to the ANL/BNL single pion tuning parameter set before a ratio with the data was taken. No significant improvement is found when moving to the ANL/BNL tunings, and at low θ_μ the models overestimation of the data is further exaggerated.

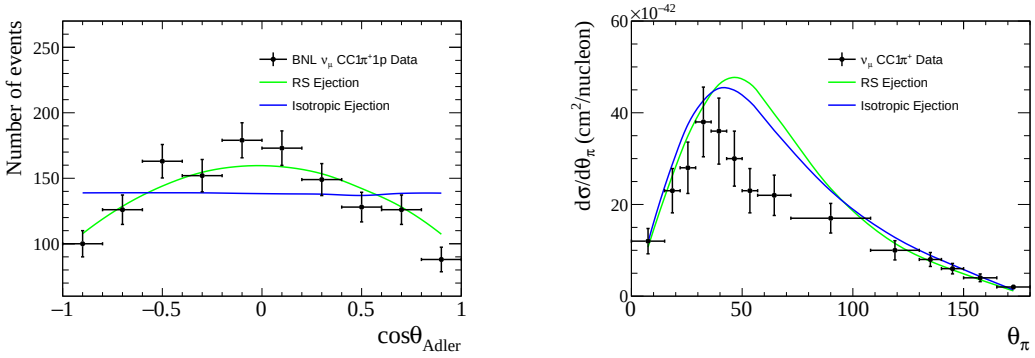

Fig. 7.9 Effect of varying the Theta$-\pi$ dial on pion angular distributions at BNL (left) and MINERvA (right). The preference for non-isotropic (RS) ejection in GENIE 2.12.0 onwards is based on comparisons to datasets such as the BNL distribution shown here.

(*Theta_Delta2Npi*), is available that allows events to be reweighted continuously between the default prediction and one where pions are ejected isotropically in the rest frame of the resonance so that systematics can be evaluated for the pion angular distributions. Moving to isotropic ejection slightly improves the data/MC agreement in the θ_π distributions at MINERvA but severely reduces agreement with the ν_μCC1π^+ data from BNL shown in Figure 7.9. The BNL Adler angle distributions (angle of the pion with respect to the three momentum transfer in the resonance rest frame) are only available for CC1π^+1p states and it has been suggested that including higher order resonances in the RS phase space calculation for the CC1π^+1n and CC1π^0 channels produces flatter angular distributions than models that consider only a single resonance [198]. GENIE only uses the $\Delta(1232)$ resonance in the calculation and it is possible that extending the model to higher resonances could improve the angular agreement.

The systematics considered so far correspond to vertex level interaction properties on a nucleon. When comparing generator models to data on carbon there exist additional systematics due to the presence of the nuclear medium that cannot be constrained by the ANL/BNL deuterium data. The GENIE hA model has associated uncertainties on each of the pion interaction cross-sections that reflect the precision of available $\pi - A$ data the model was tuned to. The total pion cross-section is significantly more constrained than each of the individual interaction cross-sections, so the GENIE FSI reweighting provides dials to vary the fraction of each possible interaction whilst keeping the total pion cross-section constant. The available fractional dials are elastic (FrElas), absorption (FrAbs), charge exchange (FrCEx), pion production (FrPiProd), and inelastic scattering (FrInel). Charge exchange and pion production FSI channels contribute small amounts to the MINERvA MC predictions and the elastic dial has a strong prior constraint from $\pi - A$ data so all three were neglected.

To maintain agreement with the $\pi - A$ data when varying an FSI dial, GENIE forms a series of "cushion" terms from the remaining dials that float to preserve the total pion scattering cross-section. When testing different FSI dial combinations this cushioning procedure was found to introduce

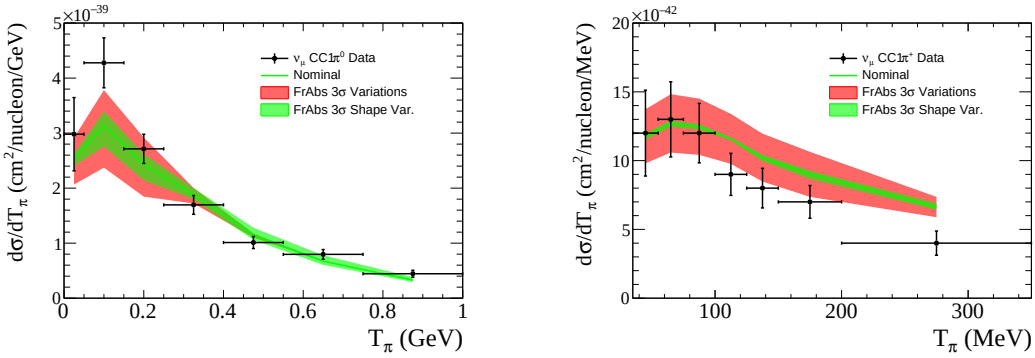

Fig. 7.10 Effect of varying the FrAbs dial on the default GENIE model predictions. A 3σ variation of the FrAbs dial corresponds to $\pm 90\%$ of the nominal pion absorption cross-section. Whilst total normalisation variations were large, shape variations introduced by this dial were found to be small. The largest shape variation was observed in the ν_μCC1π^0 T_π distribution.

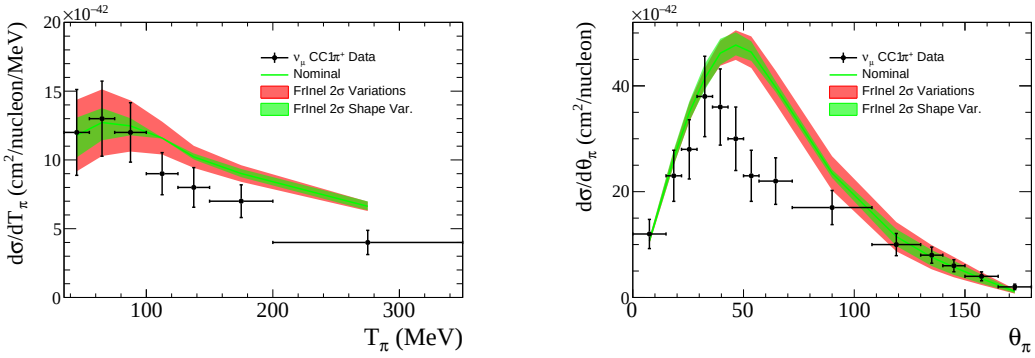

Fig. 7.11 Effect of varying the FrInel dial on the default GENIE model predictions. A $\pm 2\sigma$ variation of the FrInel dial corresponds to $\pm 80\%$ of the nominal inelastic pion scattering cross-section. This dial was found to have the largest effect on the ν_μCC1π^+ channel.

small instabilities in the event weights that made systematic reweighting of more than one FSI dial at a time unstable. To avoid these issues only a single FSI dial was varied at any one time with the remaining dials treated as cushion terms. Examples of the effect that the FrAbs and FrInel dials have are shown in Figure 7.10 and 7.11. The FrAbs dial introduces significant normalisation shifts in the $\bar{\nu}_\mu$CC1π^0 and ν_μCC1π^0 channels at low T_π. The FrInel dial in contrast produced a pile up at low T_π in the charged pion channels, whilst also introducing shifts in the shape of the θ_π spectrum. In both cases large fluctuations on the order of $\pm 3\sigma$ (close to being unphysical) were required to produce any significant shape distortions.

Previous studies by MINERvA have also found that the RS coherent pion production model needs to be suppressed by $\sim 50\%$ at $T_\pi < 500$ MeV to agree with data [195]. The ν_μCC1π^+ channel sees a small contribution from coherent production at very low Q^2 as shown in Figure 7.12. Modifications of the coherent model were found to have only a small effect on the studies in this chapter (most

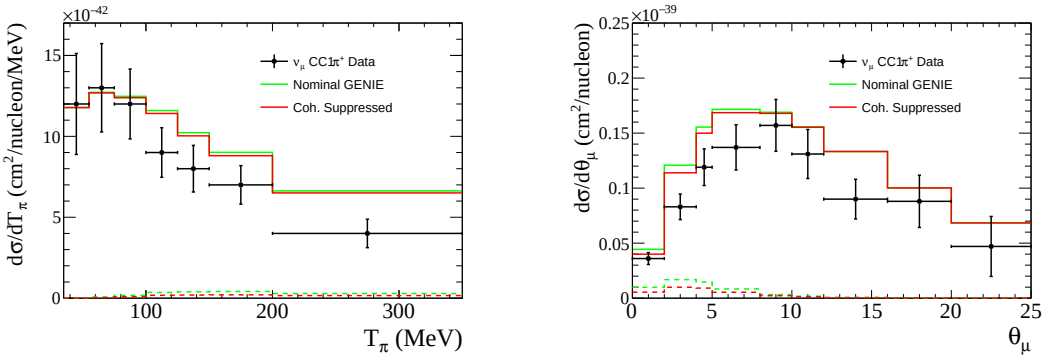

Fig. 7.12 Modification of the ν_μCC1π^+ distributions with the ad-hoc suppression of coherent pion production in Ref. [195]. Coherent scattering occurs at very low Q^2 so the dominant effect is in the lower θ_μ bins. The CCπ^0 channels are unaffected by this variation.

notably in the last section) but they are included in all tunings[1] to maintain a model similar to that currently being used by MINERvA.

One generator systematic that is difficult to quantify through event reweighting is the effect of varying the underlying nuclear model since the distribution of initial state nucleon momenta and binding energies can introduce shifts in the predicted phase space. In GENIE 2.12.6 a number of suggested alternative model combinations were released with pre-generated cross-section splines available. To evaluate the effect of switching between models, 2.5 million events were generated for each combination before being processed in NUISANCE. In large event samples greater than 2 million, statistical uncertainties are small. Note that due to the design of the NUISANCE framework the event selections and processing of the samples are identical so that observed differences are purely due to changes in the underlying physics within GENIE.

The model referred to as "nominal" GENIE throughout this work is the recommended "Default-PlusValenciaMEC" combination obtained from [199]. The "LFG+ValenciaMEC" model shown in Figure 7.13 differs from this by using a local Fermi gas implementation instead of the default Bodek Ritchie RFG. The "AltPion" model uses the updated Berger-Sehgal pion production implementation for both resonant and coherent interactions with a RFG base nuclear model [200]. The form factors for this have been tuned to MiniBooNE pion production data and the calculation includes lepton mass terms. The "ValenciaBergerSehgalCOHRES" model (labelled as "Val+Berg" in the text) is similar to the "AltPion" physics combination but again uses a LFG implementation instead of the Bodek Ritchie RFG and also uses the latest GENIE "hA" effective cascde FSI model tuning. Finally the "EffSFTEM" model uses the default RS implementation but describes the nucleus with the effective spectral function model [97] and uses the transverse enhancement model [101] to describe 2p2h interactions (the choice of 2p2h models has only a small effect in the pion production data). A comparison of each model to the available MINERvA data is shown in Figure 7.13.

[1] including the ANL/BNL tuning comparisons

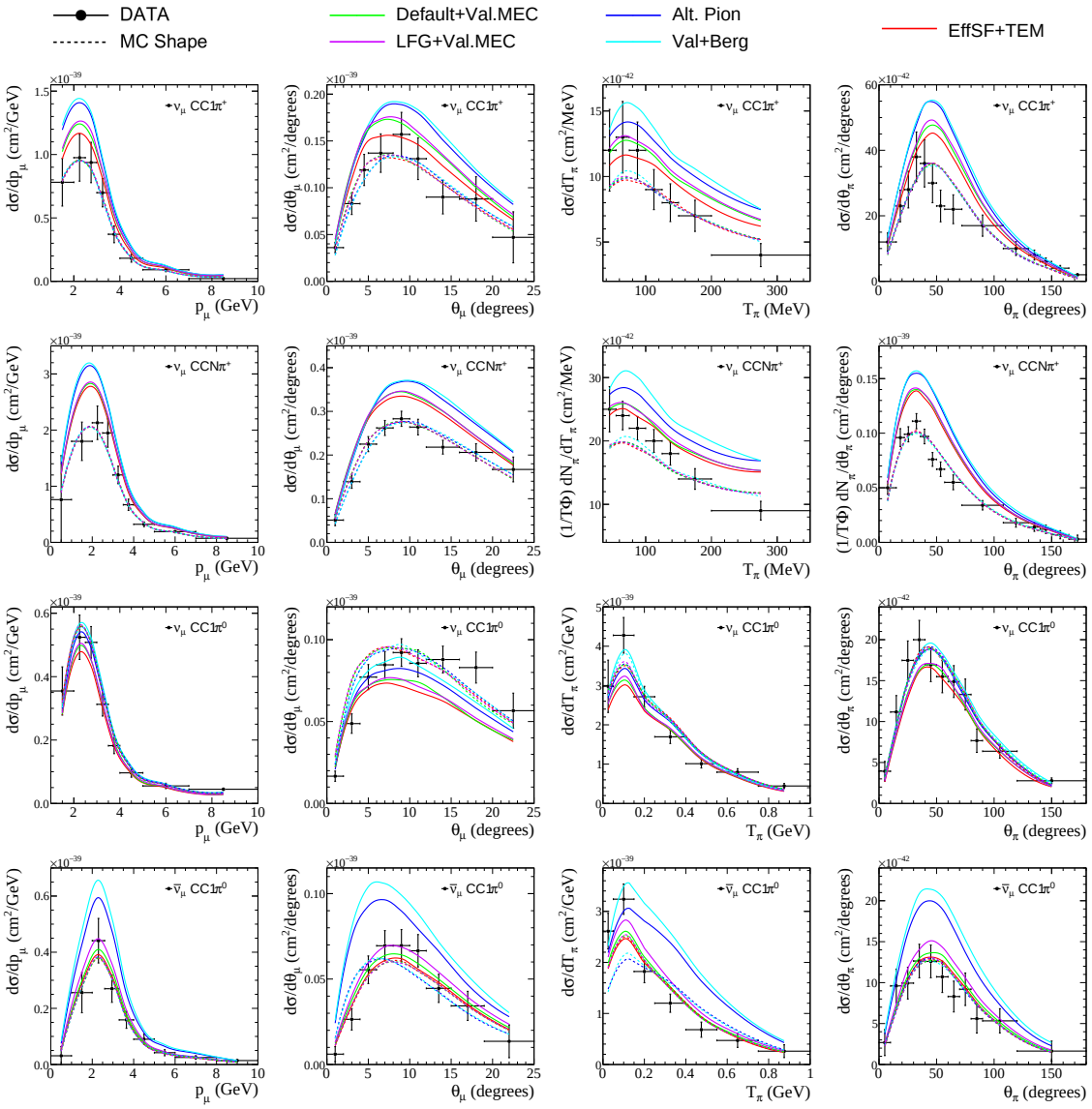

Fig. 7.13 Comparison of the different approved GENIE 2.12.6 models with which official model splines were released. Shape comparisons where the prediction has been normalised to match the total integrated cross-section of the data histogram are shown in dashed lines. "Default+Val.MEC" corresponds to the RFG based "DefaultPlusValenciaMEC" model treated as GENIE "nominal" in these studies. There is no clear model that is favoured by the data, with some of the latest models added to GENIE actually achieving far worse agreement with the MINERvA datasets under consideration.

Changing between combinations was found to introduce large shifts in the total normalisation of channels, but shape variations, shown as dashed lines in Figure 7.13, were relatively small. Moving between an RFG and LFG or EffSF based Rein-Sehgal model caused only small shifts in the total normalisation of channels with negligible shape modifications. The alternate Berger-Sehgal model predicted much larger cross-sections than the RS based models, giving a better fit to the total normalisation of the ν_μCC1π^0 channel but severely overestimating the others. It also predicted a slightly improved T_π spectrum that is shifted to higher angles for the neutrino channels but unfortunately introduces an opposite shift to the $\bar{\nu}_\mu$CC1π^0 channel, further exaggerating the shape disagreement in the θ_μ distribution. A similar behaviour is seen in the T_π distributions where the shape of the neutrino channels remain unaffected, whilst the $\bar{\nu}_\mu$CC1π^0 distribution is flattened. An even larger shift was observed when moving to the "Val+Berg" model due to the updated FSI model producing small distortions in the shape of the neutrino T_π distributions that were unable to correct the poor shape agreement in the $\bar{\nu}_\mu$CC1π^0 channel. No change in shape was observed for the p_μ or θ_π channels, but the latter is not surprising given that all combinations rely on the same angular ejection model.

Since the alternative pion models showed a clear overestimation of the data in many channels we instead chose to use the default RS pion production model (referred to as "Default+Val.MEC") whilst also including the ad-hoc MINERvA coherent correction as this is already in use by a number of experiments and has a pre-existing set of ANL/BNL tuning priors that can be applied to it. Future iterations on these studies could evaluate the shift in model parameters when using different base nuclear or pion production models.

7.5 Tuning the GENIE Model

An initial analysis of fixed MC comparisons has shown that the data prefers the nominal GENIE model despite these parameters being strongly disfavoured by the ANL/BNL tunings. It is possible however that the tunings shown in Ref. [192] give an acceptable description of free nucleon scattering in GENIE but that additional modifications to other parameters unconstrained by ANL and BNL are required to reliably fit both experiments simultaneously.

Instead of fixing the 3 parameters $M_{\mathrm{A}}^{\mathrm{RES}}$, NormRES, and NonRES1$\pi$ at their ANL/BNL best fit values we treat them as free parameters in a fit with a prior penalty term applied. Including it in this way ensures the information from ANL and BNL is included in the tuning but also allows the parameters to pull away from the priors if the MINERvA data strongly disagrees with them. The penalty term uses the covariance, M, shown in Figure 7.6b to include an additional χ^2 contribution in the fit as

$$\chi^2_{PEN} = \sum_{ij}^{N=3} (p_i - f_i) \left(M^{-1}\right)_{ij} (p_j - f_j) \tag{7.4}$$

Parameter	Starting Value	Lower Limit	Upper Limit
$M_{\mathrm{A}}^{\mathrm{RES}}$ (GeV)	1.10	0.50	1.70
NormRES (%)	100	10	190
NonRES1π (%)	100	0	300
NonRES2π (%)	100	0	300
Theta$-\pi$ (σ)	0	0	1
FrAbs (%)	100	0	190
FrInel (%)	100	0	220

Table 7.3 GENIE parameter tuning limits. These limits were all chosen to stop the GENIE model moving into unphysical parameter spaces during the fit. In cases where a best fit is found at a limit for any parameter, NUISANCE fixes the parameter at the limit and reruns the fit to ensure a stable minimum is found with appropriate errors on the remaining parameters.

where p_i is the value of parameter i at each iteration of the fit, and f_i is the best fit result for that parameter taken from Figure 7.6a. Including the penalty in this way also means the information from ANL and BNL can be included without having to explicitly make predictions for those datasets at each iteration of the fit. The GENIE nominal model is strongly disfavoured with $\chi^2_{PEN} = 299.2$ whilst a model with NonRES1$\pi = 43\%$ and the other parameters left at nominal has a reduced penalty of only $\chi^2_{PEN} = 21.8$. This is a result of strong anti-correlations between $M_{\mathrm{A}}^{\mathrm{RES}}$ and NormRES in M, and weak correlations between these parameters and the NonRES1π parameter.

To allow the fit to rectify disagreements that are not covered by these three parameters we add additional GENIE dials. The Theta-π dial is included so that the fit can directly modify the pion angular distribution if it wishes. Ideally this variation should only be applied to the channels unconstrained by ANL/BNL, but since there is no way to currently split the dial in GENIE it is applied to all channels. Theta-π is treated as completely free in the fit in the range $0.0 - 1.0\sigma$ corresponding to a continuous variation between RS and Isotropic ejection. To avoid normalisation issues in the ν_μCC$N\pi^+$ channels pulling parameters in the ν_μCC1π^+ model the NonRES2π dial is also included as a completely free parameter varied between 0-300% of the nominal value. An upper limit on the NonRES dials is chosen to ensure that their normalisations don't become comparable to the dominant resonant contributions. Finally to account for uncertainties in the FSI model the FrAbs and FrInel dials were considered as free parameters. Due to the instabilities discussed in the previous section it was not possible to include both parameters in a simultaneous fit as this made the weighting response, and the χ^2 surface, unstable. Instead two fits were performed, one with FrAbs treated as free in the range $\pm 3\sigma$ and the remaining FSI dials treated as cushion terms, and another with FrInel varied freely instead. No priors were placed on the FSI dial in either tuning so that the uncertainties extracted were driven by the MINERvA data.

The limits on the parameters used in all tunings are shown in Table 7.3 In both tunings the joint χ^2 (including prior) was passed to MINUIT [177] and the 6 free parameters were varied until the minimum χ^2 was found. Parameter errors were extrapolated using the HESSE routine in MINUIT.

Fit	Nominal	ANL/BNL Tuning Prior	FrAbs Tune	FrInel Tune
M_A^{RES} (GeV)	1.10 ± 0.20	0.94 ± 0.05	1.07 ± 0.04	1.08 ± 0.04
NormRES (%)	100 ± 30	115 ± 7	94 ± 6	92 ± 6
NonRES1π (%)	100 ± 50	43 ± 4	44 ± 4	44 ± 4
NonRES2π (%)	100 ± 50	100 ± 50	166 ± 32	161 ± 33
Theta$-\pi$ (σ)	0.0 ± 1.0	0.0 ± 1.0	1.0 (limit)	1.0 (limit)
Ejection Pref.	*RS*	*RS*	*ISO*	*ISO*
FrAbs (%)	100 ± 30	100 ± 30	109 ± 16	100 (fixed)
FrInel (%)	100 ± 40	100 ± 40	100 (fixed)	109 ± 24
MINERvA χ^2	275.6	317.6	242.3	240.7
Penalty χ^2	299.2	0.0	9.3	11.1
Total χ^2	556.8	317.6	251.6	251.8
NDOF	148	148	145	145

Table 7.4 Best fit results from tuning GENIE ReWeight parameters in NUISANCE for both FSI variations considered. The penalty χ^2 term is exactly zero when the model parameters are left at the central values of the ANL/BNL tunings. In the FrAbs (FrInel) tunings the FrInel (FrAbs) dial is left fixed at the GENIE nominal value. Since the Theta$-\pi$ dial can only vary between 0.0 and 1.0, the tuning results are at an upper limit for this parameter and no uncertainties are provided. The "Ejection Pref." refers to the physical interpretation of the value of the Theta$-\pi$ dial at the best fit.

The best fit results from the joint tuning are shown in Table 7.4. The fits converged on matching results despite the FSI dials considered in each one affecting different channels. In both cases the variations to M_A^{RES} and NormRES dials were flipped compared to the ANL/BNL tunings with a suppression of NormRES being preferred and both parameters moving to be consistent with the nominal GENIE model. The NonRES1π parameter was strongly bound by the prior and the MINERvA data did little to improve on this constraint. The penalty term contributed a minimum of $\chi^2_{PEN} = 10.7$ at the best fit points which is a significant improvement over the nominal model but suggests there is still a tension between the nucleon and nuclear data in the context of this GENIE model.

Separate fits were also performed for individual channels to estimate how each one pulled the best fit parameters. The results are shown in Tables 7.5 and 7.6. The extracted parameters were closer to the bubble chamber parameters since each channel on its own does not provide a strong enough χ^2 to overpower the prior penalty. The joint fits to all channels extracted enhanced contributions for the NonRES2π dial that disagree with the nominal model prediction. It is clear from the individual fits, however, that the ν_μCC$N\pi^+$ dataset prefers a much smaller prediction close to 100%. In the other channels with no prior on NonRES2π all other tunings extract a best fit value at a close to unphysical limit of 300% driven by the neutral pion channels trying to increase their normalisation, and the ν_μCC1π^+ channel trying to recreate the peak in θ_π by driving up the small amount of ν_μCC$N\pi^+$ contributions. Since these channels were unable to constrain this parameter it was excluded in the individual tunings, but the very weak constraint each channel introduces combine to pull the simultaneous fit to a larger average NonRES2π value than the ν_μCC$N\pi^+$ channel alone.

Fit	ν_μCC1π^+	ν_μCC$N\pi^+$	ν_μCC1π^0	$\bar{\nu}_\mu$CC1π^0
M_A^{RES} (GeV)	0.97 ± 0.05	0.97 ± 0.05	1.02 ± 0.05	0.96 ± 0.05
NormRES (%)	110 ± 7	110 ± 7	104 ± 7	111 ± 7
NonRES1π (%)	42 ± 4	42 ± 4	44 ± 4	43 ± 4
NonRES2π (%)	300 (limit)	99 ± 30	300 (limit)	300 (limit)
Theta$-\pi$ (σ)	1.00 (limit)	1.0 (limit)	1.0 (limit)	1.0 (limit)
Ejection Pref.	*ISO*	*ISO*	*ISO*	*ISO*
FrAbs (%)	156 ± 53	128 ± 34	126 ± 17	82 ± 31
MINERvA χ^2	36.6	64.1	92.3	34.6
Penalty χ^2	0.5	0.7	3.2	0.3
Total χ^2	37.1	68.3	95.5	34.9
NDOF	35	36	32	33

Table 7.5 Individual channel tuning results when the FrAbs dial is treated as the free FSI systematic. In each column, only a single channel was considered in the fit to understand the preferred parameter set for each channel. "limit" refers to a dial moving to its upper or lower limit in a fit. "Ejection Pref." refers to the spectrum of pion ejection when the Theta$-\pi$ dial is tuned to the upper limit of 1σ. All datasets apart from the ν_μCC$N\pi^+$ channel set a very weak constraint on NonRES2π, and therefore prefer an unphysical, large enhancement of this dial.

Fit	ν_μCC1π^+	ν_μCC$N\pi^+$	ν_μCC1π^0	$\bar{\nu}_\mu$CC1π^0
M_A^{RES} (GeV)	0.97 ± 0.05	0.97 ± 0.05	1.03 ± 0.02	0.96 ± 0.05
NormRES (%)	109 ± 7	108 ± 7	103 ± 3	112 ± 7
NonRES1π (%)	42 ± 4	42 ± 4	43 ± 4	43 ± 4
NonRES2π (%)	300 (limit)	110 ± 30	300 (limit)	300 (limit)
Theta$-\pi$ (σ)	1.00 (limit)	1.0 (limit)	1.0 (limit)	1.0 (limit)
Ejection Pref.	*ISO*	*ISO*	*ISO*	*ISO*
FrInel (%)	117 ± 54	127 ± 33	0 (limit)	80 ± 59
MINERvA χ^2	37.1	63.4	86.9	34.9
Penalty χ^2	0.7	1.3	3.4	0.2
Total χ^2	37.8	64.7	90.3	35.1
NDOF	35	36	32	33

Table 7.6 Individual channel tuning results when the FrInel dial is treated as the free FSI systematic. In each column, only a single channel was considered in the fit to understand the preferred parameter set for each channel. "limit" refers to a dial moving to its upper or lower limit in a fit. "Ejection Pref." refers to the spectrum of pion ejection when the Theta$-\pi$ dial is tuned to the upper limit of 1σ. All datasets apart from the ν_μCC$N\pi^+$ channel set a very weak constraint on NonRES2π, and therefore prefer an unphysical, large enhancement of this dial. When tuning to only the ν_μCC1π^0 dataset an unphysical fraction of inelastic pion FSI was also preferred (FrInel$= 0.0\%$).

The FSI parameters extracted in both simultaneous tunings were consistent with the nominal GENIE values despite having no priors placed on them, with extracted uncertainties approximately 50% of the nominal GENIE uncertainties. In the individual FrAbs tunings the $\bar{\nu}_\mu$CC1π^0 channel was found to prefer only 82% of the nominal pion absorption cross-section, in disagreement with the other channel tunings. In the FrInel tunings even stronger tensions were observed between the neutral and charged pion channels since the dial has a much larger effect on the ν_μCC1π^+ and ν_μCC$N\pi^+$ distributions. In the $\bar{\nu}_\mu$CC1π^0 fits a slightly suppressed inelastic cross-section was also preferred, but in the ν_μCC1π^0 tunings the FrInel dial was pushed to the lower limit, turning off inelastic scattering completely in an attempt to correct for the observed missing strength in the model. This gave a better fit to the ν_μCC1π^0 channel, but at the cost of moving the FSI model to an unphysical limit of zero.

In all fits isotropic ejection was preferred regardless of the χ^2 combination being tuned, driven by the disagreements in the θ_π distributions. This preference in every tuning suggests that the angular distribution of outgoing pions in GENIE needs modification. Since only a single reweightable Theta dial is available, the fit converges on a result which is in disagreement with the ANL/BNL ν_μCC1π^+ data. This apparent tension may be relaxed in the future if a dial in GENIE is developed that can vary the pion ejection spectrum for charged and neutral pion events, independent from one another. It is also possible that a significant change in the GENIE FSI model could modify this angular distribution, beyond the limited variations of the standard fractional FSI dials commonly used in analyses.

Studying the individual contributions to the joint tuning in Table 7.9 it is clear that the results are an improvement over the ANL/BNL tunes in all the shape-only comparisons, but the χ^2 contributions from p_μ datasets increase in the tuned model. Since for each channel 3 shape-only distributions are included, there is a stronger priority in the fit to improve the shape agreement over making sure the relative normalisation of each channel is correct. Whilst there is an overall improvement over the ANL/BNL tune, the combined χ^2 results neglecting the prior contributions are comparable to the nominal GENIE model. In Figures 7.14 and 7.15 it is clear there are still unresolved shape disagreements in the T_π and θ_μ kinematics. When looking at each individual distribution the ν_μCC1π^0 agreement is actually worse in the tuned model for the p_μ, θ_μ, T_π distributions, only improving in θ_π where all channels benefit from the shift to isotropic ejection.

Distribution	Channel	NBINS	Default	ANL/BNL Tuning	FrAbs Tune	FrInel Tune
p_μ (Rate)	ν_μCC1π^+	8	19.1	14.7	12.0	12.3
	$\bar{\nu}_\mu$CC1π^0	9	7.4	6.4	6.2	6.3
	ν_μCC$N\pi^+$	9	35.4	20.3	27.6	26.8
	ν_μCC1π^0	8	11.1	19.6	18.9	19.3
θ_μ(Shape)	ν_μCC1π^+	9	7.1	16.8	7.5	7.4
	$\bar{\nu}_\mu$CC1π^0	9	9.3	14.0	10.2	10.3
	ν_μCC$N\pi^+$	9	4.5	12.5	4.0	4.1
	ν_μCC1π^0	9	35.1	71.5	44.5	45.6
T_π (Shape)	ν_μCC1π^+	7	2.9	2.7	2.5	2.3
	$\bar{\nu}_\mu$CC1π^0	7	19.3	17.9	16.6	16.0
	ν_μCC$N\pi^+$	7	39.8	35.6	31.2	29.4
	ν_μCC1π^0	7	28.3	31.4	30.9	29.9
θ_π (Shape)	ν_μCC1π^+	14	25.4	26.1	13.0	12.6
	$\bar{\nu}_\mu$CC1π^0	11	5.7	5.9	3.4	3.5
	ν_μCC$N\pi^+$	14	11.7	11.0	6.9	6.2
	ν_μCC1π^0	11	13.5	15.0	8.3	8.9

Table 7.7 Contributions to the total χ^2 at the best fit points for each tuning compared to the contributions at the fixed predictions in the previous section.

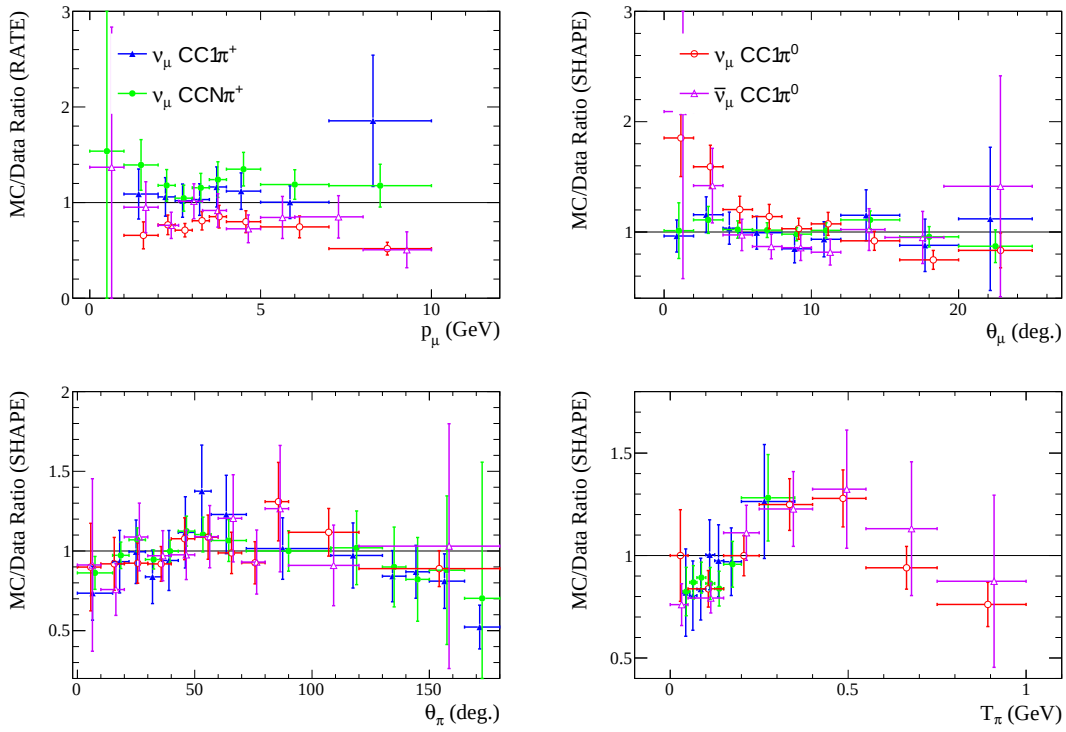

Fig. 7.14 MC/data ratios for at the best fit point for the FrAbs joint tuning.

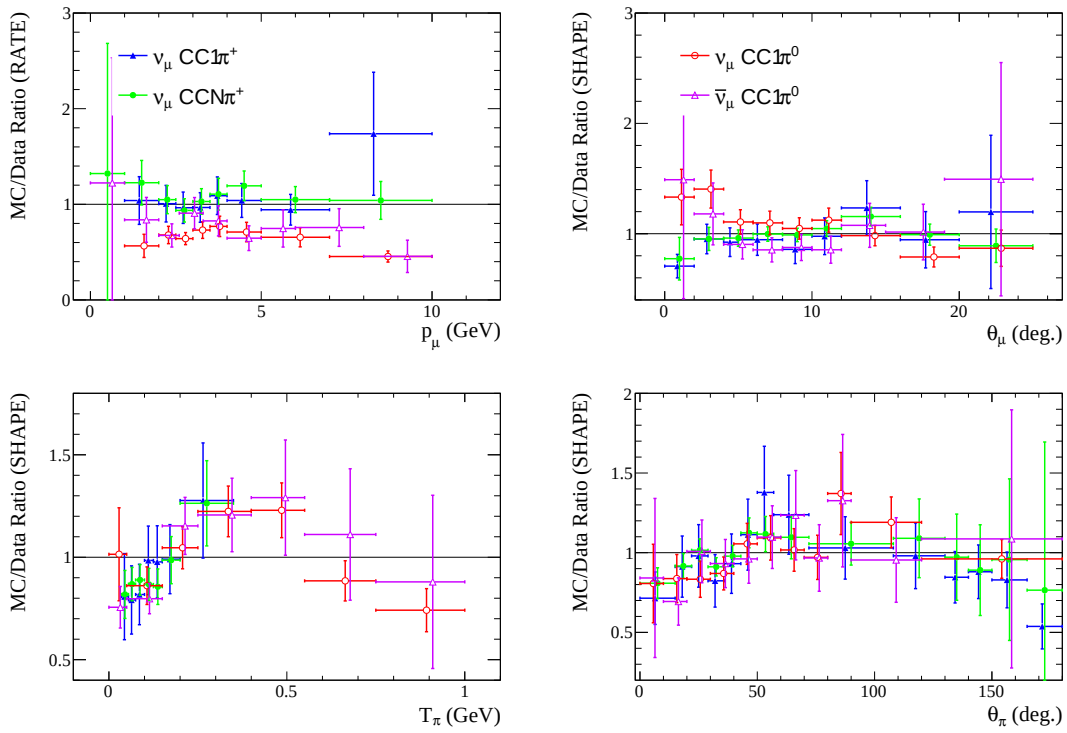

Fig. 7.15 MC/data ratios for at the best fit point for the FrInel joint tuning.

7.6 Ad-Hoc Q^2 Corrections

It is clear from the previous studies that the nominal GENIE systematics considered are insufficient and even further modifications are required to resolve the observed tensions. In this section a focus is placed on resolving problems in the θ_μ distribution by modifying of the Q^2 shape of the model, motivated by the differences at low angles shown in Figures 7.14 and 7.15 and in the Q^2 distributions shown in Figure 7.16. Whilst the very lowest Q^2 bin in the ν_μCC1π^+ channel sees contributions from coherent pion production, the suppression of 50% at $T_\pi < 500$ MeV suggested in Ref. [195] has only a small effect on the shape of the kinematic distributions considered. Measurements of ν_μCC1π^+ and ν_μCC1π^0 interactions at MiniBooNE have shown a similar data/MC shape discrepancy for the Rein-Sehgal implementation in NUANCE in both Q^2 and $\cos\theta_\mu$ kinematic distributions [171, 176]. In the MINOS quasi-elastic analysis a similar disagreement was observed when studying Δ/N^* dominated side bands [201]. The data from all 3 of these experiments point towards an underlying trend that the Rein-Sehgal implementation in each of these generators needs to be suppressed at low Q^2.

The MINOS collaboration found that introducing a suppression function that was tuned to the Δ/N^* rich side bands was capable of increasing agreement in both RES-enhanced and RES-to-DIS-enhanced samples despite each sample containing different background processes [201]. The

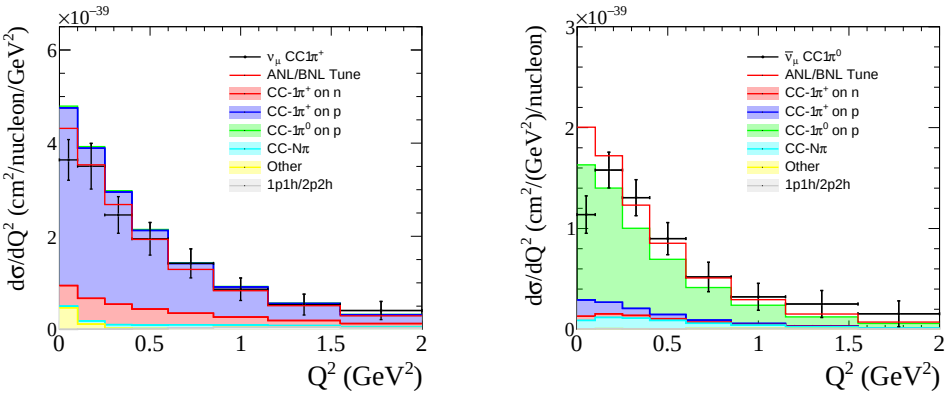

Fig. 7.16 Comparisons of the ANL/BNL tuned model to pion production Q^2 distributions published by the MINERvA collaboration. "Other" contributions are dominated by coherent charged pion production. The red ANL/BNL Tune line shows the shape of the model prediction when normalised to match the data.

suppression function can be parametrised as

$$R(Q^2 < 0.7\ \text{GeV}^2) = \frac{A}{1+\exp(1-\sqrt{Q^2/Q_0})}, \tag{7.5}$$

where the free parameters $A = 1.010$ and $Q_0 = 0.156$ GeV were empirically extracted from the data.

Instead of using the fixed MINOS low-Q^2 correction an alternative empirical function was chosen so that the shape of the suppression preferred by each of the MINERvA channels could be extracted. The suppression term was defined by choosing three points between $0.0 < x < 1.0$ and $0.0 < R < 1.0$ before Lagrangian interpolation was used to plot a smooth curve between each point. The exact form was given by: The exact form was given by:

$$R'_2 = \frac{R_2 - R_1}{1 - R_1} \tag{7.6}$$

$$R(Q^2 < x_m) = \frac{R'_2(x-x_1)(x-x_m)}{(x_2-x_1)(x_2-x_m)} + \frac{(x-x_1)(x-x_2)}{(x_m-x_1)(x_m-x_2)}, \tag{7.7}$$

$$W(Q^2) = 1 - (1 - R(Q^2))^2 \times (1 - R_1), \tag{7.8}$$

where x_m is the chosen maximum cut off above which no events are suppressed and (x_1, R_1) and (x_2, R_2) are the chosen points that define the shape of the suppression function. The substitution of R'_2 as a function of R_1 and R_2 is made to ensure the centre point of the interpolation always lies between R_1 and 1.0, creating a smooth function with no peaks. In the MINOS studies an upper limit of $Q^2 < 0.7$ GeV^2 was placed on Equation (7.5), above which no events were suppressed. In the Lagrangian function a similar bound was chosen using $x_m = 0.7$ GeV^2 motivated by comparisons in Figure 7.16, with the model predicting a smooth function approaching unity as Q^2 approaches x_m. The other points x_1 and x_2 were set to 0.0 GeV^2 and 0.35 GeV^2 respectively so that R_1 and

Fit	FrAbs Tune	FrAbs+Lag.Q^2 Tune	FrInel Tune	FrInel+Lag.Q^2 Tune
M_A^{RES} (GeV)	1.07 ± 0.04	0.92 ± 0.02	1.08 ± 0.04	0.93 ± 0.05
NormRES (%)	94 ± 6	116 ± 3	92 ± 6	116 ± 7
NonRES1π (%)	43 ± 4	46 ± 4	44 ± 4	46 ± 4
NonRES2π (%)	166 ± 32	99 ± 31	161 ± 33	120 ± 32
Theta$-\pi$ (σ)	1.0 (limit)	1.0 (limit)	1.0 (limit)	1.0 (limit)
Ejection Pref.	*ISO*	*ISO*	*ISO*	*ISO*
FrAbs (%)	109 ± 16	48 ± 21	100 (fixed)	100 (fixed)
FrInel (%)	100 (fixed)	100 (fixed)	109 ± 24	132 ± 27
Lag. R_1		0.32 ± 0.06		0.37 ± 0.09
Lag. R_2'		0.5 (limit)		0.598 ± 0.16
MINERvA χ^2	242.3	212.2	240.7	215.8
Penalty χ^2	9.3	0.7	11.1	0.5
Total χ^2	251.6	212.9	251.8	216.2
NDOF	145	143	145	143

Table 7.8 Ad-hoc low Q^2 suppression model tuning results compared to the previous tunings without the Lagrangian correction applied. "Lag. R_1" and "Lag. R_2'" refer to the free parameters in the Lagrangian low-Q^2 correction. In the FrAbs (FrInel) tunings the FrInel (FrAbs) dial is left fixed at the GENIE nominal value. "limit" refers to a dial converging on its upper or lower limit in the fits. Since the Theta$-\pi$ dial can only vary between 0.0 and 1.0, the tuning results are at an upper limit for this parameter and no uncertainties are provided. The "Ejection Pref." refers to the physical interpretation of the value of the Theta$-\pi$ dial at the best fit. The addition of the Lagrangian Q^2 correction function leads to a reduction in the total χ^2 for both fits, and a reduction in the Penalty χ^2 contribution from the ANL/BNL prior at the best fit point.

R_2 could be treated as the only free parameters to set both the intercept and curvature at the half way point of the suppression function. To avoid combinations that produce multiple peaks these parameters were limited to $0.0 < R_1 < 1.0$ and $0.5 < R_2' < 1.0$ in the fits. The correction function is applied to true resonance events based on the GENIE event information and is applied only to events with resonance decay inside the nucleus as it represents an empirical nuclear correction.

The Lagrangian model has the freedom to approximate the MINOS correction but also provides the fit with an easy way to turn off the suppression by setting $R_1 = 1$. To understand the effect that t his has on the GENIE model predictions the tunings were repeated with the low-Q^2 correction included, and R_1 and R_2 treated as additional free parameters. The best fits are shown in Table 7.8 with the extracted uncertainty bands on the Lagrangian compared to the MINOS correction in Figure 7.17. Despite running the tunings with no priors the fits produce a low Q^2 suppression with an intercept that is consistent with the MINOS model but has less curvature.

In the individual channels the tensions between topologies becomes more apparent with the neutral pions preferring a sharper drop off at low Q^2 as shown in Figure 7.17. In the charged pion fits suppressed values of $R_2 = 0.5$ at the lower limit were extracted with the suppression extending up to 0.4 GeV^2. The lower limit on R_2 was chosen to avoid fluctuations in the interpolation negatively affecting the fit, but it is possible that the π^+ channels would benefit from relaxed constraints that

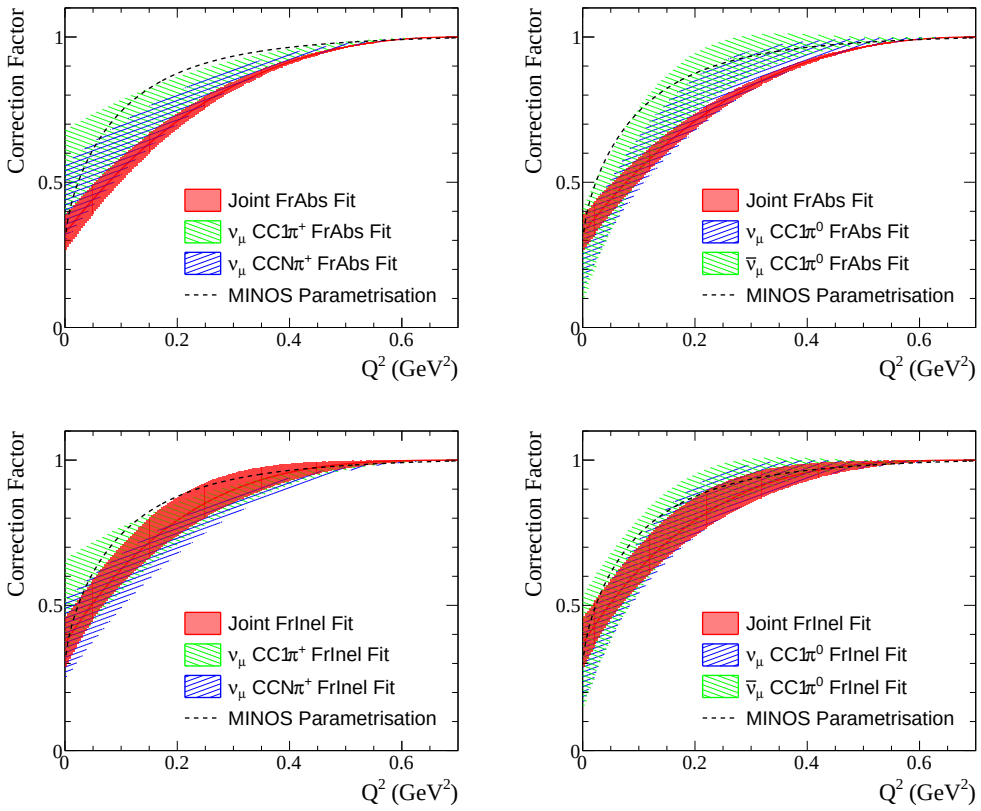

Fig. 7.17 Lagrangian suppression models extracted in both FSI tunings to individual MINERvA channels. (top) FrAbs tuning, (bottom) FrInel tuning. Each of the individual channels was found to prefer slightly different suppression functions, with a notable difference between the charged and neutral pion channels. The differences between the FrAbs and FrInel tunings suggest a tension between the GENIE model and the data, and therefore the envelope of all of these possible correction functions should be used until a suitable theoretical model for low-Q^2 suppression of pion production events is available.

Distribution	Channel	NBINS	FrAbs	FrAbs+Lag.Q^2	FrInel	FrInel+Lag.Q^2
p_μ (Rate)	ν_μCC1π^+	8	12.0	10.8	12.3	10.9
	$\bar{\nu}_\mu$CC1π^0	9	6.2	7.1	6.3	7.2
	ν_μCC$N\pi^+$	9	27.6	16.2	26.8	17.9
	ν_μCC1π^0	8	18.9	26.2	19.3	26.9
θ_μ(Shape)	ν_μCC1π^+	9	7.5	7.4	7.4	7.1
	$\bar{\nu}_\mu$CC1π^0	9	10.2	7.0	10.3	6.9
	ν_μCC$N\pi^+$	9	4.0	6.3	4.1	5.6
	ν_μCC1π^0	9	44.5	20.0	45.6	20.5
T_π (Shape)	ν_μCC1π^+	7	2.5	2.5	2.3	2.4
	$\bar{\nu}_\mu$CC1π^0	7	16.6	15.7	16.0	18.7
	ν_μCC$N\pi^+$	7	31.2	28.9	29.4	27.7
	ν_μCC1π^0	7	30.9	27.1	29.9	32.0
θ_π (Shape)	ν_μCC1π^+	14	13.0	13.4	12.6	12.6
	$\bar{\nu}_\mu$CC1π^0	11	3.4	4.4	3.5	3.7
	ν_μCC$N\pi^+$	14	6.9	7.0	6.2	6.3
	ν_μCC1π^0	11	8.3	12.2	8.9	9.4

Table 7.9 χ^2 contributions at the best fit points for the GENIE tunings with and without the low Q^2 correction included. Whilst the total χ^2 is significantly reduced when using the Lagrangian Q^2 model, not every dataset has an improved χ^2 value, suggesting there may still be unresolved tensions between the model and the MINERvA datasets.

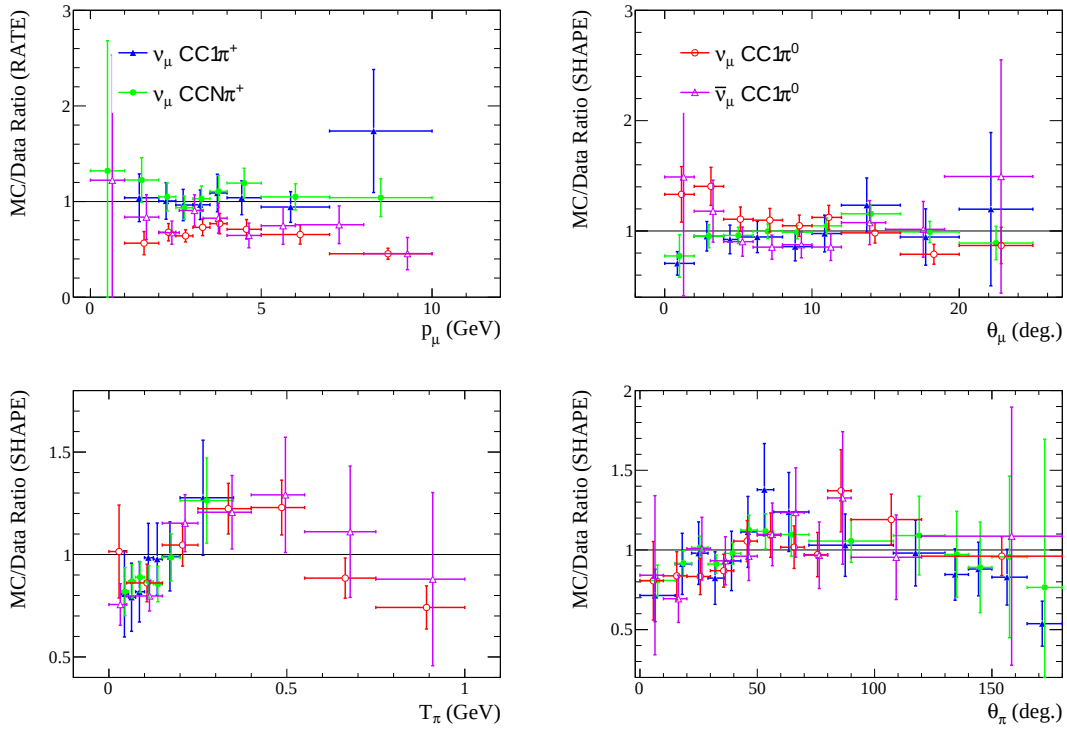

Fig. 7.18 MC/data ratios at the best fit points from the FrAbs tuning with low Q^2 suppression included. A similar shift in the θ_μ distribution was also observed in the FrInel+Lag.Q^2 tunings.

Fit	ν_μCC1π^+	ν_μCC$N\pi^+$	ν_μCC1π^0	$\bar{\nu}_\mu$CC1π^0
$M_{\mathrm{A}}^{\mathrm{RES}}$ (GeV)	0.93 ± 0.02	0.92 ± 0.02	0.96 ± 0.05	0.94 ± 0.05
NormRES (%)	115 ± 3	117 ± 3	114 ± 7	115 ± 7
NonRES1π (%)	43 ± 4	43 ± 4	45 ± 4	43 ± 4
NonRES2π (%)	300 (limit)	70 ± 28	300 (limit)	300 (limit)
Theta$-\pi$ (σ)	1.00 (limit)	1.00 (limit)	1.00 (limit)	1.00 (limit)
Ejection Pref.	*ISO*	*ISO*	*ISO*	*ISO*
FrAbs (%)	92 ± 65	79 ± 40	74 ± 22	34 ± 35
Lag. R_1	0.53 ± 0.16	0.43 ± 0.13	0.21 ± 0.14	0.14 ± 0.22
Lag. R_2'	0.50 (limit)	0.50 (limit)	0.63 ± 0.31	1.00 (limit)
MINERvA χ^2	32.2	55.7	71.2	27.7
Penalty χ^2	0.1	0.4	0.5	0.0
Total χ^2	32.3	56.1	71.7	27.7
NDOF	33	34	30	31

Table 7.10 Individual channel FrAbs+Lag.Q^2 tuning results. "Lag. R_1" and "Lag. R_2'" refer to the free parameters in the Lagrangian low-Q^2 correction. "limit" refers to a dial converging on its upper or lower limit in the fits. Since the Theta$-\pi$ dial can only vary between 0.0 and 1.0, the tuning results are at an upper limit for this parameter and no uncertainties are provided. The "Ejection Pref." refers to the physical interpretation of the value of the Theta$-\pi$ dial at the best fit. In all of the extracted corrections an intercept less than 1.0 was preferred for the Lagrangian, however very different curvatures (dictated by R_2') were preferred for each channel. $R_2' = 0.50$ corresponds to the minimum curvature, whilst $R_2' = 1.0$ corresponds to the maximum.

allowed for suppressions with even less curvature than considered here. The extracted intercept was also higher in the charged pion fits, but a model without coherent pion production suppression included found a slightly lower intercept consistent with the other channel tunings.

In all cases the χ^2 was significantly improved when moving to a model with low-Q^2 suppression and the extracted parameters were completely consistent with the ANL/BNL tunings, resulting in reduced χ^2 penalty contributions at the best fit. When looking at the individual distributions, however, the shift to a low-Q^2 suppressed model improves the θ_μ single pion channels but the shape agreement of the ν_μCC$N\pi^+$ channel is reduced as it contributes only a small amount to the total χ^2 in the fits. The other distributions are also not improved across the board with the enhanced Q^2 shape freedom exposing other tensions in the fit, producing fluctuations up and down in the χ^2 contributions from individual channels. Whilst isotropic ejection is still preferred in all tunings there are significant shifts in NormRES2π in the ad-hoc model with the ν_μCC$N\pi^+$ channel preferring a much lower contribution, and the extracted FSI parameters are pulled further away from the GENIE nominal prediction in opposite directions. The ν_μCC1π^+ channel also finds it significantly harder to constrain the FrInel dial in the ad-hoc model suggesting that the previous FSI constraint was a result of the low Q^2 tensions.

Fit	ν_μCC1π^+	ν_μCC$N\pi^+$	ν_μCC1π^0	$\bar{\nu}_\mu$CC1π^0
M_A^{RES} (GeV)	0.93 ± 0.02	0.91 ± 0.02	0.95 ± 0.05	0.94 ± 0.05
NormRES (%)	116 ± 3	117 ± 3	114 ± 7	115 ± 7
NonRES1π (%)	43 ± 4	43 ± 4	44 ± 4	43 ± 4
NonRES2π (%)	300 (limit)	78 ± 28	300 (limit)	300 (limit)
Theta$-\pi$ (σ)	1.00 (limit)	1.00 (limit)	1.00 (limit)	1.00 (limit)
Ejection Pref.	*ISO*	*ISO*	*ISO*	*ISO*
FrInel (%)	179 ± 63	173 ± 37	8 ± 125	103 ± 57
Lag. R_1	0.49 ± 0.14	0.38 ± 0.13	0.25 ± 0.17	0.31 ± 0.26
Lag. R_2'	0.50 (limit)	0.50 (limit)	0.76 ± 0.37	1.00 (limit)
MINERvA χ^2	30.8	52.1	69.5	30.9
Penalty χ^2	0.1	0.6	0.2	0.0
Total χ^2	30.9	52.7	69.7	30.9
NDOF	33	34	30	31

Table 7.11 Individual channel FrInel+Lag.Q^2 tuning results. "Lag. R_1" and "Lag. R_2'" refer to the free parameters in the Lagrangian low-Q^2 correction. "limit" refers to a dial converging on its upper or lower limit in the fits. Since the Theta$-\pi$ dial can only vary between 0.0 and 1.0, the tuning results are at an upper limit for this parameter and no uncertainties are provided. The "Ejection Pref." refers to the physical interpretation of the value of the Theta$-\pi$ dial at the best fit. In all of the extracted corrections an intercept less than 1.0 was preferred for the Lagrangian, however very different curvatures (dictated by R_2') were preferred for each channel. $R_2' = 0.50$ corresponds to the minimum curvature, whilst $R_2' = 1.0$ corresponds to the maximum.

7.7 Concluding Remarks

We have shown that there is a significant tension between the ANL/BNL tunings in Ref. [192] and MINERvA pion production data. The observed discrepancies between tunings to subsets of the data indicate an underlying problem in the relative strengths of different resonance production channels in GENIE that cannot be resolved by the simple GENIE ReWeight variations often used to define systematic uncertainties in neutrino experiments. It is possible that a shift to an alternate pion model like the Berger Sehgal implementation could introduce spectrum changes inaccessible by the event reweighting but initial comparisons suggested that this model could only relieve missing strength in the ν_μCC1π^0 channel by overestimating the other channels significantly. In all tunings considered isotropic ejection of pions was preferred by the MINERvA data and there is an apparent shape disagreement in the T_π distributions which could not be easily resolved by reweighting.

When relaxing the tensions between the nucleon and nuclear data by including a low Q^2 correction we see large shifts in the extracted results, with the joint fit extracting a suppression at $Q^2 \to 0$ GeV^2 similar to that suggested by the MINOS analysis in Ref [201]. This ad-hoc Q^2 model produces a reduced joint χ^2 when fitting to all channels simultaneously but it is clear there are still several tensions present, with only the ν_μCC1π^+ and $\bar{\nu}_\mu$CC1π^0 channels achieving a satisfactory goodness of fit in individual channel tuning studies by using very different suppression forms and FSI parameter values.

The corrections extracted in these studies represent a more up to date empirically motivated low-Q^2 suppression model for GENIE resonance interactions. Since ad-hoc empirical model corrections ultimately rely on the combined MC model used to extract them they are inherently model dependent, but the methods shown here can be easily repeated using the NUISANCE framework to evaluate whether a suppression is needed for any alternative model or generator. Those using models very similar to the one considered here can however take it as an approximate correction by implementing the Lagrangian form into their own MC and applying weights based on the parameters shown in Table 7.10-7.11. To ensure appropriate uncertainties are applied an envelope of all models should be created from both the FrAbs and FrInel fit results, considering the parameter sets obtained in each of the individual channel tunings alongside the main joint tunings. The methods developed here will be used as a basis in future MINERvA-NUISANCE tuning studies as new data and improved generator models become available.

Chapter 8

Concluding Remarks

As new data on neutrino interactions in the few-GeV region has become available in recent years, it is clear that the simple cross-section models used in previous oscillation analyses are incomplete descriptions of nature. This represents a serious challenge for future neutrino oscillation analyses which are systematics dominated, as they will require significantly reduced cross-section systematics to succeed. Whilst more advanced models are required to resolve these disagreements, the implementation of new models into Monte Carlo generators can be sometimes be extremely time consuming. In the meantime, current experiments must therefore implement ad-hoc model corrections to ensure appropriate systematics are included in their analyses. This thesis focuses on the empirical tuning of neutrino interaction generators in the few GeV region, specifically aimed at providing inputs for neutrino oscillation experiments such as T2K.

In Chapter 4, a method was developed to estimate whether uncertainties on cross-section models need to be expanded when performing sterile neutrino fits. The NEUT 5.1.4.2 cross-section model was derived from fits to MiniBooNE data, and in this chapter the effect of sterile mixing on these fits was evaluated by repeating the NEUT model extraction for many different mixing hypotheses. The analysis found that the model uncertainties were inappropriate for use in a sterile neutrino exclusion fit. The shift in model parameters extracted as a function of mixing parameters was used to define an error scaling matrix that could be used in a short baseline fit at ND280. Whilst applied to only a specific cross-section model and oscillation formalism, the methods developed in this section can be transferred to any tuning, so that the reliability of a cross-section model can be evaluated before a sterile neutrino fit is performed.

In Chapter 5, two different axial form factor models, the three-component model, and the Z-expansion model, were implemented into NEUT 5.3.6 and considered as systematics for the T2K oscillation analysis. These were chosen to ensure conservative systematic uncertainties were placed on the CCQE model in NEUT at high Q^2. Tunings to bubble chamber data within the NUISANCE framework were used to test each of the form factor implementations and produce

nominal uncertainties for the three-component model. The form factors were found to prefer slightly larger normalisations at $Q^2 = 1$ GeV^2 than previous bubble chamber tunings, producing a slightly inflated dipole axial mass of 1.10 GeV. This was driven by a higher weighting applied to Q^2 distributions than in previous form factor extractions. The tunings still produced large conservative uncertainties on F_A by design. Due to time constraints these were added to the T2K oscillation analysis in form of several approximated fake data studies. In future T2K analyses the implementation of the Z-expansion model and its associated correlations will be used as free parameters to ensure the uncertainties on F_A are captured fully.

When trying to measure CC-inclusive interactions as a function of energy and momentum transfer, the MINERvA experiment has observed clear discrepancies between the data and GENIE. In Chapter 6, the NEUT model used by T2K was shown to also disagree when compared to the same dataset. Following a similar procedure to that performed by the MINERvA collaboration, a two-dimensional Gaussian was tuned to the CC-inclusive data to extract an ad-hoc model correction as a function of (q_0, q_3) for either CCQE or 2p2h interactions. Both these corrections were found to improve the NEUT model's agreement with the MINERvA data by design, but when propagated to ND280 CC0π data, they were shown to severely overestimate the total strength required. Analysis of the hadronic structure function contributions in the Smith-Moniz interaction model, showed that the W_2 structure function is dominant at MINERvA energies, but not at ND280. Therefore, applying this ad-hoc correction only to W_2 could relieve the tensions observed at high angles in the ND280 CC0π comparisons. Whilst such ad-hoc model corrections are applicable to MINERvA, these studies have shown that great care must be taken when trying to use them in other experiments. This could have a major impact on joint T2K-NOvA analyses as it is possible the discrepancies at both experiments originate from the same model deficiency. Therefore, the energy dependence of the correction needs to be understood so that it can be properly correlated between the two. Future iterations of this work will aim to use a newer implementation of multi-nucleon interactions in NEUT to estimate the energy dependence of the 2p2h hadronic structure functions, and ensure an appropriate systematic is applied to the NEUT CC0π model.

Finally, in Chapter 7, the NUISANCE framework was used to perform a joint tuning of GENIE reweight parameters to a collection of MINERvA pion production data. Significant tensions were found between the charged and neutral pion measurements included in the fits, and the standard GENIE reweight FSI dials did not seem to provide sufficient coverage of the data/MC differences observed. An empirical tuning was able to improve the goodness-of-fit only by pulling the best fit parameters away from previous GENIE tunings to ANL and BNL data. This suggests the extension of the model from nucleon to nuclear targets is incomplete. Faced with a large shape disagreement at low muon scattering angles, an empirical Q^2 correction was added, following a similar implementation in NUANCE by the MINOS collaboration. This was found to relieve the tensions in the fit, producing an uncertainty band on the shape of the required correction. However, when tuning to individual channels it is clear that the charged and neutral pion measurements prefer different low Q^2 suppressions. The extracted functional forms will be used in future MINERvA

analyses as ad-hoc systematics applied to the pion production model in GENIE, until a more advanced model can be tested with the same procedure.

By their very nature, the outputs of empirical tunings are model dependent, relying on the comparison of the nominal predictions to the data to estimate the strength of any ad-hoc correction. Since there are significant tensions between many of the neutrino interaction measurements to date, it is difficult to extract a single "universally-valid" cross-section model through empirical tuning methods. As new, more theoretically consistent, models become available, the extracted parameter sets can also quickly become obsolete. The NUISANCE framework avoids this problem by providing the tools and methods for analysers to easily extract their own cross-section model tunings. Fits performed in the framework can also be repeated when one part of a generator model needs to be changed. A significant amount of work during my PhD has gone into the development of the NUISANCE framework, ensuring that it can be generally applied to a broad range of different global tuning problems. Whilst the analyses in this thesis have been developed with a specific purpose in mind, the methods used are all available in NUISANCE, so that they can be repeated or modified as generator models evolve in the future.

References

[1] W. Pauli. (1930). Letter of the 4th december 1930, [Online]. Available: http://microboone-docdb.fnal.gov/cgi-bin/RetrieveFile?docid=953;filename=pauli\%20letter1930.pdf.

[2] E. Fermi, "An attempt of a theory of beta radiation. 1.," *Z. Phys.*, vol. 88, pp. 161–177, 1934. DOI: 10.1007/BF01351864.

[3] H. Bethe and R. Peierls, "The 'neutrino'," *Nature*, vol. 133, p. 532, 1934. DOI: 10.1038/133532a0.

[4] F. Reines and C. L. Cowan, "Detection of the free neutrino," *Phys. Rev.*, vol. 92, pp. 830–831, 1953. DOI: 10.1103/PhysRev.92.830.

[5] R. Davis Jr., "Attempt to detect the antineutrinos from a nuclear reactor by the Cl37(anti-nu,e-) A37 reaction," *Phys. Rev.*, vol. 97, pp. 766–769, 1955. DOI: 10.1103/PhysRev.97.766.

[6] C. L. Cowan, F. Reines, F. B. Harrison, H. W. Kruse, and A. D. McGuire, "Detection of the free neutrino: A Confirmation," *Science*, vol. 124, pp. 103–104, 1956. DOI: 10.1126/science.124.3212.103.

[7] J. C. Street and E. C. Stevenson, "New Evidence for the Existence of a Particle of Mass Intermediate Between the Proton and Electron," *Phys. Rev.*, vol. 52, pp. 1003–1004, 1937. DOI: 10.1103/PhysRev.52.1003.

[8] E. P. Hincks and B. Pontecorvo, "Search for gamma-radiation in the 2.2-microsecond meson decay process," *Phys. Rev.*, vol. 73, pp. 257–258, 1948. DOI: 10.1103/PhysRev.73.257.

[9] G. Danby, J. M. Gaillard, K. A. Goulianos, L. M. Lederman, N. B. Mistry, M. Schwartz, and J. Steinberger, "Observation of High-Energy Neutrino Reactions and the Existence of Two Kinds of Neutrinos," *Phys. Rev. Lett.*, vol. 9, pp. 36–44, 1962. DOI: 10.1103/PhysRevLett.9.36.

[10] M. L. Perl *et al.*, "Evidence for Anomalous Lepton Production in e+ - e- Annihilation," *Phys. Rev. Lett.*, vol. 35, pp. 1489–1492, 1975, [,193(1975)]. DOI: 10.1103/PhysRevLett.35.1489.

[11] S. Schael *et al.*, "Precision electroweak measurements on the Z resonance," *Phys. Rept.*, vol. 427, pp. 257–454, 2006. DOI: 10.1016/j.physrep.2005.12.006. arXiv: hep-ex/0509008 [hep-ex].

[12] K. Kodama *et al.*, "Observation of tau neutrino interactions," *Phys. Lett.*, vol. B504, pp. 218–224, 2001. DOI: 10.1016/S0370-2693(01)00307-0. arXiv: hep-ex/0012035 [hep-ex].

[13] J. N. Bahcall, A. M. Serenelli, and S. Basu, "New solar opacities, abundances, helioseismology, and neutrino fluxes," *Astrophys. J.*, vol. 621, pp. L85–L88, 2005. DOI: 10.1086/428929. arXiv: astro-ph/0412440 [astro-ph].

[14] R. Davis Jr., D. S. Harmer, and K. C. Hoffman, "Search for neutrinos from the sun," *Phys. Rev. Lett.*, vol. 20, pp. 1205–1209, 1968. DOI: 10.1103/PhysRevLett.20.1205.

[15] K. S. Hirata *et al.*, "Observation of B-8 Solar Neutrinos in the Kamiokande-II Detector," *Phys. Rev. Lett.*, vol. 63, p. 16, 1989. DOI: 10.1103/PhysRevLett.63.16.

[16] J. N. Abdurashitov *et al.*, "Solar neutrino flux measurements by the Soviet-American Gallium Experiment (SAGE) for half the 22 year solar cycle," *J. Exp. Theor. Phys.*, vol. 95, pp. 181–193, 2002, [Zh. Eksp. Teor. Fiz.122,211(2002)]. DOI: 10.1134/1.1506424. arXiv: astro-ph/0204245 [astro-ph].

[17] M. Cribier, "Results of the whole GALLEX experiment," *Nucl. Phys. Proc. Suppl.*, vol. 70, pp. 284–291, 1999, [,284(1999)]. DOI: 10.1016/S0920-5632(98)00438-1.

[18] K. S. Hirata *et al.*, "Experimental Study of the Atmospheric Neutrino Flux," *Phys. Lett.*, vol. B205, p. 416, 1988, [,447(1988)]. DOI: 10.1016/0370-2693(88)91690-5.

[19] D. Casper *et al.*, "Measurement of atmospheric neutrino composition with IMB-3," *Phys. Rev. Lett.*, vol. 66, pp. 2561–2564, 1991. DOI: 10.1103/PhysRevLett.66.2561.

[20] B. Pontecorvo, "Neutrino Experiments and the Problem of Conservation of Leptonic Charge," *Sov. Phys. JETP*, vol. 26, pp. 984–988, 1968, [Zh. Eksp. Teor. Fiz.53,1717(1967)].

[21] R. N. Mohapatra *et al.*, "Theory of neutrinos: A White paper," *Rept. Prog. Phys.*, vol. 70, pp. 1757–1867, 2007. DOI: 10.1088/0034-4885/70/11/R02. arXiv: hep-ph/0510213 [hep-ph].

[22] E. K. Akhmedov and A. Yu. Smirnov, "Paradoxes of neutrino oscillations," *Phys. Atom. Nucl.*, vol. 72, pp. 1363–1381, 2009. DOI: 10.1134/S1063778809080122. arXiv: 0905.1903 [hep-ph].

[23] L. Wolfenstein, "Neutrino Oscillations in Matter," *Phys. Rev.*, vol. D17, pp. 2369–2374, 1978, [,294(1977)]. DOI: 10.1103/PhysRevD.17.2369.

[24] V. D. Barger, K. Whisnant, S. Pakvasa, and R. J. N. Phillips, "Matter Effects on Three-Neutrino Oscillations," *Phys. Rev.*, vol. D22, p. 2718, 1980, [,300(1980)]. DOI: 10.1103/PhysRevD.22.2718.

[25] S. P. Mikheev and A. Yu. Smirnov, "Resonant Neutrino Oscillations in Matter: Measuring of Neutrino Masses and Mixing," in *HEIDELBERG 1987, PROCEEDINGS, NEUTRINO PHYSICS*, 1987, 247–257.

[26] Q. R. Ahmad *et al.*, "Direct evidence for neutrino flavor transformation from neutral current interactions in the Sudbury Neutrino Observatory," *Phys. Rev. Lett.*, vol. 89, p. 011 301, 2002. DOI: 10.1103/PhysRevLett.89.011301. arXiv: nucl-ex/0204008 [nucl-ex].

[27] B. Aharmim *et al.*, "Electron energy spectra, fluxes, and day-night asymmetries of B-8 solar neutrinos from measurements with NaCl dissolved in the heavy-water detector at the Sudbury Neutrino Observatory," *Phys. Rev.*, vol. C72, p. 055 502, 2005. DOI: 10.1103/PhysRevC.72.055502. arXiv: nucl-ex/0502021 [nucl-ex].

[28] Y. Fukuda *et al.*, "Evidence for oscillation of atmospheric neutrinos," *Phys. Rev. Lett.*, vol. 81, pp. 1562–1567, 1998. DOI: 10.1103/PhysRevLett.81.1562. arXiv: hep-ex/9807003 [hep-ex].

[29] Y. Ashie *et al.*, "Evidence for an oscillatory signature in atmospheric neutrino oscillation," *Phys. Rev. Lett.*, vol. 93, p. 101 801, 2004. DOI: 10.1103/PhysRevLett.93.101801. arXiv: hep-ex/0404034 [hep-ex].

[30] C. Patrignani *et al.*, "Review of Particle Physics," *Chin. Phys.*, vol. C40, no. 10, p. 100 001, 2016. DOI: 10.1088/1674-1137/40/10/100001.

[31] A. Gando *et al.*, "Reactor On-Off Antineutrino Measurement with KamLAND," *Phys. Rev.*, vol. D88, no. 3, p. 033 001, 2013. DOI: 10.1103/PhysRevD.88.033001. arXiv: 1303.4667 [hep-ex].

[32] K. Abe *et al.*, "Measurement of neutrino and antineutrino oscillations by the T2K experiment including a new additional sample of ν_e interactions at the far detector," *Phys. Rev.*, vol. D96, no. 9, p. 092 006, 2017. DOI: 10.1103/PhysRevD.96.092006. arXiv: 1707.01048 [hep-ex].

[33] P. Adamson *et al.*, "Measurement of the neutrino mixing angle θ_{23} in NOvA," *Phys. Rev. Lett.*, vol. 118, no. 15, p. 151 802, 2017. DOI: 10.1103/PhysRevLett.118.151802. arXiv: 1701.05891 [hep-ex].

[34] R. Acciarri *et al.*, "Long-Baseline Neutrino Facility (LBNF) and Deep Underground Neutrino Experiment (DUNE)," 2016. arXiv: 1601.05471 [physics.ins-det].

[35] "Hyper-Kamiokande Design Report," 2016, KEK-PREPRINT-2016-21, ICRR-REPORT-701-2016-1.

[36] P. Minkowski, "$\mu \to e\gamma$ at a Rate of One Out of 10^9 Muon Decays?" *Phys. Lett.*, vol. 67B, pp. 421–428, 1977. DOI: 10.1016/0370-2693(77)90435-X.

[37] R. N. Mohapatra and G. Senjanovic, "Neutrino Mass and Spontaneous Parity Violation," *Phys. Rev. Lett.*, vol. 44, p. 912, 1980, [,231(1979)]. DOI: 10.1103/PhysRevLett.44.912.

[38] M. Gell-Mann, P. Ramond, and R. Slansky, "Complex Spinors and Unified Theories," *Conf. Proc.*, vol. C790927, pp. 315–321, 1979. arXiv: 1306.4669 [hep-th].

[39] J. B. Albert *et al.*, "Search for Neutrinoless Double Beta Decay with the Upgraded EXO-200 Detector," *Phys. Rev. Lett.*, vol. 120, no. 7, p. 072 701, 2018. DOI: 10.1103/PhysRevLett.120.072701. arXiv: 1707.08707 [hep-ex].

[40] R. Henning, "Current status of neutrinoless double beta decay searches," *Rev. Phys.*, vol. 1, pp. 29–35, 2016. DOI: 10.1016/j.revip.2016.03.001.

[41] K. N. Abazajian *et al.*, "Light Sterile Neutrinos: A White Paper," 2012. arXiv: 1204.5379 [hep-ph].

[42] C. Athanassopoulos *et al.*, "Evidence for neutrino oscillations from muon decay at rest," *Phys. Rev.*, vol. C54, pp. 2685–2708, 1996. DOI: 10.1103/PhysRevC.54.2685. arXiv: nucl-ex/9605001 [nucl-ex].

[43] B. Armbruster *et al.*, "Upper limits for neutrino oscillations muon-anti-neutrino —> electron-anti-neutrino from muon decay at rest," *Phys. Rev.*, vol. D65, p. 112 001, 2002. DOI: 10.1103/PhysRevD.65.112001. arXiv: hep-ex/0203021 [hep-ex].

[44] P. Astier *et al.*, "Final NOMAD results on muon-neutrino —> tau-neutrino and electron-neutrino —> tau-neutrino oscillations including a new search for tau-neutrino appearance using hadronic tau decays," *Nucl. Phys.*, vol. B611, pp. 3–39, 2001. DOI: 10.1016/S0550-3213(01)00339-X. arXiv: hep-ex/0106102 [hep-ex].

[45] A. A. Aguilar-Arevalo *et al.*, "The MiniBooNE Detector," *Nucl. Instrum. Meth.*, vol. A599, pp. 28–46, 2009. DOI: 10.1016/j.nima.2008.10.028. arXiv: 0806.4201 [hep-ex].

[46] A. A. Aguilar-Arevalo and others , "Improved Search for $\bar{\nu}_\mu \to \bar{\nu}_e$ Oscillations in the MiniBooNE Experiment," *Phys. Rev. Lett.*, vol. 110, p. 161 801, 2013. DOI: 10.1103/PhysRevLett.110.161801. arXiv: 1303.2588 [hep-ex].

[47] B. Fleming, "The MicroBooNE Technical Design Report," 2012. DOI: 10.2172/1333130.

[48] T. A. Mueller *et al.*, "Improved Predictions of Reactor Antineutrino Spectra," *Phys. Rev.*, vol. C83, p. 054 615, 2011. DOI: 10.1103/PhysRevC.83.054615. arXiv: 1101.2663 [hep-ex].

[49] G. Mention, M. Fechner, T. Lasserre, T. A. Mueller, D. Lhuillier, M. Cribier, and A. Letourneau, "The Reactor Antineutrino Anomaly," *Phys. Rev.*, vol. D83, p. 073 006, 2011. DOI: 10.1103/PhysRevD.83.073006. arXiv: 1101.2755 [hep-ex].

[50] C. Giunti and M. Laveder, "Statistical Significance of the Gallium Anomaly," *Phys. Rev.*, vol. C83, p. 065 504, 2011. DOI: 10.1103/PhysRevC.83.065504. arXiv: 1006.3244 [hep-ph].

[51] C. Giunti, "Precise determination of the ^{235}U reactor antineutrino cross section per fission," *Phys. Lett.*, vol. B764, pp. 145–149, 2017. DOI: 10.1016/j.physletb.2016.11.028. arXiv: 1608.04096 [hep-ph].

[52] J. N. Abdurashitov *et al.*, "Measurement of the solar neutrino capture rate with gallium metal. III: Results for the 2002–2007 data-taking period," *Phys. Rev.*, vol. C80, p. 015 807, 2009. DOI: 10.1103/PhysRevC.80.015807. arXiv: 0901.2200 [nucl-ex].

[53] K. Abe *et al.*, "Limits on sterile neutrino mixing using atmospheric neutrinos in Super-Kamiokande," *Phys. Rev.*, vol. D91, p. 052 019, 2015. DOI: 10.1103/PhysRevD.91.052019. arXiv: 1410.2008 [hep-ex].

[54] M. Maltoni, T. Schwetz, M. A. Tortola, and J. W. F. Valle, "Constraining neutrino oscillation parameters with current solar and atmospheric data," *Phys. Rev.*, vol. D67, p. 013 011, 2003. DOI: 10.1103/PhysRevD.67.013011. arXiv: hep-ph/0207227 [hep-ph].

[55] M. G. Aartsen *et al.*, "Searches for Sterile Neutrinos with the IceCube Detector," *Phys. Rev. Lett.*, vol. 117, no. 7, p. 071 801, 2016. DOI: 10.1103/PhysRevLett.117.071801. arXiv: 1605.01990 [hep-ex].

[56] P. Adamson *et al.*, "Search for active-sterile neutrino mixing using neutral-current interactions in NOvA," *Phys. Rev.*, vol. D96, no. 7, p. 072 006, 2017. DOI: 10.1103/PhysRevD.96.072006. arXiv: 1706.04592 [hep-ex].

[57] P. Adamson and others , "Search for sterile neutrinos in MINOS and MINOS+ using a two-detector fit," *Submitted to: Phys. Rev. Lett.*, 2017. arXiv: 1710.06488 [hep-ex].

[58] P. Adamson and others , "Limits on Active to Sterile Neutrino Oscillations from Disappearance Searches in the MINOS, Daya Bay, and Bugey-3 Experiments," *Phys. Rev. Lett.*, vol. 117, no. 15, p. 151 801, 2016, [Addendum: Phys. Rev. Lett.117,no.20,209901(2016)]. DOI: 10.1103/PhysRevLett.117.151801, 10.1103/PhysRevLett.117.209901. arXiv: 1607.01177 [hep-ex].

[59] S. Riemer-Sorensen, D. Parkinson, and T. M. Davis, "What is half a neutrino? Reviewing cosmological constraints on neutrinos and dark radiation," *Publ. Astron. Soc. Austral.*, vol. 30, e029, 2013. DOI: 10.1017/pas.2013.005. arXiv: 1301.7102 [astro-ph.CO].

[60] P. A. R. Ade *et al.*, "Planck 2015 results. XIII. Cosmological parameters," *Astron. Astrophys.*, vol. 594, A13, 2016. DOI: 10.1051/0004-6361/201525830. arXiv: 1502.01589 [astro-ph.CO].

[61] S. Bridle, J. Elvin-Poole, J. Evans, S. Fernandez, P. Guzowski, and S. Soldner-Rembold, "A Combined View of Sterile-Neutrino Constraints from CMB and Neutrino Oscillation Measurements," *Phys. Lett.*, vol. B764, pp. 322–327, 2017. DOI: 10.1016/j.physletb.2016.11.050. arXiv: 1607.00032 [astro-ph.CO].

[62] C. Wilkinson *et al.*, "Testing charged current quasi-elastic and multinucleon interaction models in the NEUT neutrino interaction generator with published datasets from the MiniBooNE and MINERvA experiments," *Phys. Rev.*, vol. D93, no. 7, p. 072 010, 2016. DOI: 10.1103/PhysRevD.93.072010. arXiv: 1601.05592 [hep-ex].

[63] Y. Hayato, "A neutrino interaction simulation program library NEUT," *Acta Phys. Polon.*, vol. B40, pp. 2477–2489, 2009.

[64] P. Stowell *et al.*, "NUISANCE: a neutrino cross-section generator tuning and comparison framework," *JINST*, vol. 12, no. 01, P01016, 2017. DOI: 10.1088/1748-0221/12/01/P01016. arXiv: 1612.07393 [hep-ex].

[65] D. Casper, "The Nuance neutrino physics simulation, and the future," *Nucl. Phys. Proc. Suppl.*, vol. 112, pp. 161–170, 2002, [,161(2002)]. DOI: 10.1016/S0920-5632(02)01756-5. arXiv: hep-ph/0208030 [hep-ph].

[66] C. Andreopoulos *et al.*, "The GENIE Neutrino Monte Carlo Generator," *Nucl. Instrum. Meth.*, vol. A614, pp. 87–104, 2010. DOI: 10.1016/j.nima.2009.12.009. arXiv: 0905.2517 [hep-ph].

[67] C. Juszczak, J. A. Nowak, and J. T. Sobczyk, "Simulations from a new neutrino event generator," *Nucl. Phys. Proc. Suppl.*, vol. 159, pp. 211–216, 2006, [,211(2005)]. DOI: 10.1016/j.nuclphysbps.2006.08.069. arXiv: hep-ph/0512365 [hep-ph].

[68] J. T. Sobczyk, J. A. Nowak, and K. M. Graczyk, "WroNG - Wroclaw Neutrino Generator of events for single pion production," *Nucl. Phys. Proc. Suppl.*, vol. 139, pp. 266–271, 2005, [,266(2004)]. DOI: 10.1016/j.nuclphysbps.2004.11.218. arXiv: hep-ph/0407277 [hep-ph].

[69] O. Buss, T. Gaitanos, K. Gallmeister, H. van Hees, M. Kaskulov, O. Lalakulich, A. B. Larionov, T. Leitner, J. Weil, and U. Mosel, "Transport-theoretical Description of Nuclear Reactions," *Phys. Rept.*, vol. 512, pp. 1–124, 2012. DOI: 10.1016/j.physrep.2011.12.001. arXiv: 1106.1344 [hep-ph].

[70] L. Alvarez-Ruso *et al.*, "NuSTEC White Paper: Status and Challenges of Neutrino-Nucleus Scattering," *Prog. Part. Nucl. Phys.*, vol. 100, pp. 1–68, 2018. DOI: 10.1016/j.ppnp.2018.01.006. arXiv: 1706.03621 [hep-ph].

[71] T. J. Leitner, "Neutrino-nucleus interactions in a coupled-channel hadronic transport model," PhD thesis, Giessen U., 2009.

[72] J. Formaggio and G. Zeller, "From eV to EeV: Neutrino Cross Sections Across Energy Scales," *Rev.Mod.Phys.*, vol. 84, p. 1307, 2012. DOI: 10.1103/RevModPhys.84.1307. arXiv: 1305.7513 [hep-ex].

[73] S. Barish, J. Campbell, G. Charlton, Y. Cho, M. Derrick, *et al.*, "Study of Neutrino Interactions in Hydrogen and Deuterium. 1. Description of the Experiment and Study of the Reaction Neutrino d –> mu- p p(s)," *Phys.Rev.*, vol. D16, p. 3103, 1977. DOI: 10.1103/PhysRevD.16.3103.

[74] G. M. Radecky *et al.*, "Study of Single Pion Production by Weak Charged Currents in Low-energy Neutrino *d* Interactions," *Phys. Rev.*, vol. D25, pp. 1161–1173, 1982, [Erratum: Phys. Rev.D26,3297(1982)]. DOI: 10.1103/PhysRevD.25.1161,10.1103/PhysRevD.26.3297.

[75] C. Baltay *et al.*, "CROSS-SECTIONS AND SCALING VARIABLE DISTRIBUTIONS OF NEUTRAL AND CHARGED CURRENT NEUTRINO NUCLEON INTERACTIONS FROM A LOW-ENERGY NARROW BAND BEAM," *Phys. Rev. Lett.*, vol. 44, pp. 916–919, 1980. DOI: 10.1103/PhysRevLett.44.916.

[76] C. Llewellyn Smith, "Neutrino Reactions at Accelerator Energies," *Phys.Rept.*, vol. 3, pp. 261–379, 1972. DOI: 10.1016/0370-1573(72)90010-5.

[77] R. Bradford, A. Bodek, H. S. Budd, and J. Arrington, "A New parameterization of the nucleon elastic form-factors," *Nucl.Phys.Proc.Suppl.*, vol. 159, pp. 127–132, 2006. DOI: 10.1016/j.nuclphysbps.2006.08.028. arXiv: hep-ex/0602017 [hep-ex].

[78] A. Bodek, S. Avvakumov, R. Bradford, and H. S. Budd, "Vector and Axial Nucleon Form Factors:A Duality Constrained Parameterization," *Eur.Phys.J.*, vol. C53, pp. 349–354, 2008. DOI: 10.1140/epjc/s10052-007-0491-4. arXiv: 0708.1946 [hep-ex].

[79] S. L. Adler, "Tests of the Conserved Vector Current and Partially Conserved Axial-Vector Current Hypotheses in High-Energy Neutrino Reactions," *Phys.Rev.*, vol. 135, B963–B966, 1964. DOI: 10.1103/PhysRev.135.B963.

[80] M. Goldberger and S. Treiman, "Form-factors in Beta decay and muon capture," *Phys.Rev.*, vol. 111, pp. 354–361, 1958. DOI: 10.1103/PhysRev.111.354.

[81] V. Bernard, L. Elouadrhiri, and U. Meissner, "Axial structure of the nucleon: Topical Review," *J.Phys.*, vol. G28, R1–R35, 2002. DOI: 10.1088/0954-3899/28/1/201. arXiv: hep-ph/0107088 [hep-ph].

[82] D. Rein and L. M. Sehgal, "Neutrino Excitation of Baryon Resonances and Single Pion Production," *Annals Phys.*, vol. 133, pp. 79–153, 1981. DOI: 10.1016/0003-4916(81)90242-6.

[83] D. Drechsel, S. S. Kamalov, and L. Tiator, "Unitary Isobar Model - MAID2007," *Eur. Phys. J.*, vol. A34, pp. 69–97, 2007. DOI: 10.1140/epja/i2007-10490-6. arXiv: 0710.0306 [nucl-th].

[84] R. P. Feynman, M. Kislinger, and F. Ravndal, "Current matrix elements from a relativistic quark model," *Phys. Rev.*, vol. D3, pp. 2706–2732, 1971. DOI: 10.1103/PhysRevD.3.2706.

[85] B. Szczerbinska, T. Sato, K. Kubodera, and T.-S. Lee, "Neutrino-nucleus reactions in the delta resonance region," *Phys.Lett.*, vol. B649, pp. 132–138, 2007. DOI: 10.1016/j.physletb.2007.03.046. arXiv: nucl-th/0610093 [nucl-th].

[86] C. Patrignani *et al.*, "Review of Particle Physics," *Chin. Phys.*, vol. C40, no. 10, p. 100 001, 2016. DOI: 10.1088/1674-1137/40/10/100001.

[87] S. Boyd, S. Dytman, E. Hernandez, J. Sobczyk, and R. Tacik, "Comparison of models of neutrino-nucleus interactions," *AIP Conf. Proc.*, vol. 1189, pp. 60–73, 2009. DOI: 10.1063/1.3274191.

[88] K. M. Graczyk, J. Żmuda, and J. T. Sobczyk, "Electroweak form factors of the Delta(1232) resonance," *Phys. Rev.*, vol. D90, no. 9, p. 093 001, 2014. DOI: 10.1103/PhysRevD.90.093001. arXiv: 1407.5445 [hep-ph].

[89] J. M. Conrad, M. H. Shaevitz, and T. Bolton, "Precision measurements with high-energy neutrino beams," *Rev.Mod.Phys.*, vol. 70, pp. 1341–1392, 1998. DOI: 10.1103/RevModPhys.70.1341. arXiv: hep-ex/9707015 [hep-ex].

[90] M. Klein, "Structure functions in deep inelastic lepton-nucleon scattering," *International Journal of Modern Physics A*, vol. 15, no. supp01b, pp. 467–494, 2000.

[91] J. Owens, A. Accardi, and W. Melnitchouk, "Global parton distributions with nuclear and finite-Q^2 corrections," *Phys.Rev.*, vol. D87, no. 9, p. 094 012, 2013. DOI: 10.1103/PhysRevD.87.094012. arXiv: 1212.1702 [hep-ph].

[92] R. Roberts and M. Whalley, "A compilation of structure functions in deep-inelastic scattering," *Journal of Physics G: Nuclear and Particle Physics*, vol. 17, no. D, p. D1, 1991.

[93] J. Blümlein, "The theory of deeply inelastic scattering," *Progress in Particle and Nuclear Physics*, vol. 69, pp. 28–84, 2013.

[94] T. Sjostrand, S. Mrenna, and P. Z. Skands, "A Brief Introduction to PYTHIA 8.1," *Comput. Phys. Commun.*, vol. 178, pp. 852–867, 2008. DOI: 10.1016/j.cpc.2008.01.036. arXiv: 0710.3820 [hep-ph].

[95] B. Andersson, G. Gustafson, G. Ingelman, and T. Sjostrand, "Parton Fragmentation and String Dynamics," *Phys. Rept.*, vol. 97, pp. 31–145, 1983. DOI: 10.1016/0370-1573(83)90080-7.

[96] C. Andreopoulos, C. Barry, S. Dytman, H. Gallagher, T. Golan, R. Hatcher, G. Perdue, and J. Yarba, "The GENIE Neutrino Monte Carlo Generator: Physics and User Manual," 2015. arXiv: 1510.05494 [hep-ph].

[97] A. Bodek, M. E. Christy, and B. Coopersmith, "Effective spectral function for quasielastic scattering on nuclei from ${}^{2}_{1}\mathrm{H}$ to ${}^{208}_{82}\mathrm{Pb}$," *AIP Conf. Proc.*, vol. 1680, p. 020 003, 2015. DOI: 10.1063/1.4931862,10.1016/j.nuclphysbps.2015.09.27. arXiv: 1409.8545 [nucl-th].

[98] T. Leitner, O. Buss, L. Alvarez-Ruso, and U. Mosel, "Electron- and neutrino-nucleus scattering from the quasielastic to the resonance region," *Phys.Rev.*, vol. C79, p. 034 601, 2009. DOI: 10.1103/PhysRevC.79.034601. arXiv: 0812.0587 [nucl-th].

[99] O. Benhar, A. Fabrocini, S. Fantoni, and I. Sick, "Spectral function of finite nuclei and scattering of GeV electrons," *Nucl.Phys.*, vol. A579, pp. 493–517, 1994. DOI: 10.1016/0375-9474(94)90920-2.

[100] T. Donnelly and I. Sick, "Superscaling of inclusive electron scattering from nuclei," *Phys.Rev.*, vol. C60, p. 065 502, 1999. DOI: 10.1103/PhysRevC.60.065502. arXiv: nucl-th/9905060 [nucl-th].

[101] A. Bodek, H. Budd, and M. Christy, "Neutrino Quasielastic Scattering on Nuclear Targets: Parametrizing Transverse Enhancement (Meson Exchange Currents)," *Eur.Phys.J.*, vol. C71, p. 1726, 2011. DOI: 10.1140/epjc/s10052-011-1726-y. arXiv: 1106.0340 [hep-ph].

[102] A. Bodek and J. Ritchie, "Fermi Motion Effects in Deep Inelastic Lepton Scattering from Nuclear Targets," *Phys.Rev.*, vol. D23, p. 1070, 1981. DOI: 10.1103/PhysRevD.23.1070.

[103] A. M. Ankowski, O. Benhar, C. Mariani, and E. Vagnoni, "Effect of the $2p2h$ cross-section uncertainties on an analysis of neutrino oscillations," *Phys. Rev.*, vol. D93, no. 11, p. 113 004, 2016. DOI: 10.1103/PhysRevD.93.113004. arXiv: 1603.01072 [hep-ph].

[104] J. Nieves, R. Gran, I. Ruiz Simo, F. Sánchez, and M. J. Vicente Vacas, "Neutrino-nucleus CCQE-like scattering," *Nucl. Part. Phys. Proc.*, vol. 273-275, pp. 1830–1835, 2016. DOI: 10.1016/j.nuclphysbps.2015.09.295. arXiv: 1411.7821 [hep-ph].

[105] G. Fiorentini *et al.*, "Measurement of Muon Neutrino Quasielastic Scattering on a Hydrocarbon Target at E??3.5??GeV," *Phys.Rev.Lett.*, vol. 111, p. 022 502, 2013. DOI: 10.1103/PhysRevLett.111.022502. arXiv: 1305.2243 [hep-ex].

[106] S. D.E. M. Author), Personal communication.

[107] R. Gran, J. Nieves, F. Sanchez, and M. Vicente Vacas, "Neutrino-nucleus quasi-elastic and 2p2h interactions up to 10 GeV," *Phys.Rev.*, vol. D88, no. 11, p. 113 007, 2013. DOI: 10.1103/PhysRevD.88.113007. arXiv: 1307.8105 [hep-ph].

[108] M. Martini, M. Ericson, G. Chanfray, and J. Marteau, "Unified approach for nucleon knock-out and coherent and incoherent pion production in neutrino interactions with nuclei," *Physical Review C*, vol. 80, no. 6, p. 065 501, 2009.

[109] J. Nieves, J. E. Amaro, and M. Valverde, "Inclusive quasi-elastic neutrino reactions," *Phys. Rev.*, vol. C70, p. 055 503, 2004, [Erratum: Phys. Rev.C72,019902(2005)]. DOI: 10.1103/PhysRevC.70.055503,10.1103/PhysRevC.72.019902. arXiv: nucl-th/0408005 [nucl-th].

[110] R. Gran, "Model uncertainties for Valencia RPA effect for MINERvA," 2017. arXiv: 1705.02932 [hep-ex].

[111] P. Sinclair *et al.*, "Implementation of a multi-nucleon interaction model into NEUT," *T2K-TN-170*, 2014.

[112] J. T. Sobczyk, "Multinucleon ejection model for Meson Exchange Current neutrino interactions," *Phys.Rev.*, vol. C86, p. 015 504, 2012. DOI: 10.1103/PhysRevC.86.015504. arXiv: 1201.3673 [hep-ph].

[113] P. A. Rodrigues *et al.*, "Identification of nuclear effects in neutrino-carbon interactions at low three-momentum transfer," *Phys. Rev. Lett.*, vol. 116, p. 071 802, 2016. DOI: 10.1103/PhysRevLett.116.071802. arXiv: 1511.05944 [hep-ex].

[114] T. Golan, C. Juszczak, and J. T. Sobczyk, "Final State Interactions Effects in Neutrino-Nucleus Interactions," *Phys. Rev.*, vol. C86, p. 015 505, 2012. DOI: 10.1103/PhysRevC.86.015505. arXiv: 1202.4197 [nucl-th].

[115] K. Abe *et al.*, "Measurement of double differential muon neutrino charged-current interactions on C_8H_8 without pions in the final state using the T2K off-axis beam," *Phys. Rev.*, vol. D93, no. 11, p. 112 012, 2016. DOI: 10.1103/PhysRevD.93.112012. arXiv: 1602.03652 [hep-ex].

[116] K. Abe *et al.*, "First measurement of the ν_μ charged-current cross section on a water target without pions in the final state," *Phys. Rev.*, vol. D97, no. 1, p. 012 001, 2018. DOI: 10.1103/PhysRevD.97.012001. arXiv: 1708.06771 [hep-ex].

[117] L. L. Salcedo, E. Oset, M. J. Vicente-Vacas, and C. Garcia-Recio, "Computer Simulation of Inclusive Pion Nuclear Reactions," *Nucl. Phys.*, vol. A484, pp. 557–592, 1988. DOI: 10.1016/0375-9474(88)90310-7.

[118] W. Y. Ma, E. S. Pinzon Guerra, M. Yu, A. Fiorentini, and T. Feusels, "Current status of final-state interaction models and their impact on neutrino-nucleus interactions," *J. Phys. Conf. Ser.*, vol. 888, no. 1, p. 012 171, 2017. DOI: 10.1088/1742-6596/888/1/012171.

[119] M. A. H, "Proceedings of the seventeenth recontre de moriond conference on elementary particle physics.," *Editions Fronriers, Gif-sur-Yvette, France, 1982*,

[120] T. Leitner, L. Alvarez-Ruso, and U. Mosel, "Charged current neutrino nucleus interactions at intermediate energies," *Phys.Rev.*, vol. C73, p. 065 502, 2006. DOI: 10.1103/PhysRevC.73.065502. arXiv: nucl-th/0601103 [nucl-th].

[121] U. Mosel and K. Gallmeister, "Muon-neutrino-induced charged current pion production on nuclei," *Phys. Rev.*, vol. C96, no. 1, p. 015 503, 2017. DOI: 10.1103/PhysRevC.96.015503. arXiv: 1702.04932 [nucl-th].

[122] J. Campbell *et al.*, "Study of the reaction nu p —> mu- pi+ p," *Phys. Rev. Lett.*, vol. 30, pp. 335–339, 1973. DOI: 10.1103/PhysRevLett.30.335.

[123] W. A. Mann *et al.*, "Study of the reaction nu n —> mu- p," *Phys. Rev. Lett.*, vol. 31, pp. 844–847, 1973. DOI: 10.1103/PhysRevLett.31.844.

[124] S. J. Barish *et al.*, "Inclusive Neutrino p and Neutrino n Charged-Current Neutrino Reactions Below 6-GeV," *Phys. Lett.*, vol. 66B, pp. 291–294, 1977. DOI: 10.1016/0370-2693(77)90883-8.

[125] S. J. Barish and others , "Study of Neutrino Interactions in Hydrogen and Deuterium. 1. Description of the Experiment and Study of the Reaction Neutrino d –> mu- p p(s)," *Phys. Rev.*, vol. D16, p. 3103, 1977. DOI: 10.1103/PhysRevD.16.3103.

[126] S. J. Barish *et al.*, "Study of Neutrino Interactions in Hydrogen and Deuterium. 1. Description of the Experiment and Study of the Reaction Neutrino d –> mu- p p(s)," *Phys. Rev.*, vol. D16, p. 3103, 1977. DOI: 10.1103/PhysRevD.16.3103.

[127] G. M. Radecky *et al.*, "Study of Single Pion Production by Weak Charged Currents in Low-energy Neutrino *d* Interactions," *Phys. Rev.*, vol. D25, pp. 1161–1173, 1982, [Erratum: Phys. Rev.D26,3297(1982)]. DOI: 10.1103/PhysRevD.25.1161,10.1103/PhysRevD.26.3297.

[128] D. Day *et al.*, "STUDY OF neutrino D CHARGED CURRENT TWO PION PRODUCTION IN THE THRESHOLD REGION," *Phys. Rev.*, vol. D28, pp. 2714–2720, 1983. DOI: 10.1103/PhysRevD.28.2714.

[129] C. Baltay *et al.*, "CROSS-SECTIONS AND SCALING VARIABLE DISTRIBUTIONS OF NEUTRAL AND CHARGED CURRENT NEUTRINO NUCLEON INTERACTIONS FROM A LOW-ENERGY NARROW BAND BEAM," *Phys. Rev. Lett.*, vol. 44, pp. 916–919, 1980. DOI: 10.1103/PhysRevLett.44.916.

[130] G. Fanourakis, L. K. Resvanis, G. Grammatikakis, P. Tsilimigras, A. Vayaki, U. Camerini, W. F. Fry, R. J. Loveless, J. H. Mapp, and D. D. Reeder, "Study of Low-energy Anti-neutrino Interactions on Protons," *Phys. Rev.*, vol. D21, p. 562, 1980. DOI: 10.1103/PhysRevD.21.562.

[131] N. J. Baker, A. M. Cnops, P. L. Connolly, S. A. Kahn, H. G. Kirk, M. J. Murtagh, R. B. Palmer, N. P. Samios, and M. Tanaka, "Quasielastic Neutrino Scattering: A Measurement of the Weak Nucleon Axial Vector Form-Factor," *Phys. Rev.*, vol. D23, pp. 2499–2505, 1981. DOI: 10.1103/PhysRevD.23.2499.

[132] J. Bell *et al.*, "Cross-section Measurements for the Reactions Neutrino $p \to \mu^- \pi^+ p$ and Neutrino $p \to \mu^- K^+ p$ at High-energies," *Phys. Rev. Lett.*, vol. 41, p. 1008, 1978. DOI: 10.1103/PhysRevLett.41.1008.

[133] T. Kitagaki *et al.*, "NEUTRINO FLUX AND TOTAL CHARGED CURRENT CROSS-SECTIONS IN HIGH-ENERGY NEUTRINO DEUTERIUM INTERACTIONS," *Phys. Rev. Lett.*, vol. 49, pp. 98–101, 1982. DOI: 10.1103/PhysRevLett.49.98.

[134] T. Kitagaki and others , "High-Energy Quasielastic Muon-neutrino n —> mu- p Scattering in Deuterium," *Phys. Rev.*, vol. D28, pp. 436–442, 1983. DOI: 10.1103/PhysRevD.28.436.

[135] P. Allen *et al.*, "Single π^+ Production in Charged Current Neutrino - Hydrogen Interactions," *Nucl. Phys.*, vol. B176, p. 269, 1980. DOI: 10.1016/0550-3213(80)90450-2.

[136] P. Allen and others , "A Study of Single Meson Production in Neutrino and Anti-neutrinos Charged Current Interactions on Protons," *Nucl. Phys.*, vol. B264, pp. 221–242, 1986. DOI: 10.1016/0550-3213(86)90480-3.

[137] D. Allasia *et al.*, "Investigation of exclusive channels in neutrino / anti-neutrino deuteron charged current interactions," *Nucl. Phys.*, vol. B343, pp. 285–309, 1990. DOI: 10.1016/0550-3213(90)90472-P.

[138] T. Kitagaki *et al.*, "Charged Current Exclusive Pion Production in Neutrino Deuterium Interactions," *Phys. Rev.*, vol. D34, pp. 2554–2565, 1986. DOI: 10.1103/PhysRevD.34.2554.

[139] D. University. (). Durham Low Energy Neutrino HepData Repository, [Online]. Available: http://hepdata.cedar.ac.uk/review/neutrino/.

[140] K. Abe *et al.*, "The T2K Experiment," *Nucl. Instrum. Meth.*, vol. A659, pp. 106–135, 2011. DOI: 10.1016/j.nima.2011.06.067. arXiv: 1106.1238 [physics.ins-det].

[141] Y. Fukuda *et al.*, "The Super-Kamiokande detector," *Nucl. Instrum. Meth.*, vol. A501, pp. 418–462, 2003. DOI: 10.1016/S0168-9002(03)00425-X.

[142] K. Abe *et al.*, "T2K neutrino flux prediction," *Phys. Rev.*, vol. D87, no. 1, p. 012 001, 2013, [Addendum: Phys. Rev.D87,no.1,019902(2013)]. DOI: 10.1103/PhysRevD.87.012001,10.1103/PhysRevD.87.019902. arXiv: 1211.0469 [hep-ex].

[143] M. Batkiewicz, "Latest Results from T2K," in *Proceedings, 17th Lomonosov Conference on Elementary Particle Physics: Moscow, Russia, August 20-26, 2015*, 2017, pp. 66–72. DOI: 10.1142/9789813224568_0010. arXiv: 1705.04277 [hep-ex]. [Online]. Available: http://inspirehep.net/record/1599081/files/arXiv:1705.04277.pdf.

[144] D. Allan *et al.*, "The Electromagnetic Calorimeter for the T2K Near Detector ND280," *JINST*, vol. 8, P10019, 2013. DOI: 10.1088/1748-0221/8/10/P10019. arXiv: 1308.3445 [physics.ins-det].

[145] S. Assylbekov *et al.*, "The T2K ND280 Off-Axis Pi-Zero Detector," *Nucl. Instrum. Meth.*, vol. A686, pp. 48–63, 2012. DOI: 10.1016/j.nima.2012.05.028. arXiv: 1111.5030 [physics.ins-det].

[146] S. Aoki *et al.*, "The T2K Side Muon Range Detector (SMRD)," *Nucl. Instrum. Meth.*, vol. A698, pp. 135–146, 2013. DOI: 10.1016/j.nima.2012.10.001. arXiv: 1206.3553 [physics.ins-det].

[147] Y. Oyama, "Current status of the T2K experiment," *PoS*, vol. PLANCK2015, p. 094, 2015. arXiv: 1510.07200 [hep-ex].

[148] R. Tacik, "The T2K fine-grained detectors," *Nucl. Instrum. Meth.*, vol. A623, pp. 309–311, 2010. DOI: 10.1016/j.nima.2010.02.231.

[149] C. Hearty and E. Mazzucato, "Time projection chambers for the T2K near detector," *J. Phys. Conf. Ser.*, vol. 136, p. 042 036, 2008. DOI: 10.1088/1742-6596/136/4/042036.

[150] N. Abgrall *et al.*, "Time Projection Chambers for the T2K Near Detectors," *Nucl. Instrum. Meth.*, vol. A637, pp. 25–46, 2011. DOI: 10.1016/j.nima.2011.02.036. arXiv: 1012.0865 [physics.ins-det].

[151] L. Aliaga *et al.*, "Design, Calibration, and Performance of the MINERvA Detector," *Nucl. Instrum. Meth.*, vol. A743, pp. 130–159, 2014. DOI: 10.1016/j.nima.2013.12.053. arXiv: 1305.5199 [physics.ins-det].

[152] A. G. Abramov, N. A. Galyaev, V. I. Garkusha, J. Hylen, F. N. Novoskoltsev, A. D. Ryabov, and V. G. Zarucheisky, "Beam optics and target conceptual designs for the NuMI project," *Nucl. Instrum. Meth.*, vol. A485, pp. 209–227, 2002. DOI: 10.1016/S0168-9002(01)02112-X.

[153] D. G. Michael *et al.*, "The Magnetized steel and scintillator calorimeters of the MINOS experiment," *Nucl. Instrum. Meth.*, vol. A596, pp. 190–228, 2008. DOI: 10.1016/j.nima.2008.08.003. arXiv: 0805.3170 [physics.ins-det].

[154] J. Evans, "The MINOS experiment: results and prospects," *Adv. High Energy Phys.*, vol. 2013, p. 182 537, 2013. DOI: 10.1155/2013/182537. arXiv: 1307.0721 [hep-ex].

[155] C. M. Marshall *et al.*, "Measurement of neutral-current K^+ production by neutrinos using MINERvA," *Phys. Rev. Lett.*, vol. 119, no. 1, p. 011 802, 2017. DOI: 10.1103/PhysRevLett.119.011802. arXiv: 1611.02224 [hep-ex].

[156] D. S. Ayres *et al.*, "The NOvA Technical Design Report," 2007, FERMILAB-DESIGN-2007-01.

[157] R. B. Patterson, "The NOvA Experiment: Status and Outlook," 2012, [Nucl. Phys. Proc. Suppl.235-236,151(2013)]. DOI: 10.1016/j.nuclphysbps.2013.04.005. arXiv: 1209.0716 [hep-ex].

[158] A. A. Aguilar-Arevalo *et al.*, "The Neutrino Flux prediction at MiniBooNE," *Phys. Rev.*, vol. D79, p. 072 002, 2009. DOI: 10.1103/PhysRevD.79.072002. arXiv: 0806.1449 [hep-ex].

[159] T. Katori, "Neutrino Cross Section Measurements for Long-Baseline Accelerator-based Neutrino Oscillation Experiments," in *Proceedings, 43rd Rencontres de Moriond on Electroweak Interactions and Unified Theories: La Thuile, Italy, March 1-8, 2008*, 2008, pp. 369–376. arXiv: 0805.2476 [hep-ex].

[160] C. Mariani *et al.*, "Measurement of inclusive π^0 production in the Charged-Current Interactions of Neutrinos in a 1.3-GeV wide band beam," *Phys. Rev.*, vol. D83, p. 054 023, 2011. DOI: 10.1103/PhysRevD.83.054023. arXiv: 1012.1794 [hep-ex].

[161] C. Anderson *et al.*, "First Measurements of Inclusive Muon Neutrino Charged Current Differential Cross Sections on Argon," *Phys. Rev. Lett.*, vol. 108, p. 161 802, 2012. DOI: 10.1103/PhysRevLett.108.161802. arXiv: 1111.0103 [hep-ex].

[162] M. Antonello *et al.*, "A Proposal for a Three Detector Short-Baseline Neutrino Oscillation Program in the Fermilab Booster Neutrino Beam," 2015. arXiv: 1503.01520 [physics.ins-det].

[163] S. Amerio *et al.*, "Design, construction and tests of the ICARUS T600 detector," *Nucl. Instrum. Meth.*, vol. A527, pp. 329–410, 2004. DOI: 10.1016/j.nima.2004.02.044.

[164] K. Abe *et al.*, "Measurement of inclusive double differential ν_μ charged-current cross section with improved acceptance in the T2K off-axis near detector," *Phys. Rev.*, vol. D98, p. 012 004, 2018. DOI: 10.1103/PhysRevD.98.012004. arXiv: 1801.05148 [hep-ex].

[165] K. Abe and others, "First measurement of the muon neutrino charged current single pion production cross section on water with the T2K near detector," *Phys. Rev.*, vol. D95, no. 1, p. 012 010, 2017. DOI: 10.1103/PhysRevD.95.012010. arXiv: 1605.07964 [hep-ex].

[166] C. E. Patrick *et al.*, "Measurement of the Muon Antineutrino Double Differential Cross Section for Quasielastic-like Scattering on Hydrocarbon at $E_\nu \sim 3.5$GeV," *Phys. Rev.*, vol. D97, no. 5, p. 052 002, 2018. DOI: 10.1103/PhysRevD.97.052002. arXiv: 1801.01197 [hep-ex].

[167] O. Altinok *et al.*, "Measurement of ν_μ charged-current single π^0 production on hydrocarbon in the few-GeV region using MINERvA," *Phys. Rev.*, vol. D96, no. 7, p. 072 003, 2017. DOI: 10.1103/PhysRevD.96.072003. arXiv: 1708.03723 [hep-ex].

[168] C. L. McGivern *et al.*, "Cross sections for ν_μ and $\bar{\nu}_\mu$ induced pion production on hydrocarbon in the few-GeV region using MINERvA," *Phys. Rev.*, vol. D94, no. 5, p. 052 005, 2016. DOI: 10.1103/PhysRevD.94.052005. arXiv: 1606.07127 [hep-ex].

[169] J. Mousseau *et al.*, "Measurement of Partonic Nuclear Effects in Deep-Inelastic Neutrino Scattering using MINERvA," *Phys. Rev.*, vol. D93, no. 7, p. 071 101, 2016. DOI: 10.1103/PhysRevD.93.071101. arXiv: 1601.06313 [hep-ex].

[170] A. A. Aguilar-Arevalo *et al.*, "First measurement of the muon antineutrino double differential charged-current quasielastic cross section," *Phys. Rev.*, vol. D88, no. 3, p. 032 001, 2013. DOI: 10.1103/PhysRevD.88.032001. arXiv: 1301.7067 [hep-ex].

[171] A. A. Aguilar-Arevalo and others , "Measurement of Neutrino-Induced Charged-Current Charged Pion Production Cross Sections on Mineral Oil at $E_\nu \sim 1$ GeV," *Phys. Rev.*, vol. D83, p. 052 007, 2011. DOI: 10.1103/PhysRevD.83.052007. arXiv: 1011.3572 [hep-ex].

[172] S. Bordoni *et al.*, "Study of muon neutrino disappearance with the ND280 tracker (Unofficial)," *T2K-TN-239*, 2016.

[173] P. Perio *et al.*, "Cross Section Parameters for 2012 Oscillation Analysis," *T2K-TN-108*, 2013.

[174] A. A. Aguilar-Arevalo *et al.*, "First Measurement of the Muon Neutrino Charged Current Quasielastic Double Differential Cross Section," *Phys. Rev.*, vol. D81, p. 092 005, 2010. DOI: 10.1103/PhysRevD.81.092005. arXiv: 1002.2680 [hep-ex].

[175] A. A. Aguilar-Arevalo *et al.*, "Measurement of ν_μ and $\bar{\nu}_\mu$ induced neutral current single π^0 production cross sections on mineral oil at $E_\nu \sim \mathcal{O}(1\text{GeV})$," *Phys. Rev.*, vol. D81, p. 013 005, 2010. DOI: 10.1103/PhysRevD.81.013005. arXiv: 0911.2063 [hep-ex].

[176] A. A. Aguilar-Arevalo *et al.*, "Measurement of ν_μ-induced charged-current neutral pion production cross sections on mineral oil at $E_\nu \in 0.5 - 2.0$ GeV," *Phys. Rev.*, vol. D83, p. 052 009, 2011. DOI: 10.1103/PhysRevD.83.052009. arXiv: 1010.3264 [hep-ex].

[177] F. James and M. Roos, "Minuit: A System for Function Minimization and Analysis of the Parameter Errors and Correlations," *Comput. Phys. Commun.*, vol. 10, pp. 343–367, 1975. DOI: 10.1016/0010-4655(75)90039-9.

[178] G. P. Lepage and S. J. Brodsky, "Exclusive Processes in Perturbative Quantum Chromodynamics," *Phys. Rev.*, vol. D22, p. 2157, 1980. DOI: 10.1103/PhysRevD.22.2157.

[179] J. E. Amaro and E. Ruiz Arriola, "Axial-vector dominance predictions in quasielastic neutrino-nucleus scattering," *Phys. Rev.*, vol. D93, no. 5, p. 053 002, 2016. DOI: 10.1103/PhysRevD.93.053002. arXiv: 1510.07532 [nucl-th].

[180] A. S. Meyer, M. Betancourt, R. Gran, and R. J. Hill, "Deuterium target data for precision neutrino-nucleus cross sections," *Phys. Rev.*, vol. D93, no. 11, p. 113 015, 2016. DOI: 10.1103/PhysRevD.93.113015. arXiv: 1603.03048 [hep-ph].

[181] B. Bhattacharya, R. J. Hill, and G. Paz, "Model independent determination of the axial mass parameter in quasielastic neutrino-nucleon scattering," *Phys. Rev.*, vol. D84, p. 073 006, 2011. DOI: 10.1103/PhysRevD.84.073006. arXiv: 1108.0423 [hep-ph].

[182] B. Bhattacharya, G. Paz, and A. J. Tropiano, "Model-independent determination of the axial mass parameter in quasielastic antineutrino-nucleon scattering," *Phys. Rev.*, vol. D92, no. 11, p. 113 011, 2015. DOI: 10.1103/PhysRevD.92.113011. arXiv: 1510.05652 [hep-ph].

[183] C. Adamuscin, E. Tomasi-Gustafsson, E. Santopinto, and R. Bijker, "Two-component model for the axial form factor of the nucleon," *Phys. Rev.*, vol. C78, p. 035 201, 2008. DOI: 10.1103/PhysRevC.78.035201. arXiv: 0706.3509 [nucl-th].

[184] F. Iachello, A. D. Jackson, and A. Lande, "Semiphenomenological fits to nucleon electromagnetic form-factors," *Phys. Lett.*, vol. 43B, pp. 191–196, 1973. DOI: 10.1016/0370-2693(73)90266-9.

[185] R. Bijker and F. Iachello, "Re-analysis of the nucleon space- and time-like electromagnetic form-factors in a two-component model," *Phys. Rev.*, vol. C69, p. 068 201, 2004. DOI: 10.1103/PhysRevC.69.068201. arXiv: nucl-th/0405028 [nucl-th].

[186] S. K. Singh, "The Effect of final state interactions and deuteron binding in neutrino d –> Mu- p p," *Nucl. Phys.*, vol. B36, pp. 419–435, 1972. DOI: 10.1016/0550-3213(72)90227-1.

[187] R. Brun and F. Rademakers, "ROOT: An object oriented data analysis framework," *Nucl. Instrum. Meth.*, vol. A389, pp. 81–86, 1997. DOI: 10.1016/S0168-9002(97)00048-X.

[188] S. Bienstock *et al.*, "Assessing the effect of cross-section model uncertainties on the T2K oscillation analyses with simulated data studies using the BANFF, MaCh3, P-Theta and VALOR fit frameworks," *T2K-TN-331*, 2018.

[189] J. Wolcott, "Recent Cross Section Work From NOvA," in *18th International Workshop on Neutrino Factories and Future Neutrino Facilities Search (NuFact16) Quy Nhon, Vietnam, August 21-27, 2016*, 2016. arXiv: 1611.02600 [hep-ex]. [Online]. Available: http://inspirehep.net/record/1496386/files/arXiv:1611.02600.pdf.

[190] R. A. Smith and E. J. Moniz, "NEUTRINO REACTIONS ON NUCLEAR TARGETS," *Nucl. Phys.*, vol. B43, p. 605, 1972, [Erratum: Nucl. Phys.B101,547(1975)]. DOI: 10.1016/0550-3213(75)90612-4,10.1016/0550-3213(72)90040-5.

[191] C. Berger and L. Sehgal, "PCAC and coherent pion production by low energy neutrinos," *Phys.Rev.*, vol. D79, p. 053 003, 2009. DOI: 10.1103/PhysRevD.79.053003. arXiv: 0812.2653 [hep-ph].

[192] P. Rodrigues, C. Wilkinson, and K. McFarland, "Constraining the GENIE model of neutrino-induced single pion production using reanalyzed bubble chamber data," *Eur. Phys. J.*, vol. C76, no. 8, p. 474, 2016. DOI: 10.1140/epjc/s10052-016-4314-3. arXiv: 1601.01888 [hep-ex].

[193] B. Eberly *et al.*, "Charged pion production in ν_μ interactions on hydrocarbon at $\langle E_\nu \rangle = 4.0$ GeV, (updated 2017 data release)," *Phys. Rev.*, vol. D92, no. 9, p. 092 008, 2015. DOI: 10.1103/PhysRevD.92.092008. arXiv: 1406.6415 [hep-ex].

[194] C. Wret, Implementation of a broad range of pion production comparisons in NUISANCE. 2017.

[195] A. Mislivec *et al.*, "Measurement of total and differential cross sections of neutrino and antineutrino coherent $\pi^\pm$ production on carbon," *Phys. Rev.*, vol. D97, no. 3, p. 032 014, 2018. DOI: 10.1103/PhysRevD.97.032014. arXiv: 1711.01178 [hep-ex].

[196] D. Rein and L. M. Sehgal, "Coherent π 0 production in neutrino reactions," *Nuclear Physics B*, vol. 223, no. 1, pp. 29–44, 1983.

[197] C. Wilkinson, P. Rodrigues, S. Cartwright, L. Thompson, and K. McFarland, "Reanalysis of bubble chamber measurements of muon-neutrino induced single pion production," *Phys. Rev.*, vol. D90, no. 11, p. 112 017, 2014. DOI: 10.1103/PhysRevD.90.112017. arXiv: 1411.4482 [hep-ex].

[198] C. Wret, Private communication. Analysis of additional resonances in pion angular distributions. 2017.

[199] G. Collaboration. (2017). Pre-generated public splines for GENIE 2.12.6, [Online]. Available: https://www.hepforge.org/archive/genie/data/2.12.6/.

[200] C. Berger and L. Sehgal, "Lepton mass effects in single pion production by neutrinos," *Phys.Rev.*, vol. D76, p. 113 004, 2007. DOI: 10.1103/PhysRevD.76.113004. arXiv: 0709.4378 [hep-ph].

[201] P. Adamson *et al.*, "Study of quasielastic scattering using charged-current numu-iron interactions in the MINOS near detector," *Phys. Rev.*, vol. D91, no. 1, p. 012 005, 2015. DOI: 10.1103/PhysRevD.91.012005. arXiv: 1410.8613 [hep-ex].

Appendix A

Simple Baseline Approximation for Short Baseline Oscillations

For some historical experiments, information on the exact experimental baseline for use in a neutrino oscillation analysis is not available. In this section we derive a simple formula for the oscillation distance of an accelerator neutrino experiment based on the dimensions of the detector and beam decay volume. This was originally developed to support the possible application of the sterile neutrino cross-section bias evaluation developed in Chapter 4 to CCQE data from the ANL and BNL experiments.

Between the target and detector a neutrino beam will pass through a decay volume of length l_V and a shielding region of length l_S, before finally reaching a detector of length l_D along the beam axis. In the MiniBooNE experiment l_V, l_S, and l_D can be approximated as 50 m, 479 m, and 12.2 m respectively [45]. A conservative approach can be taken where the distribution of meson parent decay points, x_D, is assumed to be a gaussian centred in the middle of the decay volume with a width equal to half the decay volume length.

$$x_V = \frac{l_V}{2} \quad , \quad \Delta x_V = \frac{l_D}{2} \tag{A.1}$$

A similar assumption is made to choose an interaction point inside the detector, x_B, as

$$x_D = \frac{2l_V + 2l_S + l_D}{2} \quad , \quad \Delta x_D = \frac{l_D}{2} \tag{A.2}$$

The combination of these two gaussians gives an approximation for the total oscillation distance, L, as

$$L = x_D - x_V \quad , \quad \Delta L = \sqrt{\Delta x_D^2 + \Delta x_V^2} \tag{A.3}$$

$$L = \frac{l_V + 2l_S + l_D}{2} \quad , \quad \Delta L = \sqrt{\frac{l_V^2 + l_D^2}{4}} \tag{A.4}$$

Values for L can be then randomly drawn from a Gaussian distribution given the errors and assigned to each event in a CC-inclusive event generator sample. This provides a large spread of possible L values that have creation-interaction points spanning the entire range of the decay volume and detector. Hard limits must be placed on the random draws using

$$L_{\text{minimum}} = l_S, \tag{A.5}$$

$$L_{\text{maximum}} = l_V + l_S + l_D, \tag{A.6}$$

to ensure unphysical values of L that lie outside of the experiment are not chosen.

Using large uncertainties on L averages out oscillations from a number of different baselines reducing sensitivity to short baseline oscillations. If ΔL is overestimated then the residuals evaluated for a given set of mixing parameters may be underestimated due to this reduced sensitivity. Conversely if ΔL is underestimated or L is systematically different to the true oscillation distance then the problematic residual regions defined in Chapter 4 may be shifted in and out of the mixing parameter space of interest depending on the choice of L.